Thermodynamics and kinetics of methane hydrate formation in nanoporous media : theory and molecular simulation

Dongliang Jin

To cite this version:

Dongliang Jin. Thermodynamics and kinetics of methane hydrate formation in nanoporous media : theory and molecular simulation. Other [cond-mat.other]. Université Grenoble Alpes, 2018. English. NNT : 2018GREAY076 . tel-02181782

HAL Id: tel-02181782
https://theses.hal.science/tel-02181782

Submitted on 12 Jul 2019

HAL is a multi-disciplinary open access archive for the deposit and dissemination of scientific research documents, whether they are published or not. The documents may come from teaching and research institutions in France or abroad, or from public or private research centers.

L'archive ouverte pluridisciplinaire **HAL**, est destinée au dépôt et à la diffusion de documents scientifiques de niveau recherche, publiés ou non, émanant des établissements d'enseignement et de recherche français ou étrangers, des laboratoires publics ou privés.

Communauté
UNIVERSITÉ Grenoble Alpes

THÈSE

Pour obtenir le grade de

DOCTEUR DE LA
COMMUNAUTÉ UNIVERSITÉ GRENOBLE ALPES

Spécialité : NANOPHYSIQUE

Arrêté ministériel : 25 mai 2016

Présentée par

Dongliang JIN

Thèse dirigée par **Benoît COASNE**, CNRS

préparée au sein du **Laboratoire Laboratoire Interdisciplinaire de Physique**
dans **l'École Doctorale Physique**

Thermodynamique et cinétique de la formation de l'hydrate de méthane confiné dans un milieu nanoporeux : théorie et simulation moléculaire

Thermodynamics and Kinetics of Methane Hydrate Formation in Nanoporous Media: Theory and Molecular Simulation

Thèse soutenue publiquement le **10 décembre 2018**,
devant le jury composé de :

Madame CELINE TOUBIN
PROFESSEUR, UNIVERSITE LILLE , Rapporteur
Monsieur SYLVAIN PICAUD
DIRECTEUR DE RECHERCHE, CNRS DELEGATION CENTRE-EST, Rapporteur
Monsieur BERNARD SCHMITT
DIRECTEUR DE RECHERCHE, CNRS DELEGATION ALPES, Examinateur
Monsieur JEAN-MICHEL HERRI
PROFESSEUR, ECOLE DES MINES DE SAINT-ETIENNE, Président
Monsieur ARNAUD DESMEDT
CHARGE DE RECHERCHE, CNRS DELEGATION AQUITAINE, Examinateur

Thermodynamics and Kinetics of Methane Hydrate Formation in Nanoporous Media: Theory and Molecular Simulation

Dongliang JIN

Supervisor: Dr. Benoit COASNE

Laboratoire Interdisciplinaire de Physique
Université Grenoble Alpes, Grenoble, France

A thesis submitted in partial fulfillment of the requirements for the degree
of *Doctor of Physics*

December 10, 2018

...This thesis is dedicated to

my supervisor, Dr. Benoit COASNE, for his guidance

and

my wife, Mme. Yao CHEN, for her understanding

and

my son, Chenyu JIN, for his birth...

Acknowledgements

I would like to express my sincere gratitude to my supervisor, Benoit COASNE, for his patient, guidance, and scientific training. During my PhD study, Benoit not only gives me lots of details of methods to achieve my project (e.g., molecular simulation, free energy calculations, parallel tempering, and direct coexistence method), but also trains me to construct the physical model (e.g., Gibbs-Thomson equation) high-rise from the ground. These important discussions open my mind from a physicist's insight and make it possible to achieve the topic of "nanoconfinement effects on crystallization" in the future. In academics, I would also like to thank Florent CALVO, Alexander SCHLAICH, Jean-louis BARRAT, Jean-Michel HERRI, and Lev GELB for their helpful discussions, suggestions, and comments. I also would like to thank all my colleges (Kirsten MARTENS, Eric BERTIN, Marc JOYEUX, Vivien LECOMTE, Romain MARI, Romain BEY, Jules GUIOTH, Sam COHEN, Raffaela CABRIOLU, etc.) for scientific discussions and providing a friendly environment in PSM group. Many thanks to my friends (Chen LIU, Zaiyi SHEN, Hengdi ZHANG, Baoshuang SHANG, etc.) for making my life easier and happy in Grenoble. Especially, I wish to thank my wife CHEN Yao for following me overseas to Grenoble to face the challenge for a new-start family, and thank you for all the effort of upcoming birth of our son. And for my son, I want to say "Welcome to the world!". I would like to thank these two institutes, China Scholarship Council (CSC, No. 201506450015) and Laboratoire Interdisciplinaire de Physique (LiPhy), for providing financial fund to support my PhD study.

Abstract

Methane hydrate is a non-stoichiometric crystal in which water molecules form hydrogen-bonded cages that entrap methane molecules. Abundant methane hydrate resources can be found on Earth, especially trapped in mineral porous rocks (e.g., clay, permafrost, seafloor, etc.). For this reason, understanding the thermodynamics and formation kinetics of methane hydrate confined in porous media is receiving a great deal of attention. In this thesis, we combine computer modeling and theoretical approaches to determine the thermodynamics and formation kinetics of methane hydrate confined in porous media. First, the state-of-the-art on the thermodynamics and formation kinetics of methane hydrate is presented. Second, different molecular simulation strategies, including free energy calculations using the Einstein molecule approach, the direct coexistence method, and the hyperparallel tempering technique, are used to assess the phase stability of bulk methane hydrate at various temperatures and pressures. Third, among these strategies, the direct coexistence method is chosen to determine the shift in melting point upon confinement in pores, $\Delta T_m = T_m^{pore} - T_m^{bulk}$ where T_m^{pore} and T_m^{bulk} are the melting temperatures of bulk and confined methane hydrate. We found that confinement decreases the melting temperature, $T_m^{pore} < T_m^{bulk}$. The shift in melting temperature using the direct coexistence method is consistent with the Gibbs-Thomson equation which predicts that the shift in melting temperature linearly depends on the reciprocal of pore width, i.e., $\Delta T_m / T_m^{bulk} \sim k_{GB}/D_p$. The quantitative validity of this classical thermodynamic equation to describe such confinement and surface effects is also addressed. The surface tensions of methane hydrate-substrate and liquid water-substrate interfaces are determined using molecular dynamics to quantitatively validate the Gibbs-Thomson equation. Molecular dynamics

simulations are also performed to determine important thermodynamic properties of bulk and confined methane hydrate: (a) thermal conductivity λ using the Green-Kubo formalism and the autocorrelation function of the heat-flux and (b) the thermal expansion α_P and isothermal compressibility κ_T. Finally, some conclusions and perspectives for future work are given.

Résumé

L'hydrate de méthane est un cristal non-stœchiométrique dans lequel les molécules d'eau forment des cages liées par liaison hydrogène qui piégent des molécules de méthane. Des ressources abondantes en hydrate de méthane peuvent être trouvées sur Terre, en particulier dans les roches poreuses minérales (par exemple, l'argile, le permafrost, les fonds marins, etc.). Pour cette raison, la compréhension de la thermodynamique et de la cinétique de formation de l'hydrate de méthane confiné dans des milieux poreux suscite beaucoup d'attention. Dans cette thèse, nous combinons la modélisation moléculaire et des approches théoriques pour déterminer la thermodynamique et la cinétique de formation de l'hydrate de méthane confiné dans des milieux poreux. Tout d'abord, l'état de l'art en matière de thermodynamique et de cinétique de formation de l'hydrate de méthane est présenté. Deuxièmement, différentes stratégies de simulation moléculaire, y compris des calculs d'énergie libre utilisant l'approche de la molécule d'Einstein, la méthode de coexistence directe et la technique *hyperparallel tempering*, sont utilisées pour évaluer la stabilité de l'hydrate de méthane à différentes températures et pressions. Troisièmement, parmi ces stratégies, la méthode de coexistence directe est choisie pour déterminer le déplacement du point de fusion lors du confinement dans des pores, $\Delta T_m = T_m^{pore} - T_m^{bulk}$ où T_m^{pore} et T_m^{bulk} sont les températures de fusion d'hydrate de méthane non confiné et confiné. Nous avons constaté que le confinement diminue la température de fusion, $T_m^{pore} < T_m^{bulk}$. Le changement de température de fusion en utilisant la méthode de la coexistence directe est cohérent avec l'équation de Gibbs-Thomson qui prédit que le décalage de la température de fusion dépend linéairement de l'inverse de la taille des pores, $\Delta T_m / T_m^{bulk} \sim k_{GT}/D_p$. La validité quantitative de cette équation thermodynamique classique pour décrire de tels effets

de confinement et de surface est également abordée. Les tensions de surface des interfaces hydrate-substrat et eau-substrat sont déterminées à l'aide de la dynamique moléculaire pour valider quantitativement l'équation de Gibbs-Thomson. Des simulations de dynamique moléculaire sont également effectuées pour déterminer les propriétés thermodynamiques importantes de l'hydrate de méthane non confiné et confiné: (a) conductivité thermique λ en utilisant le formalisme de Green-Kubo et la fonction d'autocorrélation du flux thermique; (b) expansion thermique α_P et compressibilité isotherme κ_T. Enfin, des conclusions et perspectives pour des travaux futurs sont présentées.

Contents

Acknowledgements **iv**

Abstract **vi**

Résumé **ix**

List of Figures **xv**

List of Tables **xxix**

Introduction **1**

1 State-of-the-art: Methane Hydrate **5**

1.1 Structure 6

1.1.1 Crystalline structure and molecular model 6

1.1.2 Order parameter 9

1.2 Thermodynamic properties 13

1.3 Formation/dissociation and phase stability 15

1.3.1 Crystallization 15

1.3.2 Melting/Dissociation 19

1.3.3 Phase diagram 19

1.4 Confinement effects at the nanoscale 28

1.5 Summary 32

2 Statistical Mechanics and Computational Methods **35**

2.1 Statistical mechanics 37

2.1.1 Classical statistical mechanics 37

2.1.2 Ensembles 39

2.2 Monte Carlo simulation 41

2.2.1 Detailed balance and Metropolis scheme 41

2.2.2 Trial moves and acceptance probabilities 43

2.2.3 Details of Monte Carlo simulation 47

2.3 Molecular Dynamics 49

2.3.1 Ergodicity 49

2.3.2 Newton's equation 49

2.3.3 Integration scheme 50

2.3.4 Thermostat and barostat 51

2.3.5 Details of molecular dynamics 53

2.4 Interaction potentials 54

2.4.1 Intramolecular potential 54

2.4.2 Intermolecular potential 55

2.5 Molecular models 59

3 Molecular Simulation of the Phase Diagram of Bulk Methane Hydrate 61

3.1 Molecular structure of methane hydrate 63

3.2 Liquid–Hydrate–Vapor equilibrium 65

3.2.1 Phase coexistence conditions 65

3.2.2 Estimation of the different chemical potentials 67

3.3 Phase diagram of methane hydrate 71

3.3.1 Free energy approach 71

3.3.2 Direct Coexistence Method in the Grand Canonical Ensemble . . 83

3.3.3 Hyper Parallel Tempering 88

3.4 Conclusion 89

4 Formation and Dissociation of Confined Methane Hydrate 93

4.1 Computational details 95

4.1.1 Molecular models 95

4.1.2 Surface tensions 96

4.1.3 Umbrella sampling 98

4.2 Formation and dissociation of confined methane hydrate 100

4.2.1 Phase stability of confined methane hydrate 100

4.2.2 Gibbs-Thomson equation 104

4.2.3 Free energy calculations and kinetics 112

4.3 Conclusion 115

5 Physical and Physicochemical Properties of Confined Methane Hydrate 119

5.1 Computational details 120

5.1.1 Molecular models 120

5.1.2 Molecular dynamics details 121

5.1.3 Thermal conductivity 122

5.2 Structure 124

5.3 Thermodynamic coefficients 128

5.4 Thermal conductivity 133

5.5 Conclusion 138

Conclusions and Perspectives 140

Conclusions et Perspectives 144

Appendix A Einstein Molecule Approach 149

A.1 Vectors **a** and **b** 149

A.2 Free energy of non-interacting Einstein molecule A_A 150

A.3 Free energy difference ΔA_1 and ΔA_2 154

A.4 Chemical potentials: water and methane 155

A.5 Contributions to chemical potential of water in methane hydrate 157

Appendix B Finite Size Effects 159

B.1 Vacuum layer width effect 159

B.2 Molecular system size effect 160

B.3 Pore width effects at $P = 10$ atm 161

B.4 Surface wettability effect 162

B.5 Surface tension γ_{HS} 163

References **165**

List of Figures

1.1 (*left*) Gas hydrate with structure I (sI): the small spheres are water molecules forming hydrogen-bonded cavities and the large spheres are the gas molecules. The gray polyhedrons represent the cavities generated by the water molecules. (*right*) Typically, the types and numbers of water cavities correspond to one of the three following structures of gas hydrate: sI, sII, and sH. The circled numbers are the numbers of such water cavities which are used to form the corresponding hydrate structure. [Picture from Ref. (Schulz and Zabel, 2006)] 7

1.2 Three criteria should be satisfied for methane hydrate with sI structure (Bernal and Fowler, 1933; Chakraborty and Gelb, 2012a): (1) proton disorder; (2) ice rules; and (3) zero dipole moment. The red and green spheres are the oxygen and hydrogen atoms of water, respectively. 8

1.3 (color online) Averaged local bond order parameters, $\langle Q_4 \rangle$–$\langle Q_6 \rangle$–plane, for liquid water (blue), hexagonal ice (red), and methane hydrate (black) at $T = 200$ K. [Picture from Ref. Reinhardt et al. (2012)] 12

1.4 Free energy (solid line), ΔG, as a function of nucleus radius, r, in the the formation process of methane hydrate. Formation can be described as the interplay between the hydrate–liquid surface free energy (surface term corresponding to the dashed line), ΔG_S, and the free energy difference between liquid water and methane hydrate (volume term corresponding to the dot dashed line), ΔG_V. The critical radius, r_c, and the corresponding free energy barrier, ΔG_{barr}, are also shown in this figure. If the nucleus radius is larger than the critical radius, i.e., $r > r_c$, the nucleus keeps growing to form methane hydrate (“growth”). For $r < r_c$, the nucleus melts into liquid water (“shrink”). 16

1.5 Pressure–temperature (P–T) phase diagram for liquid (L), ice (I), vapor (V), and hydrate (H) phases. The phase boundary – dashed line – indicates the conditions for which ice coexists with liquid water, L–I. The phase boundary – solid line AQ – indicates the conditions for which methane hydrate coexists with ice and methane vapor, I–H–V. The phase boundary – solid line QB – indicates the conditions for which methane hydrate coexists with liquid water and methane vapor, L–H–V. Four regions involving the two phase coexistence are shown: (1) hydrate coexists with ice, H+I; (2) hydrate coexists with liquid water, H+L; (3) methane vapor coexists with liquid water, V+L; and (4) methane vapor coexists with ice, V+I. Q is a four phase coexistence point, L–H–I–V. 20

1.6 Free energy, G, as a function of the normalized order parameter, OP, using biased molecular simulations. Liquid water (L) exhibits a small order parameter, while methane hydrate (H) exhibits a large order parameter. At the melting temperature, $T = T_m$, methane hydrate coexists with liquid water (i.e., the free energies of liquid water and methane hydrate are equal). At high temperature, $T > T_m$, liquid water is stable (i.e., the free energy of liquid water is smaller than that of methane hydrate). At low temperature, $T < T_m$, methane hydrate is stable (i.e., the free energy of methane hydrate is smaller than that of methane hydrate). The free energy barrier between liquid water and methane hydrate, ΔG_{barr}, upon formation is also shown. . 24

1.7 (color online) Typical molecular configurations obtained in the direct coexistence method at $T = 294$ K and $P = 600$ bar (where methane hydrate is stable): (*top*) the coexisting phases, i.e., liquid water (L) + methane hydrate (H) + methane vapor (V), are the initial configuration; (*center*) the growth of methane hydrate; and (*bottom*) the perfect methane hydrate formed at the end of the molecular simulation. The red and white lines denote the water molecules while the blue spheres are the methane molecules. [Picture from Ref. (Conde and Vega, 2010)] 26

1.8 Boltzmann factor, $\exp(-U/k_B T)$, in the phase space, Γ, as an example to illustrate the parallel tempering technique. The blue line is for the low temperature, while the red line is for the high temperature. The system in state A (blue circle) remains easily trapped into a metastable state, while the system in state B (red circle) escape more easily. Parallel tempering between A and B is used to make the escape easier. 27

3.1 (color online) Molecular configuration of methane hydrate with structure sI. The red and white spheres are the oxygen and hydrogen atoms of water, respectively. The gray spheres are the methane molecules which are trapped inside the hydrogen-bonded cages formed by water molecules (1 methane molecule for 8 water molecules). The dimensions of this molecular configuration, which corresponds to $2 \times 2 \times 2$ unit cells, are: $L_x = L_y = L_z = 2.3754$ nm. 65

3.2 Stochastic algorithm to generate methane hydrate molecular configurations with sI structure (Buch et al., 1998): (1) set the oxygen positions according to the experimental X-ray crystallographic data (Kirchner et al., 2004); (2) generate proton disorder by randomly assigning a hydrogen atom to one of the oxygen atoms in each O–O pair (step I); (3) use a stochastic MC algorithm to verify the ice rules (step II); (4) repeat steps I and II 20000 times to generate as many configurations and select the configuration with minimum dipole moment (step III); and (5) insert the methane molecules into the cages of the methane hydrate (step IV). The red and white spheres are the oxygen and hydrogen atoms of water, respectively. The gray spheres are the methane molecules. The dimensions of the system shown here are $L_x = L_y = L_z = 2.3754$ nm which correspond to $2 \times 2 \times 2$ unit cells. 66

3.3 Thermodynamic path used in the Einstein molecule approach to calculate the free energy of the zero-occupancy methane hydrate, A_{C}. Orange and green spheres are the oxygen and hydrogen atoms of water, respectively. The green box shows the periodic boundary conditions of the simulation cell. The superscript * indicates that the system has one of its water molecules at a fixed position shown by the big pink '+' sign (*see text*). A_{A} is the free energy of the non-interacting Einstein molecule while $A_{\mathrm{A}*}$ is the free energy of the same system with one of its water molecules at a fixed position. $A_{\mathrm{B}*}$ is the free energy of the interacting Einstein molecule with one of its water molecules at a fixed position. $A_{\mathrm{C}*}$ is the free energy of the zero-occupancy methane hydrate with one of its water molecules at a fixed position while A_{C} is the free energy of the same system without fixing any water molecule positions. Constraining a water molecule position (3 degrees of freedom) increases the free energy by $k_B T \ln\left(V/\Lambda^3\right)$. The change in free energy between the non-interacting and interacting Einstein molecule is $\Delta A_1 = A_{\mathrm{B}*} - A_{\mathrm{A}*}$. The change in free energy between the constrained interacting Einstein molecule and the constrained methane hydrate is $\Delta A_2 = A_{\mathrm{C}*} - A_{\mathrm{B}*}$ (*see text*). 74

3.4 Free energy changes ΔA_1 (a) and ΔA_2 (b) and free energy $A_w^H(x_m = 0)$ of the zero-occupancy methane hydrate (c) as a function of temperature T (all data reported here are for $P = 100$ atm). The empty and closed circles are for the TIP4P/Ice and TIP4P/2005 water models, respectively. Free energies are normalized to the total thermal energy Nk_BT. $\Delta A_1 = A_{\mathrm{B}^*} - A_{\mathrm{A}^*}$ is the free energy difference between the non-interacting and interacting Einstein molecules (corresponding to the zero-occupancy methane hydrate). $\Delta A_2 = A_{\mathrm{C}^*} - A_{\mathrm{B}^*}$ is the free energy difference between the interacting Einstein molecule and the zero-occupancy methane hydrate. Except for the zero-occupancy methane hydrate in (c), all systems are constrained with one of their molecules having a fixed reference position. 77

3.5 Chemical potential of methane, μ_m^H, versus number of methane molecules, N_m^{H}, in methane hydrate at $T = 250$ K and $P = 10$ atm. N_m^H is expressed as the number of methane molecules per methane hydrate unit cell. The empty and filled circles are for TIP4P/Ice anf TIP4P/2005 water models, respectively. The dotted lines correspond to cubic interpolation of the data. The insert shows the chemical potential difference of water relative to the zero-occupancy methane hydrate, $\Delta\mu_w^{\mathrm{H}} = \mu_w^{\mathrm{H}} - \mu_w^{\mathrm{H}}(x_m = 0)$, as a function of the number of methane molecules, N_m^{H} (these data are obtained from $N_m(\mu_m)$ using Eq. (3.9)). The dashed and solid lines are for the TIP4P/Ice and TIP4P/2005 water models. All chemical potentials are normalized to the thermal energy, k_BT. 81

3.6 (color online) Equilibrium number of methane, $x_m(\mu_m^{\mathrm{V}} = \mu_m^{\mathrm{H}})$ (empty circles) and $x_m(\mu_w^{\mathrm{L}} = \mu_w^{\mathrm{H}})$ (filled circles), as a function of temperature, T, at $P = 1$ (blue), 10 (red), 100 (black) atm. The corresponding interpolation cross point, $x_m(\mu_m^{\mathrm{V}} = \mu_m^{\mathrm{H}}) = x_m(\mu_w^{\mathrm{L}} = \mu_w^{\mathrm{H}})$, indicating the liquid water-methane hydrate-methane vapor (L–H–V) equilibrium temperature and methane composition at the given pressure. The left and right panels are for TI4P/2005 and TIP4P/Ice water models, respectively. 82

3.7 Pressure–Temperature phase diagram of methane hydrate as determined using free energy calculations (circles, this work), direct coexistence method (gray pentagon, this work), hyper parallel tempering method (black pentagon, this work). The empty and filled symbols are for TIP4P/Ice and TIP4P/2005 water models, respectively. The empty and filled squares are the results obtained for TIP4P/Ice and TIP4P/2005 by Conde et al. (Conde and Vega, 2010) using the direct coexistence method. The empty triangles are the free energy calculations for TIP4P/Ice by Jensen et al. (Jensen et al., 2010). The solid line shows the experimental data by Sloan et al. (Sloan, 2003). The insert shows a zoomed view of the region shown depicted as a dashed rectangle in the main figure. 84

3.8 (color online) Determination of the phase transition temperature between methane hydrate and liquid phases using the direct coexistence method. (a) Starting from a methane hydrate coexisting with the liquid phase, several Monte Carlo simulations in the Grand Canonical ensemble (μVT) at different temperatures and chemical potentials are performed (chemical potentials are chosen so that the pressure is P = 100 atm). The red and white spheres are the oxygen and hydrogen atoms of water while the grey spheres are the methane molecules. The dimensions of the simulation box are: $L_x = L_y = L_z = 2.3754$ nm. Molecules with $y < 0$ (left region) and $y > 0$ (right region) belong to the methane hydrate and liquid phases, respectively. If the temperature is lower than the melting point T_m, the liquid disappears as methane hydrate forms. In contrast, if the temperature is larger than T_m, the methane hydrate melts and is replaced by the liquid. (b) Methane (left) and water (right) mole fractions during the different GCMC simulation runs: T = 260 K (black), 270 K (purple), 280 K (blue), 290 K (red), and 300 K (orange). The x-axis, which indicates progress along the GCMC simulation, is expressed as a number of attempted MC moves where one move is a molecule translation, rotation, insertion or deletion. 87

3.9 (color online) Determination of the phase transition temperature between the methane hydrate and liquid phases using hyper parallel tempering Monte Carlo simulations. (a) Several replicas M = 16 of the system are considered in parallel. Each replica is at different temperatures and chemical potentials (the latter are chosen so that the pressure of the system is P = 100 atm). The temperature ranges from 283 K to 298 K with a temperature difference $\Delta T = 1$ K. For each replica, a regular grand canonical Monte Carlo simulation consisting of molecule translation, rotation, insertion, and deletion moves are performed. In addition to these conventional moves, replicas at two different temperature/chemical potentials sets are swapped with a probability given from the ratio of the Boltzmann factors in the Grand Canonical ensemble (*see text*). The red and white spheres are the oxygen and hydrogen atoms of water while the grey spheres are the methane molecules. The dimensions of the simulation box are: $L_x = L_y = L_x = 2.754$ nm. (b) Average methane (left) and water (right) mole fraction as a function of temperature as estimated from the different replicas considered in the hyper parallel tempering simulation. 90

4.1 (color online) Molecular configuration of the confined coexisting phases (i.e., methane hydrate + liquid water) considered in this work. The red and white spheres are the oxygen and hydrogen atoms of water, respectively. The gray spheres are the methane molecules which are inside the hydrogen-bonded cages formed by water molecules. The yellow spheres are the solid atoms in the pore walls. The two component system is confined in a pore with a width D_p made of layers of solid particles distributed according to a square structure. Each pore surface is made of 4 layers separated by a distance $D_l = 0.2159$ nm so that the total pore wall thickness is 0.7558 nm. Inside the porosity, methane hydrate is located in the region $y < 0$ (left side) and liquid water in the region $y > 0$ (right side). In this specific configuration, the pore size is $D_p = 2.8554$ nm which corresponds to $2 \times 2 \times 2$ unit cells of bulk sI methane hydrate (the lattice parameter of methane hydrate is u = 1.1877 nm). Periodic boundary conditions are used along the x, y, and z directions. The dimensions of the simulation box (defined by the dashed lines) are $L_x = L_y = 2.3754$ nm and $L_z = 4.3670$ nm. 97

4.2 (color online) Schematic illustration of the determination of the surface tension using the Kirkwood-Buff approach. (1) The configuration of phases α (orange region) and β (gray region) is prepared. These two phases define two planar α–β–interfaces perpendicular to the z axis (*left*): the surface area in the x–y–plane is A and the length of the simulation box in the z–direction is L_z. The normal and parallel pressure components are $P_T(z) = (P_{xx}(z) + P_{yy}(z))/2$ and $P_N(z) = P_{zz}(z)$. (2) A small change dA is considered in the surface area the in x–y–plane. (3) The change is compensated by a small change dz to keep the volume V constant, i.e., $L_z dA = -(A + dA)dz$. 98

4.3 (color online) Pore size, D_p, effect on the melting temperature, T_m^{pore}, of confined methane hydrate/liquid water using the direct coexistence method: methane (x_m, *left*), and water (x_w, *right*) mole fractions for $D_p = 2.8554$ nm during the different GCMC simulation runs at T = 230 K (black), 240 K (blue), 250 K (purple), 260 K (red), and 270 K (orange). The x-axis, which indicates progress along the GCMC simulation, is expressed as a number of attempted MC moves where one move is a molecule translation, rotation, insertion or deletion. 101

4.4 (color online) Melting temperature, T_m^{pore}, of confined methane hydrate/liquid water for different pore widths: $D_p = 1.6677$ nm (*left panels*), 5.2308 nm (*center panels*), and 7.6062 nm (*right panels*) as obtained using the direct coexistence method. The methane (x_m, *top panels*) and water (x_w, *bottom panels*) mole fractions during the different GCMC simulation runs are shown: T for each pore size is indicated using different colors (see figure legend). The x-axis, which indicates progress along the GCMC simulation, is expressed as a number of attempted MC moves where one move is a molecule translation, rotation, insertion or deletion. T_m^{pore} of confined methane hydrate for different D_p are summarized in Table 4.1. For bulk methane hydrate, we reported $T_m^{bulk} = 285 \pm 5$ K at $P = 100$ atm using the direct coexistence method in Chapter 3. 103

4.5 (color online) Gibbs-Thomson equation for L–H–V equilibrium upon confinement: methane hydrate (H, red region) and liquid water (L, blue region) are confined in a slit pore of a width D_p formed by two parallel substrates (S, the gray regions). Ω^{H} and P^{H} are the grand potential and pressure of methane hydrate while Ω^{L} and P^{L} are the grand potential and pressure of liquid water. γ_{LS} is the surface tension of liquid water–substrate (LS) interface while γ_{HS} is the surface tension of methane hydrate–substrate (HS) interface. $V = D_p A$ is the pore volume where A is the surface area. 104

4.6 (color online) Molar volume v (a) and molar enthalpy h (b) of liquid water (solid circles), full-methane hydrate (empty squares), and empty-methane hydrate (empty triangles). Enthalpy of melting Δh_m (c) from full-methane hydrate (empty squares) to liquid water and from empty-methane hydrate (empty triangles) to liquid water using MD simulations. The dashed lines indicate that these parameters are along the L–H–V phase boundary for bulk phase: the red, blue, and green colors are for $(T,P) = (233$ K, 1 atm), (262 K, 10 atm), and (286 K, 100 atm), respectively. All the thermodynamic parameters are per mole of water. 108

4.7 Normal (black line), $P_N = P_{zz}$, and parallel (gray line), $P_T = \frac{1}{2}(P_{xx} + P_{yy})$, pressure components of methane hydrate (*left*) and liquid water (*right*) in a slit pore $D_p = 9.9816$ nm as a function of time, t, in canonical ensemble MD simulation at $T = 290$ K. The dimensions of the simulation box are: $L_x = L_y = 2.3754$ nm and $L_z = 41.4932$ nm. 110

4.8 Shift in melting temperature of confined methane hydrate with respect to the bulk, $\Delta T_m^{pore}/T_m^{bulk}$, at $P = 100$ atm as a function of the reciprocal of pore size, $1/D_p$. The solid circles are obtained using the direct coexistence method while the solid line is determined using the revisited version of the Gibbs-Thomson equation: $\Delta T_m^{pore}/T_m^{bulk} = 2(\gamma_{LS} v^{\mathrm{L}} - \gamma_{HS} v^{\mathrm{H}})/\Delta h_m D_p$. . . 111

4.9 (color online) Free energy, G, of methane hydrate and liquid water in bulk phase (*left*) and in confined phase for $D_p = 2.8554$ nm (*right*) as a function of the local bond order parameter, Q_6. $G(Q_6)$ of bulk phase (*left*) is shown at $T = 290$ K (blue), 310 K (purple), 330 K (orange) and 350 K (red). $G(Q_6)$ upon confinement (*right*) is shown at $T = 290$ K (blue), 300 K (green), and 310 K (purple). The free energy is normalized using the thermal energy, k_BT. For the sake of clarity, a shift of +10, +20, and +30 in G/k_BT is added for the bulk phase at $T = 310$ K, 330 K, and 350 K. A shift of +10 and +20 in G/k_BT is added for the confined phase at $T = 300$ K and 310 K. 114

4.10 (color online) Free energy difference, ΔG^{LH}, between methane hydrate and liquid water as a function of temperature, T. The blue circles are for bulk methane hydrate and the red circles are for confined methane hydrate in a pore $D_p = 2.8554$ nm. The blue dashed line is a linear fit for bulk methane hydrate while the red dashed line is a linear fit for confined methane. These fits lead to $T_m^{bulk} = 302$ K and $T_m^{pore} = 257$ K for $D_p = 2.8554$ nm. The free energy is normalized using the thermal energy, k_BT. 114

4.11 (color online) Free energy barriers, $\Delta G_{barr}/k_BT$, between methane hydrate and liquid water as a function of the shift with respect to the melting point, $T - T_m$, for bulk phase (red) and for confined phase (blue): (1) free energy barriers from liquid water to methane hydrate, i.e., methane hydrate formation (*left*), $\Delta G_{barr}^{L\rightarrow H}$; and (2) free energy barrier from methane hydrate to liquid water, i.e., methane hydrate dissociation (*right*), $\Delta G_{barr}^{H\rightarrow L}$. The red cross is for bulk methane hydrate while the blue cross is for confined methane hydrate using the extroplation described in the text. The free energy barriers are normalized using the thermal energy, k_BT. 116

5.1 (color online) Molecular configuration of confined methane hydrate (*left*) and liquid water (*right*). The red and white spheres are the oxygen and hydrogen atoms of water, respectively. The gray spheres are the methane molecules which are inside the hydrogen-bonded cages formed by water molecules. The yellow spheres are the solid atoms of the pore walls. Pore walls are set as described in Chapter 4 but with pistons at the top wall and bottom wall. In this specific configuration, the sI methane hydrate with dimensions of $L_x = L_y = L_z = 2.3754$ nm is confined inside the porosity (*left*). The liquid water (*right*) is obtained by first removing methane molecules and then melting the hydrate phase in the canonical ensemble followed by simulations at constant pressure. The dimensions of the simulation box are $L_x = L_y = 2.3754$ nm and $L_z = 44.5734$ nm (*left*) and 41.4932 nm (*right*). Periodic boundary conditions are used along the x– and y–directions. 122

5.2 Density profiles along the z–axis, $\rho(z)$, of water in liquid phase (*top*), methane in hydrate phase (*center*), and water in hydrate phase (*bottom*) at $T = 240$ K and $P = 100$ atm. The red solid lines are for bulk phases while the green solid lines are for confined phases. The black dashed lines are the positions of the pore walls with the pore width D_p. The blue dashed lines are the dimension in the z–direction for bulk methane hydrate with $L_z = 2$ u. The red dashed lines are the density profiles for a duplicated bulk phase. 126

5.3 Local bond order parameters along the z–axis, $Q_6(z)$, in liquid water (*top*) and methane hydrate (*bottom*) at $T = 240$ K and $P = 100$ atm. The red solid lines are for bulk phases while the green solid lines are for confined phases. The black dashed lines are the positions of the pore walls with the pore width D_p. The blue dashed lines indicate the dimension in the z–direction for bulk methane hydrate with $L_z = 2$ u. The red dashed lines are the local bond order parameters for a duplicated bulk phase. 127

5.4 (color online) Volume (V, *left*) and thermal expansion (α_P, *right*) of bulk and confined liquid water as a function of temperature T at $P = 100$ atm. Two different ensembles were considered for bulk liquid water: NPT ensemble (blue circles) and NP_zT ensemble (black circles). For confined liquid water, a minimum value D_p^{min} (orange circles) and a maximum value D_p^{max} (red circles) of the pore width were considered. A total of 368 water molecules were used to determine these data. The dashed lines are linear fits. 130

5.5 (color online) Volume (V, *left*) and thermal expansion (α_P, *right*) of bulk and confined methane hydrate as a function of temperature T at $P = 100$ atm. Two different ensembles were considered for bulk methane hydrate: NPT ensemble (blue circles) and NP_zT ensemble (black circles). For confined methane hydrate, a minimum value D_p^{min} (orange circles) and a maximum value D_p^{max} (red circles) of the pore width were considered. The dashed lines (*left*) are linear fits. The solid black line are experimental data while the dashed black line (*right*) are simulation data for bulk methane hydrate (Ning et al., 2012, 2015). 130

5.6 (color online) Volume (V, *left*) and isothermal compressibility (κ_T, *right*) of bulk and confined liquid water as a function of pressure P at $T = 240$ K. Two different ensembles were considered for bulk liquid water: NPT ensemble (blue circles) and NP_zT ensemble (black circles). For confined liquid water, a minimum value D_p^{min} (orange circles) and a maximum value D_p^{max} (red circles) of the pore width were considered. The dashed lines are linear fits. 132

5.7 (color online) Volume (V, *left*) and isothermal compressibility (κ_T, *right*) of bulk and confined methane hydrate as a function of pressure P at $T = 240$ K. Two different ensembles were considered for bulk methane hydrate: NPT ensemble (blue circles) and NP_zT ensemble (black circles). For confined methane hydrate, a minimum value D_p^{min} (orange circles) and a maximum value D_p^{max} (red circles) of the pore width were considered. The dashed lines are linear fits. 132

5.8 (color online) Autocorrelation function of the heat-flux vector, $h(t)$, as a function of time, t, for bulk (*left*) and confined (*right*) methane hydrate. For bulk methane hydrate, the black solid line is from this work while the black dashed line is from English et al. (English and Tse, 2009; English et al., 2009). For confined methane hydrate, the red solid line is the tangential component $h_N = V/k_BT \langle J_z(t)J_z(0)\rangle$ while the green solid line is the normal component $h_T = V/2k_BT \left\langle J_x(t)J_x(0) + J_y(t)J_y(0)\right\rangle$. 133

5.9 (color online) Fourier transform $\mathscr{F}[\upsilon]$ of the autocorrelation function of the heat-flux for bulk ($h(t)$, *left*) and confined ($h_T(t)$, *center*; $h_N(t)$, *right*) methane hydrate. For bulk methane hydrate, the black solid line is from this work while the black dashed line is from English et al. (English and Tse, 2009; English et al., 2009). For confined methane hydrate, the red solid line is for $h_N = V/k_BT \langle J_z(t)J_z(0)\rangle$ while the green solid line is for $h_T = V/2k_BT \left\langle J_x(t)J_x(0) + J_y(t)J_y(0)\right\rangle$. 135

5.10 Inverse Fourier transform of the power spectrum for bulk methane hydrate. The acoustic mode (gray line) and optical mode (black line) are separated as described in the text. The maxima/peaks of the optical modes (black circles) and the smoothed points for the acoustic modes (gray circles) are considered to determine the relaxation time and amplitudes (*see text*). . . 135

5.11 (color online) Piecewise linear fits applied to the acoustic – smoothed points – (gray circles, *right panels*) and optical – maxima/peaks – (black circles, *left panels*) modes for bulk methane hydrate (*top panels*) and the tangential (*center panels*) and normal (*bottom panels*) components of confined methane hydrate. Piecewise linear fits for optical modes are shown for short-range (red solid lines), long-range (blue solid lines), and constant term (green solid lines) terms. for $h_N(t)$, two optical modes are included but only one optical mode ($\omega_j = 186.7$ rad/ps) is shown here (the fit results for the other one are shown in Table 5.2). Piecewise linear fits for acoustic modes are shown for short-range (red hashed lines), medium-range (blue dashed lines), and long-range (green dashed lines) terms. The black solid lines are for overall optical fits while the gray solid lines are for overall acoustic fits. 137

A.1 Definition of the normalized vectors **a** and **b** in the 4-site rigid water molecule (TIP4P/2005 and TIP4P/Ice). These two vectors are formed by the subtraction $\mathbf{a} = (\mathbf{l}_1 - \mathbf{l}_2)/|\mathbf{l}_1 - \mathbf{l}_2|$ and summation $\mathbf{b} = (\mathbf{l}_1 + \mathbf{l}_2)/|\mathbf{l}_1 + \mathbf{l}_2|$ of the two bond vectors, $\mathbf{l}_1$ and $\mathbf{l}_2$. The red and white spheres are the oxygen and hydrogen atoms, respectively. The green sphere is the electronic site M of the oxygen atom. 149

A.2 Intermolecular potential energy U of the zero-occupancy methane hydrate along the canonical ensemble MC simulation at $T = 250$ K and $P = 100$ atm (black line) (only the harmonic potential U_{A^*} is considered in the acceptance probability): (a) TIP4P/2005 water model; (b) TIP4P/Ice water model. Note that the figure shows $\exp\left(-(U - U^{(0)})/k_B T\right)$ where $U^{(0)}$ is the potential energy of the reference lattice system . The gray horizontal line is the canonical ensemble averaged value, $\left\langle \exp\left(-(U - U^{(0)})/k_B T\right)\right\rangle_{NVT}$. All energies are normalized to the thermal energy $k_B T$. 154

A.3 Canonical ensemble average of the harmonic potential energy U_{A^*} as a function of the coupling parameter λ at $T = 250$ K and $P = 100$ atm: (a) TIP4P/2005 water model (filled circles) and (b) TIP4P/ICE water model (empty circles). These values are obtained from several canonical ensemble MC simulations for the hybrid potential energy, $U(\lambda) = (1-\lambda)U_{\mathrm{C}^*} + \lambda U_{\mathrm{B}^*}$. The first molecule in the corresponding molecular system have a fixed position in all these MC simulations. All energies are normalized to the thermal energy k_BT. The absolute error bar for each average energy is smaller than 0.6. 154

A.4 Determination of the chemical potential of methane and water in methane hydrate using TIP4P/2005 water in combination with OPLS-UA methane model: (1) methane occupancy N_m^{H} (the number of molecules per unit cell) versus fugacity f (left panel), (2) chemical potential of methane $\mu_m^{\mathrm{H}}/k_BT = \ln\frac{f\Lambda^3}{k_BT}$ (center panel) and water $\mu_w^{\mathrm{H}}/k_BT = \mu_w^{(0)}/k_BT - \frac{1}{N_wk_BT}\int_{-\infty}^{\mu_m} N_m d\mu_m$ (right panel) versus N_m^{H}. In the left panel, the temperature increases from 180 to 350 K ($\Delta T = 10$ K) (from left to right); In the center and right panels, temperature increases from 180 to 350 K ($\Delta T = 10$ K) (from top to bottom). The pressures are $P = 1$ atm (top), 10 atm (middle), and 100 atm (bottom). All chemical potentials are normalized to the thermal energy, k_BT.155

A.5 Same as Figure A.4 but for the TIP4P/Ice water model. 156

A.6 Contributions to the chemical potential of water in methane hydrate $\mu_w^{\mathrm{H}}(x_m)/k_BT$ at $T = 250$ K and $P = 100$ atm. $\mu_w^{\mathrm{H}}(x_m)/k_BT = \mu_w^{\mathrm{H}}(x_m = 0)/k_BT + \Delta\mu_w^{\mathrm{H}}(x_m)/k_BT$ where $\mu_w^{\mathrm{H}}(x_m = 0)/k_BT$ (black solid line) is the chemical potential of water in zero-occupancy methane hydrate and $\Delta\mu_w^{\mathrm{H}}(x_m)/k_BT$ (black dashed line) is the contribution due to the methane occupancy. $\mu_w^{\mathrm{H}}(x_m = 0)/k_BT = A_w(x_m = 0)/N_wk_BT + A_{disorder}/N_wk_BT + PV/N_wk_BT$ where $A_w(x_m = 0)/k_BT$ is the contribution from the Helmholtz free energy of zero-occupancy methane hydrate using Einstein molecule approach (green solid line), $A_{disorder}$ is the proton disorder correction (blue solid line), and PV/N_wk_BT term (red solid line). The data shown here are for the TIP4P/Ice water model (similar qualitative results were obtained for the TIP4P/2005 water model). Note the use of a broken axis along the y-axis. 157

B.1 (color online) Methane (x_m, *left*) and water (x_w, *right*) mole fractions during the different GCMC simulation runs: T = 230 K (black), 240 K (blue), 250 K (purple), 260 K (red), and 270 K (orange). The x-axis, which indicates progress along the GCMC simulation, is expressed as a number of attempted MC moves where one move is a molecule translation, rotation, insertion or deletion. The dimensions of the simulation box are: $L_x = L_y = 2.3754$ nm and $L_z = 8.3674$ nm (corresponding to $D_p = 2.8554$ nm with a vacuum layer $D_v = 2.0000$ nm in each side). 159

B.2 (color online) Methane (x_m, *left panels*) and water (x_w, *right panels*), mole fractions during the different GCMC simulation runs: T = 230 K (black), 240 K (blue), 250 K (purple), 260 K (red), and 270 K (orange) for $D_p = 2.8554$ nm (*top panels*); and T = 260 K (blue), 270 K (purple), 280 K (red), and 290 K (orange) for $D_p = 5.2308$ nm (*bottom panels*). The x-axis, which indicates progress along the GCMC simulation, is expressed as a number of attempted MC moves where one move is a molecule translation, rotation, insertion or deletion. The dimensions of the simulation box are: $L_x = 2.3754$ nm, $L_y = 4.7508$ nm, and $L_z = 4.3670$ nm for $D_p = 2.8554$ nm (*top panels*) while $L_z = 6.7424$ nm for $D_p = 5.2308$ nm (*bottom panels*). 160

B.3 Shift in the melting temperature of confined methane hydrate with respect to the bulk, $\Delta T_m^{pore}/T_m^{bulk}$, as a function of the reciprocal of the pore width, $1/D_p$: the dashed line is for the larger molecular system (i.e., $L_y = 4.3670$ nm); while the solid line is for the smaller one (i.e., $L_y = 2.3754$ nm). Note that T_m^{pore} for larger system reads from Figure B.2, while T_m^{bulk} and k_{GB} are estimated using these data. 160

B.4 (color online) Methane (x_m, *left panels*) and water (x_w, *right panels*) mole fractions during the different GCMC simulation runs: T = 250 K (black), 260 K (blue), 270 K (purple), 280 K (red), and 290 K (orange) for bulk phase (*top panels*); while T = 210 K (black), 220 K (blue), 230 K (purple), 240 K (red), and 250 K (orange) for confined system with $D_p = 2.8554$ nm (*bottom panels*). The x-axis, which indicates progress along the GCMC simulation, is expressed as a number of attempted MC moves where one move is a molecule translation, rotation, insertion or deletion. The dimensions of the simulation box in x– and y–directions are $L_x = L_y = 2.3754$ nm, and in z–direction are $L_z = 2.3754$ nm for bulk system while $L_z = 4.3670$ nm for confined system. $T_m^{bulk} = 265 \pm 5$ K and $T_m^{pore} = 225 \pm 5$ K at $P = 10$ atm for methane hydrate are summarized in Table 4.1. 161

B.5 Shift in the melting temperature of confined methane hydrate with respect to the bulk, $\Delta T_m^{pore}/T_m^{bulk}$, as a function of the reciprocal of the pore width, $1/D_p$: the dashed line is for $P = 10$ atm while the solid line is for $P = 100$ atm. The black circles read from Figure B.4 (DCM simulations); while the dashed and solid lines are computed using $k_{GB} = (\gamma_{LS} v^{\mathrm{L}} - \gamma_{HS} v^{\mathrm{H}})/\Delta h_{fus}$. 161

B.6 Same as Figure 4.3 but for the decreased LJ energy parameter (two left panels: one for methane, x_m, and another one for water, x_w): $\varepsilon' = 1/2\varepsilon$ (*top panels*), $1/3\varepsilon$ (*center panels*), and $1/4\varepsilon$ (*bottom panels*); and for the increased LJ energy parameters (two right panels: one for methane, x_m, and another one for water, x_w): $\varepsilon' = 2\varepsilon$ (*top panels*), 3ε (*center panels*), 4ε (*bottom panels*). ε' is for the pair of atoms between solid walls and hydrate/liquid phase. 162

B.7 The normal (black), $P_N = P_{zz}$, and tangential (gray), $P_T = \frac{1}{2}(P_{xx} + P_{yy})$, pressure tensors for methane hydrate (*left*), and the surface tension (*right*), γ_{HS}, as a function of the vacuum layer width D_v at $T = 290$ K. $D_v \geq 15$ nm is required to determine γ_{HS}. 163

List of Tables

1 Declaration of my manuscript. 3

2.1 Interaction potential parameters corresponding to the OPLS-UA model for methane, the TIP4P/2005 and TIP4P/Ice models for water, and the atomic model used to describe the porous solid (solid atom). For the two water models, we also indicate the melting temperature T_m as predicted using molecular modeling. 60

3.1 Chemical potential, $\mu_m^{\mathrm{V}}(x_m = 1, T, P)$, and fugacity, f, of methane vapor for the OPLS-UA methane model. All chemical potentials are normalized to the thermal energy, $k_B T$. Absolute uncertainties for the chemical potentials are smaller than 3×10^{-4}. 68

3.2 Chemical potential of liquid water $\mu_w^{\mathrm{L}}(T, P)$. All chemical potentials are normalized to the thermal energy, $k_B T$. Absolute uncertainties for the chemical potentials are smaller than 3×10^{-2}. 69

3.3 Free energy contributions of zero-occupancy methane hydrate, $\mu_w^H(x_m = 0, T, P)$. ^{a} Absolute error bar is less than 0.008; ^{b} The error bar is negligible as it smaller than the last digit shown (high accuracy of the Gauss-Legendre formula); ^{c} proton disorder correction is already included here. 80

4.1 Determination of melting temperature T_m of bulk and confined methane hydrate at pressure P using the direct coexistence method. L_x and L_y are the dimensions of the molecular system in the x– and y–directions, respectively. D_p is the pore size. * is for the melting temperature of bulk methane hydrate, T_m^{bulk}, as reported in Chapter 3. 102

4.2 Thermodynamic properties of liquid water and methane hydrate (both empty and full hydrates are considered) at $T = 286^{\mathrm{a}}$ K or $T = 290^{\mathrm{b}}$ K and $P = 100$ atm. [a] Normalized per mole of water. [b] Surface tensions determined for hydrate-substrate and liquid-substrate surfaces. [c] $k_{DCM} = -0.28$ as obtained by fitting the results of the direct coexistence method. The values in parentheses are those reported by Molinero at al. (Jacobson and Molinero, 2011). 110

5.1 Relaxation times, τ_i (in ps), and amplitude, A_i (in W/mKfs), from the overall fit of the acoustic modes. Contributions, λ_i (in W/mK), of each component to the thermal conductivity, λ_{ac} (in W/mK), of acoustic modes are also listed. * is for the oscillated acoustic mode with the frequency – $\omega_{sh} = 1.2612$ rad/ps. 138

5.2 Relaxation times, τ_{jk} (in ps), and amplitude, B_{jk} (in W/mKfs), from the overall fit of the optical modes. The oscillation frequencies, ω_j (in rad/ps) obtained from the power spectra are also listed. Contributions, λ_j (in W/mK), of each component to the thermal conductivity, λ_{op} (in W/mK), of optical modes are also listed. The final thermal conductivity is shown here. 138

Introduction

Methane hydrate is a non-stoichiometric crystalline structure made up of water molecules forming a network of hydrogen–bonded cages around methane molecules (Davy, 1800; Sloan and Koh, 2007). Here "non-stoichiometric" means that the methane composition in the hydrate phase is changing with temperature, T, and pressure, P. Abundant methane hydrate resources on Earth, especially in deep seafloors and in the permafrost (Kvenvolden, 1988; MacDonald, 1990; Sloan and Koh, 2007), are important both for energy and environmental applications (Florusse et al., 2004; Lee et al., 2005; Schüth, 2005; Strobel et al., 2009; Udachin et al., 1997). In particular, in the context of climate change and global warming, even a small temperature increase could induce the melting of methane hydrate and, therefore, the release of large amounts of methane into the atmosphere (methane leads to a far larger greenhouse gas effect than carbon dioxide) (Henriet and Mienert, 1998; Petuya et al., 2018a,b). Moreover, the formation of methane hydrate in oil and gas pipelines is known to be detrimental as it hinders flow. Finally, hydrates including methane hydrates are also thought to be a key ingredient in the geochemistry of planets, comets, etc. where the coexistence of water and gases leads to hydrate formation depending on temperature and pressure (Dartois et al., 2012; Fray et al., 2010; Hersant et al., 2004; Kieffer et al., 2006; Marboeuf et al., 2010; Mousis et al., 2010; Thomas et al., 2009).

From a fundamental point of view, methane hydrate and other gas hydrates are model systems to gain insights into the complex thermodynamics and dynamics of non-stoichiometric structures including the large family of clathrates. For instance, many porous materials such as zeolites and metal organic frameworks are synthesized by crystallizing cages around an organic template, therefore sharing some important features with hydrates. In addition, owing to their nonstoichiometric nature, gas hydrates can be considered as prototypical examples of confined solids which also possess varying compositions with temperature and pressure (even though their bulk counterpart exhibits constant stoichiometry) (Coasne et al., 2004; Czwartos et al., 2005). As a result, owing to its importance for both fundamental and practical sciences, methane hydrate is receiving increasing attention with significant effort devoted to better understanding their physical and physicochemical properties (Babakhani et al., 2018; Conde and Vega, 2010; Desmedt et al., 2012; Docherty et al., 2006; English et al., 2012; Jacobson et al., 2010a; Jensen et al., 2010; Knott et al., 2012; Nguyen and Molinero, 2015; Patt et al., 2018; Pefoute et al., 2016; Said et al., 2016; Sloan and Koh, 2007; Wierzchowski and Monson, 2007).

Most methane hydrate on Earth is confined in voids formed in the various porous rocks and/or fractures, such as clay minerals, silica/sands, etc. For this reason, the motivation of this thesis is to study the thermodynamics and formation kinetics of methane hydrate confined at the nanoscale in a porous medium. More in details, this thesis focuses on:

(1) the phase stability of methane hydrate, i.e., Liquid–Hydrate–Vapor (L–H–V) phase equilibrium, both as bulk and confined phases using molecular simulation;

(2) the ability of macroscopic thermodynamic modeling using the Gibbs-Thomson equation to describe the confinement and surface effects on the phase stability of methane hydrate;

(3) the confinement effects on the formation/dissociation kinetics of methane hydrate using free energy techniques;

(4) the confinement effects on the structural and thermodynamic properties of confined methane hydrate.

The remainder of this thesis is organized as follows. In Chapter 1, a brief review is given on the state-of-the-art of methane hydrate: structure, formation/dissociation kinetics, phase stability, and confinement effect, etc. In Chapter 2, the general framework of statistical mechanics and molecular simulation is given. Several ensembles, e.g., Canonical, Isobaric-isothermal, Grand Canonical, and Semi-Grand Canonical, are considered and molecular models and interaction potentials are also presented. Some additional technical details on these methods are also presented in the different chapters. In Chapter 3, a Monte Carlo (MC) algorithm is used to (re)construct physical configurations of methane hydrate, and different molecular simulation strategies are used to assess the phase stability of methane hydrate (i.e., liquid–hydrate–vapor phase equilibrium) under various temperature and pressure conditions. In Chapter 4, the direct coexistence method (DCM) is adopted to determine the shift of melting point of methane hydrate confined at the nanoscale. The classical thermodynamic modeling – the Gibbs-Thomson equation – is revisited to account for the shift in melting point upon confinement. In Chapter 5, several thermodynamic properties of nanoconfined methane hydrate, including density profiles, thermal conductivity, thermal expansion, and isothermal compressibility, are determined using molecular dynamics (MD). The main results together with several suggestions for future works are presented in the conclusion of this manuscript.

Some parts of this manuscript were taken from my paper published in Langmuir Ref. [Jin, D. and Coasne, B. (**2017**). Molecular Simulation of the Phase Diagram of Methane Hydrate: Free Energy Calculations, Direct Coexistence Method, and Hyperparallel Tempering. *Langmuir*, 33:11217–11230.]. A detailed list of these parts can be found in the following table. Besides those parts, all written text in this manuscript is original ($\sim 80\%$). In addition, significant changes have been made to reorganize the chapters/discussion to better match PhD thesis requirements.

Table 1 Declaration of my manuscript.

Chapter	Beginning	End
Introduction	“Methane hydrate is a non-stoichiometric ...	... and physicochemical properties.”
Sec. 2.2.3	“Monte Carlo simulation in the canonical ...	... molecules in the configuration.”
Sec. 2.5	“Methane was modeled as a single ...	... ice forms (like Ice VII and Ice VIII).”
Chap. 3	all the texts	

Chapter 1

State-of-the-art: Methane Hydrate

Contents

1.1 Structure **6**
  1.1.1 Crystalline structure and molecular model 6
  1.1.2 Order parameter 9
1.2 Thermodynamic properties **13**
1.3 Formation/dissociation and phase stability **15**
  1.3.1 Crystallization 15
  1.3.2 Melting/Dissociation 19
  1.3.3 Phase diagram 19
1.4 Confinement effects at the nanoscale **28**
1.5 Summary **32**

As discussed in the introduction, fundamental understanding on methane hydrate has raised significant interest in the last decades. The dynamics and thermodynamics of this complex compound play an important role in many practical applications of methane hydrate. Most methane hydrate in nature is confined in the voids present in various porous medium and rocks. That is, methane hydrate inside this porosity interacts with the surface atoms of these host porous materials. Such pore–hydrate interactions have drastic effects on the dynamics and thermodynamics of methane hydrate. This chapter presents a brief review of methane hydrate: (1) crystalline structure, (2) physicochemical properties, (3) formation/dissociation kinetics, (4) phase stability, and (5) confinement effects at the nanoscale.

1.1 Structure

1.1.1 Crystalline structure and molecular model

Methane hydrate is a non-stoichiometric crystalline structure (crystal) made up of the hydrogen-bonded water molecules forming the cavity around methane molecules (see Figure 1.1) (Davy, 1800; Sloan and Koh, 2007). Here "non-stoichiometric" means that the methane composition, x_m, in the hydrate phase varies with temperature, T, and pressure, P. Other small gas molecules, e.g., carbon dioxide (CO_2), hydrogen sulfur (H_2S), and hydrocarbons (C_2H_6, C_3H_8, etc.), can also form gas hydrate in natural environments. To date, three primary crystalline hydrate structures have been identified: structure I (sI) (McMullan and Jeffrey, 1965), structure II (sII), (Mak and McMullan, 1965) and structure H (sH) (Ripmeester et al., 1987). The first two structures, sI and sII, are cubic crystals, while the third one is a hexagonal crystal (analogous to the hexagonal ice, I_{hex}). As shown in Figure 1.1, these three structures differ from each other in the types and numbers of water cavities (made up of four-, five- and six-member rings of water molecules). These water cavities can be classified according to their size: (1) one small size cavity, 5^{12}, consists of twelve pentagons; (2) three large size cavities, including $5^{12}6^2$, $5^{12}6^4$, and htb

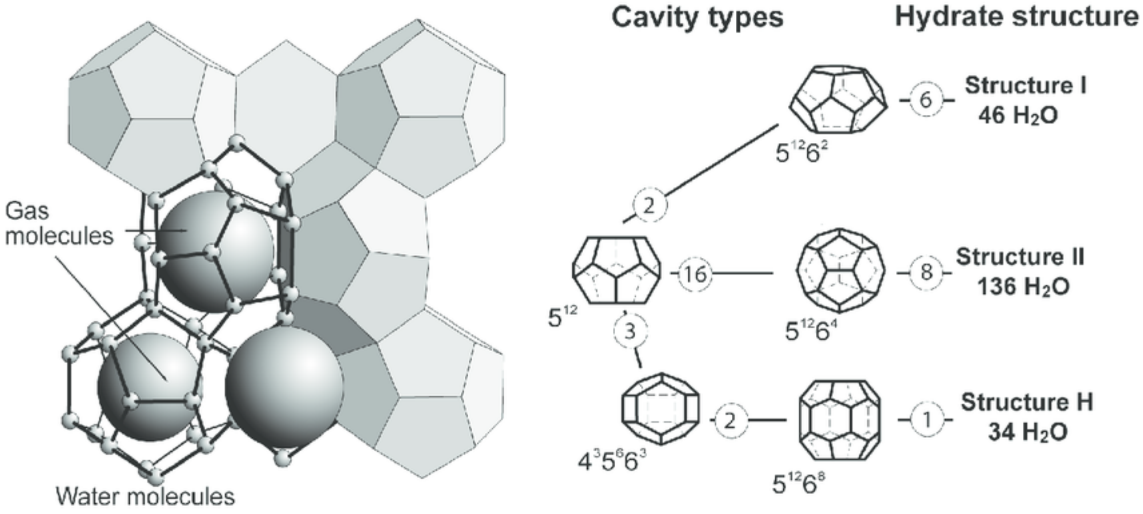

Figure 1.1 (*left*) Gas hydrate with structure I (sI): the small spheres are water molecules forming hydrogen-bonded cavities and the large spheres are the gas molecules. The gray polyhedrons represent the cavities generated by the water molecules. (*right*) Typically, the types and numbers of water cavities correspond to one of the three following structures of gas hydrate: sI, sII, and sH. The circled numbers are the numbers of such water cavities which are used to form the corresponding hydrate structure. [Picture from Ref. (Schulz and Zabel, 2006)]

$5^{12}6^{8}$, created by adding two, four, and eight hexagons in the cavity 5^{12}, respectively; (3) one medium size cavity, $4^{3}5^{12}6^{3}$, created by adding three squares and three hexagons into the cavity 5^{12}. These structures of gas hydrate can be viewed as a packing of these polyhedral water cavities. The structure sI consists of two small size cavities 5^{12} and six large size cavities $5^{12}6^{2}$. The structure sII consists of sixteen small size cavities 5^{12} and eight large size cavities $5^{12}6^{4}$. The structure sH consists of three small size cavities 5^{12}, two medium size cavities $4^{3}5^{12}6^{3}$, and one large size cavity $5^{12}6^{8}$. Each cavity can encapsulate one or two gas molecules depending on the nature of the gas molecules (typically, the molecular size). Despite the differences in these structures, i.e., numbers and types of water cavities, the molar composition of gas molecule, x_m, and water molecule, x_w, are similar for these three structures of methane hydrate: $x_m \sim 0.15$ and $x_w \sim 0.85$.

Under typical environmental conditions where methane hydrate is encountered on Earth, methane hydrate is formed as structure sI (Michalis et al., 2015; Sloan and Koh, 2007). In this crystalline structure, 46 water molecules form two small pentagonal dodecahedral cages (i.e., small size water cavity 5^{12}) and six tetracaidecahedral cages (i.e., large size water cavity $5^{12}6^{2}$) so that a maximum of 8 methane molecules can be encapsulated (Michalis et al., 2015). In addition, the structure sI of methane hydrate also obeys the following rules:

(1) proton disordered structure: the crystal lattice of methane hydrate is formed by water molecules with oxygen atoms located at regular crystalline positions. In contrast, the positions of the hydrogen atoms are disordered;

(2) ice rules (also known as Bernal–Fowler rules (Bernal and Fowler, 1933)): each oxygen atom in the methane hydrate is covalently bonded to two hydrogen atoms, and is involved in four hydrogen bonds pointing toward the neighbor oxygen atoms. Two of these hydrogen bonds are outgoing (i and ii in Figure 1.2) while the two others are incoming (iii and iv in Figure 1.2);

(3) zero dipole moment: methane hydrate has a zero dipole moment.

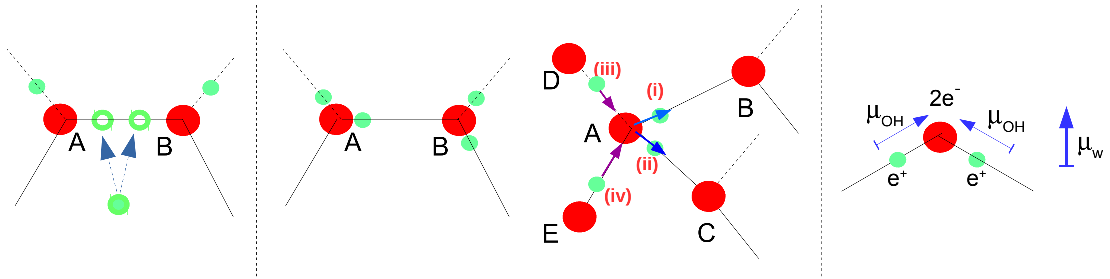

(1) proton disorder (2) ice rules (3) zero dipole moment

Figure 1.2 Three criteria should be satisfied for methane hydrate with sI structure (Bernal and Fowler, 1933; Chakraborty and Gelb, 2012a): (1) proton disorder; (2) ice rules; and (3) zero dipole moment. The red and green spheres are the oxygen and hydrogen atoms of water, respectively.

To study the thermodynamics and dynamics of methane hydrate, many molecular models for water and methane can be, in principle, used in molecular simulation. However, in practice, all water models do not reproduce accurately all available experimental data for methane hydrate. Thus, the choice of the molecular models for water and methane is very important for the description of methane hydrate. In the literature, methane molecules are usually described using a simplified model known as the unit-atom model (Damm et al., 1997). The water molecules can be described using different molecular models, e.g., TIP4P/2005 (Abascal et al., 2005), TIP4P/ICE (Abascal and Vega, 2005), and SPC/E (Docherty et al., 2006; Kaminski et al., 1994; Krouskop et al., 2006; Paschek, 2004). Among these water molecular models, only a few of them reproduce the experimental data, especially phase stability, for methane hydrate. Thanks to a reparameterization, the TIP4P/family (e.g., TIP4P/2005 and TIP4P/ICE) water molecular models show improved performance in the determination of the solid–liquid phase diagram of water, as compared with other water molecular models (e.g., SPC/E) (Abascal et al., 2005; Abascal and Vega, 2005). In combination with the united-atom (UA) model for methane molecule, these two water molecular models can reproduce the phase diagram of methane hydrate (Conde and Vega, 2010; Vega et al., 2008). Molinero et al. used the coarse-grain model for water, mW, and the Stillinger-Weber (SW) potential to speed up the molecular simulation by about a factor of 100 (Jacobson et al., 2009, 2010a,b; Jacobson and Molinero, 2010; Molinero and Moore, 2009). The drawback of this water model is that it does not provide results as accurate as those with the TIP4P/family model.

In this work, a stochastic Monte Carlo algorithm, inspired by Ref. (Buch et al., 1998), has been developed to generate the crystalline structure of methane hydrate that follows the three criteria given above. This part of the work will be discussed in Chapter 3. The TIP4P/ICE and TIP4P/2005 water molecule models, in combination with the OPLS-UA methane molecular models were used.

1.1.2 Order parameter

To identify the structure of methane hydrate, one or more order parameters were developed in recent years. In practice, these order parameters usually describe the packing of the oxygen atoms of water molecules in various phases, because it is easier to identify the regular oxygen atom network than the disordered network of hydrogen atoms. Considering typical environment conditions for methane hydrate, most studies deal with identifying the following phases: liquid water, hexagonal ice, and methane hydrate. Many order parameters allow one to distinguish liquid water from its crystalline structures, including hexagonal ice and methane hydrate, due to the striking difference between disordered and ordered oxygen atoms in liquid and crystal phases. Such order parameters include the radial distribution function, $g(r)$, the number of hydrogen bonds, N_{HB}, and the tetrahedral order parameter, ξ. In contrast, distinguishing methane hydrate and hexagonal ice is more difficult due to the fact that most oxygen atoms in these two structures are tetrahedrally connected.

The radial distribution function, $g_{\alpha\beta}(r)$, is related to the structure factor, $S(q)$, through the inverse Fourier transform (Gasser et al., 2001). $g_{\alpha\beta}(r)$ describes the number density distributions of the species β (e.g., oxygen atom, hydrogen atom, or methane molecule) surrounding a given species α: $g_{\alpha\beta}(r) = \left\langle \rho_{\alpha\beta}(r) \right\rangle / \left\langle \rho_{\beta} \right\rangle$ where $\rho_{\alpha\beta}(r) = 1/4\pi r^2 \Delta r (\sum_1^{N_\alpha} \Delta N_{\alpha\beta}(r))/N_\alpha$ is the number density of the pairs α–β separated by a distance between r and $r + \Delta r$ (the corresponding number of such pairs for each atom α is $\Delta N_{\alpha\beta}$). Summation runs over all the number of atoms in species α, N_α. ρ_β is the density of species β and $\langle \cdots \rangle$ means an ensemble average. In other words, $g_{\alpha\beta}(r)$ is the probability of finding an atom β at a distance r from an atom α. Among all $g(r)$ functions, $g_{\mathrm{O\text{-}H}}(r)$ allows identifying the hydrogen bonds formed between the water molecules for different liquid and crystal structures. A pair of water molecules, w_A–w_B, is assumed to be hydrogen-bonded if it satisfies the following criteria: (1) the distance $d_{\mathrm{O}_A\mathrm{H}_B} \leq 0.235$ nm and (2) the angle $\langle \mathrm{H}_A\mathrm{O}_A\mathrm{H}_B \rangle \leq 30°$ (Alabarse et al., 2012). The number of hydrogen bonds, $\langle N_{\mathrm{HB}} \rangle$, in liquid water is 3.54–3.65 per water molecule (Alabarse et al., 2012; Errington and Debenedetti, 2001), while $N_{\mathrm{HB}} = 3.98$ for hexagonal ice and methane hydrate at $T = 290$ K and $P = 100$ atm.

The tetrahedral order parameter, $\xi(i)$, describes the extent to which the four nearest-neighbour oxygen atoms are tetrahedrally coordinated with respect to a given oxygen atom O_i, $\xi(i) = 1 - 3/8 \sum_{j=1}^{3} \sum_{k=j+1}^{4} \left(\cos \left\langle \mathrm{O}_j\mathrm{O}_i\mathrm{O}_k \right\rangle + 1/3 \right)$ where the indices j and k run over the four nearest-neighbour oxygen atoms around O_i, and the angle $\left\langle \mathrm{O}_j\mathrm{O}_i\mathrm{O}_k \right\rangle$ is formed by the lines joining O_j and O_k associated with O_i (Errington and Debenedetti, 2001; Radhakrishnan and Trout, 2002). This definition ensures that $\xi(i) = 0$ for a completely disordered structure while $\xi(i) = 1$ for a completely ordered tetrahedral structure. An intermediate value is obtained for a partially disordered structure (e.g., liquid water, $\langle \xi \rangle =$ 0.63–0.68 (Errington and Debenedetti, 2001; Radhakrishnan and Trout, 2002)). The above order parameter shows that both hexagonal ice and methane hydrate are perfect tetrahedral crystals. Therefore, identification of liquid water is rather easy but the distinguishing between hexagonal ice and methane hydrate requires to develop a more complex order parameter.

The local bond order parameters, Q_l (l is an integer) (Steinhardt et al., 1983), are widely used to identify crystals (Lechner and Dellago, 2008; Ogata, 1992; Radhakrishnan and Trout, 2002, 2003a,b; Steinhardt et al., 1983). Q_l provides a clear indication for disordered and ordered structures, especially for crystals with different symmetries. For a given oxygen atom O_i, $Q_l(i)$ is computed using the complex vectors that link O_i to its $N_b(i)$ nearest-neighbour oxygen atoms O_j. The complex vector $Q_{lm}(i)$ is first computed,

$$Q_{lm}(i) = \frac{1}{N_b(i)} \sum_{j=1}^{N_b(i)} Y_{lm}(\mathbf{r}_{ij}) \text{ with } m \in [-l, l] \tag{1.1}$$

where $Y_{lm}(\mathbf{r}_{ij})$ are the spherical harmonics which depend on the position vectors $\mathbf{r}_{ij}$. $Q_l(i)$ are then obtained using these complex vectors,

$$Q_l(i) = \left(\frac{4\pi}{2l+1} \sum_{m=-l}^{l} \mid Q_{lm}(i) \mid^2 \right)^{1/2} \tag{1.2}$$

where the summation over m runs $[-l, +l]$. In practice, one can also use improved spatial resolution by averaging these local bond order parameters, $\langle Q_l(i) \rangle$,

$$\langle Q_l(i) \rangle = \left(\frac{4\pi}{2l+1} \sum_{m=-l}^{l} \mid \langle Q_{lm}(i) \rangle \mid^2 \right)^{1/2} \tag{1.3}$$

where $\langle Q_{lm}(i)\rangle$ is given by,

$$\langle Q_{lm}(i)\rangle = \frac{1}{N_b(i)} \sum_{k=0}^{N_b(i)} Q_{lm}(k) \tag{1.4}$$

The summation in Eq. (1.4) from $k = 0$ to $N_b(i)$ runs over all the nearest neighbouring oxygen atoms O_k and includes itself (i.e., $k = 0$). $Q_{lm}(i)$ contains the structural information on the first shell surrounding O_i. In contrast, $\langle Q_{lm}(i)\rangle$ contains the structural information on the first and second shells.

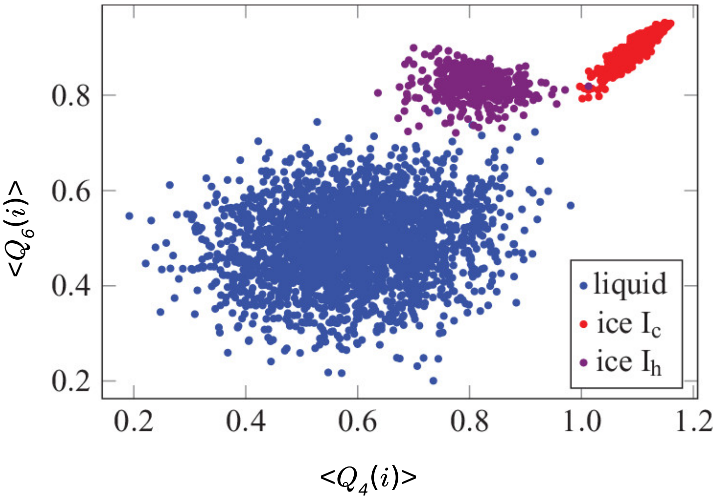

Figure 1.3 (color online) Averaged local bond order parameters, $\langle Q_4\rangle$–$\langle Q_6\rangle$–plane, for liquid water (blue), hexagonal ice (red), and methane hydrate (black) at $T = 200$ K. [Picture from Ref. Reinhardt et al. (2012)]

Usually, $l = 4$ and 6 are used since they allow the identification of the different crystal phases of water, e.g., cubic and hexagonal ices (Chau and Hardwick, 1998; Chialvo et al., 2002; Errington and Debenedetti, 2001; Ferdows and Ota, 2005; Jorgensen et al., 1983; Lechner and Dellago, 2008; Narten and Levy, 1971; Ogata, 1992; Radhakrishnan and Trout, 2002; Reinhardt et al., 2012; Soper and Benmore, 2008; Steinhardt et al., 1983). Figure 1.3 shows the scatter plot of liquid water, cubic and hexagonal ice under $T = 200$ K in the $\langle Q_4\rangle$–$\langle Q_6\rangle$–plane. As expected, these data suggest that liquid water exhibits a more disordered structure (much broader distribution) as compared with crystalline structures. Despite some overlap, this pair order parameter is suitable to identify liquid water, cubic and hexagonal ice. Recent works have shown that Q_l plays an important role in the determination of the formation/crystallization of methane hydrate, especially to identify the phase transition from liquid water to methane hydrate (Nguyen and Molinero, 2015; Radhakrishnan and Trout, 2003b; Tanaka, 2012). Another possible order parameter is the distribution of cyclic pentamers. (Báez and Clancy, 1994; Fábián et al., 2018)

In summary, complete phase identification between liquid water, hexagonal ice, and methane hydrate can be achieved using local bond order parameters. These orders parameters are efficient and simple order parameters for the identification of methane hydrate in the course of formation/crystallization. In this work, Q_6 has been used to determine the free energy barrier between liquid water and methane hydrate. The free energy calculations with the umbrella sampling will be discussed in Chapter 4.

1.2 Thermodynamic properties

Thermodynamic properties – which include physical and physicochemical properties – are essential for practical applications involving methane hydrate (Jendi et al., 2016; Ning et al., 2012, 2015). For instance, the thermal expansion coefficient, $\alpha_P = 1/v\,(\partial v/\partial T)_P$, is an important parameter for assessing the mechanical stability of methane hydrate and geological media filled with methane hydrate (Jendi et al., 2016). The exploration of methane hydrate and the storage of carbon dioxide by substitution of carbon dioxide with methane in methane hydrate can lead to mechanical instabilities. Moreover, the isothermal compressibility, $\kappa_T = -1/v\,(\partial v/\partial P)_T$, plays an important role in the detection of methane hydrate when using seismic waves. As a result, understanding the thermodynamic properties of methane hydrate has raised significant interest in the last decade (Bai et al., 2015; Burnham and English, 2016; Demurov et al., 2002; Michalis et al., 2016a; Yang et al., 2016b; Zhu et al., 2014).

Many experiments focus on the following thermodynamic properties: second-order elastic constant (Shimizu et al., 2002), isothermal compressibility (Sloan and Koh, 2007), thermal expansion (Takeya et al., 2005), heat capacity (Waite et al., 2007), and thermal conductivity (English et al., 2012, 2005). These results provide valuable information for the geophysical applications of methane hydrate. Understanding these properties at the atomic-scale level is also important. For instance, *ab initio* and classical calculations can provide accurate values for α_P and κ_T.

Using molecular dynamics, one can determine the contributions from each component (methane and water for methane hydrate) to the thermal conductivity, which is very useful in the description of heat-transfer upon methane hydrate formation/dissociation. The heat-flux vector, $\mathbf{J}$, reads,

$$\mathbf{J} = \frac{1}{V}\left[\sum_{i}^{N}(e_i + u_i)\,\mathbf{v}_i + \sum_{i}^{N}\sum_{j>i}^{N}\left(\mathbf{f}_{ij}\cdot\mathbf{v}_j\right)\mathbf{r}_{ij}\right] \tag{1.5}$$

where V is the volume of the simulation box, N is the total number of molecules, $e_i = 1/2m_iv_i^2$ is the kinetic energy of molecule i, u_i is the potential energy of molecule i which interacts with the other molecules, $\mathbf{v}_i$ is the velocity vector of molecule i, $\mathbf{f}_{ij}$ is the force between molecule i and molecule j, and $\mathbf{r}_{ij}$ is the position vector between molecule i and molecule j.

The thermal conductivity, k, can be estimated using the Green-Kubo formalism,

$$k = \frac{V}{3k_BT^2}\int_0^{+\infty}\langle\mathbf{J}(t)\cdot\mathbf{J}(0)\rangle\,dt \tag{1.6}$$

where $\langle\cdots\rangle$ denotes an ensemble average. This method provides a thermal conductivity k that includes all contributions to the heat flux (Jendi et al., 2016; Ning et al., 2012, 2015). The thermal conductivity not only can explain unusual thermal-transport phenomena but also helps to provide deep understanding of thermoelectric materials which possess similar structures as methane hydrate (e.g., semiconductor silicon clathrates).

Another important thermodynamic property is the gas mobility/diffusion of methane molecules in hydrate and liquid phases. Such dynamics plays an important role in the process of formation, dissociation, and displacement of carbon dioxide with methane (Demurov et al., 2002; Hjertenaes et al., 2016; Liang et al., 2014; Michalis et al., 2016a; Ohgaki et al., 2008; Pefoute et al., 2016; Román-Pérez et al., 2010; Trinh et al., 2015; Vidal-Vidal et al., 2016). For instance, in the process of formation of methane hydrate, the extremely low solubility of methane in liquid water does not allow transport of methane molecules to maintain the growth rate of methane hydrate; methane molecules are required to diffuse across liquid water towards the hydrate-liquid interface. Thus, the diffusion rate of methane in liquid water is one of the key steps in the formation of methane hydrate. Moreover, methane molecules in hydrate phase affect the mechanical stability of methane hydrate in seaflooor, permafrost, marine sediments, etc. Due to slow methane diffusion, hydrate phase can form with incompletely filled water cavities. On the one hand, fewer methane molecules decrease the water-methane interactions which contribute to the structure stability of methane hydrate. On the other hand, the empty water cavities can easily "open" and trigger methane hydrate dissociation (Liang et al., 2014).

1.3 Formation/dissociation and phase stability

1.3.1 Crystallization

According to the classical nucleation theory (CNT), the formation of methane hydrate includes two steps:

(1) Below the crystalization point, $T < T_m$, several water molecules in liquid phase get together to form a crystal-like nucleus with a cluster radius, r;

(2) If the radius is larger than the critical radius (i.e., $r > r_c$) the above crystal-like nucleus keeps growing and eventually form the crystalline structure of methane hydrate. In contrast, if $r < r_c$, the nucleus dissociates and eventually disappears.

The above two steps can be described in Figure 1.4. Figure 1.4 shows the free energy, ΔG, for methane hydrate formation as a function of the radius of the nucleus, r. From a thermodynamic viewpoint, the free energy, ΔG, for the methane hydrate formation can be

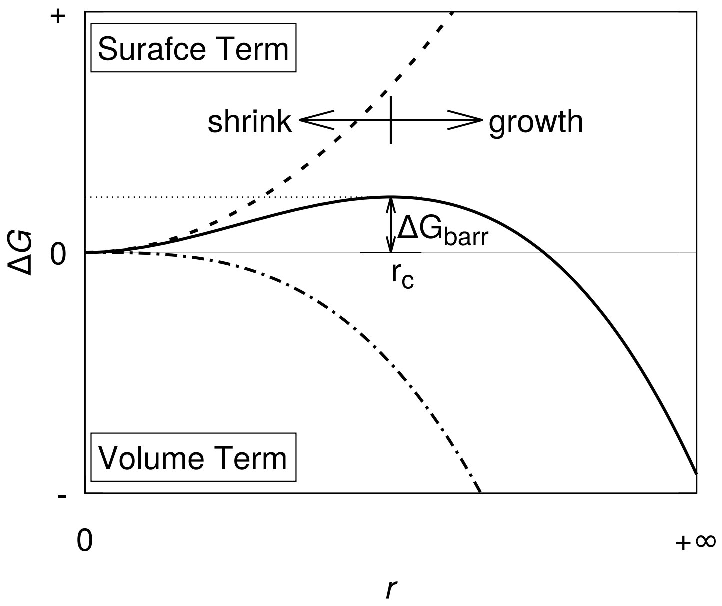

Figure 1.4 Free energy (solid line), ΔG, as a function of nucleus radius, r, in the the formation process of methane hydrate. Formation can be described as the interplay between the hydrate–liquid surface free energy (surface term corresponding to the dashed line), ΔG_S, and the free energy difference between liquid water and methane hydrate (volume term corresponding to the dot dashed line), ΔG_V. The critical radius, r_c, and the corresponding free energy barrier, ΔG_{barr}, are also shown in this figure. If the nucleus radius is larger than the critical radius, i.e., $r > r_c$, the nucleus keeps growing to form methane hydrate ("growth"). For $r < r_c$, the nucleus melts into liquid water ("shrink").

described as a combination of the hydrate–liquid surface free energy (surface contribution, see Figure 1.4), ΔG_S, and the free energy difference between liquid water and methane hydrate (volume contribution, see Figure 1.4), ΔG_V,

$$\begin{aligned} \Delta G &= \Delta G_S + \Delta G_V \\ &= 4\pi r^2 \gamma_{HL} - \frac{4}{3}\pi r^3 \rho_H \Delta\mu_{HL} \end{aligned} \tag{1.7}$$

where γ_{HL} is the surface tension of hydrate–liquid interface, $\Delta\mu_{HL}$ is the difference of the chemical potential between liquid water and methane hydrate, and ρ_H is the number density of water molecules in methane hydrate. In the above equation, the surface contribution, $\Delta G_S = 4\pi r^2 \gamma_{HL}$, corresponds to the free energy cost of creating the liquid–hydrate interface. The volume contribution, $\Delta G_V = -4/3\pi r^3 \rho_H \Delta\mu_{HL}$, describes the fact that the structure of methane hydrate is more stable than that of liquid water below the crystalization point (i.e., free energy difference between methane hydrate and liquid water). The maximum of the total free energy (as described by Eq. (1.7)) corresponds to the free energy barrier of the formation of methane hydrate, ΔG_{barr},

$$\Delta G_{barr} = \frac{16\pi}{3}\left(\frac{\gamma_{HL}^3}{\rho_H^2 \Delta\mu_{HL}^2}\right) \tag{1.8}$$

The corresponding critical radius, r_c, of the crystal-like nucleus reads,

$$r_c = \frac{2\gamma_{HL}}{\rho_H \Delta\mu_{HL}} \tag{1.9}$$

Figure 1.4 also shows the two possible scenarios as described by the classical nucleation theory: (1) "growth" for $r > r_{crit}$, the nucleus keep growing to form methane hydrate and (2) "shrink" for $r < r_c$, the nucleus melts. For bulk methane hydrate, the melting point, $T_m(r)$, of a nucleus with a radius, r, is linearly proportional to the reciprocal of its critical radius, r_c, as described by the Gibbs-Thomson equation (Jacobson and Molinero, 2011),

$$\frac{T_m(r) - T_m^{bulk}}{T_m^{bulk}} = -\frac{2\gamma_{HL}}{\rho_H \Delta h_m r} \tag{1.10}$$

where T_m^{bulk} is the melting point of an infinite bulk methane hydrate and Δh_m is the molar enthalpy of melting from methane hydrate to liquid water.

The formation kinetics of methane hydrate as described by the nucleation rate, J_f, reads,

$$J_f = J_{f,0} A \exp\left(-\beta_T \Delta G_{barr}^f\right) \tag{1.11}$$

where $J_{f,0}$ is the frequency with which methane and water molecules reach the surface area around the nucleus (i.e., nucleation sites), $A = 4\pi r^2$ is the surface area of the nucleus, and $\beta_T = 1/k_B T$ is the reciprocal of the thermal energy with the Boltzmann constant k_B. Therefore, two factors control the formation rate of methane hydrate: (1) the number density of nucleation sites, and (2) the free energy barrier, ΔG_{barr}^f, for methane hydrate formation (i.e., from liquid water to methane hydrate). For many reasons, the nucleation rate of methane hydrate is very slow in nature, in agreement with experiments and molecular simulations. For instance, the very low solubility of methane in liquid water, $x_m \sim 0.001$, makes it difficult to feed methane hydrate which further decreases the formation probability of the nucleus/crystal. Another possible reason for the slow nucleation rate is related to interfacial phenomena: after the nucleus is formed, a thin molecular interface is present between methane hydrate and liquid water of methane hydrate; such a hydrate-liquid interface decreases the diffusion of methane vapor through it which further hinders crystal growth. More importantly, there is a large free energy barrier between liquid water and methane hydrate. Such a large free energy barrier significantly affects the nucleation rate, as described by Eq. (1.11). Experimentally, it can take up to several days maybe more to synthesize methane hydrate. As for theoretical aspects, simulating methane hydrate requires to use advanced molecular simulation strategies such as free energy techniques. In practice, such slow formation/dissociation kinetics for methane hydrate is important in natural environments. For instance, the liquid-hydrate (or ice-hydrate at low temperature) interface prevents the melting of methane hydrate when the temperature increases so that the slow dissociation kinetics of methane hydrate in seafloor and permafrost decreases the release rate of methane (Angioletti-Uberti et al., 2010; Bi et al., 2016; Bi and Li, 2014; Lehmkühler et al., 2009; Mel'nikov et al., 2016; Pirzadeh and Kusalik, 2013; Saykally, 2013; Ueno et al., 2015; Zhang et al., 2015).

Many strategies are being developed to control the nucleation rate of methane hydrate. By virtue of the two factors above, one can attempt to alter the number density of nucleation sites and/or the free energy barrier. For instance, methane vapor can be injected into liquid water to increase the probability of formation of the nucleus. Various surfactants can also be used as promoters to decrease the free energy barrier for methane hydrate formation, etc. On the other hand, hydrate inhibitors (e.g., alcohol-based, glycol-based, polymer-based, ionic liquids, amino acides, etc.) can be injected into transport pipelines to avoid the formation of methane hydrate (Arora et al., 2016; Dureckova et al., 2016; Kato et al., 2016; Kumar et al., 2015; Lee et al., 2005; McLaurin et al., 2014; Sa et al., 2015, 2013; Wu et al., 2015; Xu et al., 2016; Yagasaki et al., 2015).

1.3.2 Melting/Dissociation

Understanding the dissociation of methane hydrate is important in the field of environmental science. The melting of methane hydrate in nature can release massive amounts of this greenhouse gas. Like with methane hydrate formation, many experiments but also thermodynamic models and molecular simulations have been reported on the dissociation mechanism and kinetics (Alavi and Ohmura, 2016; Bagherzadeh et al., 2015; Chakraborty and Gelb, 2012a; Liang et al., 2014; Luis et al., 2015; Misyura, 2016; Myshakin et al., 2009; Smirnov and Stegailov, 2012; Vidal-Vidal et al., 2016; Zhou et al., 2016). The kinetics rate for the dissociation of methane hydrate writes,

$$J_d = J_{d,0} \exp\left(-\beta_T \Delta G^d_{barr}\right) \tag{1.12}$$

where ΔG^d_{barr} is the activation energy for methane hydrate dissociation and $J_{d,0}$ is an exponential factor that accounts for the attempt rate for dissociation. In addition to the kinetic rate of methane hydrate dissociation, the heat transfer is another important point for the melting of methane hydrate.

1.3.3 Phase diagram

Phase stability is shown in the phase diagram provided in Figure 1.5. This phase diagram provides phase boundaries which delimitates the conditions under which methane hydrate coexists with liquid water (or ice at low temperature) and methane vapor. In other words, phase transitions occur along these equilibrium lines (phase boundaries). More in details, Figure 1.5 shows the pressure–temperature (P–T) phase diagram of methane hydrate which involves liquid water (L), ice (I), methane hydrate (H), and methane vapor (V). The melting line of ice – melting temperature T_m^{I} at a given P – indicates that ice is located in the region $T < T_m^{\mathrm{I}}$ while liquid water is located in the region $T > T_m^{\mathrm{I}}$. Similarly, the melting line of methane hydrate – melting temperature T_m^{H} at a given P – indicates that methane hydrate is located in the region $T < T_m^{\mathrm{H}}$ while liquid water and methane vapor coexist in the region $T > T_m^{\mathrm{H}}$. These two melting lines separate the phase diagram into four regions: (1) methane hydrate coexists with ice (H+ICE); (2) methane hydrate coexists with liquid water (H+L); (3) methane vapor coexists with liquid water (V+L); and (4) methane vapor coexists with ice (V+ICE). Along the melting line of methane hydrate (as indicated by line AQB in Figure 1.5), two types of three phase equilibrium exist: (1) liquid–hydrate–vapor (L–H–V) at high temperature, $T > T_m^{\mathrm{I}}$ and (2) ice–hydrate–vapor (I–H–V) at low temperature, $T < T_m^{\mathrm{I}}$.

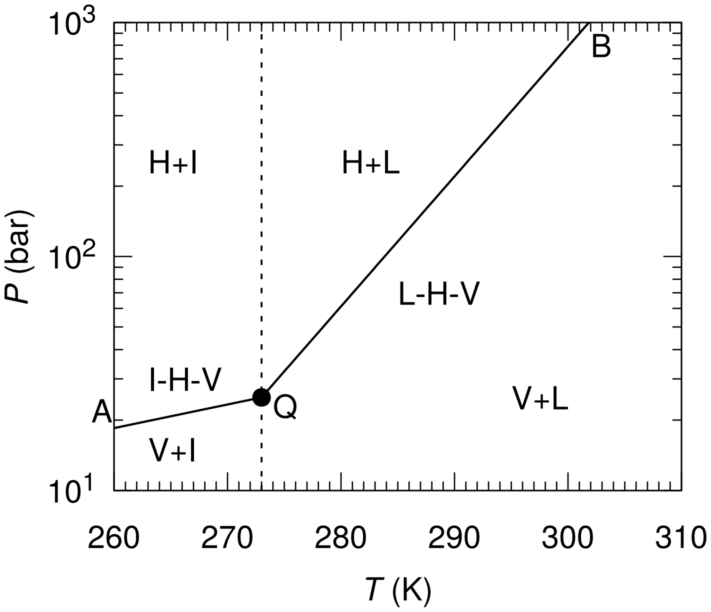

Figure 1.5 Pressure–temperature (P–T) phase diagram for liquid (L), ice (I), vapor (V), and hydrate (H) phases. The phase boundary – dashed line – indicates the conditions for which ice coexists with liquid water, L–I. The phase boundary – solid line AQ – indicates the conditions for which methane hydrate coexists with ice and methane vapor, I–H–V. The phase boundary – solid line QB – indicates the conditions for which methane hydrate coexists with liquid water and methane vapor, L–H–V. Four regions involving the two phase coexistence are shown: (1) hydrate coexists with ice, H+I; (2) hydrate coexists with liquid water, H+L; (3) methane vapor coexists with liquid water, V+L; and (4) methane vapor coexists with ice, V+I. Q is a four phase coexistence point, L–H–I–V.

Generally, the phase coexistence requires that the chemical potentials of each component are equal in all phases. In this work, methane hydrate can be viewed as a binary mixture of methane, m, and water, w; for such a system, L–H–V phase equilibrium requires that the chemical potentials of water in all phases (Φ = H, L, and V) are equal,

$$\mu_w^{\mathrm{H}}(x_m,T,P) = \mu_w^{\mathrm{L}}(x_m,T,P) = \mu_w^{\mathrm{V}}(x_m,T,P) \tag{1.13}$$

but also for methane,

$$\mu_m^{\mathrm{H}}(x_m,T,P) = \mu_m^{\mathrm{L}}(x_m,T,P) = \mu_m^{\mathrm{V}}(x_m,T,P) \tag{1.14}$$

where μ is the chemical potential as a function of the composition of methane, x_m (one could use the composition of water, $x_w = 1 - x_m$.), the temperature, T, and the pressure, P. In principle, one can determine L–H–V phase equilibrium by solving the two equations above: one is for water and one for methane. Many theoretical methods use such thermodynamic modeling, e.g., van der Waals–Platteeuw method (Conde et al., 2016; de Azevedo Medeiros et al., 2016; Duan et al., 2011; Hakim et al., 2010; Katsumasa et al., 2007; Lasich et al., 2014; Lee et al., 2012; Yoon et al., 2002), first-principles thermodynamics (Cao et al., 2016; Trinh et al., 2015), etc. In addition to the above techniques, there are other robust techniques to determine L–H–V phase equilibrium. These techniques allow probing the formation/nucleation of methane hydrate such as the direct coexistence method and the parallel tempering technique, etc.

Free energy calculations. Free energy calculations allow one to determine L–H–V phase equilibrium. Such computations are often used to determine the solid–liquid phase equilibrium for various crystalline materials (Barroso and Ferreira, 2002; Dornan et al., 2007; Frenkel and Ladd, 1984; Habershon and Manolopoulos, 2011; Jhung et al., 1991; Lyubartsev et al., 1998; Nagle, 1966; Noya et al., 2008; Okano and Yasuoka, 2006; Polson et al., 2000; Radhakrishnan and Trout, 2003a; Shen and Monson, 1995; Shetty and Escobedo, 2002; Susilo et al., 2008; Vega and Monson, 1998; Vega and Noya, 2007; Vega et al., 1992, 2008). The main goal with this technique is to compute the chemical potentials of methane and water in different phases at different T and P. Then thermodynamic equations, corresponding to Eqs. (1.13) and (1.14), are solved using these chemical potentials. To determine the L–H–V phase equilibrium, one usually chooses the following two equations: (1) L–H phase equilibrium, $\mu_w^{\mathrm{H}}(x_m,T,P) = \mu_w^{\mathrm{L}}(x_m,T,P)$ and (2) H–V phase equilibrium, $\mu_m^{\mathrm{H}}(x_m,T,P) = \mu_m^{\mathrm{V}}(x_m,T,P)$. From a physical point of view, the chemical potential can be obtained from the corresponding free energy. Many theoretical approaches were developed to determine chemical potentials: (1) the equation of state (EoS) provides an easy way to determine the chemical potential of vapor phase, μ_m^{V}; (2) the Gibbs–Duhem equation provides a way to determine the chemical potential of liquid phase especially for uncompressible liquid water, μ_w^{L}; (3) the grand canonical ensemble Monte Carlo simulation provides a way to determine the chemical potential as a function of x_m by imposing a given μ_m^{H}; (4) the Einstein molecule approach determines the chemical potential of water in the hydrate phase, μ_w^{H}, etc. The latter technique – the Einstein molecule approach – can be used to determine the chemical potential of any arbitrary solid phases but the determination of the chemical potential of water in methane hydrate is not straightforward in practice. According to the definition of chemical potential, one could determine the chemical potential of a solid phase using the free energy relationship, $\mu = (A + PV)/N$ where A is the Helmholtz free energy, PV is the mechanical contribution, and N is the number of molecules. The Einstein molecule approach provides a way to determine the free energy of methane hydrate. Within the framework of the Einstein molecule approach, one constructs a link from the ideal Einstein molecule to methane hydrate. As the reference, the Einstein molecule has an analytic free energy, A_{E}. Thermodynamic integration provides a way to compute the free energy difference between the Einstein molecule and methane hydrate, ΔA. The free energy of methane hydrate is readily obtained as $A_{\mathrm{H}} = A_{\mathrm{E}} + \Delta A$. By using this technique, researchers have determined the phase diagram of methane hydrate (Jensen et al., 2010; Waage et al., 2017; Wierzchowski and Monson, 2006, 2007; Yezdimer et al., 2002).

The umbrella sampling is a molecular simulation technique which provides a way to determine L–H–V phase equilibrium by using free energy calculations. With this technique, one prepares a single phase (e.g., methane hydrate) and forces it to transform into another one (e.g., liquid water) by adding a biasing potential energy contribution. Such biasing potential contribution is used to cancel out the free energy barrier between the two phases. In other words, the phase transition is driven by the biasing potential. In practice, to determine L–H–V phase equilibrium, one starts from methane hydrate which is then transformed into liquid water by adding a harmonic potential in the framework of the umbrella sampling technique. Usually, an order parameter (e.g., Q_6) is used in the biasing harmonic potential (e.g., $w(Q_6) = 1/2k_{us}\left(Q_{6,i} - Q_{6,0}\right)$ where k_{us} is the force constant which represent the transform rate and $Q_{6,i}/Q_{6,0}$ are the order parameters of current/reference system. By determining the probability distribution, the free energy contribution, $V^B(Q_6) = -k_B T \ln\left(w(Q_6)\right)$, of the biasing potential at a given order parameter can be obtained. The unbiased free energy profile, $G(Q_6)$, on the order parameter can be estimated by subtracting $V^B(Q_6)$ from the biased free energy profile, $G^B(Q_6)$: $G(Q_6) = G^B(Q_6) - V^B(Q_6)$. In so doing, the free energy, ΔG, as a function of the order parameter, OP, is determined (Frenkel and Smit, 2002). Figure 1.6 shows a typical free energy profile $\Delta G(OP)$ at three different T and P. At $T > T_m$, liquid water is more stable than methane hydrate. That is, the free energy of liquid water is lower than that of methane hydrate at $T > T_m$: $\Delta G_{\mathrm{L}} < \Delta G_{\mathrm{H}}$. While at $T < T_m$, methane hydrate is more stable than liquid water, $\Delta G_{\mathrm{L}} > \Delta G_{\mathrm{H}}$. The melting/crystallization temperature at equilibrium, T_m, is obtained when the free energy difference between liquid water and methane hydrate is zero, i.e., $\Delta G_{HL} = 0$. In addition, it should be noted that such free energy calculations give access to the free energy barrier between methane hydrate and liquid water. This value provides information about the formation/dissociation kinetics of methane hydrate (as mentioned in Section 1.3).

The free energy landscape such as illustrated in Figure 1.6 shows not only phase stability but also formation/dissociation kinetics of methane hydrate. In this work, two free energy techniques, involving the Einstein molecule approach and the parallel tempering technique, were used within the grand canonical ensemble to determine L–H–V phase equilibrium (Chapters 3 and 4) as well as the free energy barrier for methane hydrate formation/dissociation (Chapter 4).

Direct coexistence method. The direct coexistence method (DCM) is a robust technique to determine phase boundary in a phase diagram (Alavi and Ripmeester, 2010; Anderson, 2004; Aragones et al., 2009; Barmavath et al., 2014; Cabriolu and Li, 2015;

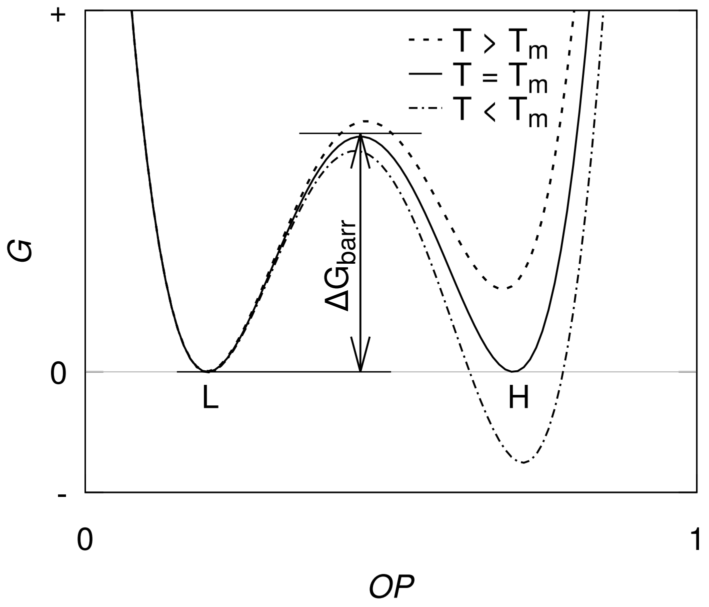

Figure 1.6 Free energy, G, as a function of the normalized order parameter, OP, using biased molecular simulations. Liquid water (L) exhibits a small order parameter, while methane hydrate (H) exhibits a large order parameter. At the melting temperature, $T = T_m$, methane hydrate coexists with liquid water (i.e., the free energies of liquid water and methane hydrate are equal). At high temperature, $T > T_m$, liquid water is stable (i.e., the free energy of liquid water is smaller than that of methane hydrate). At low temperature, $T < T_m$, methane hydrate is stable (i.e., the free energy of methane hydrate is smaller than that of methane hydrate). The free energy barrier between liquid water and methane hydrate, ΔG_{barr}, upon formation is also shown.

Cao et al., 2016; Conde et al., 2013, 2016; Conde and Vega, 2010; Conde et al., 2010; de Azevedo Medeiros et al., 2016; Duan et al., 2011; El-Sheikh et al., 2006; Fortes et al., 2004; Gai et al., 2015; Hakim et al., 2010; Huang et al., 2016a,b; Ilani-Kashkouli et al., 2013; Kang et al., 2014; Katsumasa et al., 2007; Lasich et al., 2014; Lee et al., 2012; Lee and Seo, 2010; Małolepsza et al., 2015; Míguez et al., 2015; Patchkovskii and Tse, 2003; Rodrigues and Fernandes, 2007; Seo et al., 2009; Tsimpanogiannis and Lichtner, 2013; Wu et al., 2015). In this technique, one prepares an initial simulation box with two or three coexisting phases. As shown in Figure 1.7 (*top*), the three coexisting phases, i.e., liquid water + methane hydrate + methane vapor phases, are placed in a cubic simulation box to determine L–H–V phase equilibrium. Then, one performs molecular simulations at different T and P to determine the stability domain for each phase. For a given P, the low symmetry phase (methane hydrate) will be stable below the melting temperature T_m while the high symmetry phase (liquid water coexisting with methane vapor) will be stable above T_m. In other words, liquid water and methane vapor form as methane hydrate for $T < T_m$, as shown in Figure 1.7 (*center*) and (*bottom*). On the other hand, methane hydrate melts as liquid water and methane vapor for $T > T_m$. Usually, one performs molecular dynamics to determine T_m at a given P (English et al., 2005; Fernández et al., 2006; Knott et al., 2012; Naeiji et al., 2016; Sarupria and Debenedetti, 2012; Tung et al., 2010; Yagasaki et al., 2015). For instance, by using different molecular models, some researchers have simulated the phase diagram of methane hydrate (Conde and Vega, 2010; Michalis et al., 2015, 2016b; Míguez et al., 2015). Unlike the thermodynamic models and free energy calculations, the DCM technique does not require to compute the chemical potential of each component in each phase. In addition, the DCM allows one to observe the formation process directly at the molecular scale. As shown in Figure 1.7, the growth of methane hydrate from liquid water and methane vapor can be seen using the direct coexistence method. As another example, one can prepare coexisting phases consisting of methane hydrate within a sphere (radius r), liquid water, and methane vapor. Using the DCM, one can determine the melting temperature, $T_m(r)$, at a given P (Jacobson et al., 2010a). The critical radius of the nucleus (i.e., the minimum radius to keep the nucleus growing) at $T_m(r)$ for a given P can be also described by the Gibbs-Thomson equation.

As mentioned previously, the large free energy barrier between methane hydrate and liquid water leads to very slow kinetic rates for the formation/nucleation of methane hydrate. Furthermore, the DCM technique usually requires very long molecular dynamics or Monte Carlo simulations. Typically, several hundred of nanoseconds are used when using molecular dynamics. For the sake of computational efficiency, this work extended the DCM technique within the grand canonical ensemble, as presented in Chapter 4. This ensemble allows one to: (1) use two coexisting phases instead of three in the simulation box to determine L–H–V phase equilibrium and (2) use a smaller molecular system to mimic an infinite molecular system. For instance, one can prepare a system with L–H coexistence in the simulation box that is in equilibrium with an infinite reservoir. The

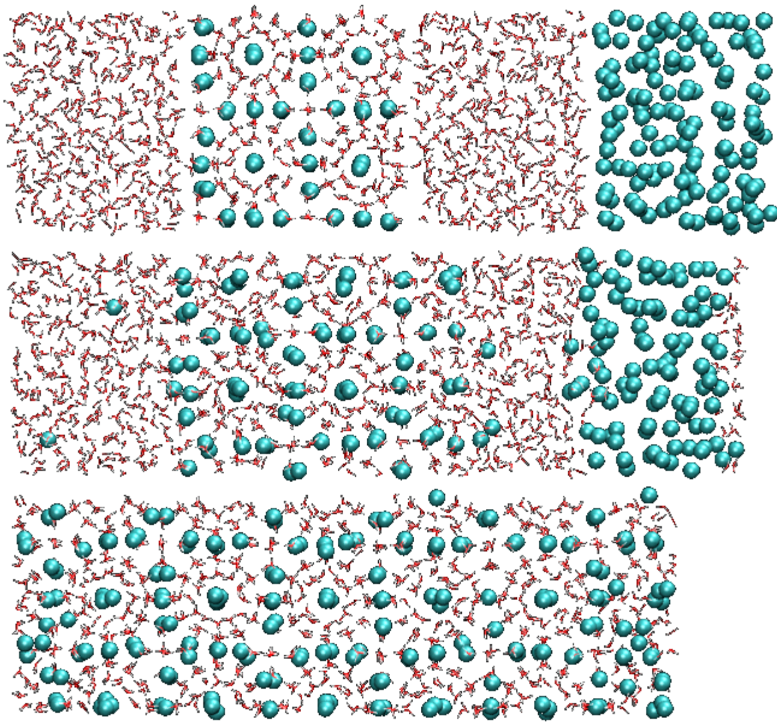

Figure 1.7 (color online) Typical molecular configurations obtained in the direct coexistence method at $T = 294$ K and $P = 600$ bar (where methane hydrate is stable): (*top*) the coexisting phases, i.e., liquid water (L) + methane hydrate (H) + methane vapor (V), are the initial configuration; (*center*) the growth of methane hydrate; and (*bottom*) the perfect methane hydrate formed at the end of the molecular simulation. The red and white lines denote the water molecules while the blue spheres are the methane molecules. [Picture from Ref. (Conde and Vega, 2010)]

reservoir imposes chemical potentials μ_m and μ_w as well as temperature T. This ensemble allows one to determine L–H–V phase equilibrium because the L–H phase also coexists implicitly with methane vapor though the fictive reservoir.

Parallel tempering. In addition to the above techniques, parallel tempering provides another way to improve computational efficiency. Figure 1.8 shows a schematic view of the Boltzmann factor in the phase space at low and high temperatures. As compared with low temperature, the system at high temperature escapes more easily from the metastable state. The Boltzmann factor at high temperature spans a border distributions, and the free energy barrier for phase transition at high temperature is much lower than at low Temperature. The parallel tempering technique helps the system to escape from the metastable states, therefore improving computational efficiency. In practice, within the parallel tempering technique, one prepares N simulation boxes (replicas) where each replica consists of either the solid phase (methane hydrate) or the liquid phase (liquid water). These N molecular replicas are equilibrated under different temperatures independently, and exchange between two configurations is used to avoid configurations to remain trapped into local metastable states. The parallel tempering technique is often used to determine two phase equilibrium, e.g., solid–liquid or liquid–vapor phases transition (Brumby et al., 2016). For instance, Malolepsza et al. used the replica exchange technique to determine L–H phase equilibrium within the framework of isobaric molecular dynamics (Małolepsza et al., 2015). Due to the constant number of molecules in this ensemble, the phase transition between liquid water and empty hydrate (β–ice) is obtained while the L–H–V phase equilibrium is impossible to reach within this ensemble. In this work, the parallel tempering technique was used in the grand canonical ensemble (i.e., hyperparallel tempering Monte Carlo simulation) to determine L–H–V phase equilibrium.

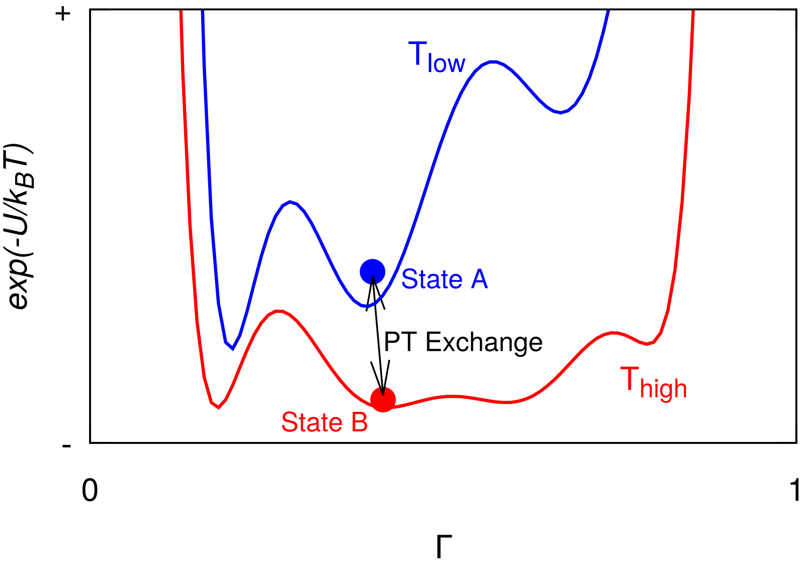

Figure 1.8 Boltzmann factor, $\exp(-U/k_BT)$, in the phase space, Γ, as an example to illustrate the parallel tempering technique. The blue line is for the low temperature, while the red line is for the high temperature. The system in state A (blue circle) remains easily trapped into a metastable state, while the system in state B (red circle) escape more easily. Parallel tempering between A and B is used to make the escape easier.

Many different molecular simulation strategies can be used to determine L–H–V phase equilibrium. In this work, four different molecular simulation strategies were used to determine L–H–V phase equilibrium. First, free energy calculations with the Einstein molecule approach was used to predict L–H–V phase equilibrium. This method exactly follows the thermodynamic definition of phase equilibrium. Second, the direct coexistence method was used to determine the phase transition between liquid water and methane hydrate. This strategy is difficult to determine three phase coexistence (unless one runs the molecular simulation at the exact melting point T and P), but this method is valid to assess the phase boundary using the Einstein molecule approach. Then, the hyperparallel tempering technique was used to accelerate the observation of phase transition due to the slow kinetics rates for the formation/dissociation of methane hydrate. Here "hyperparallel tempering" is referred rather than parallel tempering because we treated the system in the Grand Canonical ensemble. The results for the phase stability of methane hydrate will be presented in Chapter 3. Finally, free energy calculations with the umbrella sampling was used to probe not only the L–H–V phase equilibrium but also the formation/dissociation kinetics of methane hydrate (presented in Chapter 4). All these molecular simulation strategies, involving the direct coexistence method, the parallel tempering technique, and the umbrella sampling technique, were extended in the grand canonical ensemble Monte Carlo simulations.

1.4 Confinement effects at the nanoscale

In nature, most methane hydrate is confined in the voids formed in various porous rocks and/or fractures. This confined methane hydrate interacts with the surface atoms (within a specific distance, typically one or two nanometers for van der Waals interactions and several nanometers for electrostatic interactions) (Casco et al., 2017, 2015; English and MacElroy, 2004; Smirnov, 2017; Smirnov et al., 2016). This fluid–pore interaction leads to an additional contribution to the free energy of methane hydrate. Due to such fluid-pore interactions, confinement effects also lead to non isotropic pressure tensors: the pressure parallel to the interface is P_T while the pressure normal to the interface is P_N. From a physical viewpoint, such non isotropic pressure tensors generate an external surface free energy of the confined fluid which corresponds to the surface tension (Aman and Koh, 2016; Arnaudov et al., 2010). This surface tension has drastic effects on the structure, dynamics and thermodynamics of confined methane hydrate. Therefore, understanding the role of the confinement effects on methane hydrate is an important research field (Bai et al., 2011, 2012; Barmavath et al., 2014; Borchardt et al., 2016; Brovchenko et al., 2004; Casco et al., 2015; Cole et al., 2009; Di Crescenzo et al., 2016; English et al., 2005; Ghaedi et al., 2016; Hachikubo et al., 2011; Ilani-Kashkouli et al., 2013; Kang and Lee, 2010; Kang et al., 2008, 2009a,b; Kyung et al., 2015; Luis et al., 2015; Misyura, 2016; Moore et al., 2010; Seo and Kang, 2010; Seo et al., 2009; Smirnov, 2017; Smirnov et al., 2016; Sun et al., 2015; Tsiberkin et al., 2014; Tsimpanogiannis and Lichtner, 2013; Wang et al., 2015; Yang et al., 2016a; Zhang, 2015; Zhao et al., 2016, 2014). A recent review on confinement effects can be found in Ref. (Borchardt et al., 2018). This reference mainly focuses on the confinement effects on the crystallization/formation, dissociation/melting and phase stability of methane hydrate.

Confinement effects depend on many factors, e.g., surface chemistry, pore width, pore topology and morphology, etc. Thus, various porous materials will lead to different confinement effects. Many porous materials in nature (e.g., porous silica, clay minerals, etc.) and in man-made materials (e.g., polymers, zeolites, metal organic frameworks, etc.) can be used to study confinement effects on the phase stability of methane hydrate (Aladko et al., 2004; Anderson et al., 2003; Cuadrado-Collados et al., 2018; Kang et al., 2008; Seo et al., 2002, 2009; Uchida et al., 1999, 2002). Many observations suggest that confinement in micro- and meso-pores leads to a reduced phase stability (i.e., the L–H–V phase boundary is shifted towards a higher pressure and/or lower temperature) (Aladko et al., 2004; Birkedal et al., 2014; Handa and Stupin, 1992; Madden et al., 2009; Prasad et al., 2012). However, confinement in fine glass beads shows a positive effect on phase stability (Anderson et al., 2003; Hachikubo et al., 2011; Kang et al., 2008, 2009a). At a given pressure, let us consider the shift in the melting point, ΔT_m, of confined methane hydrate with respect to bulk methane hydrate: $\Delta T_m = T_m^{pore} - T_m^{bulk}$ where T_m^{pore} is the melting point of confined methane hydrate in the porous material and T_m^{bulk} is the melting point of bulk methane hydrate. This shift in phase stability is often described using the Gibbs-Thomson equation for a slit pore (Chakraborty and Gelb, 2012a; Seo et al., 2002; Uchida et al., 1999),

$$\frac{\Delta T_m}{T_m^{bulk}} = \frac{2v\gamma_{\mathrm{LH}}\cos\theta}{\Delta h_m}\frac{1}{D_p} \tag{1.15}$$

where γ_{LH} is the surface tension between liquid water and methane hydrate, θ is the angle between the surface of the substrate and the surface formed by methane hydrate and liquid water (i.e., contact angle), v is the molar volume (i.e., the reciprocal of the number density: $v = 1/\rho$) of the hydrate/liquid phase, Δh_m is the molar enthalpy of melting from methane hydrate to liquid water, and D_p is the pore width.

The Gibbs-Thomson equation suggests that the shift in the melting point of confined methane hydrate at constant pressure linearly depends on the reciprocal of the pore width: $\Delta T_m \sim 1/D_p$. Several researchers focused on the application of the Gibbs-Thomson equation to methane hydrate. For instance, Chakraborty et al. used this equation to determine the surface tension (Chakraborty and Gelb, 2012a) of methane hydrate-liquid water. Seo et al. used the Gibbs-Thomson equation for their thermodynamic modeling to predict the phase diagram of methane hydrate in pores (Seo et al., 2002, 2009). However, the validation of the Gibbs–Thomson equation for very small pores remains to be established. First, the determination of the true melting point at equilibrium is difficult in practice. Most experiments and theoretical simulations determine the dissociation point of methane hydrate (here, dissociation means the point where methane hydrate transforms to liquid water) instead of the true melting point (Aladko et al., 2004; Chakraborty and Gelb, 2012a; Seo et al., 2002; Uchida et al., 1999). However, the dissociation point can be far from the equilibrium transition point due to the large free energy barrier between methane hydrate and liquid water.

It should also be noted that the Gibbs–Thomson equation given above relies on the following approximation: the number density of molecules in the hydrate phase, ρ_{H}, and in the liquid phase, ρ_{L}, are assumed to be equal, i.e., $\rho_{\mathrm{H}} \sim \rho_{\mathrm{L}}$. In contrast, a large difference in the number density of $\sim 20\%$ is found in realistic conditions between liquid water and methane hydrate. Finally, Young's equation, $\gamma_{LH} \cos\theta = \gamma_{LS} - \gamma_{HS}$, and the contact angle $\theta = 0$ are usually imposed in the Gibbs-Thomson equation. The availability of Young's equation is unknown for small pores and the value of θ is also difficult to determine. In this work, the Gibbs-Thomson equation will be revisited by considering the different densities ($\rho_{\mathrm{H}} \neq \rho_{\mathrm{L}}$) and the different surface tensions γ_{LS} and γ_{HS} which will be determined using molecular simulation. Then, the true melting point of bulk and confined methane hydrate will be determined to check the validity of the Gibbs-Thomson equation.

Confinement in porous materials seems to lead to faster formation kinetics of methane hydrate (Borchardt et al., 2018; Casco et al., 2015; Cha et al., 1988; Ganji et al., 2007; Govindaraj et al., 2015; Li et al., 2006; Linga et al., 2012; Phan et al., 2014; Seo and Kang, 2010; Smelik and King, 1997; Yan et al., 2005). For instance, experimental data suggest a shorter formation time of methane hydrate in bentonite (clay) (Cha et al., 1988) as compared with bulk methane hydrate. Silica/sand exhibits an improved conversion up to $\sim 94\%$ (vs. $\sim 74\%$ for bulk methane hydrate) and a shorter formation time of 34 h (vs. 60 h for bulk methane hydrate) (Linga et al., 2012). These confinement effects, which arise mainly from surface chemistry and fluid–pore interactions, decrease the free energy barrier between methane hydrate and liquid water. However, the physical reasons for such faster formation kinetics remain unclear.

In addition to its effects on phase stability and formation kinetics, confinement also affects the structure of methane hydrate (Babu et al., 2013; Borchardt et al., 2016; Casco et al., 2015; Cha et al., 1988; Miyawaki et al., 1998; Siangsai et al., 2015). For instance, the hydrate phase formed in porous carbons can consist of a monolayer of methane molecules adsorbed at the pore walls and a hydrogen–bonded zigzag chain in the pore center (Borchardt et al., 2018; Miyawaki et al., 1998). Such hydrate structure is not formed as a perfect sI structure, and the stable methane composition for such hydrate phase, x_m, is $\sim$0.333 (where $x_m = n_m/(n_m + n_w)$ with the number of methane, n_m, and water, n_w, molecules in one unit cell). In contrast, we recall that for the sI structure $x_m = 0.147$

(i.e., $n_w : n_m = 5.78$). Recently, a hydrate phase was found in carbon nanotubes (Agrawal et al., 2016; Zhao et al., 2016). Another goal of the present work will be to assess such confinement effects on the structure and physical and physicochemical properties of confined methane hydrate.

1.5 Summary

In this chapter, the crystalline structure, thermodynamic properties, crystallization theory, formation/dissociation kinetics, and phase stability of methane hydrate were reviewed. Such review aims at giving some physical insights into the dynamics and thermodynamics of methane hydrate as well as the corresponding formation/dissociation kinetics. We also introduced the role of confinement effects at the nanoscale. Several key points can be summarized as follows:

Methane hydrate in typical environmental and experimental conditions forms as structure I (sI). In this structure, 46 water molecules form two small pentagonal dodecahedral cages (5^{12}) and six tetracaidecahedral cages ($5^{12}6^{2}$) so that a maximum of 8 methane molecules can be encapsulated. In addition to the above packing of water molecules, methane hydrate should obey three criteria: (1) proton disorder, (2) ice rules, and (3) zero dipole moment. On the one hand, the local bond order parameters, Q_l, provide a tool to identify the structure of liquid water, hexagonal ice, and methane hydrate. On the other hand, free energy calculations can be used to assess the formation kinetics and phase stability of methane hydrate.

The classical nucleation theory suggests that the crystallization of methane hydrate is a two-step mechanism: the formation and growth of a crystal-like nucleus in liquid water. Such mechanism suggests that the formation kinetics of methane hydrate is controlled by two factors: the number density of nucleation sites and the free energy barrier between methane hydrate and liquid water. By using additives (thermodynamic promoter/inhibitor) to alter these two factors, one can increase/decrease the nucleation rate, e.g., using the thermodynamic inhibitor to prevent the formation of methane hydrate that could block pipelines.

Phase stability is one of the most important characteristics of methane hydrate. The pressure–temperature phase diagram shows the phase boundary of liquid–hydrate–vapor phase equilibrium (or ice–hydrate–vapor at low temperature). Along this phase boundary, methane hydrate coexists with liquid water and methane vapor, i.e., the chemical potentials of water/methane in these three phases are equal. Different theoretical techniques can be used to assess the phase stability of methane hydrate, e.g., free energy calculations, direct coexistence method, parallel tempering, etc. Using suitable molecular models for methane and water molecules, one could obtain an accurate L–H–V phase diagram.

Methane hydrate can be confined at the nanoscale in different nanoporous medium. These nanoporous materials lead to strong surface interactions with methane hydrate and liquid water which provide an additional free energy contribution, i.e., surface tension γ_{LW} and γ_{HW}. At the nanoscale, confinement effects lead to reduced phase stability, i.e., a decreased melting temperature at a given pressure or an increased melting pressure at a given temperature, for methane hydrate. Although such reduced phase stability is often described using the Gibbs-Thomson equation, less effort has been devoted to establishing the validity of the Gibbs-Thomson equation for methane hydrate confined at the nanoscale level.

Chapter 2

Statistical Mechanics and Computational Methods

Contents

2.1 Statistical mechanics **37**

2.1.1 Classical statistical mechanics 37

2.1.2 Ensembles 39

2.2 Monte Carlo simulation **41**

2.2.1 Detailed balance and Metropolis scheme 41

2.2.2 Trial moves and acceptance probabilities 43

2.2.3 Details of Monte Carlo simulation 47

2.3 Molecular Dynamics **49**

2.3.1 Ergodicity 49

2.3.2 Newton's equation 49

2.3.3 Integration scheme 50

2.3.4 Thermostat and barostat 51

2.3.5 Details of molecular dynamics 53

2.4 Interaction potentials **54**

2.4.1 Intramolecular potential 54
2.4.2 Intermolecular potential 55
2.5 Molecular models 59

2.1 Statistical mechanics

2.1.1 Classical statistical mechanics

Statistical mechanics establishes the link between the macroscopic properties of a system and the motions of its microscopic elements (atoms, molecules, etc.). Statistical mechanics provides a way to determine the thermodynamic and dynamic behaviors of a molecular system at equilibrium. This chapter mainly discusses the thermodynamics and dynamics of systems for which the motion of atoms and molecules can be described using classical statistical mechanics. Taking a system having a volume V and a number of particles N, we consider the set of coordinates $\mathbf{r}^N = (\mathbf{r}_1, \mathbf{r}_2, \ldots, \mathbf{r}_N)$ and the set of momenta $\mathbf{p}^N = (\mathbf{p}_1, \mathbf{p}_2, \ldots, \mathbf{p}_N)$ for each of the N particles. The total kinetic energy, E_k, of the system is given by the following summation over these N particles,

$$E_k(\mathbf{p}^N) = \sum_i^N E_{k,i} = \sum_i^N \mathbf{p}_i^2/(2m_i) \tag{2.1}$$

where $E_{k,i}$ and m_i is the kinetic energy and mass of the i-th particle, respectively. The total potential energy, U, is a function of all particles' coordinates (and orientations if the particles are molecules),

$$U(\mathbf{r}^N) = U(\mathbf{r}_1, \mathbf{r}_2, \ldots, \mathbf{r}_N) \tag{2.2}$$

The classical Hamiltonian, $\mathscr{H}(\mathbf{r}^N, \mathbf{p}^N)$, is the sum of the kinetic and potential energy,

$$\begin{aligned} \mathscr{H}(\mathbf{r}^N, \mathbf{p}^N) &= E_k(\mathbf{p}^N) + U(\mathbf{r}^N) \\ &= \sum_i^N p_i^2/(2m_i) + U(\mathbf{r}^N) \end{aligned} \tag{2.3}$$

The partition function, Q, is defined as the following integral over all particles' coordinates and momenta:

$$Q = \frac{1}{h^{3N}N!}\int d\mathbf{r}^N d\mathbf{p}^N \exp\left[-\beta_T\left(\sum_i^N p_i^2/(2m_i) + U(\mathbf{r}^N)\right)\right] \tag{2.4}$$

where $\int d\mathbf{r}^N d\mathbf{p}^N = \int\cdots\int d\mathbf{r}_1\cdots d\mathbf{r}_N d\mathbf{p}_1\cdots d\mathbf{p}_N$. The factor $1/N!$ accounts for the fact that these N identical particles are indistinguishable. $\beta_T = 1/k_BT$ is the reciprocal of the thermal energy with k_B the Boltzmann constant. h in the above equation is Planck's constant. The partition function and its derivatives with respect to the temperature T, pressure P, and volume V, describe the thermodynamics of the system. For instance, the internal energy can be expressed as $\langle E\rangle = -\partial \ln Q/\partial\beta_T$ while the entropy can be expressed as $S = \partial\left(k_BT\ln Q\right)/\partial T$. From a statistical physics point of view, the probability, $P(s)$, to find a system in a given microstate, $s = (\mathbf{r}^N, \mathbf{p}^N)$, reads,

$$P(s) = \frac{1}{Q}\exp\left[-\beta_T\left(\sum_i^N p_i^2/(2m_i) + U(\mathbf{r}^N)\right)\right] \tag{2.5}$$

The above equation shows that the partition function Q is a normalization constant (the normalization is to ensure that the integral of the probability over all possible microstates is equal to one),

$$\begin{aligned}\int dsP(s) &= \frac{1}{Q}\int d\mathbf{r}^N d\mathbf{p}^N \exp\left[-\beta_T\left(\sum_i^N p_i^2/(2m_i) + U(\mathbf{r}^N)\right)\right] \\ &= 1\end{aligned} \tag{2.6}$$

Any thermodynamic property of interest, X, can be determined using its average, $\langle X\rangle$, over all possible microstates (i.e., ensemble average),

$$\langle X\rangle = \frac{1}{Q}\int d\mathbf{r}^N d\mathbf{p}^N \exp\left[-\beta_T\left(\sum_i^N p_i^2/(2m_i) + U(\mathbf{r}^N)\right)\right] X\left(\mathbf{r}^N, \mathbf{p}^N\right) \tag{2.7}$$

where $X\left(\mathbf{r}^N,\mathbf{p}^N\right)$ is the value taken by X when the system is in the microstate $s=(\mathbf{r}^N,\mathbf{p}^N)$. The above equation is the starting point in molecular simulation which is used to determine the thermodynamic and dynamic behaviors of a many-body system.

2.1.2 Ensembles

As previously discussed, a thermodynamic property of interest, $\langle X\rangle$, can be obtained using an ensemble average. The statistical ensemble, which is defined from the thermodynamic parameters that are constant, leads to a specific partition function. Here, I discuss the three statistical mechanics ensembles that will be used in this work.

(1) Canonical ensemble, NVT. The canonical ensemble is relevant to a system consisting of N particles in a volume V that is in equilibrium with a thermostat at a temperature T. Such a system exchanges energy, E, with the thermostat which imposes the temperature T. The canonical ensemble contains all the possible microstates that are consistent with N, V, and T as constraints. The partition function, Q_{NVT}, corresponding to this ensemble reads,

$$\begin{aligned} Q_{NVT} &= \frac{1}{h^{3N}N!}\int d\mathbf{r}^N d\mathbf{p}^N \exp\left[-\beta_T\left(\sum_i^N p_i^2/(2m_i)+U(\mathbf{r}^N)\right)\right] \\ &= \frac{1}{\Lambda^{3N}N!}\int d\mathbf{r}^N \exp\left(-\beta_T U(\mathbf{r}^N)\right) \\ &= \frac{V^N}{\Lambda^{3N}N!}\int d\mathbf{s}^N \exp\left(-\beta_T U(\mathbf{s}^N)\right) \end{aligned} \tag{2.8}$$

where $\Lambda = h/\sqrt{2\pi m k_B T}$ is the thermal de Broglie wavelength with m the mass of the particle, k_B the Boltzmann constant, and h the Planck constant. In the above equation, Λ^{3N} is the integral of the kinetic energy over all the N particles (the term $1/h^{3N}$ is included in this contribution). For the sake of convenience, the above equation can be simplified using a reduced coordinate set, $\mathbf{s}^N=(\mathbf{s}_1,\mathbf{s}_2,\cdots,\mathbf{s}_N)=(\mathbf{r}_1/L,\mathbf{r}_2/L,\cdots,\mathbf{r}_N/L)$, where these N particles are assumed to be located in a cubic box of a dimension L.

(2) Isobaric–isothermal ensemble, NPT. The isobaric–isothermal ensemble is relevant to a system of N particles in equilibrium with a thermostat imposing its temperature T and a barostat imposing its pressure P. The system exchanges thermal energy with the thermostat and mechanical energy/volume with the barostat. The NPT ensemble contains all the possible microstates that are consistent with N, P, and T as constraints. The NPT ensemble is often used to mimic experiments due to the fact that many real conditions are performed by controlling T and P. The partition function, Q_{NPT}, corresponding to this ensemble can be written as the weighted integral of Q_{NVT},

$$Q_{NPT} = \int dV \exp\left(-\beta_T PV\right) \left(\beta_T P\right) Q_{NVT} \tag{2.9}$$

(3) Grand canonical ensemble, μVT. The grand canonical ensemble is relevant to a system which has a constant volume V but with a fluctuating number N of particles. This system is in equilibrium with a reservoir which imposes its temperature T and its chemical potential μ. The system exchanges energy E and particles with the reservoir. The μVT ensemble contains all the possible microstates that are consistent with μ, V, and T as constraints. The partition function, $Q_{\mu VT}$, corresponding to this ensemble can be written as the weighted summation (N is discrete) of Q_{NVT},

$$Q_{\mu VT} \equiv \sum_{N=0}^{+\infty} \exp\left(\beta_T \mu N\right) Q_{NVT} \tag{2.10}$$

There are other statistical ensembles such as the isoenthalpic-isobaric ensemble NHP. For a binary mixture (e.g., methane hydrate in this work), combined ensembles can also be used such as the semi–grand ensemble, $\mu_1 N_2 PT$. In this thesis, the latter ensemble was used for bulk methane hydrate. Such semi–grand ensemble requires that the system has a constant number of molecules for the second species, N_2. In contrast, the first species is at constant chemical potential μ_1 so that N_1 fluctuates. The whole system is in equilibrium with the thermostat and barostat which impose the pressure P and temperature T. The partition function, $Q_{\mu_1 N_2 PT}$, corresponding to this ensemble reads,

$$Q_{\mu_1 N_2 PT} = \sum_{N_1=0}^{+\infty} \exp(N_1 \mu_1) \int dV \exp(-\beta_T PV) (\beta_T p) Q_{NVT} \tag{2.11}$$

2.2 Monte Carlo simulation

2.2.1 Detailed balance and Metropolis scheme

Monte Carlo (MC) sampling methods are widely applied to determine the thermodynamic behavior of a system in classical molecular simulation. The sampling in a Monte Carlo (MC) simulation can be done by generating microstates randomly. However, complete random sampling is generally not possible as one cannot sample efficiently the whole phase space. Also, evaluation of an integral such as $\int d\mathbf{s}^N \exp\left[-\beta_T U(\mathbf{s}^N)\right]$ is often impossible in practice. The Metropolis scheme provides an efficient sampling algorithm in which sampling is performed according to the Boltzmann factor. A system at equilibrium obeys the principle of micro-reversibility (also known as “detailed balance” in statistical mechanics), which states that the total probability of transitions from every initial microstate, o_i, to all other microstates, n_j, is equal to the total probability of transitions from these microstates n_j to the microstate o_i,

$$\sum_j \rho(o_i)\Pi(o_i \to n_j) = \sum_j \rho(n_j)\Pi(n_j \to o_i) \quad \forall i = 1, 2, \cdots \tag{2.12}$$

where $\rho(o_i)$ is the probability of a microstate o_i while $\rho(n_j)$ is the probability of a microstate n_j. $\Pi(o_i \to n_j)$ is the probability of transition from microstate o_i to n_j while $\Pi(n_j \to o_i)$ is the probability of transition from microstate n_j to o_i. Summation over j indicates the total probability of transition. The above detailed balance condition is valid and can be used for any strategy in MC simulation. In practice, a much stronger detailed balance condition is imposed as follows: the transition probability from microstate o_i to microstate n_j is taken equal to by the transition probability from microstate n_j to microstate

o_i,

$$\rho(o_i)\Pi(o_i \to n_j) = \rho(n_j)\Pi(n_j \to o_i) \quad \forall\, i = 1,2,\cdots \tag{2.13}$$

Such a stronger detailed balance condition obviously satisfies the requirement of Eq. (2.12). In practice, only one MC move is attempted at every MC step: for a current microstate o, one MC trial move $o \to n$ must therefore verifies:

$$\rho(o)\Pi(o \to n) = \rho(n)\Pi(n \to o) \tag{2.14}$$

where $\Pi(o \to n) = \alpha(o \to n)P_{acc}(o \to n)$ and $\Pi(n \to o) = \alpha(n \to o)P_{acc}(n \to o)$ so that,

$$\rho(o)\alpha(o \to n)P_{acc}(o \to n) = \rho(n)\alpha(n \to o)P_{acc}(n \to o) \tag{2.15}$$

where $\rho(o)$ and $\rho(n)$ are the probabilities to find the system in the microstate o and n (the probability can be obtained from the partition function Q which depends on the ensemble). $\alpha(o \to n)$ and $\alpha(n \to o)$ are the probabilities to attempt a trial move from o to n and from n to o. $P_{acc}(o \to n)$ and $P_{acc}(n \to o)$ are the probabilities to accept the corresponding trial moves. For most MC moves, α is chosen as a symmetric matrix, $\alpha(o \to n) = \alpha(n \to o)$, thus,

$$\frac{P_{acc}(o \to n)}{P_{acc}(n \to o)} = \frac{\rho(n)}{\rho(o)} \tag{2.16}$$

Many statistical distributions can verify this stronger detailed balance condition. Here, we choose the Metropolis scheme that generates Markov chains and accepts trial moves as follows:

$$\begin{aligned}
&(1)\text{ for } \rho(n)/\rho(o) < 1, \text{ we have } P_{acc}(o \to n) = \rho(n)/\rho(o) \text{ and } P_{acc}(n \to o) = 1\\
&(2)\text{ for } \rho(n)/\rho(o) > 1, \text{ we have } P_{acc}(o \to n) = 1 \text{ and } P_{acc}(n \to o) = \rho(n)/\rho(o)
\end{aligned} \tag{2.17}$$

or using a simplified formulation,

$$\begin{aligned} P_{acc}(o \to n) &= \min\{1, \rho(n)/\rho(o)\} \\ P_{acc}(n \to o) &= \min\{1, \rho(o)/\rho(n)\} \end{aligned} \tag{2.18}$$

Instead of complete random sampling, the Metropolis algorithm generates sampling using a relative probability to avoid sampling very low probability states. Such sampling significantly improves the efficiency of MC simulation. In the next section, the typical trial moves and the corresponding acceptance probabilities used in Monte Carlo simulation within various ensembles are discussed.

2.2.2 Trial moves and acceptance probabilities

Most real experiments can be mimicked by choosing different ensembles. Within various statistic ensembles, the different trial moves that can be used, and the corresponding acceptance probabilities vary. However, they must respect the constant thermodynamic parameters for a specific ensemble. Here, we list the typical trial moves and acceptance probabilities for various ensembles relevant to this work. By recalling the partition function for various ensembles (see Section 2.1.2), the probability to find the system in a microstate o within different ensembles, $\rho_{\dots}(o)$, reads:

$$\begin{aligned} \rho_{NVT}(o) &= \frac{1}{Q_{NVT}} \frac{V^N}{\Lambda^{3N} N!} \exp\left(-\beta_T U(\mathbf{s}^N(o))\right) \\ \rho_{NPT}(o) &= \frac{1}{Q_{NPT}} \frac{1}{\Lambda^{3N} N!} \exp\left[-\beta_T \left(PV - \frac{(N+1)\ln V}{\beta_T} + U(\mathbf{s}^N(o)\right)\right] \\ \rho_{\mu VT}(o) &= \frac{1}{Q_{\mu VT}} \frac{V^N}{\Lambda^{3N} N!} \exp\left(\beta_T(\mu N - U(\mathbf{s}^N(o))\right) \\ \rho_{\mu_1 N_2 PT}(o) &= \frac{1}{Q_{\mu_1 N_2 PT}} \frac{1}{\Lambda^{3N} N!} \exp\left[-\beta_T \left(PV - \frac{(N+1)\ln V}{\beta_T} - \mu_1 N_1 + U(\mathbf{s}^N(o)\right)\right] \end{aligned} \tag{2.19}$$

Molecule translation and rotation. These two trial moves only change the potential energy contribution in Eq. (2.19). As a result, the acceptance probability can be computed using the potential energy term only. One molecule in the old configuration o is randomly chosen (e.g., the i-th molecule), and the translation trial move consists of displacing it by a small random value to generate a new configuration n,

$$\begin{aligned} x_i(n) &= x_i(o) + \Delta_{max}(\text{ranf}() - 0.5) \\ y_i(n) &= y_i(o) + \Delta_{max}(\text{ranf}() - 0.5) \\ z_i(n) &= z_i(o) + \Delta_{max}(\text{ranf}() - 0.5) \end{aligned} \tag{2.20}$$

where Δ_{max} is the maximum displacement and ranf() is a random number uniformly distributed between 0 and 1. Rotation trial moves change the orientation of a randomly chosen molecule by a small random Euler's rotation matrix $\mathfrak{R}_{33}$ to generate a new configuration n,

$$\begin{pmatrix} x_i(n) \\ y_i(n) \\ z_i(n) \end{pmatrix} = \mathfrak{R}_{33} \begin{pmatrix} x_i(o) \\ y_i(o) \\ z_i(o) \end{pmatrix} = \begin{pmatrix} R_{11} & R_{12} & R_{13} \\ R_{21} & R_{22} & R_{23} \\ R_{31} & R_{32} & R_{33} \end{pmatrix} \begin{pmatrix} x_i(o) \\ y_i(o) \\ z_i(o) \end{pmatrix} \tag{2.21}$$

The probability to find the system in a microstate n, $\rho(n)$, can be determined by Eq. (2.19). For these two trial moves, the probability to attempt a trial move from o to n is equal to the probability to attempt a trial move from n to o, i.e., $\alpha(o \to n) = \alpha(n \to o) = 1/(2N)$. Thus, according to Eq. (2.18), the acceptance probability $P_{acc}(o \to n)$ for such trial moves can be expressed as,

$$P_{acc}(o \to n) = \min\left\{1, \frac{\rho(n)}{\rho(o)}\right\} = \min\left\{1, \exp\left(-\beta_T \Delta U(\mathbf{s}^N)\right)\right\} \tag{2.22}$$

where $\Delta U(\mathbf{s}^N) = U(\mathbf{s}^N(n)) - U(\mathbf{s}^N(o))$ is the potential energy difference before and after the trial move. The acceptance probability given above can be used for these two trial moves in all statistical ensembles.

Molecule insertion and removal. These two trial moves are only used for systems in which the number of particles N is not constant, e.g., μVT and $\mu_1 N_2 PT$ ensembles. The insertion trial move generates a new configuration n by randomly inserting a molecule at an arbitrary position into the old configuration o. Inversely, the removal trial move attempts to remove a randomly selected molecule from configuration n (note that $N+1$ molecules in the configuration n). Therefore,

$$\begin{aligned} \alpha(o \to n) &= \frac{1}{2}\frac{dr}{V} \\ \alpha(n \to o) &= \frac{1}{2}\frac{1}{N+1} \end{aligned} \tag{2.23}$$

The probability to find the system in a microstate n with $(N+1)$ molecules is given by,

$$\rho_{\mu VT}(n) = \frac{1}{Q_{\mu VT}} \frac{V^{(N+1)}}{\Lambda^{3(N+1)}(N+1)!} \exp\left(\beta_T(\mu(N+1) - U(\mathbf{s}^{(N+1)}(n))\right) \tag{2.24}$$

According to Eq. (2.18), the acceptance probability for such insertion moves can be expressed as,

$$\begin{aligned} P_{acc}(o \to n) &= \min\left\{1, \frac{\rho(n)\alpha(n \to o)}{\rho(o)\alpha(o \to n)}\right\} \\ &= \min\left\{1, \frac{V}{\Lambda^3(N+1)} \exp\left[\beta_T\left(\mu - (U(\mathbf{s}^{(N+1)}(n)) - U(\mathbf{s}^N(o))\right)\right]\right\} \end{aligned} \tag{2.25}$$

The removal trial move can be viewed as the reversible process of insertion, where the molecular number changes from N to $N-1$, not from $N+1$ to N so that,

$$\begin{aligned} \alpha(o \to n) &= \frac{1}{2}\frac{1}{N} \\ \alpha(n \to o) &= \frac{1}{2}\frac{dr}{V} \end{aligned} \tag{2.26}$$

According to Eq. (2.18), the acceptance probability for such removal trial moves can be expressed as,

$$\begin{aligned} P_{acc}(n \to o) &= \min\left\{1, \frac{\rho(o)\alpha(o \to n)}{\rho(n)\alpha(n \to o)}\right\} \\ &= \min\left\{1, \frac{\Lambda^3 N}{V} \exp\left[-\beta_T\left(\mu + \left(U(\mathbf{s}^{(N-1)}(n)) - U(\mathbf{s}^N(o))\right)\right)\right]\right\} \end{aligned} \tag{2.27}$$

Volume change. Volume change is necessary to treat systems in the isobaric ensemble, such as NPT and $\mu_1 N_2 PT$. Here, we take the NPT ensemble as an example to establish the acceptance probability for this trial move. Volume trial moves generate a new volume, $V(n)$, based on the old volume, $V(o)$, for the molecular system using a small random change in volume,

$$V(n) = \lambda V(o) = (1 + \Delta V_{max}(\text{rand}() - 0.5))\, V(o) \tag{2.28}$$

where ΔV_{max} is the maximum volume change allowed at each Monte Carlo step. $\lambda = V(n)/V(o)$ is the rescaling factor for the coordinates of system molecules. The new coordinates of each molecule ($\mathbf{r}_i(n)$) are obtained by rescaling their old coordinates ($\mathbf{r}_i(o)$), $\mathbf{r}_i(n) = \lambda^{1/3}\mathbf{r}_i(o)$. The probability to find the system in a microstate n is given by,

$$\rho_{NPT}(n) = \frac{1}{Q_{NPT}} \frac{1}{\Lambda^{3N} N!} \exp\left[-\beta_T \left(PV(n) - \frac{(N+1)\ln V(n)}{\beta_T} + U(\mathbf{s}^N(n))\right)\right] \tag{2.29}$$

The probability to attempt such trial moves is,

$$\begin{aligned} \alpha(o \to n) &= \frac{1}{2}\frac{dv}{V} \\ \alpha(n \to o) &= \frac{1}{2}\frac{dv}{V} \end{aligned} \tag{2.30}$$

According to Eq. (2.18), the acceptance probability for such volume trial moves can be expressed as,

$$\begin{aligned} P_{acc}(o \to n) &= \min\left\{1, \frac{\rho(n)\alpha(n \to o)}{\rho(o)\alpha(o \to n)}\right\} \\ &= \min\left\{1, \left(\frac{V(n)}{V(o)}\right)^{(N+1)} \exp\left[-\beta_T (P(V(n) - V(0)) - \left(U(\mathbf{s}^{(N)}(n)) - U(\mathbf{s}^N(o))\right)\right]\right\} \end{aligned} \tag{2.31}$$

2.2.3 Details of Monte Carlo simulation

Monte Carlo simulation in the canonical ensemble (CMC) were used in our free energy calculations to determine (1) the free energy change between the non-interacting and the interacting Einstein molecules ΔA_1 and (2) the free energy change from the Einstein molecule to the methane hydrate ΔA_2 (again, details of the free energy calculations will be given later). In these canonical simulations (constant number of particles N, temperature T, and volume V), MC moves include rotations for the water molecules and translations for the water and methane molecules. In the framework of the Metropolis algorithm, each move from an old (o) to a new (n) microscopic states was accepted or rejected according to the acceptance probability $P_{acc} = \min\{1, p^n_{NVT}/p^o_{NVT}\}$ where p_{NVT} for a given configuration corresponds to the density of states in the canonical ensemble:

$$p_{NVT}(\mathbf{s}^N) \propto \frac{V^N}{N!} \exp\left(\frac{-U(\mathbf{s}^n)}{k_B T}\right) \tag{2.32}$$

where $\mathbf{s}^N$ is the set of coordinates of the N molecules in a given microscopic configuration and $U(\mathbf{s}^N)$ is the corresponding intermolecular potential energy.

Semi-Grand Monte Carlo (SGMC) simulations were performed to determine the number of methane molecules N_m^{H} inside the methane hydrate as a function of their chemical potential μ_m^{H} at given T and P (here, the subscript m refers to methane while the superscript H refers to the hydrate phase). In this hybrid ensemble, methane is treated at constant chemical potential μ_m^{H} and temperature T while water is treated at constant number of molecules N_w^{H} and temperature T. On the other hand, the volume V is allowed to fluctuate since the system is at constant pressure P. For each T and P, we start from an equilibrium configuration obtained using isobaric-isothermal MD simulations. MC moves in SGMC simulations include rotations and translations for water and translations, insertions, and deletions for methane. Moreover, volume changes are also attempted. In the framework of the Metropolis algorithm, moves from an old (o) to a new (n) microscopic states are accepted or rejected according to the acceptance probability

$P_{acc} = \min\{1, p^{n}_{\mu_m N_w PT}/p^{o}_{\mu_m N_w PT}\}$ where $p_{\mu_m N_w PT}$ for a given configuration corresponds to the density of states in the semi-grand canonical ensemble:

$$p_{\mu_m N_w PT}(\mathbf{s}^N) \propto \frac{V^N}{N!} \exp\left(\frac{-PV}{k_B T}\right) \exp\left(\frac{N_m \mu_m}{k_B T}\right) \exp\left(\frac{-U(\mathbf{s}^n)}{k_B T}\right) \tag{2.33}$$

As in the case of canonical Monte Carlo simulations, $\mathbf{s}^N$ is the set of coordinates for the N molecules in the microscopic configuration while $U(\mathbf{s}^N)$ is the corresponding intermolecular potential energy. V and N_m are the volume and number of methane molecules in the configuration.

Grand Canonical Monte Carlo simulations (GCMC) were used in the direct coexistence method and the hyper parallel tempering technique. In the grand canonical ensemble, the system has a constant volume and methane and water are at constant chemical potentials μ_m, μ_w and temperature T. Monte Carlo moves in the grand canonical ensemble include rotations, translations, insertions, and deletions for both water and methane. In this ensemble, moves from an old (o) to a new (n) microscopic states are accepted or rejected using a Metropolis scheme with an acceptance probability $P_{acc} = \min\{1, p^{n}_{\mu_m \mu_w VT}/p^{o}_{\mu_m \mu_w VT}\}$ where $p_{\mu_m \mu_w VT}$ for a given configuration corresponds to the density of states in the grand canonical ensemble:

$$p_{\mu_m \mu_w VT}(\mathbf{s}^N) \propto \frac{V^N}{N!} \exp\left(\frac{N_m \mu_m + N_w \mu_w}{k_B T}\right) \exp\left(\frac{-U(\mathbf{s}^n)}{k_B T}\right) \tag{2.34}$$

$\mathbf{s}^N$ is the set of coordinates of the N molecules in the microscopic configuration while $U(\mathbf{s}^N)$ is the corresponding intermolecular potential energy. N_w and N_m are the numbers of water and methane molecules in the configuration.

2.3 Molecular Dynamics

2.3.1 Ergodicity

The ergodic hypothesis, which is often invoked in statistical physics, states that an ensemble average, $\langle X \rangle$, is equal to an average over time, $\langle X \rangle_\tau$,

$$\langle X \rangle = \langle X \rangle_\tau = \lim_{\tau \to \infty} \frac{1}{\tau} \int_0^\tau X(\tau) d\tau \tag{2.35}$$

The above equation indicates that the thermodynamic behavior can be determined from the trajectories generated over a long period τ obtained using molecular dynamics. Using the ergodic hypothesis, molecular dynamics is performed as follows: starting from an initial configuration, after a time corresponding to equilibrium, the system evolves over a long time within a specific ensemble to generate a very long trajectory. This trajectory is used to determine the thermodynamic behavior of the system.

2.3.2 Newton's equation

Let us consider a molecular system of N particles. These N particles have a set of mass $(m_1, m_2, \cdots, m_N)$, a set of positions $(\mathbf{r}_1(t=0), \mathbf{r}_2(t=0), \cdots, \mathbf{r}_N(t=0))$, and a set of velocities $(\mathbf{v}_1(t=0), \mathbf{v}_2(t=0), \cdots, \mathbf{v}_N(t=0))$ at the time $t=0$. The sampling used to determine a time average derive from the trajectories of these N particles. In classical mechanics, these N particles obey the Newton's equation:

$$m_i \ddot{\mathbf{r}}_i(t) = \mathbf{F}_i(t), \quad i = 1, 2, \cdots, N \tag{2.36}$$

where $\mathbf{F}_i(t)$ is the force acting on the particle i at time t. The force $\mathbf{F}_i(t)$ derives from the potential energy $U(r_{ij})$ arising from the interactions with all the other particles at time t,

$$\mathbf{F}_i(t) = -\sum_{j=1}^{N} \nabla_i U(r_{ij}(t)), \quad i = 1, 2, \cdots, N \tag{2.37}$$

where $r_{ij}(t) = |\mathbf{r}_i(t) - \mathbf{r}_j(t)|$ is the distance between particles i and j. Summation over j indicates that all the other particles interacts with particle i.

2.3.3 Integration scheme

In general, Newton's equation of motion does not have an analytical solution (or have a complicated solution). Thus, several integration algorithms have been developed to integrate the equation of motion numerically. The usual integration algorithms include: (1) verlet algorithm; (2) leap-frog algorithm; and (3) velocity-verlet algorithm.

(1) Verlet algorithm. This algorithm updates the new position $r(t+\delta t)$ at time $t+\delta t$ using the position $r(t)$ and force $F(t)$ at time t and the position $r(t-\delta t)$ at time $t-\delta t$,

$$\begin{aligned} r(t+\delta t) &\approx 2r(t) - r(t-\delta t) + \frac{F(t)}{m}\delta t^2 \\ v(t) &\approx \frac{r(t+\delta t) - r(t-\delta t)}{2\delta t} \end{aligned} \tag{2.38}$$

The verlet algorithm is straightforward, and requires modest memory storage capacities. However, the algorithm is of moderate precision.

(2) Leap-frog algorithm. In the leap-frog algorithm, the velocity $v(t+0.5\delta t)$ at time $t+0.5\delta t$ is first computed using the velocity $v(t-0.5\delta t)$ at time $t-0.5\delta t$ and the force $F(t)$ at time t. Then, the position $r(t+\delta t)$ at $t+\delta t$ is updated using the position $r(t)$ at time t and velocity $v(t+0.5\delta t)$ at time $t+0.5\delta t$,

$$\begin{aligned} v(t+\delta t) &\approx v(t-0.5\delta t) + \frac{F(t)}{m}\delta t \\ r(t+\delta t) &\approx r(t) + v(t+0.5\delta t)\delta t \end{aligned} \tag{2.39}$$

The velocity $v(t)$ at time t is updated using the average of velocity $v(t+0.5\delta t)$ at time $t+0.5\delta t$ and velocity $v(t-0.5\delta t)$ at time $t-0.5\delta t$,

$$v(t) \approx \frac{1}{2}\left[v(t+0.5\delta t)+v(t-0.5\delta t)\right] \tag{2.40}$$

(3) Velocity-verlet algorithm. The velocity-verlet algorithm updates the position and velocity at the same time. The position $r(t+\delta t)$ and velocity $v(t+\delta)$ at time $t+\delta t$ are computed using the position $r(t)$, velocity $v(t)$, and force $F(t)$ at time t but also the force $F(t+\delta t)$ at time $t+\delta t$,

$$\begin{aligned} r(t+\delta t) &\approx r(t)+v(t)\delta t+\frac{1}{2}\frac{F(t)}{m}\delta t^2 \\ v(t+\delta t) &\approx v(t)+\frac{1}{2}\left[\frac{F(t)}{m}+\frac{F(t+\delta t)}{m}\right]\delta t \end{aligned} \tag{2.41}$$

In the present work, the velocity-verlet algorithm is adopted in all the molecular dynamics simulations.

2.3.4 Thermostat and barostat

In molecular dynamics, the temperature for a molecular system is determined using the ensemble average of the kinetic energy,

$$\frac{3}{2}Nk_BT = \left\langle \frac{1}{2}\sum_{i}^{N} m_i \mathbf{v}_i^2 \right\rangle \tag{2.42}$$

while the pressure is determined from the virial theorem,

$$P = \rho k_BT + \frac{1}{3V}\left\langle \sum_{i=1}^{N}\sum_{j>i}^{N} \mathbf{F}_{ij}\cdot\mathbf{r}_{ij} \right\rangle \tag{2.43}$$

where $\rho = N/V$ is the number density of particles. The factor of 3 for T and 1/3 for P are for a 3-D system.

Most experiments are at constant T and/or P. As a result, MD simulations are usually performed in the NPT or NVT ensemble rather than the NVE ensemble. To do so, a thermostat and barostat are used to control T and P in MD simulation. Four primary strategies can be employed,

(1) Stochastic approach. The controlling variable (e.g., velocity for T) is reassigned to the preset distribution function at each MD step. For example, the Andersen thermostat assigns the velocity of one particle (randomly chosen) to a new velocity from the Maxwellian velocity distribution.

(2) Strong-coupling approach. The controlling variable is rescaled to an exact preset value at each MD step. For example, the isokinetic/Gaussian thermostat rescales the velocity of each particle using the current velocity (i.e., velocity in Newton's equation) multiplied by a rescaling factor, $\lambda = \sqrt{T_{desired}/T_{current}}$.

(3) Weak-coupling approach. The controlling variable is rescaled towards the desired value. For example, the Berendsen thermostat introduces a coupling parameter, τ, to the external bath using a rescaling factor $\lambda = \sqrt{1 + \delta t/\tau(T_{desired}/T_{current} - 1)}$ to control T.

(4) Extended system dynamics. This approach requires to introduce an additional external degree of freedom that allows controlling T and P. For example, the Nosé-Hoover thermostat corrects the equation of motion using an additional degree of freedom, s. This additional degree of freedom s induces a friction with a "heat bath mass, Q_m" and has the potential energy of $(N+1)k_BT_{desired}\ln(s)$. The parameter Q_m determines the coupling strength and energy flow between the thermostat and the molecular system. Large Q_m leads to weak coupling and it is recommended to use $Q_m \sim 6Nk_BT$.

The different constant temperature algorithms above are given as example to illustrate the strategies when performing MD simulation in a constant temperature ensemble such as the canonical ensemble. The constant pressure algorithm is analogous; the volume V is the controlling variable and the positions of all particles are rescaled as,

$$\mathbf{r}_i(t+\delta t) = \sqrt{\lambda}\mathbf{r}_i(t), \qquad i = 1,2,\cdots .N \tag{2.44}$$

where $\lambda = 1 - k\delta t/3\tau(P_{desired} - P_{current})$ is the rescaling factor, τ is a coupling parameter, and $k = \beta_T \left(\langle V^2\rangle - \langle V\rangle^2\right)/\langle V\rangle$ is the isothermal compressibility that determines the volume fluctuations in MD simulation. In this work, T and P were maintained constant using the Nose-Hoover algorithm.

2.3.5 Details of molecular dynamics

In the context of the free energy calculations carried out in Chapter 3, Molecular Dynamics (MD) in the isobaric–isothermal ensemble (constant number of molecule N, temperature T, and pressure P) was used to determine (1) the density of methane vapor and (2) the volume of zero-occupancy methane hydrate at different temperatures T and pressures P (details of the free energy calculations will be discussed later in this manuscript).

To determine the thermodynamic parameters that are inputs for the Gibbs-Thomson equation in Chapter 4, molecular dynamics in the isobaric–isothermal ensemble (constant number of molecule N, temperature T, and pressure P) was also used to determine the molar volume v and enthalpy of liquid water, h^{L}, and methane hydrate, h^{H}, at bulk phase coexistence conditions: $T = T_m(P)$. Molecular dynamics in the canonical ensemble (constant number of molecule N, volume V, and temperature T) was used to determine the solid–hydrate γ_{HS} and solid–liquid γ_{LS} surface tensions at bulk phase coexistence conditions (details of the surface tension will also be discussed later).

Calculations of the physical and physicochemical properties in Chapter 5 were assessed using molecular dynamics. (1) For bulk methane hydrate and liquid water, the thermal expansion α_P and isothermal compressibility κ_T were determined using molecular dynamics in the isobaric–isothermal ensemble (constant number of molecule N, temperature T, and pressure P). (2) Molecular dynamics at constant number of molecule N, temperature T and pressure component P_{zz} was used to determine the thermal expansion $\alpha_{P_{zz}}$ and isothermal compressibility $\kappa_{T(P_{zz})}$ for bulk methane hydrate and liquid water (z is the direction normal to the pore surface). (3) Molecular dynamics in the microcanonical ensemble (constant number of molecule N, volume V, and energy E) was used to determine the thermal conductivity λ of bulk methane hydrate. (4) For the confined methane hydrate and liquid water, molecular dynamics were performed in the microcanonical ensemble for porous solid atoms while the canonical ensemble for methane hydrate/liquid water.

All molecular dynamics simulations were performed using *LAMMPS* (Plimpton, 1995). The Velocity-Verlet algorithm (Verlet, 1967) was used to integrate the equation of motion with a total time of at least 2 ns and a timestep of 1 fs. For the ensembles with constant temperature and/or constant pressure, T, P, and P_{zz} were controlled using Nose-Hoover thermostat/barostat with a typical relaxation time of 2 ps (Hoover, 1985; Nosé, 1984).

2.4 Interaction potentials

The interaction potential, U, determines not only the force in molecular dynamics but also the acceptance probability in Monte Carlo simulations. Generally, U in molecular simulation includes intramolecular (i.e., bonded) interactions, U_{intra}, and intermolecular (i.e., non-bonded) interactions, U_{inter},

$$U_{total} = U_{intra} + U_{inter} \tag{2.45}$$

2.4.1 Intramolecular potential

The intramolecular potential maintains all atoms together within a molecule so that it describes chemical bonding. Such a strong interaction potential accounts for bond stretching,

U_{bond}, bond angle bending, U_{angle}, and torsional rotation, $U_{dihedral}$,

$$\begin{aligned} U_{intra} &= U_{bond} + U_{angle} + U_{dihedral} \\ &= \frac{1}{2}k_l(l - l_c)^2 + \frac{1}{2}k_\theta(\theta - \theta_c)^2 + k_\phi[1 + \cos(n\phi - \delta)] \end{aligned} \tag{2.46}$$

where the first term is for bond stretching with the alteration of the optimized bond length, l_c, to a less favorable bond length, l; the second term is for angle bending with the alteration of the optimized bond angle, θ_c, to a less favorable bond angle, θ; and the third term corresponds to the torsional rotation and describes the interaction potential when the number of atoms in the molecule is 4 or more (in this term, n is the periodicity as rotation repeats around 2π, ϕ is the dihedral angle, and δ is the offset of the function). k_l, k_θ, and k_ϕ are the force constants. For each potential contribution, any change of the bond length/angle will increase the interaction potential. In this thesis, the contribution from the intramolecular interactions is always zero, $U_{intra} = 0$, since only rigid water models and a united-atom model for methane are considered.

2.4.2 Intermolecular potential

The intermolecular potential describes non-bonded interactions, i.e., the attractive/repulsive energies among molecules or atomic groups. It usually includes the three following contributions: (1) repulsive interaction originating from the Pauli exclusion principle that prevents the overlap of atoms; (2) electrostatic interactions (attractive or repulsive) between point charges, dipoles, quadrupoles, and multipoles; and (3) attractive/dispersion interactions between atoms due to instantaneous multipoles. In practice, the above three contributions are often represented using the Lennard-Jones (LJ) potential and the Coulombic potential,

$$U_{inter} = U_{LJ} + U_C \tag{2.47}$$

Lennard-Jones potential. The Lennard-Jones (LJ) potential between two atoms i and j includes a short-range repulsive contribution (the first term in Eq. (2.48)) and an attractive dispersion contribution (the second term in Eq. (2.48)):

$$u_{LJ}(r_{ij}) = 4\varepsilon_{ij}\left[\left(\frac{\sigma_{ij}}{r_{ij}}\right)^{12} - \left(\frac{\sigma_{ij}}{r_{ij}}\right)^{6}\right] \tag{2.48}$$

where r_{ij} is the distance between atoms i and j while ε_{ij} and σ_{ij} are the corresponding LJ parameters, i.e., the characteristic energy and distance. The total LJ interaction potentials for the whole system, U_{LJ}, are truncated within a cutoff distance due to the short-range nature of these interactions,

$$U_{LJ} = \sum_{i=1}^{N}\sum_{j>i}^{N} 4\varepsilon_{ij}\left[\left(\frac{\sigma_{ij}}{r_{ij}}\right)^{12} - \left(\frac{\sigma_{ij}}{r_{ij}}\right)^{6}\right] \quad (r \leq r_c) \tag{2.49}$$

where N is the number of atoms. The like-atom LJ parameters are presented in Table 2.1 of Section 2.5. The LJ parameters between unlike atoms are determined using the Lorentz–Berthelot mixing rules, i.e., $\varepsilon_{ij} = (\varepsilon_{ii}\varepsilon_{jj})^{1/2}$, $\sigma_{ij} = (\sigma_{ii} + \sigma_{jj})/2$.

Coulombic potential and ewald summation. In addition to the above repulsion/dispersion interactions, the intermolecular potential includes the electrostatic interaction between two atoms i and j separated by a distance r_{ij} as described via the coulombic potential,

$$u_C(r_{ij}) = \frac{1}{4\pi\varepsilon_o}\frac{q_i q_j}{r_{ij}} \tag{2.50}$$

where q_i and q_j are the atomic charges on atoms i and j, respectively; $\varepsilon_0 = 8.8541878176 \times 10^{-12}$ Fm^{-1} is the vacuum permittivity. The coulombic potential is a long-range contribution but the usual simulation boxes typically have lengths of the order of nanometers. This implies that one has to consider several periodic images to estimate accurately the coulombic contribution,

$$\begin{aligned} U_C &= \frac{1}{2}\sum_{i=1}^{N} q_i \left(\frac{1}{4\pi\varepsilon_0} \sum_{\mathbf{n}} \sum_{j=1}^{N} \frac{q_j}{|\mathbf{r}_{ij} + \mathbf{n}L|} \right) \\ &= \frac{1}{2}\sum_{i=1}^{N} q_i \phi(r_i) \end{aligned} \tag{2.51}$$

for a system consisting of N atoms in a cubic box with dimensions $L_x = L_y = L_z = L$. $\mathbf{n}$ is a vector of three integer numbers, e.g., $\mathbf{n} = [0,0,1]$. $\phi(r_i) = \sum_{j \neq i}(r_i)$ is the electrical field generated at the position r_i of atom i by all the other atoms in the cubic box and their periodic images. Note that the term with $i = j$ for $\mathbf{n} = [0,0,0]$ should be excluded as it corresponds to self-interaction. In practice, the above equation cannot be considered in real molecular simulations as it would require huge computational cost. The ewald summation technique provides a way to correct for the small size of the simulation box:

(1) the atom i has the atomic charge $q_i\delta(\mathbf{r} - \mathbf{r}_i)$ where $\delta(\mathbf{r} - \mathbf{r}_i)$ is the Dirac delta function;

(2) a Gaussian charge distribution (with a width $\sqrt{2/\alpha}$), $\rho_{\mathrm{G}}(\mathbf{r}) = -q_i(\alpha/\pi)^{3/2}\exp(-\alpha r^2)$, is added for each charge i to make the electrostatic interaction short-ranged. Such distribution has an integrated charge of the same magnitude but with an opposite sign, $-q_i$;

(3) a compensating charge distribution is used to cancel out the Gaussian charge introduced in (2).

Locally, the effective charge for the atom i at the position r in the ewald summation reads,

$$\rho_i(\mathbf{r}) = [q_i\delta(\mathbf{r} - \mathbf{r}_i) + \rho_{\mathrm{G}}(\mathbf{r})]^S - [\rho_{\mathrm{G}}(\mathbf{r})]^L \tag{2.52}$$

where $\rho_i(\mathbf{r})$ is the total charge distribution at the position vector $\mathbf{r}$. The electrical field, $\phi_i(r)$, created by this effective charge $\rho_i(\mathbf{r})$ at a position r is expressed as,

$$\begin{aligned}\phi_i(r) &= \phi_i^S(r) + \phi_i^L(r) \\ &= \left[\frac{q_i}{4\pi\varepsilon_o r}\operatorname{erfc}\left(r\sqrt{\alpha}\right)\right]^S + \left[\frac{q_i}{4\pi\varepsilon_o r}\operatorname{erf}(r\sqrt{\alpha})\right]^L\end{aligned} \tag{2.53}$$

where $r = |\mathbf{r}|$, $\operatorname{erf}(x) = 2/\sqrt{\pi}\int_0^x dt \exp(-t^2)$ is the error function, and $\operatorname{erfc}(x) = 1 - \operatorname{erf}(x)$ is the complementary error function. $\phi_i^S(r)$ is the electric field created by the charge $[\cdots]^S$ in Eq. (2.52) while $\phi_i^L(r)$ is the electric field created by the charge $[\cdots]^L$ in Eq. (2.52). Due to the fast decay of $\operatorname{erfc}(x)$, i.e., $\lim_{x\to\infty}\operatorname{erf}(x) = 1$, the term $[\cdots]^S$ in Eq. (2.53) is a very short-range term whose sum quickly converges in the real space (the cutoff distance is set to r_c). The term $[\cdots]^L$ in Eq. (2.53) represents a long-range contribution whose sum can be estimated in the reciprocal space (the cutoff wave vector is set to $k_c = \frac{2\pi}{Ln_c}$ where n_c is a positive integer). The electrostatic potential field, U_C, can be rewritten as,

$$\begin{aligned}U_C &= \frac{1}{2}\sum_{i=1}^{N} q_i\phi_i^S(\mathbf{r}_i) + \frac{1}{2}\sum_{i=1}^{N} q_i\phi_{i,\mathbf{n}\neq\mathbf{0}}^L(\mathbf{r}_i) \\ &= \frac{1}{2}\sum_{i=1}^{N} q_i\phi_i^S(\mathbf{r}_i) + \frac{1}{2}\sum_{i=1}^{N} q_i\phi_{i,\mathbf{n}}^L(\mathbf{r}_i) - \frac{1}{2}\sum_{i=1}^{N} q_i\phi_{i,\mathbf{n}=\mathbf{0}}^L(\mathbf{r}_i) \\ &= \frac{1}{4\pi\varepsilon_0}\sum_{i=1}^{N}\sum_{j>i}^{N}\frac{q_iq_j}{r_{ij}}\operatorname{erfc}(\sqrt{\alpha}r_{ij}) \quad (r_{ij} < r_c) \\ &\quad + \frac{1}{2L^3\varepsilon_0}\sum_{0<k<k_c}\sum_{i=1}^{N}\sum_{j=1}^{N}\frac{q_iq_j}{k^2}\exp\left(\mathbf{ik}\cdot(\mathbf{r}_i - \mathbf{r}_j)\right)\exp\left(-\frac{k^2}{4\alpha}\right) \\ &\quad - \frac{\alpha}{4\pi^{3/2}\varepsilon_0}\sum_{i=1}^{N} q_i^2\end{aligned} \tag{2.54}$$

where $\mathbf{k}$ is the reciprocal vector chosen so that $\exp(-i\mathbf{k}\cdot\mathbf{n}L) = 1$.

The computational accuracy of the ewald summation depends on r_c, n_c, and α. The ewald summation introduces cutoff errors because of (1) the cutoff r_c in the real-space,

δU_R, and (2) the cutoff k_c in the reciprocal-space, δU_F,

$$\begin{aligned} \delta U_R &\sim \sum_{i=1}^{N} q_i^2 \sqrt{\frac{r_c}{2L^3}} \frac{\exp[-(\alpha r_c)^2]}{(\alpha r_c)^2} \\ \delta U_F &\sim \sum_{i=1}^{N} q_i^2 \frac{\sqrt{n_c}}{\alpha L^2} \frac{\exp[-(\pi n_c/\alpha L)^2]}{(\pi n_c/\alpha L)^2} \end{aligned} \tag{2.55}$$

Owing to the form $\exp(-x^2)/x^2$, these two error contributions have the same accuracy ε ($\varepsilon = 1.0 \times 10^{-5}$ is used in this thesis), i.e., $\varepsilon = exp(-s^2)/s^2$. Therefore,

$$\alpha = s/r_c \text{ and } n_c = sL\alpha/\pi \tag{2.56}$$

2.5 Molecular models

Methane was modeled as a single Lennard-Jones (LJ) sphere with the parameters taken from the OPLS-UA forcefield (UA stands for united-atom) (Jorgensen et al., 1984, 1996). Water was modeled using the TIP4P model which consists of a rigid model containing 4 sites: an LJ site located on the oxygen atom, two sites corresponding to the hydrogen atoms, and a fourth site M corresponding to the negative charge of the oxygen atom located at a distance d_{OM} from the oxygen atom toward the hydrogen atoms along the H–O–H angle bisector. Two versions of the TIP4P water model (Vega et al., 2006), namely TIP4P/2005 (Abascal et al., 2005) and TIP4P/Ice (Abascal and Vega, 2005) models, were used to describe the water molecules in methane hydrate. In both water models, the water molecule has an O–H bond length of 0.9572 Å and an H–O–H angle of 104.52°. The LJ potential parameters for methane and water as well as the atomic charges and distance d_{OM} for the two water models are given in Table 2.1. The TIP4P/2005 model reproduces qualitatively the liquid/solid coexistence for water but with a shift in temperature (20–30 K) and in pressure (100 MPa) (Aragones et al., 2009; Vega et al., 2006). In contrast, the TIP4P/Ice model accurately reproduces the liquid/solid phase diagram for water but with some deviations in the coexistence lines for some dense ice forms (like Ice VII and Ice VIII) (Vega et al., 2006).

Table 2.1 Interaction potential parameters corresponding to the OPLS-UA model for methane, the TIP4P/2005 and TIP4P/Ice models for water, and the atomic model used to describe the porous solid (solid atom). For the two water models, we also indicate the melting temperature T_m as predicted using molecular modeling.

Model	ε/k_B (K)	σ (Å)	q_H (e)	q_O (e)	d_{OM} (Å)	T_m (K)
TIP4P/2005	93.2	3.1589	0.5564	-1.1128	0.1546	252.2
TIP4P/Ice	106.1	3.1668	0.5879	-1.1758	0.1577	272.2
methane	147.5	3.7300	- -	- -	- -	- -
solid atom	65.55	3.5810	- -	- -	- -	- -

Chapter 3

Molecular Simulation of the Phase Diagram of Bulk Methane Hydrate

Contents

3.1 Molecular structure of methane hydrate 63

3.2 Liquid–Hydrate–Vapor equilibrium 65

3.2.1 Phase coexistence conditions 65

3.2.2 Estimation of the different chemical potentials 67

3.3 Phase diagram of methane hydrate 71

3.3.1 Free energy approach 71

3.3.2 Direct Coexistence Method in the Grand Canonical Ensemble . 83

3.3.3 Hyper Parallel Tempering 88

3.4 Conclusion 89

In this chapter, different molecular simulation strategies are considered to assess the thermodynamics of bulk methane hydrate. First, for two different water models – TIP4P/2005 and TIP4P/Ice –, free energy calculations based on the Einstein molecule approach developed by Vega and coworkers (Noya et al., 2008; Vega et al., 2008) are used to determine the pressure–temperature phase diagram of methane hydrate (in all simulations, methane is treated using a coarse-grained model known as the united-atom model). More precisely, the stability conditions for three pressures are determined: $P = 1$, 10 and 100 atm. For each pressure, in addition to determining the temperature range where methane hydrate is stable, the methane occupancy of the hydrate is also estimated and the non negligible effect of the approximation used to treat methane vapor (exact equation of state as probed using molecular simulation versus thermodynamic integration from an ideal gas) is discussed. While free energy calculations obviously constitute the most rigorous scheme to determine the phase diagram of such complex phases, less demanding strategies is also considered in a second step. First, we consider the direct coexistence method in which one generates an initial configuration where both liquid water and methane hydrate coexist to determine using molecular simulation the final, stable phase for many temperature and pressure conditions. While the direct coexistence method has already been used to investigate the thermodynamic stability of methane hydrate (Conde and Vega, 2010; Michalis et al., 2015), here a novel version is proposed; both water and methane are treated in the Grand Canonical ensemble using Monte Carlo simulations to account for large variations in the number of molecules upon melting and formation of the hydrate. Second, we also consider hyper parallel tempering molecular simulations in which several replicas of the system, taken at different temperatures and chemical potentials, are considered in parallel (following the work by De Pablo and coworkers, these simulations are referred to hyper parallel tempering rather than parallel tempering as the system is treated in the Grand Canonical ensemble) (de Pablo et al., 1992; Yan and de Pablo, 1999, 2000). While this method has been already used for simulating solid–liquid phase diagrams of confined mixtures (Coasne, 2005; Coasne et al., 2004), it is the first time that such a hyper parallel tempering strategy is considered for methane hydrate.

The remainder of this chapter is organized as follows. In Section 3.1, the Monte Carlo algorithm to generate methane hydrate with structure sI is presented. In Section 3.2, general considerations regarding the liquid–hydrate–vapor phase equilibrium is presented. In Section 3.3, free energy calculations of methane hydrate are first presented to determine the phase diagram of methane hydrate for the two water models selected in this work. In this part, we also determine the chemical potential for each species as well as methane occupancy for the different pressure/temperature coexistence conditions. In Section 3.2, we also present the stability conditions obtained using the direct coexistence method and the hyper parallel tempering method. The results obtained using the different methods above are compared with experimental data as well as data obtained in previous theoretical works. In Section 3.4, some concluding remarks are presented.

3.1 Molecular structure of methane hydrate

Figure 3.1 shows a molecular configuration of methane hydrate corresponding to 2 × 2 × 2 unit cells of the sI structure (the unit cell has a length of 1.1877 nm). This section describes the strategy used to generate such a molecular configuration of methane hydrate from the experimental crystallographic data. For methane hydrate, three criteria should be verified (more details can be found in Section 1.1.1): (1) proton disorder, (2) ice rules also known as Bernal–Fowler rules, and (3) zero dipole moment. To build a molecular structure obeying these criteria, we followed the stochastic strategy proposed by Buch et al. (Buch et al., 1998).

1. A cubic box with dimensions $L_x = L_y = L_z = 2.3754$ nm, corresponding to $2 \times 2 \times 2$ unit cells, is constructed by first placing the oxygen atoms according to the experimental X-ray crystallographic data (Kirchner et al., 2004).

2. In order to comply with the ice rule, each pair of nearest neighbor oxygens must share a hydrogen atom which belongs either to the first or second oxygen atom. In what follows, the two oxygen atoms in each O-O pair are labelled O_1 and O_2.

Initially, a hydrogen atom is randomly assigned either to O_1 or O_2 for each O-O pair. The distance from the selected oxygen atom to this hydrogen atom is set according to the chemical O–H bond length of the TIP4P water model, $d_{OH} = 0.09578$ nm. Due to the random assignment of the hydrogen atoms, the initial structure obtained according to this strategy is unrealistic; oxygen atoms are coordinated to N_c = 0, 1, 2, 3 or 4 hydrogen atoms (obviously, coordination numbers $N_c \neq 2$ are not physical).

3. The following stochastic/Monte Carlo approach is then performed to relax these non-physical coordination numbers and reach realistic configurations where $N_c = 2$ for all oxygen atoms. An O-O pair is randomly chosen. If the hydrogen atom is bonded to O_1 (O_2), attempt is made to transfer the hydrogen atom to O_2 (O_1). This move is accepted or rejected based on the change in the absolute difference in coordination numbers $\Delta N_c = |N_c^{O_1} - N_c^{O_2}|$. More precisely, the move is accepted if the change in the absolute difference in coordination numbers $\Delta(\Delta N_c) < 0$ (because this leads overall to configurations with oxygen atoms having the same coordination numbers i.e. $N_c = 2$). The move is accepted with a probability 0.5 if $\Delta(\Delta N_c) = 0$. In contrast, the move is rejected if $\Delta(\Delta N_c) > 0$. Such moves are attempted until each oxygen atom is linked to two hydrogen atoms (in practice, 20000 moves are performed as it is found sufficient to reach physical configurations for the system size considered in this work).

The strategy above, which is illustrated in Figure 3.2, is repeated 20000 times to obtain 20000 possible configurations for methane hydrate. For each configuration, we compute the total dipole moment, $\mathbf{p} = \sum_{i=1}^{N} q_i \mathbf{r}_i$, where q_i and $\mathbf{r}_i$ are the charge and position of the i-th atom (N is the total number of atoms in the system). Among these 20000 configurations, we eventually select the configuration with the smallest dipole moment (typically, $\mathbf{p} < 10^{-9}$ D). Finally, the methane molecules (64 methane molecules for the $2 \times 2 \times 2$ primitive cell) are inserted into the hydrate cages. The addition of methane molecules does not change the dipole moment of the methane hydrate structure owing to its non polar nature.

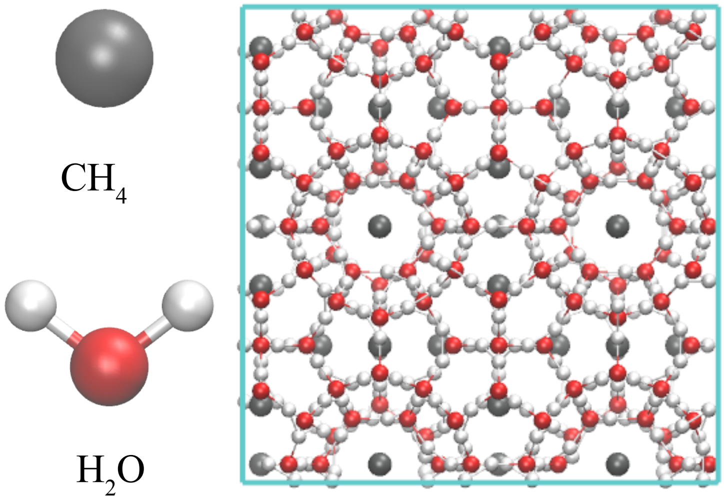

Figure 3.1 (color online) Molecular configuration of methane hydrate with structure sI. The red and white spheres are the oxygen and hydrogen atoms of water, respectively. The gray spheres are the methane molecules which are trapped inside the hydrogen-bonded cages formed by water molecules (1 methane molecule for 8 water molecules). The dimensions of this molecular configuration, which corresponds to $2 \times 2 \times 2$ unit cells, are: $L_x = L_y = L_z = 2.3754$ nm.

3.2 Liquid–Hydrate–Vapor equilibrium

3.2.1 Phase coexistence conditions

Methane hydrate (H) is a binary mixture of water (w) and methane (m) that coexists with liquid water (L) (or ice at sufficient low T) and methane vapor (V) in specific temperature T and pressure P ranges (i.e., for a given P, there exists a T at which the three phases L–H–V coexist – the hydrate phase being stable at low T/high P). At P and T where the three phases coexist, the chemical potentials μ_i^{Φ} for each species ($i = w$, m) in all phases ($\Phi = \text{L, H, V}$) are equal. μ_i^{Φ} at given T and P varies with the methane and water mole fractions (x_m and x_w, respectively) so that L–H–V equilibrium depends also on x_m and x_w (Huo et al., 2003; Sloan, 2003). Since $x_w = 1 - x_m$ for a binary system, the L–H–V equilibrium condition can be expressed using x_m only:

$$\begin{aligned} \mu_w^{\mathrm{L}}(x_m, T, P) = \mu_w^{\mathrm{H}}(x_m, T, P) = \mu_w^{\mathrm{V}}(x_m, T, P) \\ \mu_m^{\mathrm{L}}(x_m, T, P) = \mu_m^{\mathrm{H}}(x_m, T, P) = \mu_m^{\mathrm{V}}(x_m, T, P) \end{aligned} \tag{3.1}$$

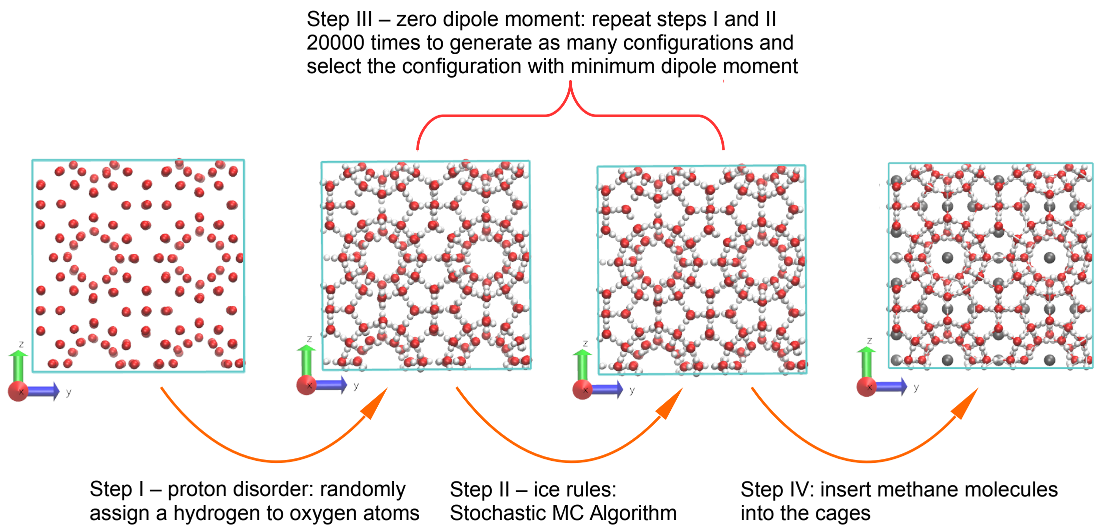
Step III – zero dipole moment: repeat steps I and II 20000 times to generate as many configurations and select the configuration with minimum dipole moment
z
y
Step I – proton disorder: randomly assign a hydrogen to oxygen atoms
Step II – ice rules: Stochastic MC Algorithm
Step IV: insert methane molecules into the cages

Figure 3.2 Stochastic algorithm to generate methane hydrate molecular configurations with sI structure (Buch et al., 1998): (1) set the oxygen positions according to the experimental X-ray crystallographic data (Kirchner et al., 2004); (2) generate proton disorder by randomly assigning a hydrogen atom to one of the oxygen atoms in each O–O pair (step I); (3) use a stochastic MC algorithm to verify the ice rules (step II); (4) repeat steps I and II 20000 times to generate as many configurations and select the configuration with minimum dipole moment (step III); and (5) insert the methane molecules into the cages of the methane hydrate (step IV). The red and white spheres are the oxygen and hydrogen atoms of water, respectively. The gray spheres are the methane molecules. The dimensions of the system shown here are $L_x = L_y = L_z = 2.3754$ nm which correspond to $2 \times 2 \times 2$ unit cells.

Such L–H–V equilibrium can be recast as 2 two-phase coexistence conditions: (1) liquid water–methane hydrate (L–H) and (2) methane hydrate–methane vapor (H–V):

$$\begin{aligned} \mu_w^{\mathrm{L}}(x_m, T, P) &= \mu_w^{\mathrm{H}}(x_m, T, P) \\ \mu_m^{\mathrm{H}}(x_m, T, P) &= \mu_m^{\mathrm{V}}(x_m, T, P) \end{aligned} \tag{3.2}$$

As indicated by the experimental Henry constant ($x_m \sim$0.003–0.001 for methane in liquid water at 100 bar for T ranging between 275 and 310 K) (Harvey, 1996; Harvey and Sengers, 1990), the solubility of methane in liquid water is very low so that the effect of methane on the chemical potential of water in the liquid phase can be neglected, i.e. $\mu_w^{\mathrm{L}}(x_m \sim 0, T, P) \sim \mu_w^{\mathrm{L}}(x_m = 0, T, P)$ (Docherty et al., 2006; Jensen et al., 2010). Similarly, the chemical potential of methane in the vapor can be approximated by that of pure methane vapor, i.e. $\mu_m^{\mathrm{V}}(x_m \sim 1, T, P) \sim \mu_m^{\mathrm{V}}(x_m = 1, T, P)$. With these approximations, the L–H–V coexistence conditions defined in Eqs. (3.2) become

$$\begin{aligned}\mu_w^{\mathrm{L}}(x_m = 0, T, P) &= \mu_w^{\mathrm{H}}(x_m, T, P) \\ \mu_m^{\mathrm{H}}(x_m, T, P) &= \mu_m^{\mathrm{V}}(x_m = 1, T, P)\end{aligned} \tag{3.3}$$

The description above shows that determining phase coexistence requires to estimate the four following chemical potentials: $\mu_m^{\mathrm{H}}(x_m, T, P)$, $\mu_w^{\mathrm{H}}(x_m, T, P)$, $\mu_w^{\mathrm{L}}(x_m = 0, T, P)$, and $\mu_m^{\mathrm{V}}(x_m = 1, T, P)$.

3.2.2 Estimation of the different chemical potentials

In the previous section, it was shown that the following chemical potentials are required to estimate rigorously L–H–V phase coexistence: $\mu_m^{\mathrm{H}}(x_m, T, P)$, $\mu_w^{\mathrm{H}}(x_m, T, P)$, $\mu_w^{\mathrm{L}}(x_m = 0, T, P)$, and $\mu_m^{\mathrm{V}}(x_m = 1, T, P)$. The next paragraph shows that the two chemical potentials for pure phases, $\mu_w^{\mathrm{L}}(x_m = 0, T, P)$ and $\mu_m^{\mathrm{V}}(x_m = 1, T, P)$, can be estimated in a straightforward way. In contrast, $\mu_m^{\mathrm{H}}(x_m, T, P)$ and $\mu_w^{\mathrm{H}}(x_m, T, P)$ will be estimated in a second step using free energy calculations.

$\mu_m^{\mathbf{V}}(x_m = 1, T, P)$ and $\mu_w^{\mathbf{L}}(x_m = 0, T, P)$. The chemical potential of methane in the vapor phase $\mu_m^{\mathrm{V}}(T, P)$ was computed using its equation of state determined as follows. At a given T, isobaric-isothermal MD simulations are performed to determine the density of methane as a function of pressure, i.e., $\rho_m(T, P)$. In parallel, GCMC simulations are performed to determine the relation between the chemical potential and density of methane vapor, i.e., $\rho_m(\mu_m^{\mathrm{V}}, T)$. By inverting these two relationships, one obtains $\mu_m^{\mathrm{V}}(T, P)$ as a function of T and P. Table 3.1 displays $\mu_m^{\mathrm{V}}(T, P)$ for the various T and P considered in this work.

The chemical potential of pure liquid water, $\mu_w^{\mathrm{L}}(x_m = 0, T, P)$, at given T and P can be estimated using the Gibbs-Duhem equation:

$$N_w^{\mathrm{L}} d\mu_w^{\mathrm{L}} = -S_w^{\mathrm{L}} dT + V_w^{\mathrm{L}} dP \tag{3.4}$$

Table 3.1 Chemical potential, $\mu_m^{\mathrm{V}}(x_m = 1, T, P)$, and fugacity, f, of methane vapor for the OPLS-UA methane model. All chemical potentials are normalized to the thermal energy, $k_B T$. Absolute uncertainties for the chemical potentials are smaller than 3×10^{-4}.

	$p = 1$ atm		$p = 10$ atm		$p = 100$ atm	
T/K	f (bar)	$\frac{\mu_m^{\mathrm{V}}}{k_B T}$	f (bar)	$\frac{\mu_m^{\mathrm{V}}}{k_B T}$	f (bar)	$\frac{\mu_m^{\mathrm{V}}}{k_B T}$
180	1.0009	-13.4927	9.4291	-11.2497	29.2235	-10.1186
190	1.0021	-13.6266	9.4609	-11.3815	38.9995	-9.9652
200	1.0074	-13.7496	9.6774	-11.4871	44.7003	-9.9570
210	1.0122	-13.8668	9.6409	-11.6129	52.0088	-9.9275
220	1.0081	-13.9871	9.7581	-11.7171	58.5239	-9.9258
230	1.0121	-14.0943	9.7937	-11.8246	64.1186	-9.9456
240	1.0132	-14.1996	9.8883	-11.9214	68.8134	-9.9813
250	1.0147	-14.3002	9.8559	-12.0267	72.6275	-10.0294
260	1.0155	-14.3975	9.9965	-12.1106	76.4827	-10.0758
270	1.0116	-14.4957	9.9077	-12.2139	78.9855	-10.1379
280	1.0152	-14.5830	9.8759	-12.3080	81.7055	-10.1950
290	1.0162	-14.6698	10.0320	-12.3801	84.0855	-10.2540
300	1.0203	-14.7505	10.0357	-12.4644	85.7526	-10.3191
310	1.0195	-14.8333	9.9720	-12.5528	87.8612	-10.3768
320	1.0164	-14.9156	10.0045	-12.6289	89.3645	-10.4392
330	1.0127	-14.9962	10.0725	-12.6991	90.7896	-10.5003
340	1.0111	-15.0724	10.0968	-12.7713	91.8352	-10.5635
350	1.0187	-15.1375	10.0219	-12.8512	92.8797	-10.6247

where S_w^{L}, N_w^{L}, and V_w^{L} are the entropy, number of water molecules, and volume of the liquid phase. If one assumes that the density $\rho_w^{\mathrm{L}} = N_w^{\mathrm{L}}/V_w^{\mathrm{L}}$ of liquid water is constant (incompressible liquid), integration of the Gibbs-Duhem equation at constant temperature $T = T_0$ leads to:

$$\mu_w^{\mathrm{L}}(x_m = 0, T_0, P) = \mu_w^{\mathrm{L}}(x_m = 0, T_0, P_0) + \frac{P - P_0}{\rho_w(T_0, P_0)} \tag{3.5}$$

It is convenient to take the L–V phase coexistence of water (T_0, P_0) as a reference state since it is well-known for the different water models considered in this work (Vega et al., 2006). In particular, for the temperature and pressure ranges considered here, water vapor along the L–V coexistence line can be treated as an ideal gas so that the chemical potential at coexistence is readily obtained from the bulk saturating vapor pressure $\mu_w^{\mathrm{V}}(T_0, P_0) = \mu_w^{\mathrm{L}}(T_0, P_0) = k_B T_0 \ln\left(P_0 \Lambda^3 / k_B T_0\right)$ ($\Lambda = h/\sqrt{2\pi m k_B T}$ is the thermal wavelength with h Planck constant and m the molecular mass of water). Table 3.2 shows the chemical potential of water as a function of T and P (both the data for TIP4P/2005 and TIP4P/Ice are shown).

Table 3.2 Chemical potential of liquid water $\mu_w^{\mathrm{L}}(T,P)$. All chemical potentials are normalized to the thermal energy, k_BT. Absolute uncertainties for the chemical potentials are smaller than 3×10^{-2}.

water model	T/K	P_{triple}	$P = 1$ atm		$P = 10$ atm		$p = 100$ atm	
			f (Pa)	$\frac{\mu_m^{\mathrm{L}}}{k_BT}$	f (Pa)	$\frac{\mu_m^{\mathrm{L}}}{k_BT}$	f (Pa)	$\frac{\mu_m^{\mathrm{L}}}{k_BT}$
TIP4P /2005	180	2.371E-09	2.37E-04	-33.53	2.40E-04	-33.52	2.68E-04	-33.40
	190	2.090E-08	2.09E-03	-31.49	2.11E-03	-31.47	2.35E-03	-31.37
	200	1.400E-07	1.40E-02	-29.71	1.42E-02	-29.70	1.56E-02	-29.60
	210	7.482E-07	7.49E-02	-28.16	7.56E-02	-28.15	8.31E-02	-28.05
	220	3.314E-06	3.32E-01	-26.79	3.35E-01	-26.78	3.67E-01	-26.69
	230	1.254E-05	1.25E+00	-25.57	1.27E+00	-25.56	1.38E+00	-25.47
	240	4.147E-05	4.15E+00	-24.48	4.19E+00	-24.47	4.55E+00	-24.38
	250	1.223E-04	1.22E+01	-23.50	1.23E+01	-23.49	1.34E+01	-23.41
	260	3.268E-04	3.27E+01	-22.61	3.30E+01	-22.60	3.56E+01	-22.53
	270	8.010E-04	8.02E+01	-21.81	8.08E+01	-21.80	8.69E+01	-21.73
	280	1.821E-03	1.82E+02	-21.08	1.84E+02	-21.07	1.97E+02	-21.00
	290	3.876E-03	3.88E+02	-20.41	3.91E+02	-20.41	4.18E+02	-20.34
	300	7.781E-03	7.79E+02	-19.80	7.84E+02	-19.79	8.38E+02	-19.73
	310	1.483E-02	1.48E+03	-19.24	1.49E+03	-19.23	1.59E+03	-19.17
	320	2.698E-02	2.70E+03	-18.72	2.72E+03	-18.71	2.89E+03	-18.65
	330	4.711E-02	4.71E+03	-18.24	4.74E+03	-18.23	5.04E+03	-18.17
	340	7.922E-02	7.93E+03	-17.79	7.97E+03	-17.79	8.45E+03	-17.73
	350	1.288E-01	1.29E+04	-17.38	1.30E+04	-17.37	1.37E+04	-17.32
TIP4P /Ice	180	5.051E-11	5.06E-06	-37.38	5.11E-06	-37.36	5.72E-06	-37.25
	190	6.058E-10	6.06E-05	-35.03	6.13E-05	-35.02	6.81E-05	-34.91
	200	5.283E-09	5.29E-04	-32.99	5.34E-04	-32.98	5.91E-04	-32.88
	210	3.549E-08	3.55E-03	-31.21	3.59E-03	-31.20	3.95E-03	-31.10
	220	1.920E-07	1.92E-02	-29.63	1.94E-02	-29.62	2.12E-02	-29.53
	230	8.664E-07	8.67E-02	-28.24	8.75E-02	-28.23	9.55E-02	-28.14
	240	3.352E-06	3.36E-01	-26.99	3.38E-01	-26.98	3.68E-01	-26.90
	250	1.137E-05	1.14E+00	-25.87	1.15E+00	-25.86	1.24E+00	-25.78
	260	3.446E-05	3.45E+00	-24.86	3.48E+00	-24.85	3.75E+00	-24.78
	270	9.465E-05	9.47E+00	-23.95	9.54E+00	-23.94	1.03E+01	-23.86
	280	2.386E-04	2.39E+01	-23.11	2.41E+01	-23.10	2.58E+01	-23.03
	290	5.581E-04	5.59E+01	-22.35	5.62E+01	-22.34	6.03E+01	-22.27
	300	1.221E-03	1.22E+02	-21.65	1.23E+02	-21.64	1.32E+02	-21.57
	310	2.520E-03	2.52E+02	-21.01	2.54E+02	-21.00	2.71E+02	-20.94
	320	4.934E-03	4.94E+02	-20.42	4.97E+02	-20.41	5.29E+02	-20.35
	330	9.216E-03	9.22E+02	-19.87	9.28E+02	-19.86	9.86E+02	-19.80
	340	1.650E-02	1.65E+03	-19.36	1.66E+03	-19.36	1.76E+03	-19.30
	350	2.845E-02	2.85E+03	-18.89	2.86E+03	-18.88	3.03E+03	-18.83

$\mu_m^{\mathbf{H}}(x_m,T,P)$ and $\mu_w^{\mathbf{H}}(x_m,T,P)$. While the chemical potentials for pure phases (L and V) are rather easy to assess, $\mu_m^{\mathrm{H}}(x_m,T,P)$ and $\mu_w^{\mathrm{H}}(x_m,T,P)$ must be computed using a more complex formalism which requires to combine SGMC simulations and free energy calculations. Let us consider a methane hydrate made up of N_m methane molecules and N_w water molecules at given T and P. For this system, an infinitely small change in the internal energy dU writes:

$$\mathrm{d}U = T\mathrm{d}S - P\mathrm{d}V + \mu_m^{\mathrm{H}}\mathrm{d}N_m + \mu_w^{\mathrm{H}}\mathrm{d}N_w \tag{3.6}$$

where V and S are the volume and entropy of the methane hydrate, respectively. Legendre transformation of U with respect to S, V, N_w and N_m leads to:

$$U = TS - PV + \mu_m^{\mathrm{H}}N_m + \mu_w^{\mathrm{H}}N_w \tag{3.7}$$

By comparing Eq. (3.6) with the derivative of Eq. (3.7), one obtains:

$$N_w\mathrm{d}\mu_w^{\mathrm{H}} = -S\mathrm{d}T + V\mathrm{d}P - N_m\mathrm{d}\mu_m^{\mathrm{H}} \tag{3.8}$$

which is the Gibbs–Duhem equation for a binary mixture. Considering that N_w is constant in methane hydrate (owing to its crystalline structure), one can integrate Eq. (3.8) at constant T and P to obtain the change $\Delta\mu_w^{\mathrm{H}}$ in the chemical potential for water between the zero-occupancy and occupied methane hydrate (i.e., as the methane mole fraction increases from 0 to x_m):

$$\Delta\mu_w^{\mathrm{H}} = \mu_w^{\mathrm{H}}(x_m) - \mu_w^{H}(x_m = 0) = -\frac{1}{N_w}\int_{\mu_m^{\mathrm{H}}(x_m=0)}^{\mu_m^{\mathrm{H}}(x_m)} N_m\mathrm{d}\mu_m \tag{3.9}$$

While N_m can be determined as a function of μ_m^{H} using SGMC simulations as described in Section 2.2.3, the later equation shows that determining the chemical potential of water μ_w^{H} in the hydrate phase requires to estimate the same chemical potential in the zero-occupancy hydrate phase $\mu_w^{\mathrm{H}}(x_m = 0)$. The determination of $\mu_w^{\mathrm{H}}(x_m = 0)$ is not straightforward and requires free energy calculations that are reported in the next section.

3.3 Phase diagram of methane hydrate

3.3.1 Free energy approach

Einstein molecule method. In Section 3.2, it was shown that determining the condition for L–H–V phase coexistence requires to estimate the chemical potentials for water in the liquid and hydrate phases and for methane in the vapor and hydrate phases: $\mu_w^{\mathrm{L}}(x_m = 0, T, P)$, $\mu_w^{\mathrm{H}}(x_m, T, P)$, $\mu_m^{\mathrm{V}}(x_m = 1, T, P)$ and $\mu_m^{\mathrm{H}}(x_m, T, P)$. While the estimation of the chemical potentials for the pure phases $\mu_w^{\mathrm{L}}(x_m = 0, T, P)$ and $\mu_m^{\mathrm{V}}(x_m = 1, T, P)$ and for methane in the hydrate phase $\mu_m^{\mathrm{H}}(x_m, T, P)$ does not raise important technical issues, the estimation of the the chemical potential for water in the hydrate phase $\mu_w^{\mathrm{H}}(x_m, T, P)$ is not straightforward. However, as shown at the end of Section 3.2.2, $\mu_w^{\mathrm{H}}(x_m, T, P)$ can be estimated from its value in the zero-occupancy hydrate $\mu_w^{\mathrm{H}}(x_m = 0, T, P)$ (See Eq. (3.9)). By noting that the chemical potential is defined as the Gibbs free energy per water molecule $\mu_w^{\mathrm{H}}(x_m = 0, T, P) = G_w^{\mathrm{H}}(x_m = 0)/N_w$, the chemical potential of water in the zero-occupancy methane hydrate can be estimated from the Helmholtz free energy $A_w^{\mathrm{H}}(x_m = 0)$:

$$\mu_w^{\mathrm{H}}(x_m = 0) = \frac{G_w^{\mathrm{H}}(x_m = 0)}{N_w} = \frac{A_w^{\mathrm{H}}(x_m = 0) + PV}{N_w} \tag{3.10}$$

where the contribution PV is determined using molecular dynamics in the isobaric-isothermal ensemble (NPT).

In this section, we estimate $A_w^{\mathrm{H}}(x_m = 0)$ using free energy calculations based on the Einstein molecule approach developed by Vega and coworkers (Conde et al., 2016; Vega et al., 2008). This technique, which derives from the Einstein crystal approach, consists of estimating $A_w^{\mathrm{H}}(x_m = 0)$ along a reversible thermodynamic path linking the real solid to an Einstein molecule; the Einstein molecule is an ideal crystalline structure without any intermolecular interactions in which each molecule is attached to its reference lattice position and orientation by a harmonic potential. The canonical partition function and free energy of this reference state are known analytically. For technical reasons, it is convenient to compute the partition function of the Einstein molecule with one of its molecules at a fixed reference position (it should be noted that the position of this reference molecule is constant but molecular rotation is allowed).

Figure 3.3 shows the thermodynamic path used in the Einstein molecule approach to determine the free energy of the zero-occupancy methane hydrate. Throughout the manuscript, the superscript * indicates that the system has one of its water molecules at a fixed position (this molecule is shown by the big pink '+' sign in Figure 3.3). The reversible integration path considered in the Einstein molecule approach consists of four steps which transform the ideal Einstein molecule into the zero-occupancy methane hydrate:

1. Let us start from the non-interacting Einstein molecule (A) whose free energy A_{A} is known analytically; $A_{\mathrm{A}} = -k_B T \ln Q_{\mathrm{A}}$ where Q_{A} is the canonical partition function of the non-interacting Einstein molecule. The first step in the Einstein molecule approach consists of fixing the position of one of its water molecules to form a constrained, non–interacting Einstein molecule (A*). The free energy change corresponding to this transformation is simply $\Delta A_{\mathrm{A}\to\mathrm{A}^*} = A_{\mathrm{A}^*} - A_{\mathrm{A}} = k_B T \ln\left(V/\Lambda^3\right)$ where V is the volume of the Einstein molecule and Λ the thermal wavelength of the water molecule;

2. The constrained, non-interacting Einstein molecule (A*) is transformed into the corresponding interacting Einstein molecule (B*) by adding the intermolecular potential energy between water molecules (which includes the Lennard-Jones and Coulomb potentials as described in Chapter 2). That is, the interacting Einstein molecule consists of the non-interacting Einstein molecule and the intermolecular interactions of water–water. In this step, both the non-interacting and interacting Einstein molecules have one of their water molecules at a fixed position so that both of these structures are referred to as "constrained". The free energy difference along this step, $\Delta A_1 = A_{\mathrm{B}^*} - A_{\mathrm{A}^*}$, is determined using a perturbation treatment described below.

3. The constrained interacting Einstein molecule (B*) is transformed into the corresponding constrained, zero-occupancy methane hydrate (C*) by gradually switching off the harmonic potentials U_{A} that attach the water molecules to their reference lattice position in the Einstein molecule. The free energy difference in this step, $\Delta A_2 = A_{\mathrm{C}^*} - A_{\mathrm{B}^*}$, is determined by thermodynamic integration as described below;

4. The zero-occupancy methane hydrate (C) is obtained from the constrained, zero-occupancy methane hydrate (C*) by releasing the constraint over the fixed water molecule. The free energy change for this step simply writes $\Delta A_{\mathrm{C}^* \to \mathrm{C}} = A_{\mathrm{C}} - A_{\mathrm{C}^*} = -k_B T \ln\left(V/\Lambda^3\right)$.

The thermodynamic path above allows writing the free energy of the zero-occupancy methane hydrate as

$$\begin{aligned} A_{\mathrm{C}} &= A_{\mathrm{A}} + (A_{\mathrm{A}^*} - A_{\mathrm{A}}) + (A_{\mathrm{B}^*} - A_{\mathrm{A}^*}) + (A_{\mathrm{C}^*} - A_{\mathrm{B}^*}) + (A_{\mathrm{C}} - A_{\mathrm{C}^*}) \\ &= A_{\mathrm{A}} + k_B T \ln \frac{V}{\Lambda^3} + \Delta A_1 + \Delta A_2 - k_B T \ln \frac{V}{\Lambda^3} = A_{\mathrm{A}} + \Delta A_1 + \Delta A_2 \end{aligned} \tag{3.11}$$

where it used that constraining (step 1) and unconstraining (step 4) the position of one reference water molecule in the thermodynamic path cancel out. While these free energy calculations should not depend on a specific choice for the Einstein molecule (provided a reasonable configuration is used), we followed here the annealing approach suggested by Noya and coworkers (Noya et al., 2008). First, the Einstein molecule is selected with a volume identical to that of real methane hydrate as obtained using isobaric–isothermal MD simulations at $P = 1$, 10, and 100 atm. Then, a simulated annealing strategy (canonical ensemble) is used to determine the final configuration; the temperature is decreased from $T = 180$ K to 1 K with temperature steps of 10 K. Eq. (3.11) shows that only the three following contributions must be calculated to determine the free energy of the zero-occupancy methane hydrate: A_{A}, ΔA_1 and ΔA_2. In the rest of this subsection, we determine these three contributions before gathering all the data to estimate the free energy of the zero-occupancy methane hydrate $A_{\mathrm{C}} = A_w^{\mathrm{H}}(x_m = 0)$ and the chemical potentials μ_w^{H} and μ_m^{H} in the real (i.e., methane occupied) methane hydrate.

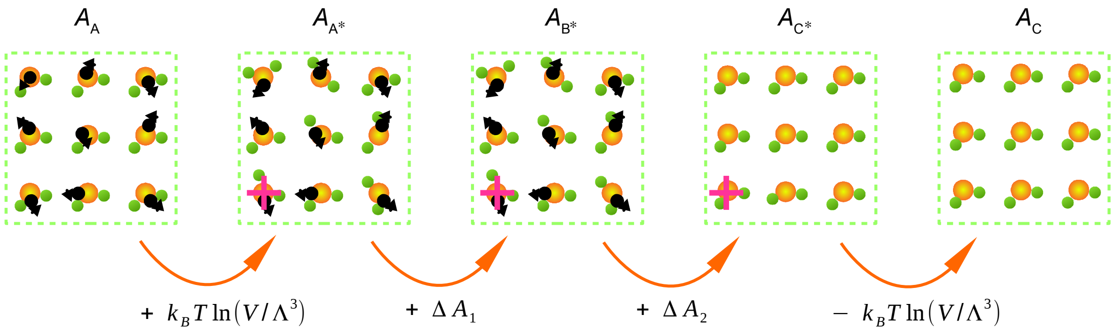

Figure 3.3 Thermodynamic path used in the Einstein molecule approach to calculate the free energy of the zero-occupancy methane hydrate, A_{C}. Orange and green spheres are the oxygen and hydrogen atoms of water, respectively. The green box shows the periodic boundary conditions of the simulation cell. The superscript * indicates that the system has one of its water molecules at a fixed position shown by the big pink '+' sign (*see text*). A_{A} is the free energy of the non-interacting Einstein molecule while $A_{\mathrm{A}*}$ is the free energy of the same system with one of its water molecules at a fixed position. $A_{\mathrm{B}*}$ is the free energy of the interacting Einstein molecule with one of its water molecules at a fixed position. $A_{\mathrm{C}*}$ is the free energy of the zero-occupancy methane hydrate with one of its water molecules at a fixed position while A_{C} is the free energy of the same system without fixing any water molecule positions. Constraining a water molecule position (3 degrees of freedom) increases the free energy by $k_BT\ln\left(V/\Lambda^3\right)$. The change in free energy between the non-interacting and interacting Einstein molecule is $\Delta A_1 = A_{\mathrm{B}*} - A_{\mathrm{A}*}$. The change in free energy between the constrained interacting Einstein molecule and the constrained methane hydrate is $\Delta A_2 = A_{\mathrm{C}*} - A_{\mathrm{B}*}$ (*see text*).

Free Energy A_{A} of the non-interacting Einstein molecule. Water molecules in the non-interacting Einstein molecule (A) are attached to their reference lattice position and orientation through harmonic potentials so that its potential energy writes:

$$U_{\mathrm{A}}(\mathbf{R}_i,\phi_{\mathbf{a},i},\phi_{\mathbf{b},i}) = \lambda_T\sum_{i=1}^{N}(\mathbf{R}_i-\mathbf{R}_i^{(0)})^2+\lambda_R\sum_{i=1}^{N}[(\sin^2\phi_{\mathbf{a},i}+(\frac{\phi_{\mathbf{b},i}}{\pi}^2)] \tag{3.12}$$

where the sum runs over each molecule i of the N molecules in the system. The first term in Eq. (3.12) corresponds to harmonic potentials acting on each molecule position $\mathbf{R}_i$ with an equilibrium position defined as the reference position $\mathbf{R}_i^{(0)}$. Similarly, the second term in Eq. (3.12) corresponds to harmonic potentials acting on each molecule orientation defined by two vectors $\mathbf{a}$ and $\mathbf{b}$ with equilibrium vectors $\mathbf{a}_i^{(0)}$ and $\mathbf{b}_i^{(0)}$ corresponding to the reference molecule orientation. As shown in Figure A.1 of the Appendix A, the two orientation vectors can be chosen as $\mathbf{a} = (\mathbf{l}_1-\mathbf{l}_2)/|\mathbf{l}_1-\mathbf{l}_2|$ and $\mathbf{b} = (\mathbf{l}_1+\mathbf{l}_2)/|\mathbf{l}_1+\mathbf{l}_2|$ where

$\mathbf{l}_1$ and $\mathbf{l}_2$ are the vectors along the O–H bonds in the water molecule. For each water molecule i, $\phi_{\mathbf{a},i} = \cos(\mathbf{a}_i \cdot \mathbf{a}_i^{(0)})$ and $\phi_{\mathbf{b},i} = \cos(\mathbf{b}_i \cdot \mathbf{b}_i^{(0)})$. Following previous works (Jensen et al., 2010; Vega and Noya, 2007; Vega et al., 2008; Wierzchowski and Monson, 2007), the spring constants in $U_{\mathrm{A}}(\mathbf{R}_i, \phi_{\mathbf{a},i}, \phi_{\mathbf{b},i})$ were selected as $\lambda_R/k_BT\mathring{\mathrm{A}}^2 = \lambda_T/k_BT = 25000$ (note that when reasonable choices are made for these parameters, A_{A} is independent of these values as harmonic oscillators only depend on temperature).

The Helmholtz free energy A_{A} of the non-interacting Einstein molecule, which can be computed from its canonical partition function Q_{A}, subdivides into a translation $A_{\mathrm{A},T}$ and a rotation $A_{\mathrm{A},R}$ contributions:

$$\frac{A_{\mathrm{A}}}{Nk_BT} = -\frac{\ln Q_{\mathrm{A}}}{N} = \frac{A_{\mathrm{A},T}}{Nk_BT} + \frac{A_{\mathrm{A},R}}{Nk_BT} \tag{3.13}$$

where all free energy contributions are normalized to the total thermal energy Nk_BT. As shown in Section A.2 of the Appendix A, these two contributions can be expressed as:

$$\begin{aligned} \frac{A_{\mathrm{A},T}}{Nk_BT} &= \frac{1}{N}\ln\left(\frac{N\Lambda^3}{V}\right) + \frac{3}{2}\left(1-\frac{1}{N}\right)\ln\left(\frac{\Lambda^2\lambda_T}{k_BT\pi}\right) \\ &\sim_{N\to\infty} \left[\frac{3}{2}\ln\left(\frac{\Lambda^2\lambda_T}{k_BT\pi}\right)\right] \end{aligned} \tag{3.14}$$

$$\frac{A_{\mathrm{A},R}}{Nk_BT} = -\ln\left[\int_0^1 \exp\left(-\frac{\lambda_R}{k_BT}(1-x^2)\right)dx \int_0^1 \exp\left(-\frac{\lambda_R}{k_BT}y^2\right)dy\right] \tag{3.15}$$

Calculations based on these expressions, including numerical integration of Eq. (3.15), can be found in Section A.2 of the Appendix A and lead to $A_{A,T}/(Nk_BT) = 29.43$, $A_{E,R}/(Nk_BT) = 16.01$. These values are fully consistent with those reported by Vega and coworkers for hexagonal ice (Vega et al., 2008).

Free energy difference ΔA_1. The free energy change $\Delta A_1 = A_{\mathrm{B}*} - A_{\mathrm{A}*}$ between the non-interacting and interacting Einstein molecules is estimated through a perturbation approach. One can write that the potential energy in the interacting Einstein molecule U_{B*}

is the sum of the non-interacting Einstein molecule U_{A*} and the intermolecular potential energy U, i.e., $U_{B*} = U_{A*} + U$. For large λ_R and λ_T, $U << U_{B*} \sim U_{A*}$ and a perturbation treatment allows determining ΔA_1 from an average over a canonical distribution $\langle ... \rangle_{NVT}$:

$$\frac{\Delta A_1}{Nk_BT} = -\frac{1}{N} \ln \left\langle \exp\left(-\frac{U}{k_BT}\right)\right\rangle_{NVT} \tag{3.16}$$

In fact, U is not small since the intermolecular potential energy in the reference lattice $U^{(0)}$ is not negligible. To overcome this technical problem, one can estimate ΔA_1 through a perturbation approach in which one considers $U - U^{(0)}$. With this approach, Eq. (3.16) becomes:

$$\frac{\Delta A_1}{Nk_BT} = \frac{U^{(0)}}{Nk_BT} - \frac{1}{N} \ln \left\langle \exp\left(-\frac{U - U^{(0)}}{k_BT}\right)\right\rangle_{NVT} \tag{3.17}$$

In practice, Monte Carlo simulations in the canonical ensemble (CMC) are used to estimate the canonical average defined in Eq. (3.17). Figure 3.4(a) shows $\Delta A_1(T,P)$ as a function of temperature T for a pressure $P = 100$ atm (data for other pressures are not shown for the sake of clarity). Both the results for TIP4P/2005 and TIP4P/Ice are reported. As expected, $\Delta A_1(T,P)$ is negative since the intermolecular potential in the interacting Einstein molecule (which stabilizes the structure) decreases its energy and therefore its free energy. Moreover, upon increasing the temperature, $\Delta A_1(T,P)$ is less significant as the thermal energy and entropy contribution become more important.

Free energy difference ΔA_2. The free energy change $\Delta A_2 = A_{\mathrm{C}*} - A_{\mathrm{B}*}$ between the constrained interacting Einstein molecule (B*) and the constrained zero-occupancy methane hydrate (C*) is estimated by means of thermodynamic integration. More precisely, we considers a hybrid potential that depends linearly on the potential energies of B* and C*:

$$U(\lambda) = (1-\lambda)U_{\mathrm{C}*} + \lambda U_{\mathrm{B}*} = U + \lambda U_{\mathrm{A}*} \tag{3.18}$$

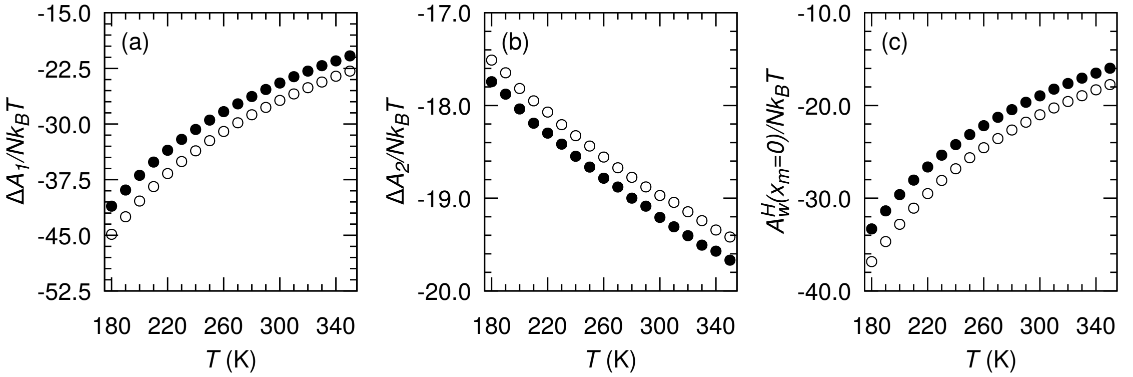

Figure 3.4 Free energy changes ΔA_1 (a) and ΔA_2 (b) and free energy $A_w^H(x_m = 0)$ of the zero-occupancy methane hydrate (c) as a function of temperature T (all data reported here are for $P = 100$ atm). The empty and closed circles are for the TIP4P/Ice and TIP4P/2005 water models, respectively. Free energies are normalized to the total thermal energy Nk_BT. $\Delta A_1 = A_{\mathrm{B}*} - A_{\mathrm{A}*}$ is the free energy difference between the non-interacting and interacting Einstein molecules (corresponding to the zero-occupancy methane hydrate). $\Delta A_2 = A_{\mathrm{C}*} - A_{\mathrm{B}*}$ is the free energy difference between the interacting Einstein molecule and the zero-occupancy methane hydrate. Except for the zero-occupancy methane hydrate in (c), all systems are constrained with one of their molecules having a fixed reference position.

where λ is a coupling parameter. The second equality in the equation above is obtained by noting that $U_{\mathrm{B}*} = U_{\mathrm{A}*} + U$ and $U_{\mathrm{C}*} = U$. Thermodynamic integration is performed by varying infinitesimally λ from 0 to 1 (so that the hybrid system considered in Eq. (3.18) varies slowly from B* to C*). Within this framework, ΔA_2 can be obtained from the following integration:

$$\begin{aligned}\Delta A_2 = A_{\mathrm{C}^*} - A_{\mathrm{B}^*} &= -[A(\lambda = 0) - A(\lambda = 1)] \\ &= -\int_0^1 d\lambda \left\langle \frac{\partial U(\lambda)}{\partial \lambda} \right\rangle_{NVT\lambda} = -\int_0^1 d\lambda \, \langle U_{\mathrm{A}*} \rangle_{NVT\lambda}\end{aligned} \tag{3.19}$$

where $\langle \cdots \rangle_{NVT\lambda}$ denotes canonical averages over a system with a hybrid potential energy $U(\lambda)$ sampled using Monte Carlo simulations. In practice, integration in the equation above is performed for several λ in the range of [0,1] (the 31-point Gauss-Legendre integration method was adopted).

Figure 3.4(b) shows $\Delta A_2(T,P)$ as a function of temperature T for a pressure $P =$ 100 atm (again, data for other pressures are not shown for the sake of clarity). Like for $\Delta A_1(T,P)$, both the results for TIP4P/2005 and TIP4P/Ice are reported. $\Delta A_2(T,P)$ is negative since removing the harmonic potential contributions (necessarily positive) when switching from B* to C* leads to lower energies and hence free energies. Finally, as the temperature increases, $\Delta A_2(T,P)$ becomes less pronounced as the entropy contribution becomes more important.

Proton Disorder Correction. While oxygen atoms occupy well-defined positions in a zero-occupancy hydrate, hydrogen atoms fluctuate and lead to significantly disordered water molecule orientations (known as the proton disorder rule discussed above). As a result, an additional contribution to the free energy of the zero-occupancy methane hydrate must therefore be considered to account for such proton disorder. This proton disorder correction, which is independent of the molecular interaction potential considered, can be approximated as the residual entropy of ice Nagle (1966); Vega et al. (2008):

$$\frac{A_{disorder}}{Nk_BT} = -\frac{S_{disorder}}{Nk_B} = -\ln W \tag{3.20}$$

Using the values reported by Nagle ($1.50683 < W < 1.50687$) Nagle (1966), one obtain a proton disorder correction $A_{disorder}/Nk_BT \sim -0.41$.

Chemical potential of water and methane in methane hydrate, μ_w^{H} and μ_m^{H}. Figure 3.4(c) shows the free energy of the zero-occupancy methane hydrate $A_w^H(x_m = 0)$ as a function of temperature T. This contribution was obtained using Eq. (3.11) from the calculations of the free energy $A_w^H(x_m = 0)$ and the free energy changes ΔA_1 and ΔA_2. Thanks to this free energy curve, we obtain readily the chemical potential of water in zero-occupancy methane hydrate $\mu_w^{\mathrm{H}}(x_m = 0, T, P)$ using Eq.(3.10). Once $\mu_w^{\mathrm{H}}(x_m = 0, T, P)$ has been obtained using free energy calculations, several SGMC simulations need to be performed to determine the methane occupancy N_m^{H} (expressed as the number of methane molecules per methane hydrate unit cell) as a function of the chemical potential of methane μ_m^{H} at given T and P. Figure 3.5 shows the methane occupancy as a function of μ_m^{H} at $T = 250$ K and $P =$

100 atm (similar data were obtained for other T and P). These results, which are consistent with those reported by Wierzchowski and Monson (Wierzchowski and Monson, 2007), shows that the methane occupancy increases rapidly with μ_m and then plateaus as the methane occupancy reaches its maximum. Fifty different chemical potentials μ_m were considered in the SGMC simulations to determine the methane occupancy N_m as a function of chemical potential μ_m (See Figures A.4 and A.5 of the Appendix A). To determine the correction $\Delta\mu_w^{\mathrm{H}}(x_m, T, P)$ to the water chemical potential due to methane occupancy, the data $N_m(\mu_m)$ were interpolated using a cubic interpolation procedure to obtain 2.5×10^5 points. Thanks to such finely desecrated data, we could estimate very accurately the contribution to the water chemical potential due to methane occupancy using the simple trapezoidal rule. Such a numerical integration leads to error bars that are at most $\pm 2 \times 10^{-3}$ for the correction term. While the calculations above can be considered very accurate, possible size effects due to the finite size of the methane hydrate considered. However, considering that the system size in this work ($2 \times 2 \times 2$ methane hydrate unit cell) allowed one to use a large interaction cutoff, finite size effects are believed to be negligible. Figure 3.5 also shows the correction term $\Delta\mu_w^{\mathrm{H}} = \mu_w^{\mathrm{H}}(x_m) - \mu_w^{\mathrm{H}}(x_m = 0) = -\frac{1}{N_w}\int_{\mu_m^H(x_m=0,T,P)}^{\mu_m^H(x_m,T,P)} N_m d\mu_m$ as a function of methane occupancy N_m. As expected, $\Delta\mu_w^{\mathrm{H}}$ is small as the chemical potential of water is not very sensitive to the methane occupancy (due to the fact that water density in hydrate does not change significantly with the methane occupancy and that water weakly interacts with methane). For the different T and P considered in this work, the chemical potential of water in methane hydrate is obtained by adding the correction term due to methane occupancy to the chemical potential for the zero-occupancy hydrate. The chemical potentials of water in the methane-occupied hydrate, μ_w^{H}, in the temperature range $T =$ 180–350K and for $P = 1$, 10, 100 atm are shown in Figures A.4 and A.5 of the Appendix A (which correspond to the data for TIP4P/2005 and TIP4P/Ice, respectively). Figure A.6 of the Appendix A also shows the different contributions to the water chemical potential: free energy of the zero occupancy hydrate, pressure-volume term, proton disorder correction and correction due to methane occupancy.

Table 3.3 Free energy contributions of zero-occupancy methane hydrate, $\mu_w^H(x_m = 0, T, P)$. ^{a} Absolute error bar is less than 0.008; ^{b} The error bar is negligible as it smaller than the last digit shown (high accuracy of the Gauss-Legendre formula); ^{c} proton disorder correction is already included here.

water model	T/K	$\frac{A_\mathrm{A}}{Nk_BT}$	$\frac{A_1}{Nk_BT}^a$	$\frac{A_2}{Nk_BT}^b$	$\frac{A^\mathrm{H}}{Nk_BT}^c$	μ_w^H/k_BT $P = 1$ atm	μ_w^H/k_BT $P = 10$ atm	μ_w^H/k_BT $P = 100$ atm
TIP4P	180	25.8835	-41.0685	-17.7439	-33.3149	-33.3134	-33.3000	-33.1664
/2005	190	25.8024	-38.9023	-17.8783	-31.3642	-31.3628	-31.3501	-31.2233
	200	25.7255	-36.9117	-18.0376	-29.6098	-29.6084	-29.5963	-29.4755
	210	25.6523	-35.1278	-18.1918	-28.0532	-28.0520	-28.0404	-27.9249
	220	25.5825	-33.5345	-18.2980	-26.6360	-26.6348	-26.6237	-26.5136
	230	25.5158	-32.0754	-18.4169	-25.3625	-25.3613	-25.3507	-25.2446
	240	25.4520	-30.7312	-18.5484	-24.2136	-24.2124	-24.2023	-24.1006
	250	25.3907	-29.4746	-18.6645	-23.1343	-23.1333	-23.1235	-23.0258
	260	25.3319	-28.3381	-18.7843	-22.1764	-22.1754	-22.1660	-22.0718
	270	25.2753	-27.2826	-18.8799	-21.2732	-21.2722	-21.2631	-21.1724
	280	25.2207	-26.2871	-19.0000	-20.4523	-20.4513	-20.4425	-20.3549
	290	25.1681	-25.3486	-19.0865	-19.6530	-19.6520	-19.6435	-19.5585
	300	25.1172	-24.4787	-19.2073	-18.9547	-18.9538	-18.9456	-18.8632
	310	25.0680	-23.6105	-19.3084	-18.2368	-18.2359	-18.2279	-18.1482
	320	25.0204	-22.8603	-19.4048	-17.6306	-17.6298	-17.6221	-17.5447
	330	24.9742	-22.1325	-19.5058	-17.0500	-17.0492	-17.0417	-16.9663
	340	24.9294	-21.4812	-19.5715	-16.5092	-16.5084	-16.5011	-16.4277
	350	24.8859	-20.8100	-19.6685	-15.9785	-15.9777	-15.9705	-15.8993
TIP4P	180	25.9299	-44.8718	-17.5103	-36.8382	-36.8367	-36.8231	-36.6873
/Ice	190	25.8488	-42.4988	-17.6474	-34.6834	-34.6820	-34.6691	-34.5404
	200	25.7719	-40.3826	-17.8168	-32.8134	-32.8120	-32.7998	-32.6774
	210	25.6987	-38.4410	-17.9498	-31.0781	-31.0768	-31.0651	-30.9483
	220	25.6289	-36.6783	-18.0710	-29.5064	-29.5052	-29.4940	-29.3822
	230	25.5622	-35.0610	-18.2072	-28.0919	-28.0907	-28.0800	-27.9729
	240	25.4984	-33.6109	-18.3264	-26.8249	-26.8237	-26.8135	-26.7107
	250	25.4371	-32.2472	-18.4380	-25.6340	-25.6329	-25.6230	-25.5242
	260	25.3783	-30.9968	-18.5562	-24.5607	-24.5596	-24.5501	-24.4548
	270	25.3217	-29.8351	-18.6717	-23.5711	-23.5701	-23.5609	-23.4690
	280	25.2671	-28.7567	-18.7756	-22.6510	-22.6501	-22.6412	-22.5524
	290	25.2145	-27.7576	-18.8784	-21.8074	-21.8064	-21.7978	-21.7119
	300	25.1637	-26.8127	-18.9704	-21.0054	-21.0045	-20.9962	-20.9130
	310	25.1145	-25.9463	-19.0452	-20.2630	-20.2621	-20.2540	-20.1733
	320	25.0668	-25.1055	-19.1462	-19.5708	-19.5699	-19.5620	-19.4838
	330	25.0207	-24.3386	-19.2423	-18.9461	-18.9453	-18.9377	-18.8616
	340	24.9759	-23.5634	-19.3428	-18.3162	-18.3154	-18.3080	-18.2340
	350	24.9324	-22.8693	-19.4184	-17.7412	-17.7404	-17.7332	-17.6611

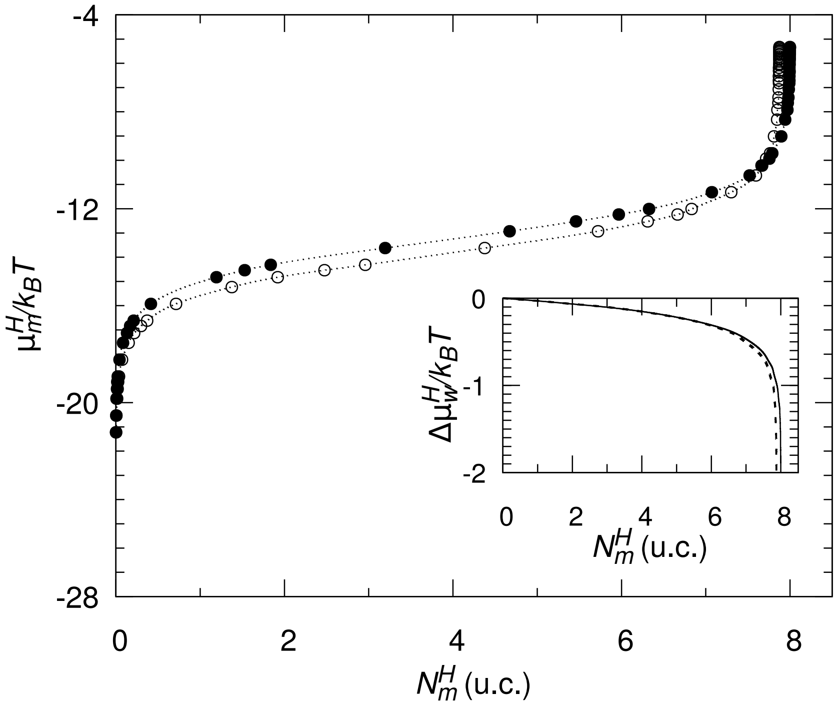

Figure 3.5 Chemical potential of methane, μ_m^H, versus number of methane molecules, N_m^{H}, in methane hydrate at $T = 250$ K and $P = 10$ atm. N_m^H is expressed as the number of methane molecules per methane hydrate unit cell. The empty and filled circles are for TIP4P/Ice anf TIP4P/2005 water models, respectively. The dotted lines correspond to cubic interpolation of the data. The insert shows the chemical potential difference of water relative to the zero-occupancy methane hydrate, $\Delta\mu_w^{\mathrm{H}} = \mu_w^{\mathrm{H}} - \mu_w^{\mathrm{H}}(x_m = 0)$, as a function of the number of methane molecules, N_m^{H} (these data are obtained from $N_m(\mu_m)$ using Eq. (3.9)). The dashed and solid lines are for the TIP4P/Ice and TIP4P/2005 water models. All chemical potentials are normalized to the thermal energy, k_BT.

Pressure–temperature phase diagram. The previous sections were devoted to determining the different chemical potentials for water in the liquid and methane hydrate phases and for methane in the vapor and methane hydrate phases. These quantities are crucial as they are required to predict phase coexistence for methane hydrate using the conditions given in Eq. (3.3) (which simply correspond to chemical potential equalities for water and methane in each of the three coexisting phases). As discussed above, these L–H–V coexistence conditions correspond to two important equalities: (1) $\mu_m^{\mathrm{V}} = \mu_m^{\mathrm{H}}$ and (2) $\mu_w^{\mathrm{L}} = \mu_w^{\mathrm{H}}$. These two equations lead to two solutions for x_m in methane hydrate at given T and P; the first solution $x_m(1)$ is obtained from the coexistence of pure liquid water (L) with methane hydrate (H) while the second solution $x_m(2)$ is obtained from the coexistence of methane hydrate (H) and pure methane vapor (V). For a given P, the temperature corresponding to L–H–V equilibrium is given by $x_m(1) = x_m(2)$. In contrast, if $x_m(1) \neq x_m(2)$, the set P and T does not correspond to L–H–V equilibrium. In order to determine L–H–V phase coexistence, we plot $x_m(1)$ and $x_m(2)$ as a function of T in Figure 3.6. we show the data corresponding to $P = 1$, 10, and 100 atm for the two water models considered in this work. These data show that the L–H–V coexistence condition is determined unambiguously using this strategy.

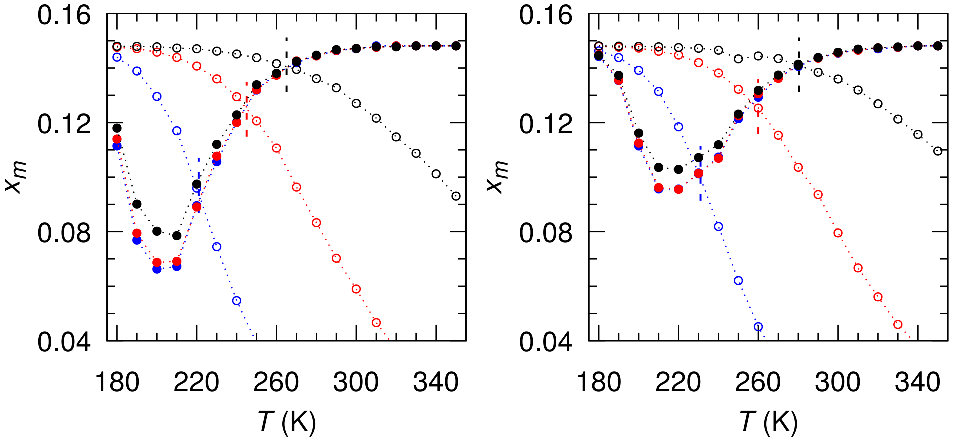

Figure 3.6 (color online) Equilibrium number of methane, $x_m(\mu_m^{\mathrm{V}} = \mu_m^{\mathrm{H}})$ (empty circles) and $x_m(\mu_w^{\mathrm{L}} = \mu_w^{\mathrm{H}})$ (filled circles), as a function of temperature, T, at $P = 1$ (blue), 10 (red), 100 (black) atm. The corresponding interpolation cross point, $x_m(\mu_m^{\mathrm{V}} = \mu_m^{\mathrm{H}}) = x_m(\mu_w^{\mathrm{L}} = \mu_w^{\mathrm{H}})$, indicating the liquid water-methane hydrate-methane vapor (L–H–V) equilibrium temperature and methane composition at the given pressure. The left and right panels are for TI4P/2005 and TIP4P/Ice water models, respectively.

The pressure–temperature phase diagram of sI methane hydrate determined using the free energy calculations above are shown in Figure 3.7. For the TIP4P/2005 water model, the hydrate melting temperatures are 221 K, 244 K, and 265 K for P = 1, 10, and 100 atm, respectively. For these three coexistence points, the corresponding methane mole fractions are $x_m \sim 0.10$, 0.12, and 0.14 (these values correspond to $N_m^{\mathrm{H}} \sim 4.94$, 6.56 and 7.56). For the TIP4P/Ice water model, the hydrate melting temperatures are 232 K, 262 K, and 287 K for $P = 1$, 10, and 100 atm, respectively, with methane mole fractions $x_m \sim 0.10$, 0.13, and 0.14 (these values correspond to $N_m^{\mathrm{H}} \sim 5.19$, 6.63, and 7.56). As shown in Figure 3.7, in agreement with previous data by Conde et al. (Conde and Vega, 2010), the TIP4P/2005 water model underestimates the melting temperature of methane hydrate by ~ 20 K (such a shift is consistent with the fact that this model underestimates the crystallization temperature of different ice forms) (Abascal et al., 2005; Abascal and Vega, 2005). In contrast, the TIP4P/Ice water model accurately captures the experimental pressure–temperature phase diagram of methane hydrate (Sloan, 2003). Interestingly, the data for TIP4P/Ice lead to data which are in better agreement with the experimental data than those by Jensen et al. (Jensen et al., 2010) although these authors consider the same model and strategy. Such a discrepancy is due to the approximation made by these authors to describe methane vapor; While we consider the exact equation of state for methane as probed by a combination of isobaric-isothermal and Grand Canonical molecular simulations, Jensen et al. determined the chemical potential of methane vapor using thermodynamic integration starting from an ideal gas approximation. The differences between the two sets of results, which were are consistent with differences observed by Conde et al. (Conde and Vega, 2010), necessarily arise from the chemical potential of methane in the vapor phase as all other results are in very good agreement (free energy of the zero-occupancy methane hydrate and water chemical potential in the liquid phase). Moreover, one could trust that the data obtained using the free calculations in this work are robust because the phase diagram obtained with TIP4P/2005 is consistent with the results by Conde et al. (Conde and Vega, 2010). Moreover, the dissociation temperature obtained using our free energy calculations is also consistent with those obtained using the direct coexistence method and the hyper parallel tempering technique (these data will be discussed later). The important shift between the data obtained in the present work and those obtained by Jensen et al. shows that all approximations made in the free energy calculations are important. The data reported in the present work were also found to be in very good agreement with the recent results obtained by Waage et al. (Waage et al., 2017).

3.3.2 Direct Coexistence Method in the Grand Canonical Ensemble

Two other strategies, including the direct coexistence method and hyper parallel tempering method, were also adopted to assess phase boundary between methane hydrate and liquid water. For these two strategies, we only use the TIP4P/Ice water model (as this model

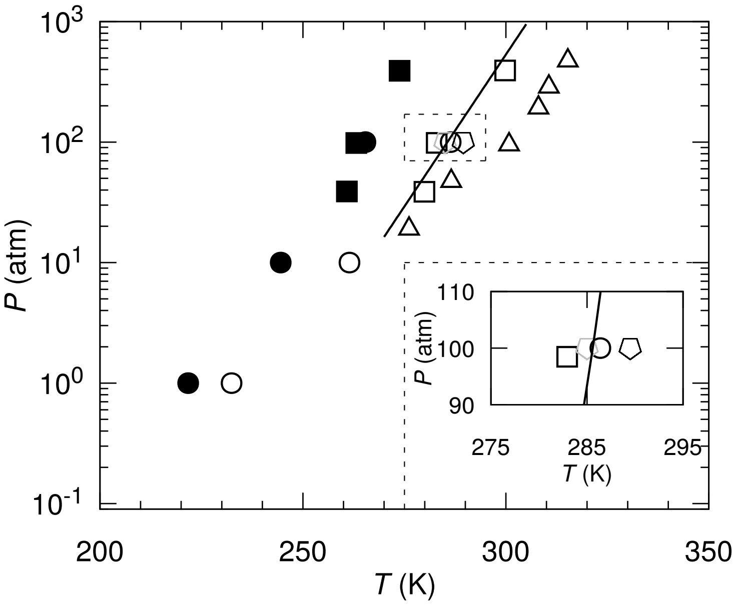

Figure 3.7 Pressure–Temperature phase diagram of methane hydrate as determined using free energy calculations (circles, this work), direct coexistence method (gray pentagon, this work), hyper parallel tempering method (black pentagon, this work). The empty and filled symbols are for TIP4P/Ice and TIP4P/2005 water models, respectively. The empty and filled squares are the results obtained for TIP4P/Ice and TIP4P/2005 by Conde et al. (Conde and Vega, 2010) using the direct coexistence method. The empty triangles are the free energy calculations for TIP4P/Ice by Jensen et al. (Jensen et al., 2010). The solid line shows the experimental data by Sloan et al. (Sloan, 2003). The insert shows a zoomed view of the region shown depicted as a dashed rectangle in the main figure.

was found to better capture the experimental phase diagram). Moreover, to keep the discussion as simple as possible, we only consider the pressure $P = 100$ atm. With the direct coexistence method, one prepares an initial simulation box in which the two phases coexist (here, the methane hydrate and the liquid phase). Then, several simulations are performed at different T and P to determine the stability domain for each phase; for a given P, the high symmetry phase (hydrate) will be stable below the melting temperature T_m while the low symmetry phase (liquid) will be stable above T_m. In other words, the region occupied by the liquid transforms into methane hydrate for $T < T_m$ while the region occupied by the methane hydrate transforms into liquid for $T > T_m$. In general, such direct coexistence simulations are conducted in the isobaric-isothermal ensemble (NPT) because phase transitions occurs at constant T and P. As a result, all direct coexistence method strategies applied to methane hydrate have been carried out so far in this ensemble (Conde and Vega, 2010; Michalis et al., 2015; Tung et al., 2010). However, for binary compounds such as methane hydrate, such coexistence simulations can be performed in the Grand Canonical ensemble where the system volume V, temperature T, and chemical potentials for water μ_w and methane μ_m are constant. We adopted this strategy which has not been considered previously to the best of our knowledge. Considering such an open ensemble in which the numbers of water and methane molecules fluctuate present several advantages over constant number of molecules ensemble (such as NVT or NPT simulations). First, this allows considering small system sizes since the number of methane molecules will adjust upon methane hydrate formation even though the initial number of methane molecules is small. In contrast, with constant N simulations, one has to simulate a large domain of methane molecules that acts as a methane source to fill the water cages upon methane hydrate formation. Moreover, by considering an ensemble where density will change through molecule numbers fluctuations, one avoids difficulties due to inefficient/limited sampling in volume changes. Finally, in GCMC simulations, molecule insertion/deletions are attempted randomly, homogeneously throughout the simulation box so that difficulties inherent to slow diffusion between the methane hydrate and liquid/fluid phases are overcome.

For such complex systems, DCM should be used with caution because of the initial coexisting system can be chosen in different ways. According to Gibbs' phase rule, in the temperature/pressure range where methane hydrate is stable, it coexists with the liquid (water-rich) and vapor (methane-rich) phases. As a result, initial phase coexistence in DCM can be chosen as a system made of two of these three phases or three phases. In the present work, we chose to consider phase coexistence between the liquid phase and methane hydrate; while this corresponds to an approximation, the use of the Grand Canonical ensemble ensures that three-phase coexistence is simulated in fact; because the system is in equilibrium with an infinite reservoir of bulk molecules at chemical potentials corresponding to those of the water-rich liquid and methane-rich vapor, DCM simulations in this specific ensemble are equivalent to simulating a system with three-phase coexistence.

In order to prepare the initial system (i.e., methane hydrate coexisting with liquid water), several strategies are possible. we started from a methane hydrate phase having the following dimensions: $L_x = L_y = L_z = 2.3754$ nm. Periodic boundary conditions were applied in each direction to avoid finite size effects. we started from a hydrate phase equilibrated at low T (it should be noted that the pressure was set to 100 atm). Then, molecules located in the region $z < 0$ were frozen while the rest of the simulation box was equilibrated at high temperature T to melt the hydrate located in the region $z > 0$. In so doing, one obtains a coexisting system made of methane hydrate in equilibrium with the liquid phase (Figure 3.8(a)). Obviously, this system is maintained at coexistence condition in an unphysical fashion and, depending on the temperature used in subsequent GCMC simulations, the system will melt or form hydrate (unless in the very unlikely event that the chosen temperature and chemical potentials exactly correspond to phase coexistence). From a practical point of view, for $P = 100$ atm, we performed $M = 18$ simulations with temperatures in the range $T = 180$–350 K (the temperature interval is 10 K). The DCM simulations in the Grand Canonical ensemble at a given pressure and temperature require to specify chemical potentials for water and methane. In the present work, as described in Section 3.2.2, the chemical potential for water in the liquid phase was chosen equal to that of pure liquid water while that the chemical potential for methane in the vapor phase was chosen equal to that or pure methane vapor.

Figure 3.8(b) shows the methane x_m and water x_w mole fractions in the system in the course of the GCMC simulation (i.e., the number of MC moves performed with one MC move corresponding to a molecule translation, rotation, insertion or creation). Results for different temperatures are shown: T = 260, 270, 280, 290, and 300 K. On the one hand, at high temperature, $T \geq 290$ K, the system melts as evidenced by the decrease in the methane mole fraction x_m. As expected, $x_m \sim 0$ ($x_w \sim 1$) in the liquid phase, which further justifies our choice in the L–H–V equilibrium condition to assume that $\mu_w^{\mathrm{L}}(x_m, T, P) \sim \mu_w^{\mathrm{L}}(x_m = 0, T, P)$. On the other hand, at low temperature, $T \leq 280$ K, the methane mole fraction increases (while x_w decreases) upon methane hydrate formation.

While melting does not suffer from ambiguity since all methane hydrate is transformed into liquid, it should be emphasized that hydrate formation was found to be inefficient; due to the low probability to nucleate hydrate cages (inherent to their very small entropy), it was observed that formation of the hydrate is incomplete. As a result, despite the coexistence with an already formed hydrate, many long GCMC runs (about 7-8 $\times 10^8$ MC moves for a system size of the order of $\sim 10^2 - 10^3$ molecules) were not sufficient to lead to perfect methane hydrates. Despite this drawback of the direct coexistence method, the results above show that the equilibrium temperature for hydrate/liquid coexistence is comprised between 280 K and 290 K. As can be seen in Figure 3.7, this coexistence temperature is in very good agreement with the results from the free energy calculations $T_m = 287$ K. This value is also consistent with the experimental data as well as with other theoretical results obtained for the same water/methane molecular models.

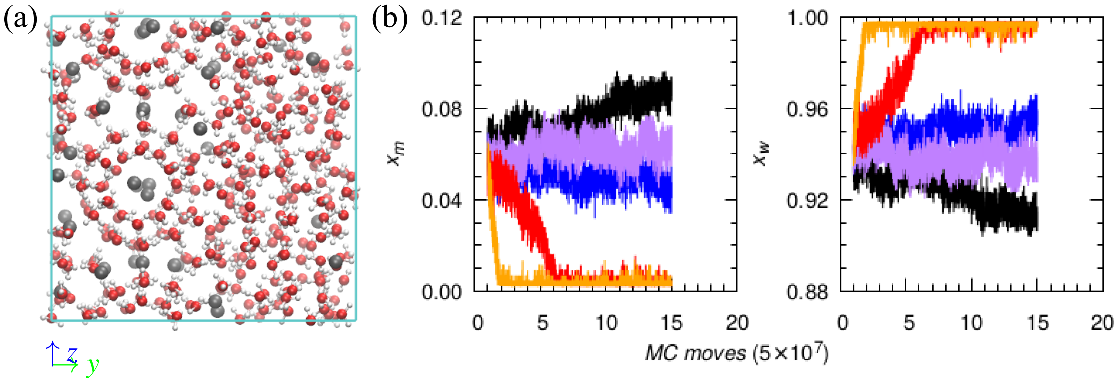

Figure 3.8 (color online) Determination of the phase transition temperature between methane hydrate and liquid phases using the direct coexistence method. (a) Starting from a methane hydrate coexisting with the liquid phase, several Monte Carlo simulations in the Grand Canonical ensemble (μVT) at different temperatures and chemical potentials are performed (chemical potentials are chosen so that the pressure is $P = 100$ atm). The red and white spheres are the oxygen and hydrogen atoms of water while the grey spheres are the methane molecules. The dimensions of the simulation box are: $L_x = L_y = L_z = 2.3754$ nm. Molecules with $y < 0$ (left region) and $y > 0$ (right region) belong to the methane hydrate and liquid phases, respectively. If the temperature is lower than the melting point T_m, the liquid disappears as methane hydrate forms. In contrast, if the temperature is larger than T_m, the methane hydrate melts and is replaced by the liquid. (b) Methane (left) and water (right) mole fractions during the different GCMC simulation runs: T = 260 K (black), 270 K (purple), 280 K (blue), 290 K (red), and 300 K (orange). The x-axis, which indicates progress along the GCMC simulation, is expressed as a number of attempted MC moves where one move is a molecule translation, rotation, insertion or deletion.

3.3.3 Hyper Parallel Tempering

In the hyper parallel tempering method (Coasne, 2005; Coasne et al., 2004; Czwartos et al., 2005; Yan and de Pablo, 1999, 2000), which is an extended version of the parallel tempering method (Frenkel and Smit, 2002), several replicas of the same system are considered in parallel in to circumvent the difficulty to form/dissociate methane hydrate (large free energy barrier between the liquid and solid states). Each of the $M = 16$ replicas consists of a mixture of water and methane molecules at a given set of temperature/chemical potentials (T, μ_w, μ_m). For each replica, conventional GCMC moves are performed: molecule translation, rotation, deletion and insertion. Moreover, trial swap moves between configuration α (energy U^α, N_w^α water molecules and N_m^α methane molecules) in replica (1) and configuration β (energy U^β, N_w^β water molecules and N_m^β methane molecules) in replica (2) are attempted. The swap move is accepted or rejected according to the following Metropolis probability:

$$\begin{aligned} P_{acc}\left(\alpha_1,\beta_2 \rightarrow \alpha_2,\beta_1\right) = \min \Bigg\{ & 1, \left(\frac{T_2}{T_1}\right)^{3(N_m^\beta+N_w^\beta-N_m^\alpha-N_m^\alpha)/2} \\ & \exp\left[\left(\frac{1}{k_B T_2}-\frac{1}{k_B T_1}\right)\left(U^\beta-U^\alpha\right)\right] \\ & \prod_{i=m,w} \exp\left[\left(\frac{\mu_i^1}{k_B T_1}-\frac{\mu_i^2}{k_B T_2}\right)\left(N_i^\beta-N_i^\alpha\right)\right]\Bigg\} \end{aligned} \tag{3.21}$$

In this work, the different replicas were considered at temperatures and chemical potentials corresponding to a pressure $P = 100$ atm. The temperature of the different replicas ranges from 283 to 298 K with a temperature difference between two successive replicas of $\Delta T = 1$ K. In theory, hyper parallel tempering should provide a rigorous description of methane hydrate formation/dissociation as a function of temperature provided that both configurations corresponding to the liquid phase and the methane hydrate phase are considered in the initial replicas; for long enough simulations, swapping between the liquid and solid phases at different temperatures should lead to an accurate estimate of the phase transition temperature T_m with liquid configurations for $T > T_m$ and methane hydrate configurations for $T < T_m$. However, in practice, very low swapping probabilities were observed between liquid and methane hydrate configurations due to the large differences in water and methane molecule numbers in these two states (as can be seen in the acceptance probability in the equation above, the difference in the number of molecules is an important parameter). In this work, we found that this issue can be overcome by considering in the initial replicas composite configurations corresponding to mixtures of the liquid and hydrate phases (in the spirit of the mixture considered as the initial configuration for the direct coexistence method). As shown in Figure 3.9(a), in addition to pure liquid and hydrate configurations, several configurations corresponding to methane hydrate regions coexisting with the liquid phase were considered (these mixtures correspond to different hydrate volume fractions ranging from 0.25 to 0.75). The total number of methane and water molecules in each replica is of the order of $\sim 10^2 - 10^3$. Equilibration was reached after 9×10^8 Monte Carlo steps and water and methane mole fractions were averaged over another 1×10^8 Monte Carlo steps.

Figure 3.9(b) shows the methane x_m and water x_w mole fractions as a function of temperature T once equilibrium has been reached. The sharp decrease (increase) at $T_m = 289.5$ K in x_m (x_w) indicates melting of the methane hydrate. Such a transition temperature for $P = 100$ atm is consistent with the values obtained using free energy calculations and the direct coexistence method. These results show that such a hyper parallel tempering technique improves the sampling of phase space and allows determining accurately the melting temperature of complex, non stoichiometric systems such as methane hydrates (by preventing the system from being ‘trapped’ in local metastable states).

3.4 Conclusion

Using different molecular simulation strategies, the pressure–temperature phase diagram for bulk methane hydrate is determined. For two different water models, in this chapter,

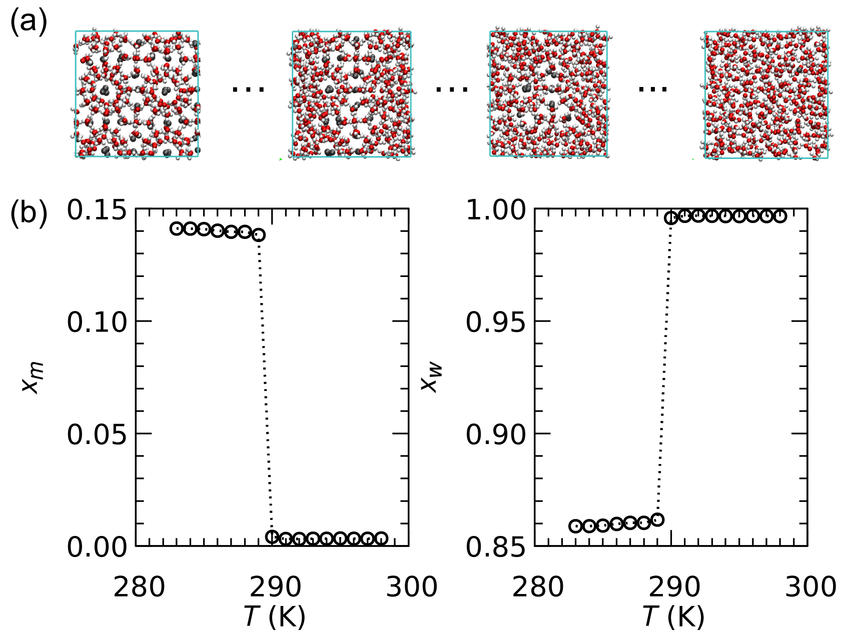

Figure 3.9 (color online) Determination of the phase transition temperature between the methane hydrate and liquid phases using hyper parallel tempering Monte Carlo simulations. (a) Several replicas M = 16 of the system are considered in parallel. Each replica is at different temperatures and chemical potentials (the latter are chosen so that the pressure of the system is P = 100 atm). The temperature ranges from 283 K to 298 K with a temperature difference $\Delta T = 1$ K. For each replica, a regular grand canonical Monte Carlo simulation consisting of molecule translation, rotation, insertion, and deletion moves are performed. In addition to these conventional moves, replicas at two different temperature/chemical potentials sets are swapped with a probability given from the ratio of the Boltzmann factors in the Grand Canonical ensemble (*see text*). The red and white spheres are the oxygen and hydrogen atoms of water while the grey spheres are the methane molecules. The dimensions of the simulation box are: $L_x = L_y = L_x = 2.754$ nm. (b) Average methane (left) and water (right) mole fraction as a function of temperature as estimated from the different replicas considered in the hyper parallel tempering simulation.

we first determined the liquid–hydrate–vapor phase coexistence using rigorous free energy calculations based on the Einstein molecule approach. The data presented in the present work, which are consistent with previous molecular simulation works, shows that the different thermodynamic approximations such as the description of methane vapor are important. Overall, in agreement with previous studies, it is shown that the choice of the water model is a key problem and that TIP4P/Ice, which was specifically developed to reproduce crystalline phases of water, reproduces accurately the experimental phase diagram of methane hydrate.

While free energy techniques are obviously robust strategies to estimate the phase diagram of such complex, non stoichiometric compounds, we also considered two direct molecular simulations approaches. First, we extended the direct coexistence method to treat both methane and water in the Grand Canonical ensemble; this is an important aspect as it allows taking into account large fluctuations in the number of methane and water molecules upon hydrate dissociation/formation. This allows considering calculations with the direct coexistence method using system sizes that remains small (otherwise, large methane regions in the system have to be considered to act as methane molecules source/sink upon melting/crystallization of the hydrate). In addition to the direct coexistence method extended to the grand canonical ensemble, we also considered hyper parallel tempering which consists of considering several replicas of the system at different temperatures and chemical potentials – the system being therefore treated in the grand canonical ensemble to allow for large changes in its composition upon hydrate formation/dissociation.

Despite the reduced accuracy/robustness compared to more rigorous approaches based on free energy techniques, both the direct coexistence method and hyper parallel tempering technique were found to lead to reasonable predictions for phase coexistence. However, while the results reported in this work shows that these two direct techniques can be used to estimate stability conditions for methane hydrate, we emphasizes that several refinements and "tricks" were needed to lead to sufficient sampling of the phase space and accurate phase coexistence predictions. First, as mentioned above, both the direct coexistence and hyper parallel techniques were used with water and methane treated in the Grand Canonical ensemble; we found that this was needed to efficiently sample large molecule number fluctuations upon hydrate formation/dissociation. Moreover, in the case of hyper parallel tempering, we also found that the initial replicas (i.e. at different temperatures and chemical potentials) must include composite systems where both the hydrate and liquid phases coexist. Such coexisting states allow sufficient swapping along the hyper parallel tempering simulation between the low and high temperature replicas. Otherwise, considering the Metropolis acceptance probability in this hyper grand canonical ensemble given in Eq. (3.21), the large difference in the numbers of water and methane molecules between the liquid and hydrate phases lead to very low swapping probabilities (too low to allow efficient sampling). As a result, while our data show that accurate hydrate stability conditions can be estimated in principle using hyper parallel tempering, the latter drawback constitutes an important limitation to this technique. Finally, in addition to being more robust than the direct coexistence and hyper parallel tempering methods, free energy calculations provide accurate estimates for the chemical potentials for water and methane in the hydrate phase, including their values at phase coexistence (in contrast, with the two direct techniques, one has to estimate in an approximate fashion the chemical potentials that lead to phase equilibrium). This is a key asset of the free energy technique over direct methods since such chemical potentials at phase coexistence will be used in subsequent work on the stability of methane hydrate confined in porous media (which are in equilibrium with an external methane and water mixture or hydrate imposing its chemical potentials at constant temperature).

Chapter 4

Formation and Dissociation of Confined Methane Hydrate

Contents

4.1 Computational details 95

4.1.1 Molecular models 95

4.1.2 Surface tensions 96

4.1.3 Umbrella sampling 98

4.2 Formation and dissociation of confined methane hydrate 100

4.2.1 Phase stability of confined methane hydrate 100

4.2.2 Gibbs-Thomson equation 104

4.2.3 Free energy calculations and kinetics 112

4.3 Conclusion 115

This chapter aims at exploring the phase stability and formation/dissociation kinetics of methane hydrate confined at the nanoscale. First, the direct coexistence method (DCM) within the framework of Grand Canonical Monte Carlo (GCMC) simulations is used to assess liquid–hydrate–vapor (L–H–V) phase equilibrium of sI methane hydrate confined in a porous solid with different pore widths. Then, the Gibbs-Thomson equation is derived to describe the shift in the phase stability of the confined methane hydrate. In this work, an extended formula of the Gibbs-Thomson equation which relaxes the two following important hypotheses, is redrived: (1) the molar volumes of methane hydrate (v_H) and liquid water (v_L) are equal, i.e., $v_\mathrm{L} = v_\mathrm{H}$ ($v = 1/\rho$ where ρ is number density) and (2) Young's equation is used to estimate the surface tension between methane hydrate and liquid water (γ_{LH}), $\gamma_{LS} - \gamma_{HS} = \gamma_{LH} \cos\theta$ where γ_{HS} is the surface tension between methane hydrate and the substrate surface and γ_{LS} is the surface tension between liquid water and the substrate surface. Moreover, a contact angle $\theta \sim 180^\circ$ is used in the Gibbs-Thomson equation. These hypotheses are crude assumptions to assess the validity of the Gibbs-Thomson equation. First, the difference between the molar volumes of methane hydrate and liquid water is not small. Second, the validity of Young's equation is unclear for a small pore. Our work does not rely on these hypotheses. To assess the validity of the Gibbs-Thomson equation, we compute the hydrate–solid γ_{HS} and liquid–solid γ_{LS} surface tensions (here, "solid" refers to the pore walls), the molar volume of bulk (i.e., non-confined) methane hydrate and liquid water, and the molar enthaply of melting Δh_m from methane hydrate to liquid water using molecular dynamics (MD). Our findings show that confinement at the nanoscale level has a negative effect on the L–H–V phase equilibrium (i.e., phase equilibrium is shifted towards lower temperature). The shift in the phase coexistence temperature relative to the bulk, $\Delta T_m/T_m$, is found to linearly depend on the reciprocal pore size $1/D_p$. Our molecular simulations results from the DCM technique are found to be in quantitative agreement with the derived Gibbs-Thomson equation. In addition, the effects of the surface wettablity on the L–H–V phase equilibrium is studied by modifying the LJ parameters (i.e., tuning the wetting properties of the porous medium). Finally, free energy calculations using the umbrella sampling technique is used to show that confinement decreases the free energy barrier, ΔG_{HL}, between methane hydrate and liquid water.

The remainder of this chapter is organized as follows. In Section 4.1, we present the computational details: molecular model of porous solid, determination of the solid-liquid and solid-hydrate surface tensions, and free energy calculations using the umbrella sampling technique. In Section 4.2, the phase stability of confined methane hydrate at a given pressure ($P = 100$ atm) is first presented using the direct coexistence method (DCM) (see Section 4.2.1). Then, we derive the Gibbs-Thomson equation to describe L–H–V phase equilibrium in confinement (see Section 4.2.2). In this part, we also present the effects of surface wettability on the phase stability of confined methane hydrate. In addition, free energy calculations using the umbrella sampling technique are performed to determine the formation/dissociation kinetics of bulk and confined methane hydrate (see Section 4.2.3). All results are compared with previous experimental data as well as data obtained in previous theoretical works. Section 4.3 presents some concluding remarks.

4.1 Computational details

4.1.1 Molecular models

Porous solid. To study confinement effects, we consider phase coexistence between methane hydrate and liquid water located between two parallel solid walls as shown in Figure 4.1. We use here a hypothetical model for porous solids. The dimensions of the system in the x– and y–directions are $L_x = L_y = 2.3754$ nm (corresponding to 2×2 unit cells of methane hydrate with the size of each unit cell being u = 1.1877 nm). This x–y–plane (i.e., $L_x = L_y = 2.3754$ nm) is partitioned into 11×11 small squares, and solid atoms are located at the vertex and center of these small squares so that a total number of 242 solid atoms are present in one solid layer. The distance separating solid atom pairs is 0.1527 nm which is close to the typical chemical C–C bond length, $\sim$0.142 nm, in most porous carbonaceous materials. We use two solid walls: one at the top and one at the bottom to form a slit pore. Each pore wall consists of four layers defined above with an interlayer distance $D_l = 0.216$ nm. In this work, we consider pores with the following widths $D_p = 1.6677$ nm, 2.8554 nm, 5.2308 nm, and 7.6062 nm. The direct coexistence method is used to determine the melting temperature as a function of D_p at a given pressure. For the determination of the surface tensions between methane hydrate and the solid wall, γ_{HS}, and between liquid water and the solid wall, γ_{LS}, the pore with $D_p = 9.9816$ nm is used. The final dimensions are $L_x = L_y = 2.3754$ nm, and $L_z = 3.1793$ nm, 4.3670 nm, 6.7424 nm, 9.1178 nm, and 11.4936 nm (corresponding to $D_p = 1.6677$ nm, 2.8554 nm, 5.2308 nm, 7.6062 nm, and 9.9816 nm, respectively). These exact values were used because they correspond to the multiple integer of the unit cell (u = 1.1877 nm) of bulk methane hydrate. All the solid atoms are maintained frozen and all the interactions between solid atom pairs are excluded in all our molecular simulations.

4.1.2 Surface tensions

The surface tension between a phase α (e.g., methane hydrate or liquid water in this work) and a phase β (e.g., porous solid in this work), $\gamma_{\alpha\beta}$, can be determined using the Kirkwood and Buff approach (Kirkwood and Buff, 1949). Figure 4.2 shows the scheme used in this approach to determine $\gamma_{\alpha\beta}$. For a molecular system with a planar interface (perpendicular to the z axis) between phases α and β, a small increase dA in the surface area A in the x–y–plane leads to a small decrease dz in the size L_z if we maintain the volume L_zA constant, i.e., $L_z dA = -(A+dA)dz$. The surface tension $\gamma_{\alpha\beta}$ is defined as,

$$\gamma_{\alpha\beta} = \frac{1}{2}\int_0^{L_z} \left(P_N(z) - P_T^*(z)\right) dz = \frac{L_z}{2}\left(\langle P_N\rangle - \langle P_T^*\rangle\right) \tag{4.1}$$

where the factor 1/2 is due to the fact that there are two interfaces between phase α and phase β. $P_N(z) = P_{zz}(z)$ and $P_T(z) = \frac{1}{2}\left(P_{xx}(z) + P_{yy}(z)\right)$ are the pressure components normal and parallel to the interface. The meaning of the asterisk will be discussed below.

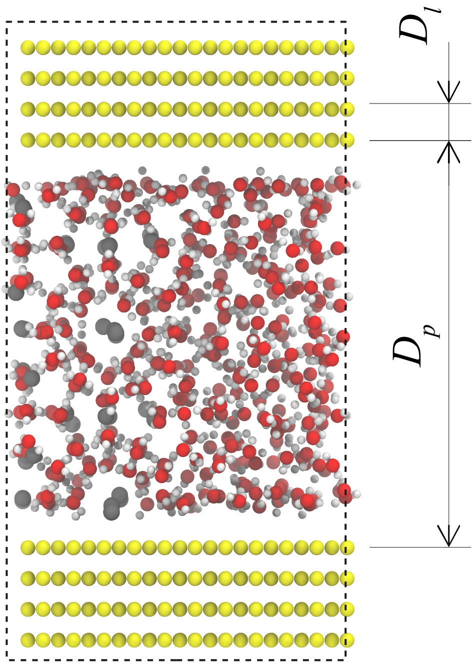

Figure 4.1 (color online) Molecular configuration of the confined coexisting phases (i.e., methane hydrate + liquid water) considered in this work. The red and white spheres are the oxygen and hydrogen atoms of water, respectively. The gray spheres are the methane molecules which are inside the hydrogen-bonded cages formed by water molecules. The yellow spheres are the solid atoms in the pore walls. The two component system is confined in a pore with a width D_p made of layers of solid particles distributed according to a square structure. Each pore surface is made of 4 layers separated by a distance $D_l = 0.2159$ nm so that the total pore wall thickness is 0.7558 nm. Inside the porosity, methane hydrate is located in the region $y < 0$ (left side) and liquid water in the region $y > 0$ (right side). In this specific configuration, the pore size is $D_p = 2.8554$ nm which corresponds to $2 \times 2 \times 2$ unit cells of bulk sI methane hydrate (the lattice parameter of methane hydrate is u = 1.1877 nm). Periodic boundary conditions are used along the x, y, and z directions. The dimensions of the simulation box (defined by the dashed lines) are $L_x = L_y = 2.3754$ nm and $L_z = 4.3670$ nm.

$P_{dd}(z)$ with $d = x$, y or z are the diagonal elements of the pressure tensor at a position z. $\langle P_N \rangle$ and $\langle P_T \rangle$ in the above equation are macroscopic components of the pressure tensor defined in terms of a volume average. According to the work by Nijmeijer et al. (Nijmeijer et al., 1990), for an interface involving a frozen solid phase, we include interactions with the frozen solid atoms when computing $\langle P_N \rangle = \langle P_{zz} \rangle$ but we do not include such interactions in the calculation of $\langle P_T^* \rangle = \left(\langle P_{xx} \rangle + \langle P_{yy} \rangle \right) /2$. The asterisk in $\langle P_T^* \rangle$ indicates that such interactions are omitted. In case of fluid-fluid interfaces, such interactions must be included.

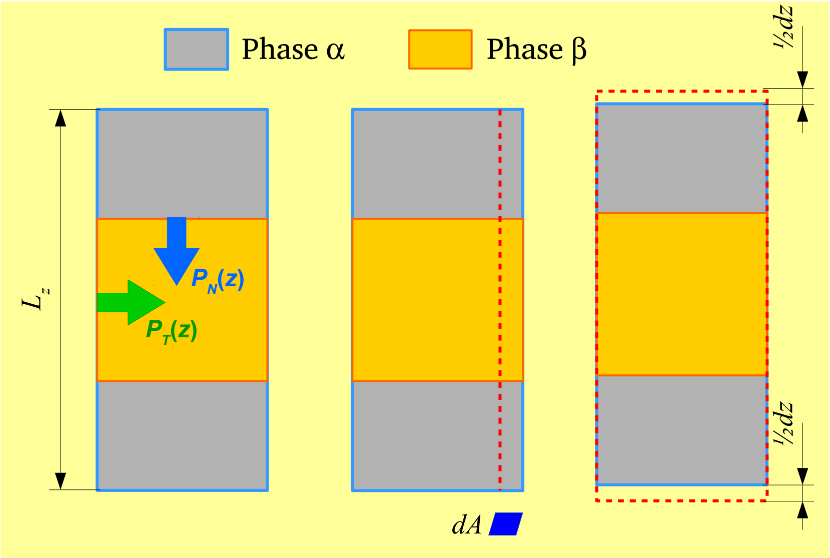

Figure 4.2 (color online) Schematic illustration of the determination of the surface tension using the Kirkwood-Buff approach. (1) The configuration of phases α (orange region) and β (gray region) is prepared. These two phases define two planar α–β–interfaces perpendicular to the z axis (*left*): the surface area in the x–y–plane is A and the length of the simulation box in the z–direction is L_z. The normal and parallel pressure components are $P_T(z) = (P_{xx}(z) + P_{yy}(z))/2$ and $P_N(z) = P_{zz}(z)$. (2) A small change dA is considered in the surface area the in x–y–plane. (3) The change is compensated by a small change dz to keep the volume V constant, i.e., $L_z dA = -(A + dA)dz$.

4.1.3 Umbrella sampling

In order to obtain the free energy barrier between methane hydrate and liquid water, ΔG_{barr}, we used the umbrella sampling technique to determine the free energy G as a function of the local bond order parameter Q_6. Both bulk and confined systems were considered ($D_p = 2.8554$ nm was considered for the latter). The umbrella sampling technique is a robust method in molecular simulation to study the thermodynamics of rare events. As mentioned in Chapter 1, the local bond order parameter Q_6, which is found to be a suitable order parameter to identify liquid water and methane hydrate (Nguyen and Molinero, 2015; Radhakrishnan and Trout, 2002; Steinhardt et al., 1983), is defined for a given oxygen atom O_i as follows:

$$Q_6(i) = \left(\frac{4\pi}{13} \sum_{m=-6}^{6} | Q_{6m}(i) |^2 \right)^{1/2} \tag{4.2}$$

where $m \in [-6,6]$ and $Q_{6m}(i)$ is a set of complex vectors:

$$Q_{6m}(i) = \frac{1}{N_b(i)} \sum_{j=1}^{N_b(i)} Y_{6m}(\mathbf{r}_{ij}) \tag{4.3}$$

The summation from $j = 1$ to $N_b(i)$ in Eq. (4.3) runs over all the nearest neighbor oxygen atoms $N_b(i)$ for O_i. $Y_{lm}(\mathbf{r}_{ij})$ are the spherical harmonics which depend on the position vector $\mathbf{r}_{ij}$.

In the umbrella sampling technique, considering methane hydrate as the initial configuration, we force it to transform into liquid water by using a biasing potential, $w(Q_6)$, that depends on Q_6. By determining the probability distribution, $P^B(Q_6)$, of Q_6 in such biased simulations, the unbiased free energy profile, $G(Q_6)$, can be obtained by subtracting the biasing potential contribution, $w(Q_6)$, from the biased free energy profile, $G^B(Q_6) = -k_BT \ln\left(P^B(Q_6)\right)$,

$$G(Q_6)/k_BT = -\ln\left(P^B(Q_6)\right) - w(Q_6)/k_BT \tag{4.4}$$

where k_BT is the thermal energy. To sample the entire domain of Q_6 (0.300–0.6), we run $N_{windows} = 61$ windows with a spacing of 0.05 (i.e., $N_{windows}$ GCMC simulations with different references $Q_{6,i}^{(0)}$). In practice, this means that for the i–th window, we use the following biasing harmonic potential $w_i(Q_6)$,

$$w_i(Q_6) = \frac{1}{2}K\left(Q_6 - Q_{6,i}^{(0)}\right)^2 \tag{4.5}$$

where $K = 5 \times 10^7$ K is the force constant and $Q_{6,i}^{(0)}$ is the center of the biasing harmonic potential for the i–th window. We use the weighted average of the unbiased probabilities of each window P_i^U to determine the full unbiased probability distribution P^U,

$$P^U(Q) = \sum_{i}^{N_{windows}} N_i P_i^U(Q_6) \exp\left[-\left(w_i(Q_6) - G_i\right)/k_BT\right] \tag{4.6}$$

where P_i^U is the unbiased probability, N_i is the number of samples, and G_i is the unbiased free energy,

$$\exp\left(-G_i/k_BT\right) = \int dQ_6 P^U\left(Q_6\right)\exp\left(-w_i(Q_6)/k_BT\right) \tag{4.7}$$

By starting from Eq. (4.6) with $G_i = 0$, we iterate between Eqs. (4.7) and (4.6) until a convergence tolerance of 10^{-3} is reached in a self-consistent manner for G_i/k_BT. In this work, the probability distributions were analyzed using the *weighted histogram analysis method* (*WHAM*) to solve Eqs. (4.7) and (4.6) in a self-consistent manner.

4.2 Formation and dissociation of confined methane hydrate

4.2.1 Phase stability of confined methane hydrate

Using the direct coexistence method (DCM), we reproduced the phase diagram of bulk methane hydrate as discussed in Chapter 3. In the present chapter, we apply the DCM technique in the framework of GCMC simulations to study the effect of confinement on L–H–V phase equilibrium at a given pressure. As described previously, the initial configuration in DCM is chosen as a coexisting phase consisting of liquid water and methane hydrate confined between two parallel solid walls. The use of the Grand Canonical ensemble ensures that three-phase (L–H–V) coexistence in the porous solid is simulated in fact; because the system is in equilibrium with an infinite reservoir of bulk molecules at chemical potentials corresponding to those of the water-rich liquid and methane-rich vapor, DCM simulations in this specific ensemble are equivalent to simulating a system with three–phase coexistence. The melting temperature, T_m^{pore}, of confined methane hydrate in four different pore widths are determined: $D_p = 1.6677$ nm, 2.8554 nm, 5.2308 nm, and 7.6062 nm. The preparation of these initial configurations are described in the previous section. In all these simulations, periodic boundary conditions were applied in each direction to avoid finite size effects.

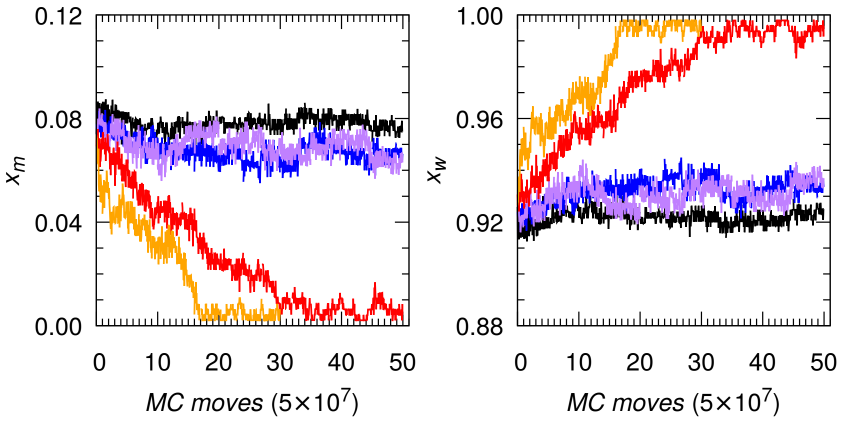

Figure 4.3 (color online) Pore size, D_p, effect on the melting temperature, T_m^{pore}, of confined methane hydrate/liquid water using the direct coexistence method: methane (x_m, *left*), and water (x_w, *right*) mole fractions for $D_p = 2.8554$ nm during the different GCMC simulation runs at T = 230 K (black), 240 K (blue), 250 K (purple), 260 K (red), and 270 K (orange). The x-axis, which indicates progress along the GCMC simulation, is expressed as a number of attempted MC moves where one move is a molecule translation, rotation, insertion or deletion.

In practice, for each pore size, we performed $M = 18$ simulations at $P = 100$ atm with temperatures in the range $T = 180$–350 K (the temperature interval is 10 K). Our DCM simulations in the Grand Canonical ensemble at given pressure and temperature require to specify chemical potentials for water μ_w and methane μ_m. μ_w and μ_m obtained in Chapter 3 were used for this purpose. Figure 4.3 shows the methane x_m and water x_w mole fractions of the coexisting system confined in the nanoporous solid with $D_p = 2.8554$ nm in the course of GCMC simulations (i.e., the number of MC moves performed with one MC move corresponding to a molecule translation, rotation, insertion or creation). Results for different temperatures are shown: T = 230 K, 240 K, 250 K, 260 K, and 270 K. On the one hand, at high temperature, $T \geq 260$ K, the system melts as evidenced by the decrease in the methane mole fraction x_m. As expected, $x_m \sim 0$ ($x_w \sim 1$) in the liquid phase. On the other hand, at low temperature, $T \leq 250$ K, the methane mole fraction increases (while x_w decreases) upon methane hydrate formation. While melting does not suffer from ambiguity since all methane hydrate is transformed into liquid water, hydrate formation was found to be inefficient; due to the low probability to nucleate hydrate cages (inherent to their very small entropy), it was observed that formation of the hydrate is incomplete. Such slow transformation kinetics will be illustrated in a following section Using free energy calculations with the umbrella sampling technique. As a result, despite the coexistence with an already formed hydrate, many GCMC runs (about the order of $\sim 10^5 - 10^6$ MC moves per molecule) were not sufficient to lead to perfect methane hydrates. Despite this drawback, the DCM technique above shows that the L–H–V equilibrium temperature for hydrate/liquid coexistence is $T_m^{pore} = 255 \pm 5$ K for $D_p = 2.8554$ nm. In constrast, $T_m^{bulk} = 285 \pm 5$ K at the same pressure $P = 100$ atm (see Chapter 3). The shift in the coexistence temperature is therefore $\Delta T_m^{pore} = T_m^{pore} - T_m^{bulk} \sim -30$ K for $D_p = 2.8554$ nm, indicating that confinement in such porous solids tends to lower the coexistence temperature. As will be further discussed in the next section, this is consistent with the Gibbs-Thomson equation with a lower hydrate-substrate surface tension than the liquid-substrate surface tension. For the three other pore sizes $D_p = 1.6677$ nm, 5.2308 nm, and 7.6062 nm, the methane x_m and water x_w mole fractions confined in the porous solids in the course of GCMC simulations are shown in Figure 4.4. These GCMC simulations lead to $T_m^{pore} = 235 \pm 5$ K for $D_p = 1.6677$ nm, $T_m^{pore} = 265 \pm 5$ K for $D_p = 5.2308$ nm, and $T_m^{pore} = 275 \pm 5$ K for $D_p = 7.6062$ nm. These data are summarized in Table 4.1.

Table 4.1 Determination of melting temperature T_m of bulk and confined methane hydrate at pressure P using the direct coexistence method. L_x and L_y are the dimensions of the molecular system in the x– and y–directions, respectively. D_p is the pore size. * is for the melting temperature of bulk methane hydrate, T_m^{bulk}, as reported in Chapter 3.

P (atm)	L_x (nm)	L_y (nm)	$L_z (nm)$	D_p (nm)	T_m (K)
100	2.3754	2.3754	2.3754	∞	285±5*
100	2.3754	2.3754	9.1178	7.6062	275±5
100	2.3754	2.3754	6.7424	5.2308	265±5
100	2.3754	2.3754	4.3670	2.8554	255±5
100	2.3754	2.3754	3.1793	1.6677	235±5
100	2.3754	4.7508	6.7424	5.2308	285±5
100	2.3754	4.7508	4.3670	2.8554	265±5
10	2.3754	2.3754	2.3754	∞	265±5
10	2.3754	2.3754	4.3670	2.8554	225±5

Finite size effects from (1) the vacuum layer and (2) the molecular system size were also considered in the present work. A vacuum layer (with a size of D_v) is usually used on each side of the porous solid to remove the interactions with the periodic images in the z–direction. In this work, two different sizes $D_v = 0.0000$ nm and 2.0000 nm were

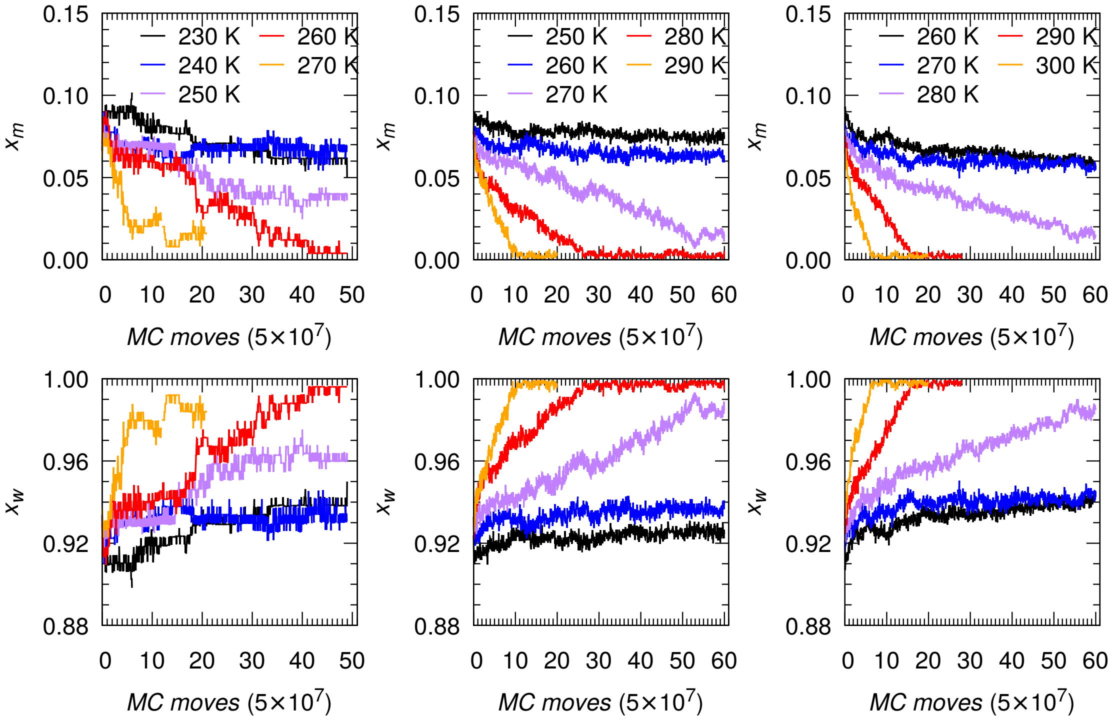

Figure 4.4 (color online) Melting temperature, T_m^{pore}, of confined methane hydrate/liquid water for different pore widths: $D_p = 1.6677$ nm (*left panels*), 5.2308 nm (*center panels*), and 7.6062 nm (*right panels*) as obtained using the direct coexistence method. The methane (x_m, *top panels*) and water (x_w, *bottom panels*) mole fractions during the different GCMC simulation runs are shown: T for each pore size is indicated using different colors (see figure legend). The x-axis, which indicates progress along the GCMC simulation, is expressed as a number of attempted MC moves where one move is a molecule translation, rotation, insertion or deletion. T_m^{pore} of confined methane hydrate for different D_p are summarized in Table 4.1. For bulk methane hydrate, we reported $T_m^{bulk} = 285 \pm 5$ K at $P = 100$ atm using the direct coexistence method in Chapter 3.

considered for $D_p = 2.8554$ nm. At $P = 100$ atm, we obtained $T_m^{pore} = 255 \pm 5$ K for both sizes (the data of $D_v = 0.0000$ nm are shown in Figure 4.3 while the data for $D_v = 2.0000$ nm are shown in Figure B.1 of the Appendix B). The fact that we obtain the same melting temperature indicates a negligible influence of the vacuum layer on T_m^{pore}. Molecular systems with a bigger dimension in the y–axis $L_y = 4.7508$ nm (while keeping L_x and L_z identical) were considered for the pores $D_p = 2.8554$ nm and 5.2308 nm. The calculations performed using the DCM technique lead to $T_m^{pore} = 265 \pm 5$ K for $D_p = 2.8554$ nm and $T_m^{pore} = 285 \pm 5$ K for $D_p = 5.2308$ nm as shown in Figure B.2 of the Appendix B. By comparing with the melting temperature obtained using the small systems (see Figures 4.3 and 4.4), the finite size effect on melting temperature is 10 K for each pore size. However, with respect to bulk methane hydrate, the shifts in the melting temperature of confined system were found to be consistent between the big and small systems (as shown in Figure B.3 of the Appendix B).

4.2.2 Gibbs-Thomson equation

To describe the confinement effect on the melting point T_m^{pore}, we revisited the Gibbs-Thomson equation. To relax the two following hypotheses: (1) the molar volumes in methane hydrate and liquid water are equal $v^{\mathrm{L}} = v^{\mathrm{H}}$ and (2) Young's equation is used to compute the surface tension difference $\gamma_{LS} - \gamma_{HS} = \gamma_{LH} \cos\theta$ where γ_{LS}, γ_{HS}, and γ_{LH} are the surface tensions of the liquid water-substrate interface, the methane hydrate-substrate interface, and liquid water-methane hydrate interface. In this work, we did not rely on these hypotheses.

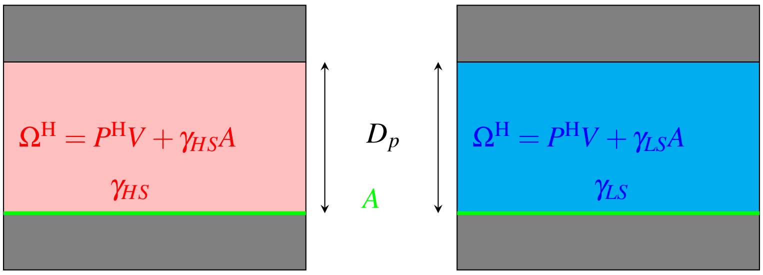
$\Omega^{\mathrm{H}} = P^{\mathrm{H}}V + \gamma_{HS}A$
γ_{HS}
D_p
A
$\Omega^{\mathrm{H}} = P^{\mathrm{H}}V + \gamma_{LS}A$
γ_{LS}

Figure 4.5 (color online) Gibbs-Thomson equation for L–H–V equilibrium upon confinement: methane hydrate (H, red region) and liquid water (L, blue region) are confined in a slit pore of a width D_p formed by two parallel substrates (S, the gray regions). Ω^{H} and P^{H} are the grand potential and pressure of methane hydrate while Ω^{L} and P^{L} are the grand potential and pressure of liquid water. γ_{LS} is the surface tension of liquid water–substrate (LS) interface while γ_{HS} is the surface tension of methane hydrate–substrate (HS) interface. $V = D_pA$ is the pore volume where A is the surface area.

As shown in Figure 4.5, methane hydrate (H, *left*) and liquid water with methane molecules solubilized (L, *right*) considered to derive the Gibbs-Thomson equation are confined in a slit pore of a width D_p. These two confined systems within the volume V ($V = D_pA$) are in equilibrium with the reservoir which imposes the chemical potential of water μ_w, the chemical potential of methane μ_m, and temperature T. The grand potentials for confined methane hydrate Ω^{H} and confined liquid water Ω^{L} are defined as,

$$\begin{aligned} \Omega^{\mathrm{H}} &\hat{=} - P^{\mathrm{H}}V + \gamma_{HS}A \\ \Omega^{\mathrm{L}} &\hat{=} - P^{\mathrm{L}}V + \gamma_{LS}A \end{aligned} \tag{4.8}$$

where P^{H} is the pressure of methane hydrate while P^{L} is the pressure of liquid water. γ_{LS} is the surface tension of liquid water–substrate (LS) interface while γ_{HS} is the surface tension of methane hydrate–substrate (HS) interface. $V = D_pA$ is the pore volume where A is the surface area. At L–H–V equilibrium,[1] we have,

$$\Omega^{\mathrm{L}} = \Omega^{\mathrm{H}} \tag{4.9}$$

In details,

$$-P^{\mathrm{H}}V + 2\gamma_{HS}A = -P^{\mathrm{L}}V + 2\gamma_{LS}A \tag{4.10}$$

Using $V = D_pA$, we obtain the Laplace equation:

$$P^{\mathrm{L}} - P^{\mathrm{H}} = 2\left(\gamma_{LS} - \gamma_{HS}\right)\frac{1}{D_p} \tag{4.11}$$

We assume that: (a) the confined liquid water at a pressure P^{L} has the same properties as the bulk liquid water; and (b) the confined methane hydrate at a pressure P^{H} has the same properties as the bulk methane hydrate. To determine the pressures P^{H} and P^{L} at (μ_w, μ_m, T), we use a first-order Taylor expansion of the pressure P around a reference point ($\mu_{w,0}$, $\mu_{m,0}$, T_0):

$$\begin{aligned} P &\sim P_0 + (T - T_0)\left(\frac{\partial P}{\partial T}\right)_{\mu_{w,0},\mu_{m,0}} + \sum_{i=m,w}\left(\mu_i - \mu_{i,0}\right)\left(\frac{\partial P}{\partial \mu_i}\right)_T \\ &\sim P_0 + (T - T_0)\frac{s_0}{v_0} + \sum_{i=m,w}\left(\mu_i - \mu_{i,0}\right)\frac{n_{i,0}}{v_0} \end{aligned} \tag{4.12}$$

---

[1] The derivation of the grand potential reads: $d\Omega = -SdT - PdV - Nd\mu + \gamma dA$. At constant T, V, μ, and A, $d\Omega = 0$.

where $P = P(\mu_w, \mu_m, T)$ and $P_0 = P(\mu_{w,0}, \mu_{m,0}, T_0)$ is the pressure at the reference point ($\mu_{w,0}$, $\mu_{m,0}$, T_0). $s_0/v_0 = (\partial P/\partial T)_{\mu_{w,0},\mu_{m,0},T_0}$ is the molar entropy s_0 (note that s is the total entropy which includes both methane and water contributions) devided by the molar volume v_0 at ($\mu_{w,0}$, $\mu_{m,0}$, T_0). $n_{i,0}/v_0 = (\partial P/\partial \mu_i)_{T_0}$ is the number $n_{i,0}$ of molecules of type i ($i = m, w$) devided by the molar volume v_0 at ($\mu_{w,0}$, $\mu_{m,0}$, T_0). Using Eq. (4.12), we have for P^{H} and P^{L}:

$$\begin{aligned} P^{\mathrm{H}} &= P_0^{\mathrm{H}} + (T - T_0)\frac{s_0^{\mathrm{H}}}{v_0^{\mathrm{H}}} + \sum_{i=m,w}\left(\mu_i^{\mathrm{H}} - \mu_{i,0}^{\mathrm{H}}\right)\frac{n_{i,0}^{\mathrm{H}}}{v_0^{\mathrm{H}}} \\ P^{\mathrm{L}} &= P_0^{\mathrm{L}} + (T - T_0)\frac{s_0^{\mathrm{L}}}{v_0^{\mathrm{L}}} + \sum_{i=m,w}\left(\mu_i^{\mathrm{L}} - \mu_{i,0}^{\mathrm{L}}\right)\frac{n_{i,0}^{\mathrm{L}}}{v_0^{\mathrm{L}}} \end{aligned} \tag{4.13}$$

We select the melting point (T_m^{bulk}, P_0) of bulk methane hydrate as the reference point: ($\mu_{m,0}^{\mathrm{H}} = \mu_{m,0}^{\mathrm{L}} = \mu_{m,0}$, $\mu_{w,0}^{\mathrm{H}} = \mu_{w,0}^{\mathrm{L}} = \mu_{w,0}$, $T_0 = T_m^{bulk}$, $P_0^{\mathrm{H}} = P_0^{\mathrm{L}} = P_0$) where $\mu_{i,0}^{\Phi}$ is the chemical potential of species i in phases Φ ($\Phi = \mathrm{H}$ for hydrate and L for liquid) at (T_m^{bulk}, P_0). Using Eq. (4.13), we determine the pressures P^{H} and P^{L} at T_m^{pore}:

$$\begin{aligned} P^{\mathrm{H}} &= P_0 + \frac{1}{v_0^{\mathrm{H}}}\left(\Delta T_m^{pore} s_0^{\mathrm{H}} + \sum_{i=m,w}\Delta\mu_i^{\mathrm{H}} n_{i,0}^{\mathrm{H}}\right) \\ P^{\mathrm{L}} &= P_0 + \frac{1}{v_0^{\mathrm{L}}}\left(\Delta T_m^{pore} s_0^{\mathrm{L}} + \sum_{i=m,w}\Delta\mu_i^{\mathrm{L}} n_{i,0}^{\mathrm{L}}\right) \end{aligned} \tag{4.14}$$

where $\Delta T_m^{pore} = T_m^{pore} - T_m^{bulk}$ is the shift of the melting point T_m^{pore} of confined methane hydrate with respect to the melting point T_m^{bulk} of bulk methane hydrate. $\Delta\mu_i^{\Phi} = \mu_i^{\Phi} - \mu_{i,0}^{\Phi}$ is the difference of chemical potential of species i at T_m^{pore} and T_m^{bulk} for phases Φ. We can replace $\Delta\mu_i^{\Phi}$ by $\Delta\mu_i$ because that $\mu_i^{\mathrm{H}} = \mu_i^{\mathrm{L}} = \mu_i$ at T_m^{pore} and $\mu_{i,0}^{\mathrm{H}} = \mu_{i,0}^{\mathrm{L}} = \mu_{i,0}$ at T_m^{bulk}. Using Eqs. (4.14), we estimate the pressure difference:

$$\begin{aligned} v_0^{\mathrm{H}}\left(P^{\mathrm{H}} - P_0\right) - v_0^{\mathrm{L}}\left(P^{\mathrm{L}} - P_0\right) &= -\Delta T_m^{pore}\Delta s_{m,0} + \sum_{i=m,w}\Delta\mu_i\left(n_{i,0}^{\mathrm{H}} - n_{i,0}^{\mathrm{L}}\right) \\ &= -\frac{\Delta T_m^{pore}}{T_m^{pore}}\Delta h_{m,0} + \sum_{i=m,w}\Delta\mu_i\left(n_{i,0}^{\mathrm{H}} - n_{i,0}^{\mathrm{L}}\right) \end{aligned} \tag{4.15}$$

where $\Delta s_{m,0} = s^{\mathrm{L}}_{m,0} - s^{\mathrm{H}}_{m,0}$ and $\Delta h_{m,0} = \Delta s_{m,0}/T_m^{bulk}$ are the molar entropy and enthalpy of melting from methane hydrate to liquid water (plus methane vapor) at T_m^{bulk}. Using Eq. (4.15), the shift of melting point reads:

$$\begin{aligned}\frac{\Delta T_m^{pore}}{T_m^{bulk}} = -\frac{v_0^{\mathrm{H}}}{\Delta h_{m,0}} \bigg[& P^{\mathrm{H}} - P^{\mathrm{L}} + \left(1 - \frac{v_0^{\mathrm{L}}}{v_0^{\mathrm{H}}}\right)\left(P^{\mathrm{L}} - P_0\right) \\ & + \frac{1}{v_0^{\mathrm{H}}} \sum_{i=m,w} \Delta\mu_i \left(n^{\mathrm{L}}_{i,0} - n^{\mathrm{H}}_{i,0}\right) \bigg]\end{aligned} \tag{4.16}$$

Using the Laplace equation in Eq. (4.11), Eq. (4.16) is rewritten as,

$$\begin{aligned}\frac{\Delta T_m^{pore}}{T_m^{bulk}} = \frac{v_0^{\mathrm{H}}}{\Delta h_{m,0}} \bigg[& 2\left(\gamma_{LS} - \gamma_{HS}\right)\frac{1}{D_p} + \left(\frac{v_0^{\mathrm{L}}}{v_0^{\mathrm{H}}} - 1\right)\left(P^{\mathrm{L}} - P_0\right) \\ & - \frac{1}{v_0^{\mathrm{H}}} \sum_{i=m,w} \Delta\mu_i \left(n^{\mathrm{L}}_{i,0} - n^{\mathrm{H}}_{i,0}\right) \bigg]\end{aligned} \tag{4.17}$$

The above equation, which is a revisited version of the Gibbs-Thomson equation, shows that the shift in melting temperature of confined methane hydrate with respect to the bulk phase, $\Delta T_m^{pore}/T_m^{bulk} = (T_m^{pore} - T_m^{bulk})/T_m^{bulk}$, linearly depends on the reciprocal pore width, $1/D_p$. However, we note that in this extended approach there is two additional terms that do not depend directly on pore width D_p. If we assume as is usually done in the literature: (a) $v_0^{\mathrm{H}} = v_0^{\mathrm{L}}$; (b) $n^{\mathrm{H}}_{i,0} = n^{\mathrm{L}}_{i,0}$ $(i = m, w)$; and (c) $\gamma_{LS} - \gamma_{HS} = \gamma_{LH}\cos\theta$ with $\theta = \pi$, Eq. (4.17) leads to the classical formulation of the Gibbs-Thomson equation:

$$\frac{\Delta T_m^{pore}}{T_m^{bulk}} = -\frac{2\gamma_{LH} v_0^{\mathrm{H}}}{\Delta h_{m,0}} \frac{1}{D_p} \tag{4.18}$$

In what precedes, we rederived the Gibbs-Thomson equation under the formula given in Eq. (4.17). Such a Gibbs-Thomson equation indicates that the shift in melting temperature $\Delta T_m/T_m^{bulk}$ linearly depends on the reciprocal pore width $1/D_p$ with two additional terms for enthalpy and chemical potentials. The Gibbs-Thomson coefficient, $k_{GB} = 2(\gamma_{LS} - \gamma_{HS})v^{\mathrm{H}}/\Delta h_m$, describes the proportionality coefficient. In the next paragraph, we will determine the following parameters using molecular simulation to check the validity of Eq. (4.17): γ_{HS}, γ_{LS}, v^{H}, v^{L}, Δh_m at (T_m^{bulk}, P).

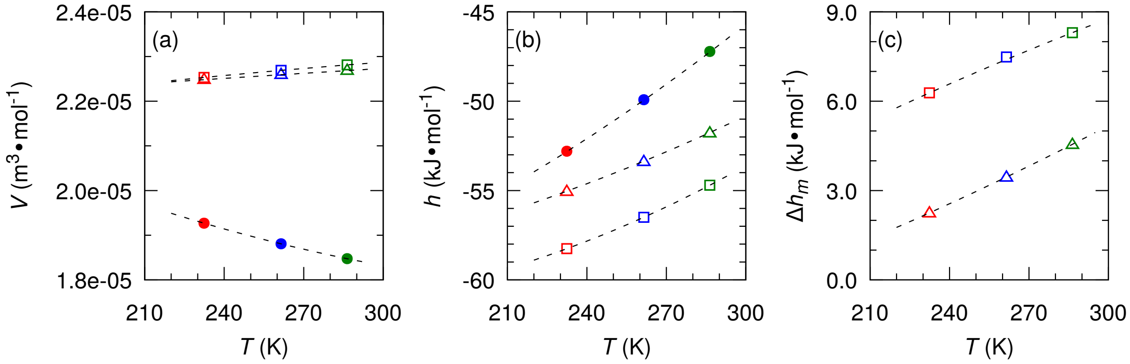

Figure 4.6 (color online) Molar volume v (a) and molar enthalpy h (b) of liquid water (solid circles), full-methane hydrate (empty squares), and empty-methane hydrate (empty triangles). Enthalpy of melting Δh_m (c) from full-methane hydrate (empty squares) to liquid water and from empty-methane hydrate (empty triangles) to liquid water using MD simulations. The dashed lines indicate that these parameters are along the L–H–V phase boundary for bulk phase: the red, blue, and green colors are for $(T,P) = $ (233 K, 1 atm), (262 K, 10 atm), and (286 K, 100 atm), respectively. All the thermodynamic parameters are per mole of water.

Molar volume of methane hydrate, v^{H}, molar volume of liquid water, v^{L}, and molar enthalpy of melting from methane hydrate to liquid water (+ methane vapor), Δh_m. Δh_m is defined by subtracting the enthalpy of liquid water and the enthalpy of methane vapor from the enthalpy of methane hydrate using the appropriate stoichiometry: $\Delta h_m = \left(h_w^{\mathrm{L}} + h_m^{\mathrm{V}}\right) - h_{m,w}^{\mathrm{H}}$. In practice, the contribution of methane vapor is ignored, $\Delta h_m = h_w^{\mathrm{L}} - h_{m,w}^{\mathrm{H}}$. The configurations of methane hydrate and liquid water are equilibrated using isobaric-isothermal molecular dynamics until the density and energy converge to an equilibrium value. v^{H}, v^{L}, h^{H}, h^{L}, and Δh_m at different bulk phase equilibrium conditions, $(T,P) = $ (233 K, 1 atm), (262 K, 10 atm), and (286 K, 100 atm), are shown in Figure 4.6. From these calculations, we obtain $\Delta h_m = 8.35$ kJ·mol^{-1}, $v^{\mathrm{L}} = 1.8475 \times 10^{-5}$ m^3·mol^{-1}, and $v^{\mathrm{H}} = 2.2813 \times 10^{-5}$ m^3·mol^{-1} at $T = 286$ K and $P = 100$ atm. Such an enthalpy of melting, Δh_m, leads to an entropy of melting, $\Delta s_m = \Delta h_m / T_m^{bulk} = 29.3$ J·K^{-1}·mol^{-1} which is comparable to that reported by Molinero et al. (Jacobson and Molinero, 2011). For the sake of clarity, these values are summarized in Table 4.2. These thermodynamic parameters for an empty hydrate (i.e., the framework of sI methane hydrate obtained after removing methane molecules) were also computed for comparison (see Figure 4.6).

Surface tensions between the solid wall and methane hydrate, γ_{HS}, or liquid water, γ_{LS}. The Gibbs–Thomson equation as defined in Eq. (4.17) requires to determine the two following surface tensions: γ_{HS} and γ_{LS}. Here, we use the Kirkwood-Buff approach to determine γ_{HS} and γ_{LS} as described in Section 4.1.2. With this approach, one must determine the normal, P_N, and tangential, P_T, pressure components in the canonical ensemble (i.e., at constant number of molecules N, volume V, and temperature T). For γ_{HS}, the $2 \times 2 \times 8$ unit cells of methane hydrate is confined in a slit pore with $D_p = 9.9816$ nm. For γ_{LS}, liquid water is first adsorbed in the porous solid using GCMC simulations at $T = 290$ K. In so doing, each molecular system includes two interfaces (top and bottom walls) and we perform canonical ensemble MD simulations to determine the ensemble averages $\langle P_N \rangle = \langle P_{zz} \rangle$ and $\langle P_T \rangle = \left(\langle P_{xx} \rangle + \langle P_{yy} \rangle \right) /2$. Figure 4.7 shows $\langle P_T \rangle$ and $\langle P_N \rangle$ at $T = 290$ K during the MD simulation in the last 2.5 ns (a total of > 20 ns was used for each molecular dynamics). In practice, the finite size effects from the vacuum layer (added at each side of the simulation box along the z–axis), D_v, is first considered. We determine γ_{HS} at $T = 290$ K with $D_v = 0 - 20$ nm (as shown in Figure B.7 of Appendix B); it was found that the influence of D_v can be ignored when $D_v \geq 15$ nm. In this work, $D_v = 15$ nm was thus used to calculate γ_{HS} and γ_{LS}. These calculations lead to $\gamma_{HS} = 15$ mJ$\cdot$m^2 and $\gamma_{LS} = -56$ mJ$\cdot$m^2 at $T = 290$ K. These results are shown in Table 4.2.

Validity of the Gibbs-Thomson equation. In the previous section, the following thermodynamic proprieties, v_{H}, v_{L}, Δh_m, γ_{HS} and γ_{LS} were computed using MD and GCMC simulations. The resulting values are summarized in Table 4.2. These calculations lead to the Gibbs-Thomson constant $k_{GT} = -0.39$ where $k_{GT} = 2\left(\gamma_{LS} - \gamma_{HS}\right) v^{\mathrm{H}} / \Delta h_m$ as shown in Eq. (4.17). In the context of the results obtained using the direct coexistence method, the constant $k_{DCM} = -0.28$ was estimated using a linear fit with the following equation $\Delta T_m^{pore} = k_{DCM}/D_p$. Figure 4.8 shows the shift in melting temperature of confined methane with respect to bulk phase, ΔT_m^{pore}, as a function of the reciprocal of pore width,

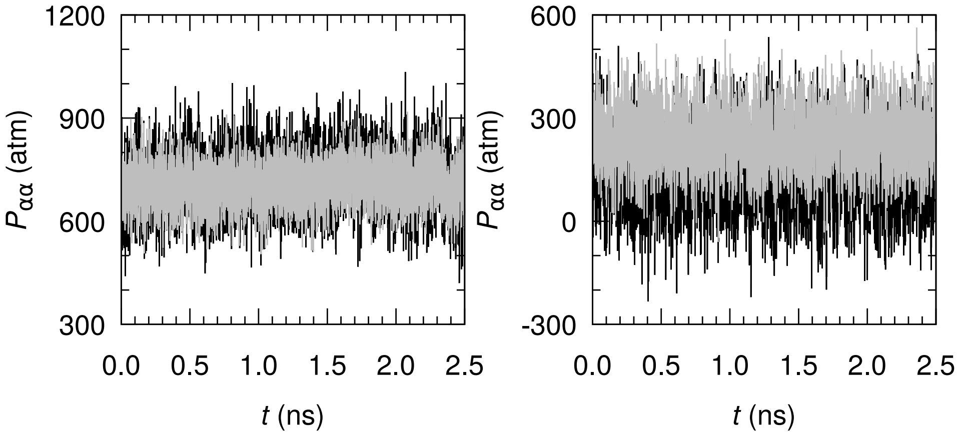

Figure 4.7 Normal (black line), $P_N = P_{zz}$, and parallel (gray line), $P_T = \frac{1}{2}(P_{xx} + P_{yy})$, pressure components of methane hydrate (*left*) and liquid water (*right*) in a slit pore $D_p = 9.9816$ nm as a function of time, t, in canonical ensemble MD simulation at $T = 290$ K. The dimensions of the simulation box are: $L_x = L_y = 2.3754$ nm and $L_z = 41.4932$ nm.

$1/D_p$. The two values k_{GT} and k_{DCM} are in fair agreement. The results obtained using the DCM technique are therefore reasonably described by using the revisited Gibbs–Thomson equation. In other words, the shift in the melting temperature of confined methane hydrate relative to the bulk phase $\Delta T_m/T_m$ linearly depends on the reciprocal pore size $1/D_p$ with a slope that can be described using the Gibbs-Thomson equation.

Table 4.2 Thermodynamic properties of liquid water and methane hydrate (both empty and full hydrates are considered) at $T = 286^a$ K or $T = 290^b$ K and $P = 100$ atm. [a] Normalized per mole of water. [b] Surface tensions determined for hydrate-substrate and liquid-substrate surfaces. [c] $k_{DCM} = -0.28$ as obtained by fitting the results of the direct coexistence method. The values in parentheses are those reported by Molinero at al. (Jacobson and Molinero, 2011).

property	liquid water	methane hydrate	
		full	empty
v (10^{-5} m^3 mol^{-1}) [a]	1.85	2.28	2.27
Δh_{fus} (kJ mol^{-1}) [a]	–	8.35 (6.53)	4.55 (4.40)
Δs_{fus} (J K^{-1}mol^{-1}) [a]	–	29.3 (21.3)	16.0
γ (mJ m^2) [b]	-56	15	–
k_{GT} [c]	–	-0.39	–

Pressure effects. Using the DCM technique, the melting temperature at a lower pressure $P = 10$ atm was also determined. For bulk and confined methane hydrate in a pore width $D_p = 2.8554$ nm, we obtained $T_m^{bulk} = 265 \pm 5$ K and $T_m^{pore} = 225 \pm 5$ K (see Figure B.4 of the Appendix B). As compared with $P = 100$ atm, a larger shift in

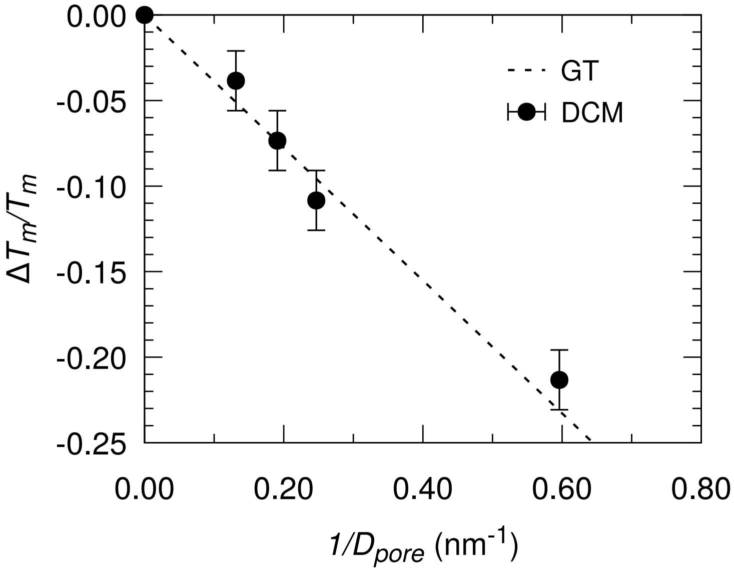

Figure 4.8 Shift in melting temperature of confined methane hydrate with respect to the bulk, $\Delta T_m^{pore}/T_m^{bulk}$, at $P = 100$ atm as a function of the reciprocal of pore size, $1/D_p$. The solid circles are obtained using the direct coexistence method while the solid line is determined using the revisited version of the Gibbs-Thomson equation: $\Delta T_m^{pore}/T_m^{bulk} = 2(\gamma_{LS}\nu^{\mathrm{L}} - \gamma_{HS}\nu^{\mathrm{H}})/\Delta h_m D_p$.

melting temperature, $\Delta T_m^{pore} = T_m^{pore} - T_m^{bulk} \sim -40$ K, is obtained for $D_p = 2.8554$ nm. As a result, a more negative Gibbs-Thomson coefficient k_{GT} is expected at $P = 10$ atm (as compared with $P = 100$ atm). we recall that γ_{HS} is determined using the canonical ensemble in this work. We obtained $\gamma_{LS} = -48$ mJ·m^2 at $P = 10$ atm. ν_{L}, ν_{H}, and Δh_m at $T = 262$ K and $P = 10$ atm can be found in Figure 4.6. These calculations lead to $k'_{GT} = -0.38$ according to Eq. (4.17) for $P = 10$ atm. These results are in agreement with the data obtained using the DCM technique as shown in Figure B.5 of the Appendix B. Decreasing the pressure leads therefore to a larger shift in the phase stability of confined methane hydrate.

Surface wettability effects. The effect of surface wettability was assessed by changing the LJ energy parameter, ε', of the pair interactions between methane hydrate and the porous solid, U_{HS}. $\varepsilon' = 1/2$, $1/3$, $1/4$, 2, 3, and 4 ε (where ε is the original LJ energy parameters used in the previous sections) were adopted to mimic stronger or weaker solid-fluid interactions. By using the DCM technique, the melting temperature using different ε' at $P = 100$ atm were determined as shown in Figure B.6 of the Appendix B. We found that the melting temperature remains constant. This result can be explained using the Gibbs-Thomson equation; k_{GT} depends on γ_{HS} and γ_{LS} (the values v^{H}, v^{L}, and Δh_m are those for bulk methane hydrate and/or liquid water). At constant T and P, a first-order Taylor expansion for γ leads to:

$$\gamma(\varepsilon') \sim \gamma(\varepsilon) + \left(\frac{\partial \gamma}{\partial \varepsilon}\right)_{\varepsilon} (\varepsilon' - \varepsilon) \tag{4.19}$$

Since $U_{HS}/U \leq 5\%$ (where U is the total potential energy and U_{HS} is the potential energy contribution arising from solid-fluid interactions), the contribution from U_{HS} in γ can be ignored: $(\partial\gamma/\partial\varepsilon)_{\varepsilon} \sim 0$. As a result, $\gamma_{HS}(\varepsilon') \sim \gamma_{HS}(\varepsilon')$ and $\gamma_{LS}(\varepsilon') \sim \gamma_{LS}(\varepsilon)$, so that $k_{GT}(\varepsilon') \sim k_{GT}(\varepsilon)$ considering the range of ε' used here.

4.2.3 Free energy calculations and kinetics

To estimate the free energy barriers for methane hydrate formation/dissociation, we combined grand canonical ensemble Monte Carlo (GCMC) simulations with the umbrella sampling technique to explore the free energy landscape for this complex system. The details of these umbrella sampling calculations were discussed in Section 4.1.3. Due to the slow formation/dissociation kinetics, large computational resources are required from a technical point of view even if the umbrella sampling technique is used. In particular, low temperatures lead to very slow methane hydrate dissociation. Therefore, it is difficult to explore the free energy profile at low temperature (e.g., at melting temperature $T_m \sim 255$ K of confined methane hydrate for $D_p = 2.8554$ nm). In this work, four temperatures ($T = 290$ K, 310 K, 330 K, and 350 K) around $T_m^{bulk} = 285$ K were considered for bulk methane hydrate/liquid water. As for confined methane hydrate/liquid water, three temperatures ($T = 290$ K, 300 K, and 310 K) above $T_m^{pore} = 255K$ were considered. Lower temperatures were also considered for confined methane hydrate/liquid water. However, even if $\sim 10^6$ MC moves per molecule were used in the umbrella sampling technique, we did not obtain meaningful results for these low temperatures.

Figure 4.9 shows the normalized free energy, G/k_BT, of bulk and confined ($D_p =$ 2.8554 nm) methane hydrate/liquid water as a function of the local bond order parameter, Q_6, at different temperatures. For bulk methane hydrate/liquid water (see Figure 4.9 (left)), methane hydrate is favorable at low temperature $T < T_m$; for instance, the free energy difference between methane hydrate and liquid water shows a positive value, $\Delta G^{LH}/k_BT = \left(G^{\mathrm{L}} - G^{\mathrm{H}}\right)/k_BT = 8.1 > 0$ at $T = 290$ K. While at high temperature $T > T_m$, liquid water is favorable; for instance, the free energy difference shows a negative value $\Delta G^{LH}/k_BT = -3.1 < 0$ at $T = 310$ K. For the confined phase (see Figure 4.9 (right)), all the free energy calculations were performed above the expected melting temperature of confined methane hydrate as the results at lower temperatures were found to be too noisy to be used to analysis. As expected, liquid water is the favorable phase at these temperatures; indeed, free energy profiles at these three temperature give a negative free energy difference between methane hydrate and liquid water. To estimate the melting temperature of bulk and confined methane hydrate, the free energy difference, ΔG_{LH}, as a function of temperature, T, is shown in Figure 4.10. We found that the free energy difference depends linearly on temperature. Therefore, we used a linear fit for both bulk and confined phases to extrapolate ΔG_{LH} at T_m^{pore}. In so doing, this fit leads to $T_m^{bulk} = 302$ K and $T_m^{pore} = 257$ K for $D_p = 2.8554$ nm which are in fair agreement with the results obtained using the direct coexistence method.

Each free energy profile, $G\left(Q_6\right)$, in Figure 4.9 shows two free energy barriers, ΔG_{barr}: one is for the phase transition from liquid water to methane hydrate (i.e., formation), $\Delta G_{barr}^{L\rightarrow H}$ while the other one is for the phase transition from methane hydrate to liquid water (i.e., dissociation), $\Delta G_{barr}^{H\rightarrow L}$. As said previously, the slow formation/dissociation kinetics makes it difficult to determine the free energy profiles of confined methane hydrate close to its melting temperature even when the umbrella sampling technique is used. In order to overcome this problem, we compare the free energy barriers as a function of the temperature difference with respect to the melting point for the bulk and confined systems. This makes it possible to compare the formation/dissociation

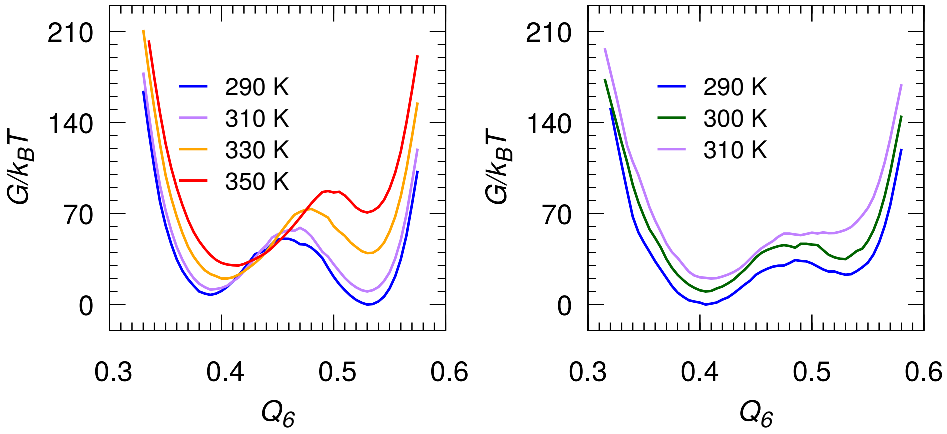

Figure 4.9 (color online) Free energy, G, of methane hydrate and liquid water in bulk phase (*left*) and in confined phase for $D_p = 2.8554$ nm (*right*) as a function of the local bond order parameter, Q_6. $G(Q_6)$ of bulk phase (*left*) is shown at $T = 290$ K (blue), 310 K (purple), 330 K (orange) and 350 K (red). $G(Q_6)$ upon confinement (*right*) is shown at $T = 290$ K (blue), 300 K (green), and 310 K (purple). The free energy is normalized using the thermal energy, k_BT. For the sake of clarity, a shift of +10, +20, and +30 in G/k_BT is added for the bulk phase at $T = 310$ K, 330 K, and 350 K. A shift of +10 and +20 in G/k_BT is added for the confined phase at $T = 300$ K and 310 K.

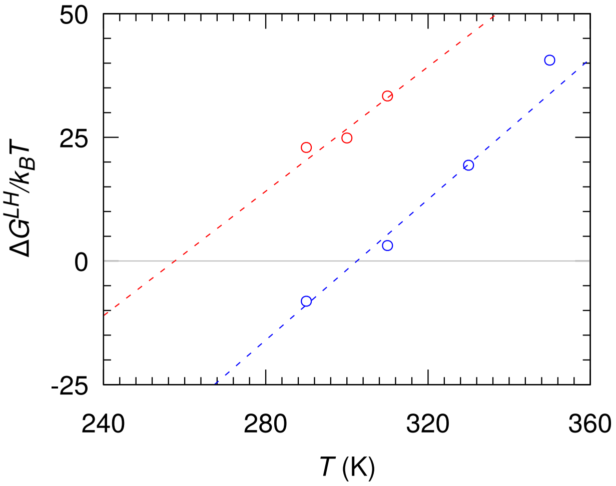

Figure 4.10 (color online) Free energy difference, ΔG^{LH}, between methane hydrate and liquid water as a function of temperature, T. The blue circles are for bulk methane hydrate and the red circles are for confined methane hydrate in a pore $D_p = 2.8554$ nm. The blue dashed line is a linear fit for bulk methane hydrate while the red dashed line is a linear fit for confined methane. These fits lead to $T_m^{bulk} = 302$ K and $T_m^{pore} = 257$ K for $D_p = 2.8554$ nm. The free energy is normalized using the thermal energy, k_BT.

kinetics between bulk and confined phases at the same “distance” to the melting point. In particular, for confined methane hydrate, we can extrapolate and estimate ΔG_{barr} at T_m^{pore}. These data are shown in Figure 4.11. On the one hand, as described in the classical nucleation theory (see Section 1.3), the formation/dissociation rate, J, is defined as $J = J_0 \exp\left(-\Delta G_{barr}/k_B T\right)$. Using the extrapolation, we obtain $\Delta G_{barr}/k_B T = 50.7$ for bulk methane hydrate while $\Delta G_{barr}/k_B T = 33.8$ for confined methane hydrate. A larger free energy barrier $\Delta G_{barr}/k_B T = 300$ for bulk methane hydrate is found at $T = 273$ K and $P = 900$ atm by Knott et al. (Knott et al., 2012). The large free energy barrier between liquid water and methane hydrate at the melting point ($\Delta G_{barr}^{L\to H} = \Delta G_{barr}^{H\to L}$ at this point) indicates that the phase transition between methane hydrate and liquid water (i.e., $L \to H$ and $H \to L$) is extremely slow. On the other hand, as compared with bulk methane hydrate, confinement decreases the free energy barrier $G_{barr}/k_B T$ (for both $L \to H$ and $H \to L$). This result suggests that the phase transition between methane hydrate and liquid water is much easier (i.e., faster kinetics) when confined in a porous solid.

4.3 Conclusion

Using molecular simulation, the confinement effects on the phase stability and formation/dissociation kinetics of methane hydrate were determined. For different pore widths, we first determined the melting temperature, T_m^{pore}, of confined methane hydrate at a given pressure using the direct coexistence method. Our results show a reduced phase stability with a shift in the melting temperature, ΔT_m^{pore}, pointing to low temperature, as compared with bulk methane hydrate: $\Delta T_m^{pore} = T_m^{pore} - T_m^{bulk} < 0$ where T_m^{bulk} is the melting temperature of bulk methane hydrate and T_m^{pore} is the melting temperature of confined methane hydrate.

A revised version of the Gibbs–Thomson equation was also derived. For this revised Gibbs-Thomson equation, we first determined important thermodynamic parameters such as the molar volume and enthalpy for both methane hydrate and liquid water. And, the

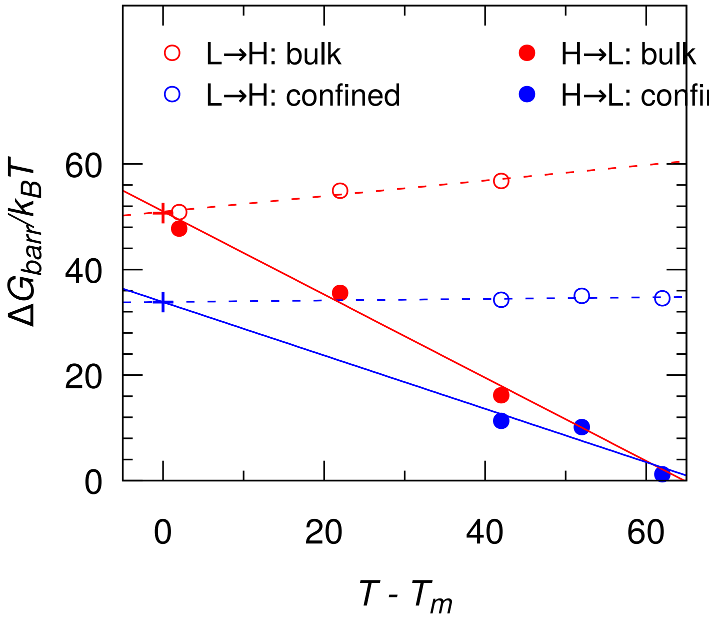

Figure 4.11 (color online) Free energy barriers, $\Delta G_{barr}/k_BT$, between methane hydrate and liquid water as a function of the shift with respect to the melting point, $T - T_m$, for bulk phase (red) and for confined phase (blue): (1) free energy barriers from liquid water to methane hydrate, i.e., methane hydrate formation (*left*), $\Delta G_{barr}^{L \rightarrow H}$; and (2) free energy barrier from methane hydrate to liquid water, i.e., methane hydrate dissociation (*right*), $\Delta G_{barr}^{H \rightarrow L}$. The red cross is for bulk methane hydrate while the blue cross is for confined methane hydrate using the extroplation described in the text. The free energy barriers are normalized using the thermal energy, k_BT.

chemical potential of methane and water upon phase equilibrium is necessary to correct the Gibbs-Thomson equation. Then, we determined the surface tensions between the porous solid and methane hydrate γ_{HS} or liquid water γ_{LS}. The Gibbs-Thomson coefficient obtained using these data, which is agreement with that inferred using the direct coexistence method, shows that the shift in melting temperature of confined methane hydrate as a function of pore width can be well-described using the Gibbs-Thomson equation.

Slow formation kinetics was observed in the direct coexistence method. This was further validated using free energy calculations. More in details, using the umbrella sampling technique, we determined the free energy profiles of bulk and confined methane hydrate at different temperatures. Our finding suggests that confinement leads to faster formation/dissociation kinetics (i.e., decreases the free energy barriers between methane hydrate and liquid water) of methane hydrate. However, we note that formation/dissociation of confined methane hydrate remains overall very slow.

Chapter 5

Physical and Physicochemical Properties of Confined Methane Hydrate

Contents

5.1 Computational details 120

  5.1.1 Molecular models 120

  5.1.2 Molecular dynamics details 121

  5.1.3 Thermal conductivity 122

5.2 Structure 124

5.3 Thermodynamic coefficients 128

5.4 Thermal conductivity 133

5.5 Conclusion 138

In this chapter, we focus on the physical and physicochemical properties of methane hydrate confined at the nanoscale. These physical and physicochemical properties include (1) density distribution, (2) order parameter, (3) thermal expansion, (4) isothermal compressibility, and (5) thermal conductivity. Both bulk and confined methane hydrates are considered as they play an important role in practical applications (Bai et al., 2015; Burnham and English, 2016; Demurov et al., 2002; Jendi et al., 2016; Michalis et al., 2016a; Yang et al., 2016b; Zhu et al., 2014). The remainder of this chapter is organized as follows. In Section 5.1, we present the computational details: molecular configurations of confined methane hydrate and liquid water, molecular dynamics in the isobaric-isothermal ensemble, molecular dynamics in the canonical ensemble, piston method to apply a given pressure, the Green-Kubo formalism to determine the thermal conductivity. In Section 5.2, the density profiles of bulk and confined methane hydrates as well as liquid water are presented. In this part, we also show local bond order parameters. In Section 5.3, the thermal expansion and isothermal compressibility are presented. In Section 5.4, we use the Green-Kubo formalism to compute the thermal conductivity of bulk and confined methane hydrate. Section 5.5 presents some concluding remarks.

5.1 Computational details

5.1.1 Molecular models

Figure 5.1 shows the molecular configurations of confined methane hydrate (*left*) and liquid water (*right*) considered in this work. We first duplicate the unit cell of bulk methane hydrate along the z-axis to build a larger configuration. Then, we remove all the molecules (water and methane) $|z| > z_c$ where $z_c = 1.3809$ nm. In so doing, a total number of 392 water molecules and 76 methane molecules are included in the configuration of confined methane hydrate. A similar method was proposed by Chakraborty et al. (Chakraborty and Gelb, 2012b). The pore walls are the same as those used in Chapter 4; the pore width, D_p, is defined as the distance between the center of the innermost layer solid atoms of the two pore walls. The configuration of confined liquid water is generated by melting the empty hydrate structure in the canonical ensemble followed by simulation at constant pressure. To determine density profiles, order parameters, thermal expansion, and isothermal compressibility, the following box dimensions $L_x = L_y = L_z = 2.3754$ nm are used for bulk methane hydrate/liquid water while $L_x = L_y = 2.3754$ nm and $L_z = 44.5734$ nm are used for confined methane hydrate/liquid water. To determine the thermal conductivity, $L_x = L_y = L_z = 3.5631$ nm (corresponding to $3 \times 3 \times 3$ unit cells) are used for bulk methane hydrate following the work by English et al. (English and Tse, 2009; English et al., 2009). The following simulation box dimensions $L_x = L_y = 3.5631$ nm and $L_z = 49.4754$ nm (corresponding to $3 \times 3 \times 6$ unit cells) are used to determine the thermal conductivity of confined methane hydrate. Periodic boundary conditions are used in the x– and y–directions while the system is non-periodic in the z–direction.

5.1.2 Molecular dynamics details

Molecular dynamics (MD) in the isobaric–isothermal (NPT) ensemble are used to relax the configuration (energy, density, etc.) and to determine the density profiles of water $\rho_w(z)$ and methane $\rho_m(z)$, order parameter profiles $Q_6(z)$, thermal expansion α_P, isothermal compressibility κ_T of bulk methane hydrate and liquid water. To relax such confined molecular systems, a pressure component along the z-axis, P_{zz}, was applied using two pistons (one is the top wall and the other one is the bottom wall). Each piston applies an external force, $f_{zz,ex}^{wh}$ where $wh = bot$ is for the bottom wall and $wh = top$ is for the top wall, to each piston atom (each piston is made of N_s^{wh} atoms). These forces are $f_{zz,ex}^{\text{top}} = -P_{zz}/\left(L_x L_y N_s^{\text{top}}\right)$ and $f_{zz,ex}^{\text{bot}} = P_{zz}/\left(L_x L_y N_s^{\text{bot}}\right)$ where L_x and L_y are the dimensions of the simulation box in the x– and y–directions. In addition to $f_{zz,ex}$, there is another force, $f_{zz,in}^{wh}$, for each solid atom. Such force arises from the LJ interactions with the methane hydrate atoms (or liquid water atoms). To determine $f_{zz,in}^{wh}$, the total force from LJ pair interactions on the pore wall is first calculated, $F_{zz,in}^{wh}$. Then, this force is averaged and reassigned to every atom: $f_{zz,in}^{wh} = F_{zz,in}^{wh}/N_s^{wh}$. Therefore, the force on each solid atom is $f_{zz}^{wh} = f_{zz,ex}^{wh} + f_{zz,in}^{wh}$ at each timestep of the molecular dynamics simulation.

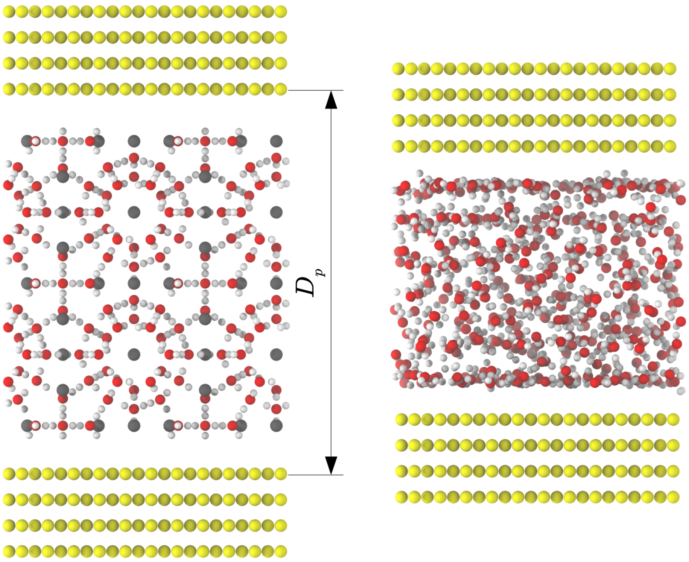

Figure 5.1 (color online) Molecular configuration of confined methane hydrate (*left*) and liquid water (*right*). The red and white spheres are the oxygen and hydrogen atoms of water, respectively. The gray spheres are the methane molecules which are inside the hydrogen-bonded cages formed by water molecules. The yellow spheres are the solid atoms of the pore walls. Pore walls are set as described in Chapter 4 but with pistons at the top wall and bottom wall. In this specific configuration, the sI methane hydrate with dimensions of $L_x = L_y = L_z = 2.3754$ nm is confined inside the porosity (*left*). The liquid water (*right*) is obtained by first removing methane molecules and then melting the hydrate phase in the canonical ensemble followed by simulations at constant pressure. The dimensions of the simulation box are $L_x = L_y = 2.3754$ nm and $L_z = 44.5734$ nm (*left*) and 41.4932 nm (*right*). Periodic boundary conditions are used along the x– and y–directions.

5.1.3 Thermal conductivity

For bulk methane hydrate, molecular dynamics in the isobaric-isothermal (NPT) ensemble is first used to relax its density and energy. While for confined methane hydrate, methane hydrate is treated in a similar way but with pistons used to apply a pressure P_{zz}. Once equilibrium is reached, molecular dynamics simulations in the microcanonical (NVE) ensemble are used to determine the heat-flux vector as a function of time, $\mathbf{J}(t)$, of bulk and confined methane hydrate. The heat-flux vector, $\mathbf{J}(t)$, at time, t, can be computed using the following microscopic expression:

$$\begin{aligned}\mathbf{J}(t) =& \frac{1}{V}\left[\sum_i \left(\frac{1}{2}m_i\mathbf{v}_i^2(t)\right)\mathbf{v}_i(t)\right.\\ &+\frac{1}{2}\sum_i\sum_{i<j} u_{ij}(t)\left(\mathbf{v}_i(t)+\mathbf{v}_j(t)\right)\\ &\left.+\frac{1}{2}\sum_i\sum_{i<j}\left[\mathbf{f}_{ij}(t)\cdot\left(\mathbf{v}_i(t)+\mathbf{v}_j(t)\right)\mathbf{r}_{ij}(t)\right]\right]\end{aligned} \tag{5.1}$$

where V is the volume, $\frac{1}{2}m_i\mathbf{v}_i^2$ is the kinetic energy of molecule i with the molecular mass m_i, u_{ij} is the interaction energy between molecules i and j, $\mathbf{v}_i$ ($\mathbf{v}_j$) are the velocity of the molecule i (molecule j), $\mathbf{f}_{ij}$ is the force on molecule i exerted by molecule j, and $\mathbf{r}_{ij}$ is the position vector separating molecules i and j. k_B is Boltzmann's constant. The first, second, and third terms in Eq. (5.1) correspond to the kinetic energy, potential energy, and stress. In Eq. (5.1), $\mathbf{J}(t)$ is a vector which has three components – $[J_x(t), J_y(t), J_z(t)]$.

The Green-Kubo formalism relates the ensemble average of the time autocorrelation of the heat flux to the thermal conductivity, λ:

$$\lambda = \frac{V}{3k_BT^2}\int_0^\infty \langle\mathbf{J}(0)\cdot\mathbf{J}(t)\rangle\,dt \tag{5.2}$$

where $h(t) = V/3k_BT\,\langle\mathbf{J}(0)\cdot\mathbf{J}(t)\rangle$ is the normalized autocorrelation function of the heat-flux. For bulk methane hydrate, $\mathbf{J}(t)$ is symmetrical in x–, y–, and z–directions and the heat-flux vector components are equal in each direction: $J_x(t) = J_y(t) = J_z(t)$. In contrast, for confined methane hydrate: $J_x(t) = J_y(t) \neq J_z(t)$. We computed the thermal conductivity using the two following components:

$$\begin{aligned}\lambda_T &= \frac{V}{2k_BT^2}\int_0^\infty \left\langle J_x(0)J_x(t)+J_y(0J_y(t))\right\rangle dt\\ \lambda_N &= \frac{V}{k_BT^2}\int_0^\infty \langle J_z(0)J_z(t))\rangle\,dt\end{aligned} \tag{5.3}$$

where λ_T and λ_N are the tangential and normal components of the thermal conductivity. $h_T(t) = V/2k_BT \left\langle J_x(0)J_x(t) + J_y(0)J_y(t) \right\rangle$ and $h_N(t) = V/k_BT \left\langle J_z(0)J_z(t) \right\rangle$ are the corresponding autocorrelation functions.

The autocorrelation function $h(t)$ in Eq. (5.2) and $h_N(t)$ and $h_T(t)$ in Eqs. (5.3) can be extracted using the energy transfer between neighboring atoms. Such energy transfer is the sum of exponentially decaying functions that correspond to acoustic and optical components together with a cosine-modulated term for the optical component,

$$h(t) = \sum_{i=1}^{n_{ac}} A_i \exp\left(-t/\tau_i\right) + \sum_{j=1}^{n_{op}} \left[\sum_{k=1}^{n_{op,j}} B_{ij} \exp\left(-t/\tau_{jk}\right)\right] \cos\omega_j t + \sum_{j=1}^{n_{op}} C_j \cos\omega_j t \tag{5.4}$$

In this equation, the first term corresponds to two or three (i.e., $n_{ac} = 2$ or 3) acoustic modes (namely, short range, *sh*, long range, *lg*, and, possibly, medium range, *me*). The second term corresponds to one or two ($n_{op} = 1$ or 2) optical modes. The third term corresponds to the residual oscillations beyond the acoustic and optical modes. The relaxation times for the acoustic modes are τ_{sh}, τ_{me}, and τ_{lg} while those for the optical modes are τ_{jk}. A_i, B_{jk}, and C_j are the amplitudes of the acoustic, optical, and residual terms, respectively. ω_j are the oscillation frequencies which correspond to peaks in the optical region of the power spectrum, $\mathscr{F}(\nu)$. $\mathscr{F}(\nu)$ is obtained in this work using the Fourier transform of $h(t)$. It should be noted that the residual terms are omitted in the Fourier transform as it only leads to a delta function in the Fourier space.

5.2 Structure

Density profiles. The density profiles, $\rho_s^{\Phi}(z)$, of a species s in the phase Φ along the z–axis are computed as follows:

$$\rho_s^{\Phi}(z) = \frac{\langle \Delta N_s(z, z+\Delta z)\rangle M_s}{N_A L_x L_y \Delta z} \tag{5.5}$$

where $\langle \Delta N(z, z+\Delta z)\rangle$ is the ensemble average of the number of species s located in the region between z and $z+\Delta z$, M_s is the molar mass of molecule s, and N_A is Avogadro's constant. $s = m$ is for methane molecules while $s = w$ is for water molecules. $\Phi = \mathrm{L}$ is for liquid water while $\Phi = \mathrm{H}$ is for methane hydrate. The following density profiles were determined at $T = 240$ K and $P = 100$ atm (or $P_{zz} = 100$ atm for confined systems): water in liquid phase, $\rho_w^{\mathrm{L}}(z)$, and methane, $\rho_m^{\mathrm{H}}(z)$, and water, $\rho_w^{\mathrm{H}}(z)$, in hydrate phase. These data are shown in Figure 5.2. Multi-layer distributions are observed for confined liquid water (see Figure 5.2 (*top*)). In these layers, liquid water exhibits a high density close to the pore wall. By comparing water molecules in the bulk and confined methane hydrate (Figure 5.2 (*center*)), the density profiles do not show significant differences. Moreover, comparison between the density of methane molecules in bulk methane hydrate and that for confined methane hydrate (see Figure 5.2 (*bottom*)), the later exhibits a higher density only close to the pore walls.

Order parameter. The order parameter profiles of water along the z–axis, $Q_6(z)$, are computed as follows:

$$Q_6(z) = \left\langle \frac{\sum_i^{\Delta N_w(z,z+\Delta z)} Q_{6,i}}{\Delta N_w(z, z+\Delta z)} \right\rangle \tag{5.6}$$

where $\langle \cdots \rangle$ denotes an ensemble average. $\Delta N_w(z, z+\Delta z)$ is the number of water molecules located in the region between z and $z+\Delta z$. The index i runs over all these water molecules. The i–th water molecule exhibits a local bond order parameter $Q_{6,i}$ (as defined in Chapter 4). Figure 5.3 shows the order parameter Q_6 of liquid water and methane hydrate along the z-axis. First, liquid water exhibits a much more ordered structure at such low temperature $T = 240$ K (as compared with the data at temperatures above the melting point of ice). For instance, $Q_6 \sim 0.39$ for liquid water at $T = 290$ K is obtained using the free energy calculations in Figure 4.9 of Chapter 4. In contrast, $Q_6 \sim 0.48$ is obtained at $T = 240$ K as shown in Figure 5.3. The latter value is closer to the value of crystalline structures of water such as $Q_6 \sim 0.55$ for methane hydrate and hexagonal ice at $T = 250$ K and $P = 10$ atm. Q_6 for hexagonal ice and methane hydrate were determined using molecular dynamics in the NPT ensemble. Second, by comparing Q_6 for bulk and confined liquid water (see

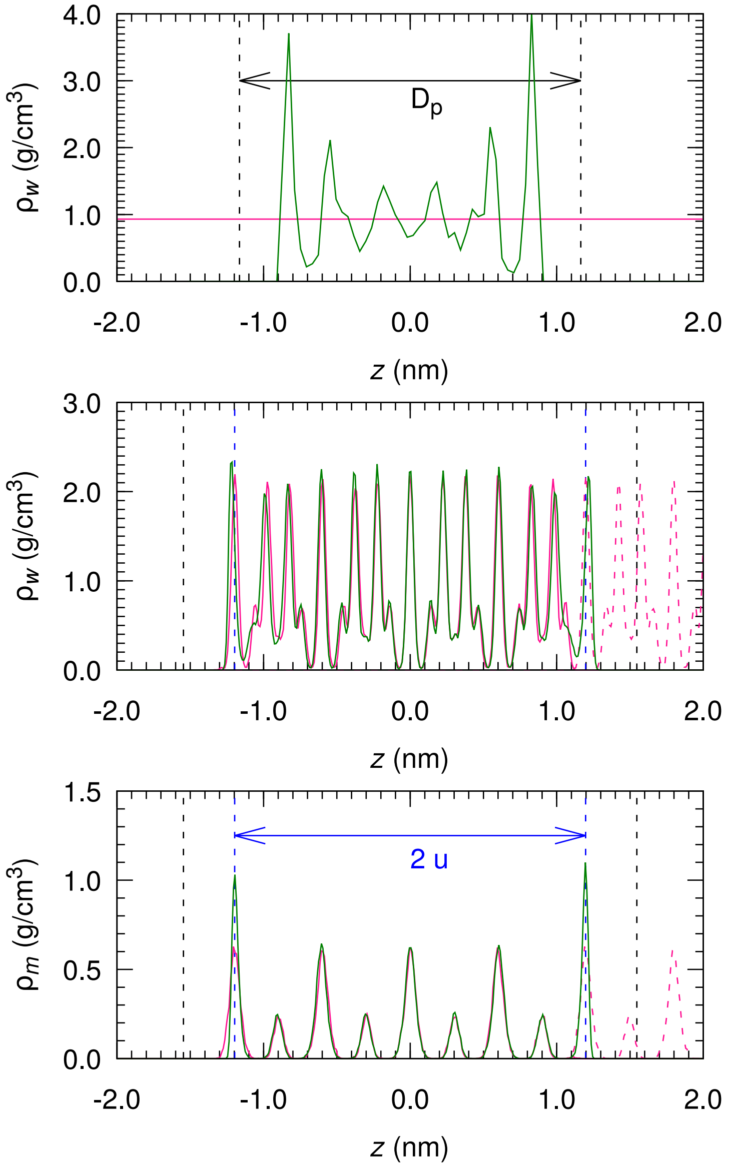

Figure 5.2 Density profiles along the z–axis, $\rho(z)$, of water in liquid phase (*top*), methane in hydrate phase (*center*), and water in hydrate phase (*bottom*) at $T = 240$ K and $P = 100$ atm. The red solid lines are for bulk phases while the green solid lines are for confined phases. The black dashed lines are the positions of the pore walls with the pore width D_p. The blue dashed lines are the dimension in the z–direction for bulk methane hydrate with $L_z = 2$ u. The red dashed lines are the density profiles for a duplicated bulk phase.

Figure 5.3 (*top*)), it is seen that confinement decreases Q_6. This might be caused by the fact that the larger density leads to a larger number of neighbors for a water molecule in the layers while the lower density corresponds to fewer neighbors for a water molecule between two layers. Q_6 for confined liquid water around the pore center is close to the value for bulk liquid water. This is due to the fact that their densities are similar. Finally, Q_6 for bulk and confined methane hydrate are similar along the z–axis (see Figure 5.3 (*bottom*)) except for slight differences close to the pore walls. These slight differences are due to the fact that the water molecules in this region possess fewer neighbors. The number of neighbors is $N_b = 4$ for water molecules in bulk methane hydrate and confined methane hydrate in pore center while $N_b = 2$ or 3 for water in the region close to the pore walls.

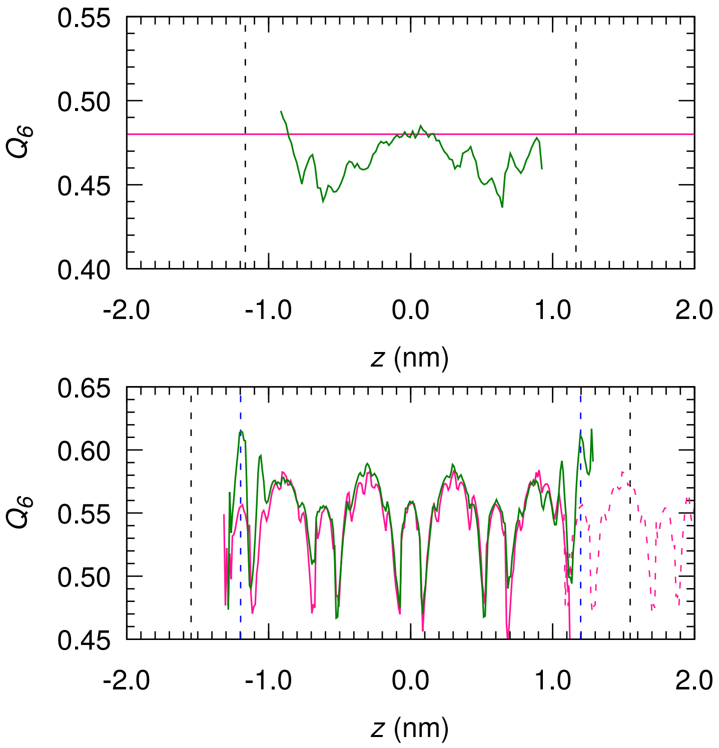

Figure 5.3 Local bond order parameters along the z–axis, $Q_6(z)$, in liquid water (*top*) and methane hydrate (*bottom*) at $T = 240$ K and $P = 100$ atm. The red solid lines are for bulk phases while the green solid lines are for confined phases. The black dashed lines are the positions of the pore walls with the pore width D_p. The blue dashed lines indicate the dimension in the z–direction for bulk methane hydrate with $L_z = 2$ u. The red dashed lines are the local bond order parameters for a duplicated bulk phase.

5.3 Thermodynamic coefficients

Thermal expansion, α_P. The thermal expansion, α_P^{Φ}, describes the ability of methane hydrate ($\Phi = \mathrm{H}$) or liquid water ($\Phi = \mathrm{L}$) to change its volume V in response to a change in temperature, T, at constant pressure, P,

$$\alpha_P^{\Phi} = \frac{1}{V}\left(\frac{\partial V}{\partial T}\right)_P \tag{5.7}$$

According to the above definition, the estimation of α_P requires to determine the volume, $V(T)$, as a function of temperature T at a given pressure P. For bulk liquid water/methane hydrate, $V(T)$ is determined using molecular dynamics in the NPT ensemble. Due to the fact that there is no unique definition of the volume V for a confined phase, we consider here two volumes, V_{pore}^{dmin} and V_{pore}^{dmax} (definitions will be given later), to compute the thermal expansion. According to Eq. (5.7), this leads to two thermal expansions, $\alpha_{P_{zz},pore}^{\Phi,dmin}$ and $\alpha_{P_{zz},pore}^{\Phi,dmax}$,

$$\begin{aligned} \alpha_{P_{zz},pore}^{\Phi,dmin} &= \frac{1}{V_{pore}^{dmin}}\left(\frac{\partial V_{pore}^{dmin}}{\partial T}\right)_{P_{zz}} \\ \alpha_{P_{zz},pore}^{\Phi,dmax} &= \frac{1}{V_{pore}^{dmax}}\left(\frac{\partial V_{pore}^{dmax}}{\partial T}\right)_{P_{zz}} \end{aligned} \tag{5.8}$$

where $V_{pore}^{dmax} = L_x L_y D_p$ and $V_{pore}^{dmin} = L_x L_y (D_p - \sigma_{OS})$ are the maximum and minimum volumes that can be considered. We recall that D_p is defined as the distance between the centers of solid atoms of the innermost layer of pore walls. σ_{OS} is the LJ parameter for unlike atomic pairs of oxygen-solid atoms. P_{zz} is the pressure applied to the pistons (the details of such piston calculations can be found in Section 5.1). As a comparison with confined systems, the thermal expansion using the molecular dynamics in the $NP_{zz}T$ ensemble, $\alpha_{p_{zz}}^{\Phi}$, reads:

$$\alpha_{P_{zz}}^{\Phi} = \frac{1}{V_z}\left(\frac{\partial V_z}{\partial T}\right)_{P_{zz}} \tag{5.9}$$

where $V_z = L_xL_yL_z$ is the volume of bulk phase in the $NP_{zz}T$ ensemble. In this work, different temperatures were considered: $T = 160$ K, 180 K, 200 K, 220 K, and 240 K at $P = 100$ atm (or $P_{zz} = 100$ atm). For the calculations of $\alpha^{\Phi,dmax}_{P_{zz},pore}$, $\alpha^{\Phi,dmin}_{P_{zz},pore}$ and $\alpha^{\Phi}_{P_{zz}}$, $L_x = L_y = 2.3754$ nm is kept constant.

Figure 5.4 shows the volume (*left*) and the corresponding thermal expansion (*right*) as a function of temperature for liquid water. First, the volume V increases with temperature T at $P = 100$ atm for both bulk and confined liquid water. Second, calculations in the NPT and $NP_{zz}T$ ensembles leads to the same volume of bulk liquid water at each temperature, i.e., $V(T) \sim V_z(T)$ and $(\partial V/\partial T)_P \sim (\partial V_z/\partial T)_{P_{zz}}$, so that as expected the thermal expansion of bulk liquid water determined using the NPT ensemble is the same as that determined using the $NP_{zz}T$ ensemble, $\alpha^{\mathrm{L}}_P = \alpha^{\mathrm{L}}_{P_{zz}}$. Finally, comparing α^{L}_P and $\alpha^{\mathrm{L},dmax}_{P_{zz},pore}$ (or $\alpha^{\mathrm{L},dmin}_{P_{zz},pore}$) suggests that the thermal expansion of confined water is small or equal to that of bulk liquid water.

Figure 5.5 shows the volume (*left*) and the corresponding thermal expansion (*right*) as a function of temperature for methane hydrate. Similarly to liquid water, we found that: (1) $V(T)$, $V_z(T)$, $V^{dmax}_{pore}(T)$, and $V^{dmin}_{pore}(T)$ increases with T; (2) $V(T) \sim V_z(T)$, $(\partial V/\partial T)_P \sim (\partial V_z/\partial T)_{P_{zz}}$, so that $\alpha^{\mathrm{H}}_P = \alpha^{\mathrm{H}}_{P_{zz}}$; (3) $\alpha^{\mathrm{H}}_P > \alpha^{\mathrm{H},dmin}_{P_{zz},pore} > \alpha^{\mathrm{H},dmax}_{P_{zz},pore}$. Confinement decreases the thermal expansion up to 44.3% for methane hydrate. In addition, by comparing the thermal expansion between methane hydrate and liquid water, methane hydrate shows a smaller thermal expansion than liquid water in the temperature range 160–240 K: $\alpha^{\mathrm{L}}_P > \alpha^{\mathrm{H}}_P$, $\alpha^{\mathrm{L},dmax}_{P_{zz},pore} > \alpha^{\mathrm{H},dmax}_{P_{zz}}$, and $\alpha^{\mathrm{L},dmin}_{P_{zz},pore} > \alpha^{\mathrm{H},dmin}_{P_{zz},pore}$.

Isothermal compressibility, κ_T. The isothermal compressibility describes the ability of methane hydrate or liquid water to change its volume in response to a change in pressure at constant temperature. As with the thermal expansion, the three following isothermal compressibilities at $T = 240$ K and $P = 100$ atm, 300 atm, 500 atm, 700 atm, and 900 atm are considered in this work:

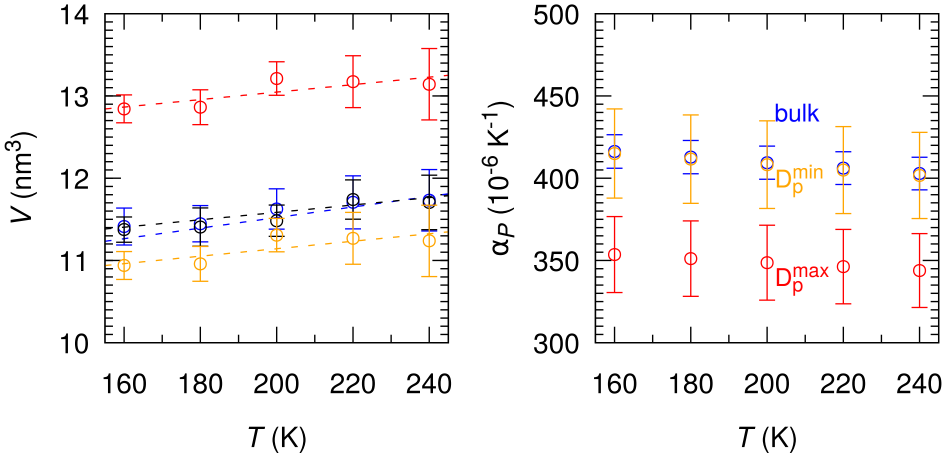

Figure 5.4 (color online) Volume (V, *left*) and thermal expansion (α_P, *right*) of bulk and confined liquid water as a function of temperature T at $P = 100$ atm. Two different ensembles were considered for bulk liquid water: NPT ensemble (blue circles) and NP_zT ensemble (black circles). For confined liquid water, a minimum value D_p^{min} (orange circles) and a maximum value D_p^{max} (red circles) of the pore width were considered. A total of 368 water molecules were used to determine these data. The dashed lines are linear fits.

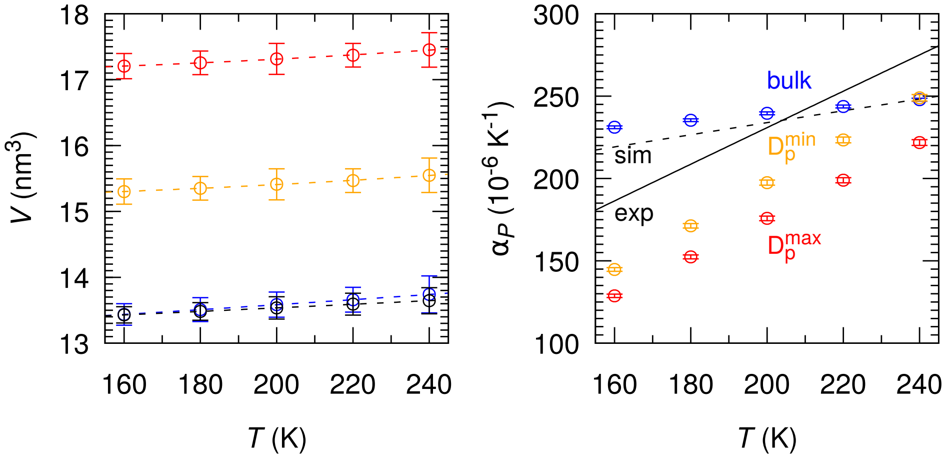

Figure 5.5 (color online) Volume (V, *left*) and thermal expansion (α_P, *right*) of bulk and confined methane hydrate as a function of temperature T at $P = 100$ atm. Two different ensembles were considered for bulk methane hydrate: NPT ensemble (blue circles) and NP_zT ensemble (black circles). For confined methane hydrate, a minimum value D_p^{min} (orange circles) and a maximum value D_p^{max} (red circles) of the pore width were considered. The dashed lines (*left*) are linear fits. The solid black line are experimental data while the dashed black line (*right*) are simulation data for bulk methane hydrate (Ning et al., 2012, 2015).

(1) the isothermal compressibility, κ_T^{Φ}, for bulk phase is determined using molecular dynamics in the NPT ensemble,

$$\kappa_T^{\Phi} = -\frac{1}{V}\left(\frac{\partial V}{\partial P}\right)_T \tag{5.10}$$

(2) the isothermal compressibility, $\kappa_{T,pore}^{\Phi,dmax}$ and $\kappa_{T,pore}^{\Phi,dmin}$, for the confined phases is determined using the piston method,

$$\begin{aligned}
\kappa_{T,pore}^{\Phi,dmin} &= -\frac{1}{V_{pore}^{dmin}}\left(\frac{\partial V_{pore}^{dmin}}{\partial P_{zz}}\right)_T \\
\kappa_{T,pore}^{\Phi,dmax} &= -\frac{1}{V_{pore}^{dmax}}\left(\frac{\partial V_{pore}^{dmax}}{\partial P_{zz}}\right)_T
\end{aligned} \tag{5.11}$$

(3) the isothermal compressibility, $\kappa_{T,P_{zz}}^{\Phi}$, for the bulk phase is determined using molecular dynamics in the $NP_{zz}T$ ensemble,

$$\kappa_{T,Pzz}^{\Phi} = \frac{1}{V_z}\left(\frac{\partial V_z}{\partial P_{zz}}\right)_T \tag{5.12}$$

The volume and the isothermal compressibility as a function of pressure P (or pressure component P_{zz}) for liquid water and methane hydrate are shown in Figures 5.6 and 5.7. For both liquid water and methane hydrate, the volumes obtained using different simulations (V^{L}, V_z^{L}, $V_{pore}^{\mathrm{L},dmin}$, and $V_{pore}^{\mathrm{L},dmax}$ for liquid water and V^{H}, V_z^{H}, $V_{pore}^{\mathrm{H},dmin}$, and $V_{pore}^{\mathrm{H},dmax}$ for methane hydrate) decrease as the pressure increases. As a result, positive values of the isothermal compressibility are always observed for both methane hydrate and liquid water. For both bulk and confined liquid water (see Figure 5.6), the isothermal compressibility (κ_T^{L}, $\kappa_{T,pore}^{\mathrm{L},dmin}$, and $\kappa_{T,pore}^{\mathrm{L},dmax}$) increases with pressure. Confinement decreases the isothermal compressibility of liquid water: $\kappa_T^{\mathrm{L}} > \kappa_{T,pore}^{\mathrm{L},dmin} > \kappa_{T,pore}^{\mathrm{L},dmax}$. The isothermal compressibility of bulk methane hydrate (κ_T^{H}) increases with pressure while the isothermal compressibility ($\kappa_{T,pore}^{\mathrm{H},dmin}$ and $\kappa_{T,pore}^{\mathrm{H},dmax}$) of confined methane hydrate decreases with increasing pressure. Compared with bulk methane hydrate, confinement increases the isothermal compressibility at low pressure $P < 500$ atm ($\kappa_T^{\mathrm{H}} < \kappa_{T,pore}^{\mathrm{H},dmax} < \kappa_{T,pore}^{\mathrm{H},dmin}$) while it decreases the isothermal compressibility at high pressure $P > 500$ atm ($\kappa_T^{\mathrm{H}} > \kappa_{T,pore}^{\mathrm{H},dmin} > \kappa_{T,pore}^{\mathrm{H},dmax}$).

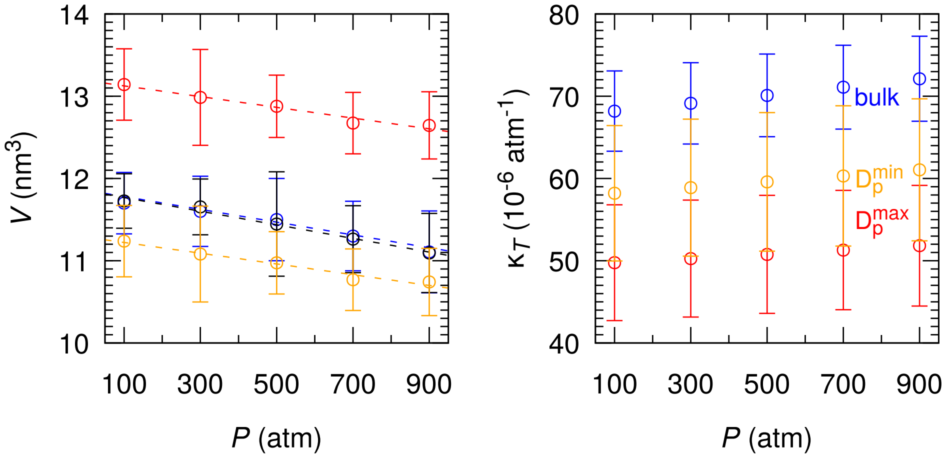

Figure 5.6 (color online) Volume (V, *left*) and isothermal compressibility (κ_T, *right*) of bulk and confined liquid water as a function of pressure P at $T = 240$ K. Two different ensembles were considered for bulk liquid water: NPT ensemble (blue circles) and NP_zT ensemble (black circles). For confined liquid water, a minimum value D_p^{min} (orange circles) and a maximum value D_p^{max} (red circles) of the pore width were considered. The dashed lines are linear fits.

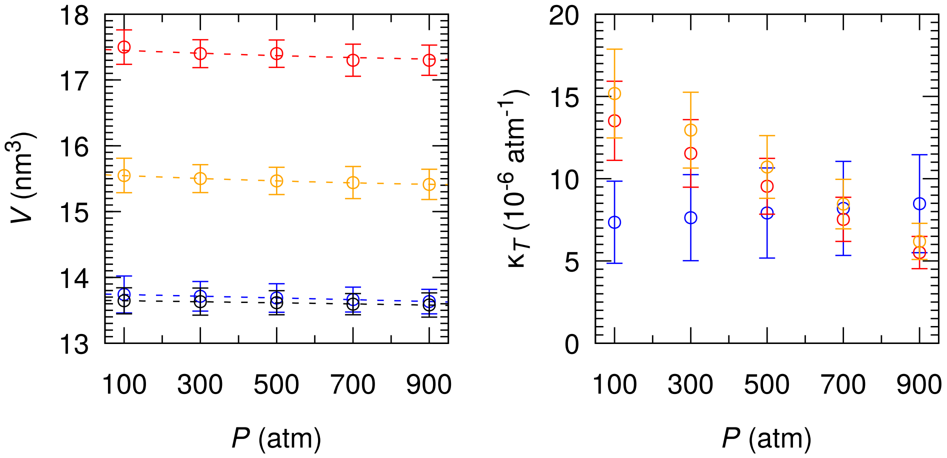

Figure 5.7 (color online) Volume (V, *left*) and isothermal compressibility (κ_T, *right*) of bulk and confined methane hydrate as a function of pressure P at $T = 240$ K. Two different ensembles were considered for bulk methane hydrate: NPT ensemble (blue circles) and NP_zT ensemble (black circles). For confined methane hydrate, a minimum value D_p^{min} (orange circles) and a maximum value D_p^{max} (red circles) of the pore width were considered. The dashed lines are linear fits.

5.4 Thermal conductivity

In this work, the thermal conductivity of bulk (λ) and confined (λ_N and λ_T are tangential and normal components) methane hydrate are determined using molecular dynamics simulation. The details of these molecular dynamics simulations can be found in Section 5.1.3. To determine λ, λ_N and λ_T, the heat-flux vectors are first determined using Eq. (5.1). Then, the (normalized) autocorrelation functions of these heat-flux vectors for bulk methane hydrate, $h(t)$, and for confined methane hydrate, $h_T(t)$ and $h_N(t)$, are estimated using Eqs. (5.2) and (5.3). Figure 5.8 shows these autocorrelation functions at $T = 250$ K – $h(t)$ (*left*), $h_T(t)$ and $h_N(t)$ (*right*) – as obtained from our simulations. we also show the autocorrelation function $h(t)$ obtained by English et al. for bulk methane hydrate. We obtained data for bulk methane hydrate that are consistent with those reported by English et al. (English and Tse, 2009; English et al., 2009). For confined methane hydrate, the tangential component $h_T(t)$ shows a similar trend as $h(t)$ for bulk methane hydrate but with a slight different oscillation frequency. The normal component $h_N(t)$ exhibits two oscillation frequencies.

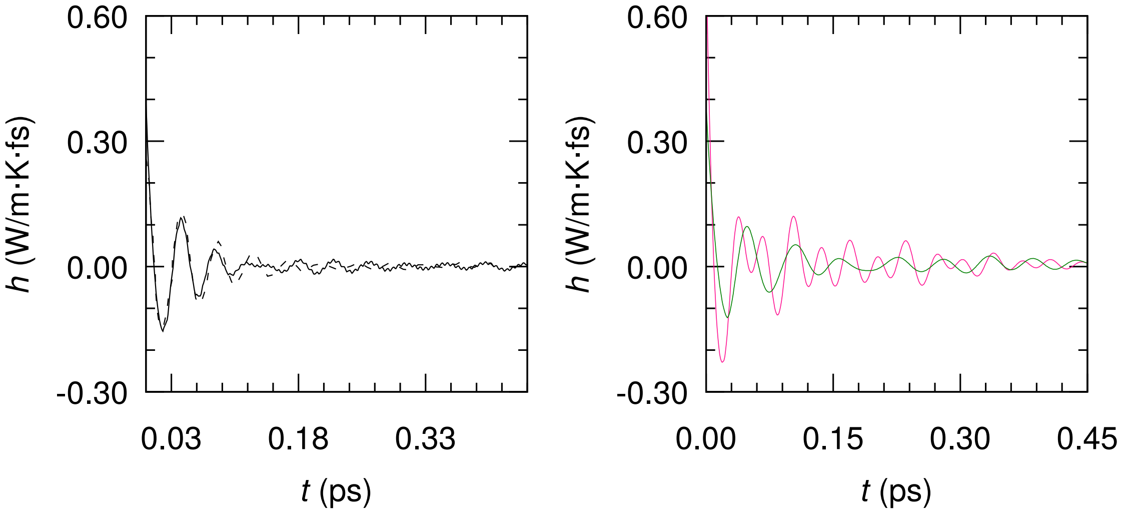

Figure 5.8 (color online) Autocorrelation function of the heat-flux vector, $h(t)$, as a function of time, t, for bulk (*left*) and confined (*right*) methane hydrate. For bulk methane hydrate, the black solid line is from this work while the black dashed line is from English et al. (English and Tse, 2009; English et al., 2009). For confined methane hydrate, the red solid line is the tangential component $h_N = V/k_B T \langle J_z(t) J_z(0) \rangle$ while the green solid line is the normal component $h_T = V/2k_B T \left\langle J_x(t) J_x(0) + J_y(t) J_y(0) \right\rangle$.

As described in Section 5.1.3, we can use Eq. (5.4) to fit these autocorrelation functions. These fits require us to separate the acoustic and optical modes. We take the Fourier transform of Eq. (5.4):

$$\mathscr{F}[\upsilon]=\sum_{i=1}^{n_{ac}} A_i \frac{\tau_i^{-1}}{\upsilon^2+\tau_i^{-2}}+\sum_{j=1}^{n_{op}}\left[\sum_{k=1}^{n_{op,j}} B_{jk} \frac{\tau_{jk}^{-1}}{\left(\upsilon-\omega_j\right)^2+\tau_{jk}^{-2}}\right] \tag{5.13}$$

We recall that the residual terms corresponding to $\sum_j^{n_{op}} C_j \cos\omega_j$ are omitted in this equation as it leads to a Dirac peak when calculating the Fourier transform (see Section 5.1.3). In the Fourier space, the acoustic modes (including short, medium, and long range) are centered around zero frequency while the optical modes are centered around a localized vibration frequency, i.e., w_j. The power spectra obtained using Fourier transform are shown in Figure 5.9. For bulk methane hydrate, one optical mode with the oscillation frequency $\omega_1 = 148.3$ rad/ps is found. For the tangential component of confined methane hydrate, only one optical mode with $\omega_1 = 115.5$ rad/ps is also found. For the normal component of confined methane hydrate, two optical modes with $\omega_1 = 137.7$ rad/ps and $\omega_2 = 186.7$ rad/ps are found. To obtain the acoustic contributions, a low-pass filter approach is adopted as first described by English et al. (English and Tse, 2009; English et al., 2009). The optical modes are first removed from the Fourier transform of the autocorrelation of the heat-flux (i.e., set zero for $\upsilon > 350$ cm^{-1}). Then, we calculate the inverse Fourier transform to obtain the acoustic modes. In so doing, the acoustic and optical modes are separated using inverse Fourier transforms of the power spectrum $\mathscr{F}(\upsilon)$. Figure 5.10 shows the separated acoustic and optical modes for bulk methane hydrate. We use these two plots to determine the relaxation times, τ_i and τ_{jk}, and amplitudes, A_i, B_{jk}, and C_j, for each component of the acoustic and optical modes in Eq. (5.4). On the one hand, all the maximum/peak points of the autocorrelation functions ($h(t)$, $h_T(t)$ and $h_N(t)$) are taken to fit the optical modes. On the other hand, a smoothed form for the acoustic modes is constructed by taking the function values of the inverse Fourier transform at half-way in time between two peaks of the optical modes. This treatment aims at eliminating the artificial periodicity introduced by the square cut-off when we perform the low-pass filter. These maxima and smoothed points are also shown in Figure 5.11 using a logarithm scale.

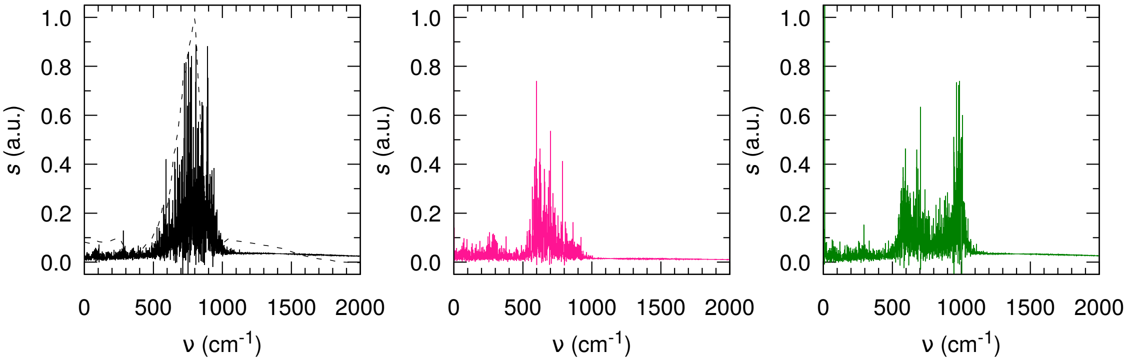

Figure 5.9 (color online) Fourier transform $\mathscr{F}[\upsilon]$ of the autocorrelation function of the heat-flux for bulk ($h(t)$, *left*) and confined ($h_T(t)$, *center*; $h_N(t)$, *right*) methane hydrate. For bulk methane hydrate, the black solid line is from this work while the black dashed line is from English et al. (English and Tse, 2009; English et al., 2009). For confined methane hydrate, the red solid line is for $h_N = V/k_BT\,\langle J_z(t)J_z(0)\rangle$ while the green solid line is for $h_T = V/2k_BT\,\left\langle J_x(t)J_x(0)+J_y(t)J_y(0)\right\rangle$.

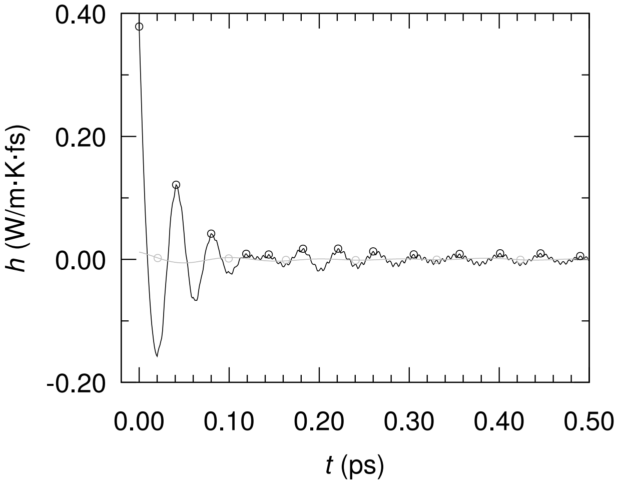

Figure 5.10 Inverse Fourier transform of the power spectrum for bulk methane hydrate. The acoustic mode (gray line) and optical mode (black line) are separated as described in the text. The maxima/peaks of the optical modes (black circles) and the smoothed points for the acoustic modes (gray circles) are considered to determine the relaxation time and amplitudes (*see text*).

Until now, we obtained all the points needed to fit the acoustic modes (smoothed points) and the optical modes (maxima/peaks). Piecewise linear fits are then applied to the acoustic and optical modes as shown in Figure 5.11. On the one hand, three linear fits are performed to determine the signal corresponding to the acoustic modes: A_{sh} and τ_{sh} for the short-range contribution, A_{me} and τ_{me} for the medium-range contribution, and A_{lg} and τ_{lg} for the long-range contribution. On the other hand, another three (more if the system has more optical modes) linear fits are performed to determine the signal corresponding to the optical modes: B_{11} and τ_{11} for the short-range contribution, B_{12} and τ_{12} for the long-range contribution, and C_1 for the constant term. Using the fitting results (i.e., relaxation time τ and oscillation amplitudes A, B, C) given above as the initial parameters, two overall fits are then performed: one is for the acoustic and the other one is for the optical modes. These fits results are also shown in Figure 5.11. The final fit results were used to determine the corresponding thermal conductivity in Eqs. (5.2) and (5.3),

$$\lambda = \int_0^\infty h(t)dt = \sum_i^{n_{ac}} A_i\tau_i + \sum_j^{n_{op}} \left[\sum_k^{n_{op,j}} \frac{B_{jk}\tau_{jk}}{1+(\tau_{jk}\omega_j)^2} \right] \tag{5.14}$$

In practice, the fit of the acoustic modes given above is accurate for bulk methane hydrate (see Figure 5.11 (*right top*)) while not for confined methane hydrate (see Figure 5.11 (*right center*) and (*right bottom*)). On the one hand, Figure 5.11 (*right center*) shows that the fit does not work well for the acoustic modes of the tangential component of confined methane hydrate. Therefore, the trapezoidal integration algorithm is also used to estimate the total (including acoustic and optical modes) tangential component of the thermal conductivity of confined methane hydrate. On the other hand, Figure 5.11(*right bottom*) indicates that the acoustic modes for the normal component exhibits a low-frequency oscillated decay. According to the Fourier transform, as shown in Figure 5.9, the oscillation frequency reads $\omega = 1.2612$ rad/ps. Considering this observation, the fit equation for the acoustic modes of the normal component of the confined methane hydrate is rewritten as,

$$h(t) = \sum_{i=1}^{n_{ac}} A_i \exp\left(-t/\tau_i\right)\cos\left(\omega_i t\right) + \sum_{j=1}^{n_{op}} \left[\sum_{k=1}^{n_{op,j}} B_{ij} \exp\left(-t/\tau_{jk}\right) \right] \cos\omega_j t + \sum_{j=1}^{n_{op}} C_j \cos\omega_j t \tag{5.15}$$

and the corresponding integration reads,

$$\lambda_N = \int_0^\infty h(t)dt = \sum_i^{n_{ac}} \frac{A_i\tau_i}{1+(\tau_i\omega_i)^2} + \sum_j^{n_{op}} \left[\sum_k^{n_{op,j}} \frac{B_{jk}\tau_{jk}}{1+(\tau_{jk}\omega_j)^2} \right] \tag{5.16}$$

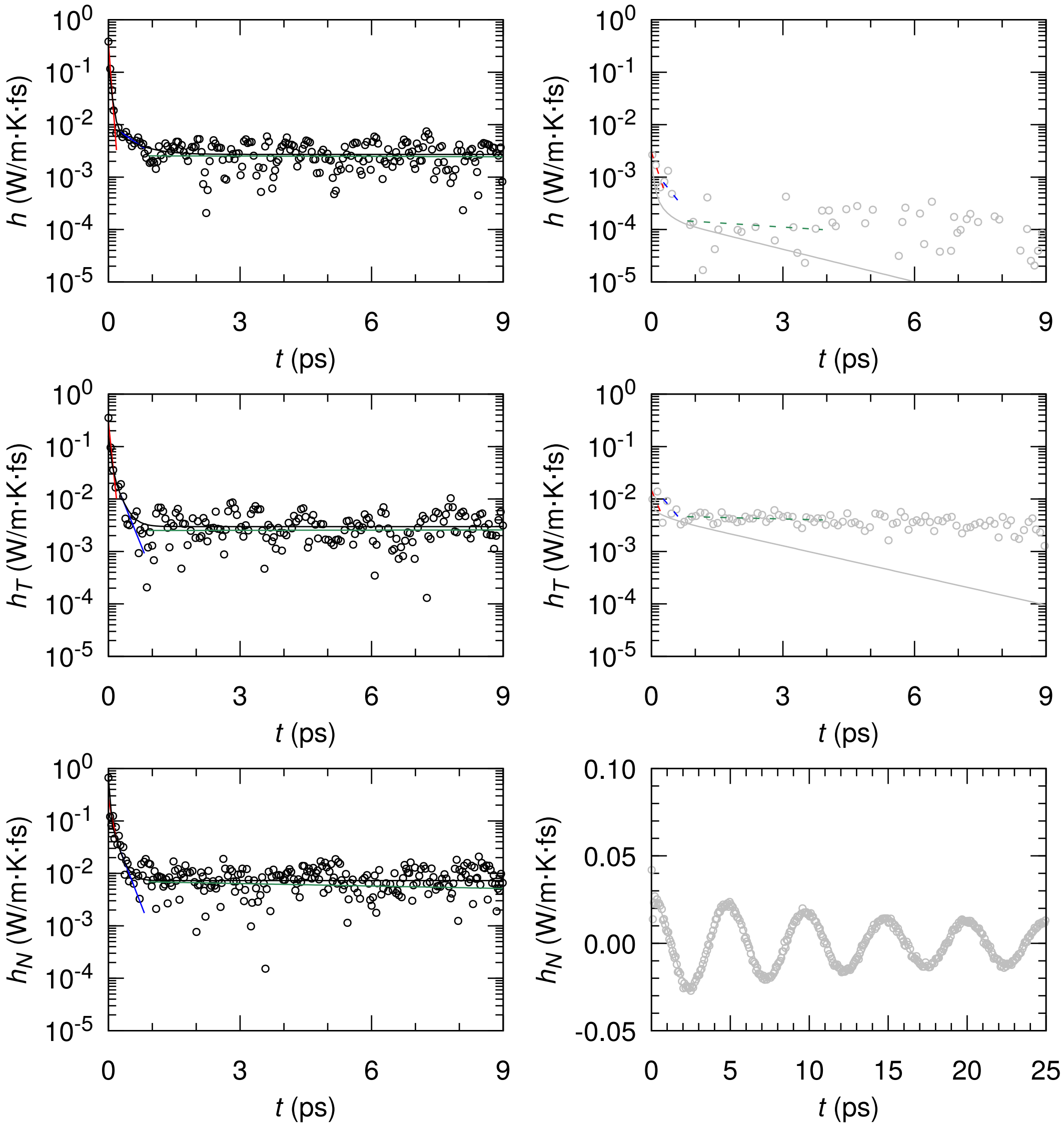

Figure 5.11 (color online) Piecewise linear fits applied to the acoustic – smoothed points – (gray circles, *right panels*) and optical – maxima/peaks – (black circles, *left panels*) modes for bulk methane hydrate (*top panels*) and the tangential (*center panels*) and normal (*bottom panels*) components of confined methane hydrate. Piecewise linear fits for optical modes are shown for short-range (red solid lines), long-range (blue solid lines), and constant term (green solid lines) terms. for $h_N(t)$, two optical modes are included but only one optical mode ($\omega_j = 186.7$ rad/ps) is shown here (the fit results for the other one are shown in Table 5.2). Piecewise linear fits for acoustic modes are shown for short-range (red hashed lines), medium-range (blue dashed lines), and long-range (green dashed lines) terms. The black solid lines are for overall optical fits while the gray solid lines are for overall acoustic fits.

All the data related to the fits are summarized in Tables 5.1 and 5.2. These calculations lead to $\lambda = 0.616$ W/mK, $\lambda_T = 1.857$ (using trapezoidal integration) – 20.743 W/mK (using energy transfer fits), and $\lambda_N = 0.729$ W/mK. The value obtained in this work for bulk methane hydrate is close to the simulation data ($\lambda = 0.64$ W/mK) reported by English et al. (English and Tse, 2009; English et al., 2009) and experimental data (0.68 (Rosenbaum et al., 2007) and 0.62 (Waite et al., 2007)). Confinement increases the thermal conductivity of confined methane hydrate, especially for the tangential component: $\lambda < \lambda_N < \lambda_T$.

Table 5.1 Relaxation times, τ_i (in ps), and amplitude, A_i (in W/mKfs), from the overall fit of the acoustic modes. Contributions, λ_i (in W/mK), of each component to the thermal conductivity, λ_{ac} (in W/mK), of acoustic modes are also listed. * is for the oscillated acoustic mode with the frequency – $\omega_{sh} = 1.2612$ rad/ps.

obj.	A_{sh}	τ_{sh}	λ_{sh}	A_{me}	τ_{me}	λ_{me}	A_{lg}	τ_{lg}	λ_{lg}	λ_{ac}
$h(t)$	0.0014	0.0455	0.063	0.0004	0.2001	0.073	0.0002	2.1069	0.369	0.504
$h_T(t)$	0.0022	0.0453	0.100	0.0016	0.3027	0.497	0.0047	4.2780	20.146	20.743
$h_N(t)^*$	0.0261	29.0935	0.564	–	–	–	–	–	–	0.564

Table 5.2 Relaxation times, τ_{jk} (in ps), and amplitude, B_{jk} (in W/mKfs), from the overall fit of the optical modes. The oscillation frequencies, ω_j (in rad/ps) obtained from the power spectra are also listed. Contributions, λ_j (in W/mK), of each component to the thermal conductivity, λ_{op} (in W/mK), of optical modes are also listed. The final thermal conductivity is shown here.

obj.	ω_j	τ_{jk}	B_{jk}	λ_{jk}	τ_{jk}	B_{jk}	λ_{jk}	C_j	λ_{op}	λ
$h(t)$	148.3	0.0534	0.1331	0.112	0.4567	0.0065	0.001	0.0027	0.113	0.616
$h_T(t)$	115.1	0.0428	0.1120	0.190	0.1692	0.0449	0.020	0.0032	0.210	20.953
$h_N(t)$	186.7	0.0462	0.1484	0.091	0.1882	0.1408	0.022	0.0030	0.112	0.729
	137.7	0.1225	0.1228	0.053	–	–	–	0.0003	0.0527	

5.5 Conclusion

In this chapter, we use molecular dynamics simulation to determine the confinement effects on the physical and physicochemcial properties of methane hydrate such as structure, thermal coefficients, and thermal conductivity. For bulk system, these thermodynamics are determined using molecular dynamics in the isobaric-isothermal ensemble. For confined system, the piston method are applied to determine these thermodynamics at desired temperature and pressure. First, structural profiles, including density and local bond order parameters are determined. Confinement increases the ordered structure of liquid water but slightly affects the structure of methane hydrate. Then, the thermal expansion and isothermal compressibility of bulk and confined methane hydrate/liquid water are also determined. For both methane hydrate and liquid water, their thermal expansions determined using the $NP_{zz}T$ ensemble are close to the results obtained using the NPT ensemble, as well for isothermal compressibility. On the one hand, at the temperature considered in this work, confinement decreases the thermal expansion of liquid water and methane hydrate. On the other hand, at the pressure considered in this work, confinement also decreases the isothermal compressibility of liquid water but increases or decreases that of methane hydrate relates to the pressure. Finally, the thermal conductivity of bulk and confined methane hydrate are also addressed using the Green-Kubo formalism. We reproduced the thermal conductivity of bulk methane hydrate. As compared with bulk methane hydrate, confined methane hydrate exhibits different autocorrelation function of the heat-flux: the tangential component shows a lower oscillation frequency for the optical mode while the normal component exhibits two optical modes and one oscillated acoustic mode. Our data suggest that confinement increases the thermal conductivity for both the tangential and normal components.

Conclusions and Perspectives

Methane hydrate, which is a crystalline structure made of water molecules forming a network of hydrogen-bonded cages around methane molecules, is important for many applications in the field of environment and energy science. In nature, methane hydrate is often confined at the surface or inside porous rocks and media where it interacts with mineral surfaces. Understanding the role of these confinement and surface effects on the thermodynamics and dynamics of methane hydrate is an important concern. In this thesis, different molecular simulation strategies were used to assess the structure, phase stability, formation kinetics, and physical properties of methane hydrate confined at the nanoscale. First, different molecular simulation strategies, including free energy calculations using the Einstein molecule approach, the hyperparallel tempering technique, and the direct coexistence method, are used to determine the phase stability of bulk methane hydrate. Then, the direct coexistence method is chosen to determine the phase stability of confined methane hydrate. To describe the shift in melting temperature, we also revisit the Gibbs-Thomson equation. We also use molecular dynamics to determine the thermodynamic parameters in the Gibbs-Thomson equation ans address its validity. Finally, free energy calculations using the umbrella sampling technique are performed to determine the formation/dissociation kinetics of bulk and confined methane hydrate. In addition, confinement effects on several physical and physicochemical properties of methane hydrate are also determined. Our findings are as follows:

(1) Using different molecular simulation strategies, the pressure–temperature phase diagram for bulk methane hydrate is determined. In this part, we found that the

choice of TIP4P/Ice water and OPLS-UA methane models allows one to reproduce the phase diagram of methane hydrate. The data presented in the present work are consistent with previous molecular simulation works and the experimental phase diagram of methane hydrate.

(2) Using the direct coexistence method, decreased melting temperatures are observed for confined methane hydrate with respect to bulk methane hydrate. In other words, the shift in melting temperature of confined methane hydrate is negative $\Delta T_m = T_m^{pore} - T_m^{bulk} < 0$.

(3) The Gibbs-Thomson equation is revisited, and several thermodynamic parameters needed in this equation are determined using molecular dynamics. Compared with the liquid-substrate surface tension, a larger hydrate-substrate surface tension is observed, $\gamma_{LS} - \gamma_{HS} < 0$. The data obtained using the direct coexistence method are found to be consistent with the Gibbs-Thomson equation determined using molecular dynamics. The shift in the melting point is found to be quantitatively described using the Gibbs–Thomson equation, which predicts that the shift in melting point linearly depends on the reciprocal of the pore width.

(4) Using the umbrella sampling technique, the free energy barriers between methane hydrate and liquid water are determined. We found that confinement decreases these free energy barriers and leads to faster formation/dissociation kinetics of methane hydrate.

(5) Confinement decreases the thermal expansion and isothermal compressibility of methane hydrate.

Despite the suitability of molecular simulation to determine confinement effects on the physics of methane hydrate, many challenges are still to be faced:

(1) Understanding formation/dissociation mechanisms. Faster formation/dissociation kinetics (corresponding to a decreased free energy barrier) was observed in this PhD

work. However, understanding the growth mechanism of methane hydrate in porous materials remains to be achieved as it is important for practical applications.

(2) Understanding surface chemistry effects and salt effects on the thermodynamics and dynamics of methane hydrate. Natural porous materials exhibit various surface chemistries (chemical composition, hydrophilicity/hydrophobicity, heterogeneity/homogeneity, etc.). These differences should be considered to mimic real environmental conditions. For methane hydrate trapped in marine sediments, salt in seawater could also have drastic effects on phase stability of methane hydrate.

(3) Knowledge transfer to other gas hydrates. Understanding the role of confinement on methane hydrate should allow one to explore other gas hydrates (e.g., carbon dioxide, nitrogen, hydrogen, other hydrocarbons, etc.) and other clathrate structures (e.g., zeolites, Metal Organic Frameworks, etc.).

(4) Decreasing computational costs. A large free energy barrier between methane hydrate and liquid water leads to slow formation kinetics. Such a low nucleation rate requires to perform large-scale molecular dynamics or Monte Carlo simulations combined with free energy calculations. In this PhD work, we used the grand canonical ensemble as it simplifies the calculations to determine the L–H–V phase equilibrium. Despite the success of these calculations, they still require extensive computational resources.

Conclusions et Perspectives

L’hydrate de méthane, une structure cristalline constituée de molécules d’eau formant un réseau de cages liés par liaison hydrogène autour de molécules de méthane, est important pour de nombreuses applications dans le domaine de l’environnement et de l’énergie. Dans la nature, l’hydrate de méthane est souvent confiné à la surface ou à l’intérieur de roches poreuses où il interagit avec des surfaces minérales. Comprendre le rôle de ces effets de confinement et de surface sur la thermodynamique et la dynamique de l’hydrate de méthane est une préoccupation importante. Dans cette thèse, différentes stratégies de simulation moléculaire ont été utilisées pour évaluer la structure, la stabilité, la cinétique de formation et les propriétés physiques de l’hydrate de méthane confiné à l’échelle nanométrique. Premièrement, différentes stratégies de simulation moléculaire, y compris des calculs d’énergie libre utilisant l’approche de la molécule d’Einstein, la technique *hyperparallel tempering* et la méthode de la coexistence directe, sont utilisées pour déterminer la stabilité de la phase d’hydrate de méthane non confinée. Ensuite, la méthode de la coexistence directe est choisie pour déterminer la stabilité de l’hydrate de méthane nanoconfinée. Pour décrire le changement de température de fusion, nous redérivons l’équation de Gibbs-Thomson. Nous utilisons également la dynamique moléculaire pour déterminer les paramètres thermodynamiques de cette équation de Gibbs-Thomson et en évaluer sa validité. Enfin, des calculs d’énergie libre utilisant la technique umbrella sampling sont effectués pour déterminer la cinétique de formation/dissociation de l’hydrate de méthane non confiné et confiné. En outre, l’effet de confinement sur plusieurs propriétés physiques et physicochimiques de l'hydrate de méthane est également déterminé. Nos constatations sont les suivantes:

(1) En utilisant différentes stratégies de simulation moléculaire, le diagramme de phase pression-température pour l'hydrate de méthane non confiné est déterminé. Dans cette partie, nous avons constaté que le choix des modèles de méthane TIP4P / Ice Water et OPLS-UA est important pour reproduire le diagramme de phase de l'hydrate de méthane. Les données présentées dans ce travail sont en bon accord avec des travaux antérieurs de simulation moléculaire mais aussi le diagramme de phase expérimental de l'hydrate de méthane.

(2) En utilisant la méthode de la coexistence directe, des températures de fusion diminuées sont observées pour l'hydrate de méthane confiné par rapport à l'hydrate de méthane non confiné. En d'autres termes, le décalage de la température de fusion de l'hydrate de méthane confiné est négatif. $\Delta T_m = T_m^{pore} - T_m^{bulk} < 0$.

(3) L'équation de Gibbs-Thomson est revue et plusieurs paramètres thermodynamiques nécessaires dans cette équation sont déterminés en utilisant la dynamique moléculaire. En comparaison avec la tension de surface entre le liquide et le substrat, on observe une tension superficielle hydrate-substrat plus importante, $\gamma_{LS} - \gamma_{HS} < 0$. Les données obtenues à l'aide de la méthode de coexistence directe sont cohérentes avec l'équation de Gibbs-Thomson. Le déplacement du point de fusion est décrit de manière quantitative en utilisant l'équation de Gibbs-Thomson, qui prédit que le décalage du point de fusion dépend linéairement de l'inverse de la taille des pores.

(4) En utilisant la technique umbrella sampling, les barrières d'énergie libre entre l'hydrate de méthane et l'eau liquide sont déterminées. Nous avons constaté que le confinement diminue ces barrières d'énergie libre et conduit à une cinétique de formation/dissociation plus rapide de l'hydrate de méthane.

(5) Le confinement diminue la dilatation thermique et la compressibilité isotherme de l'hydrate de méthane.

Malgré la pertinence de la simulation moléculaire pour déterminer les effets du confinement sur la physique de l'hydrate de méthane, de nombreux défis restent à relever:

(1) Comprendre les mécanismes de formation/dissociation. Une cinétique de formation/dissociation plus rapide (correspondant à une diminution de la barrière d'énergie libre) a été observée dans ce travail de thèse. Cependant, il reste à comprendre le mécanisme de croissance de l'hydrate de méthane dans les matériaux poreux.

(2) Comprendre les effets de la chimie de surface et les effets de sel sur la thermodynamique et la dynamique de l'hydrate de méthane. Les matériaux poreux naturels présentent diverses chimies de surface (composition chimique, hydrophilie/hydrophobie, hétérogénéité/homogénéité, etc.). Ces différences doivent être considérées pour imiter les conditions environnementales réelles. Pour l'hydrate de méthane piégé dans les sédiments marins, le sel dans l'eau de mer pourrait également avoir des effets importants sur la stabilité de la phase de l'hydrate de méthane.

(3) Transfert de connaissances vers d'autres hydrates de gaz. Comprendre le rôle du confinement sur l'hydrate de méthane devrait permettre d'explorer d'autres hydrates de gaz (par exemple le dioxyde de carbone, l'azote, l'hydrogène, d'autres hydrocarbures, etc.) et d'autres structures de clathrates (zéolithes, Metal Organic Framework, etc.).

(4) Coûts de calcul. Une grande barrière d'énergie libre entre l'hydrate de méthane et l'eau liquide conduit à une cinétique de formation lente. Une vitesse de nucléation aussi faible nécessite d'effectuer des simulations moléculaires à grande échelle ou des simulations Monte Carlo ou de dynamique moléculaire combinées à des calculs d'énergie libre. Dans cette thèse, nous avons utilisé l'ensemble grand canonique car il simplifie les calculs pour déterminer l'équilibre de phase L–H–V. Malgré le succès de ces calculs, ils nécessitent encore des ressources informatiques considérables.

Appendix A

Einstein Molecule Approach

A.1 Vectors a and b

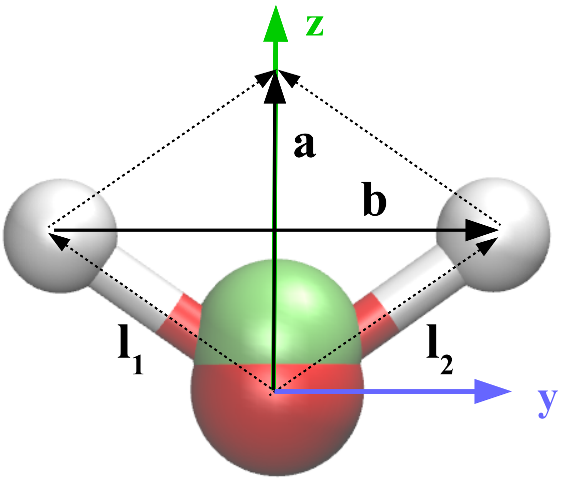

Figure A.1 Definition of the normalized vectors **a** and **b** in the 4-site rigid water molecule (TIP4P/2005 and TIP4P/Ice). These two vectors are formed by the subtraction $\mathbf{a} = (\mathbf{l}_1 - \mathbf{l}_2)/|\mathbf{l}_1 - \mathbf{l}_2|$ and summation $\mathbf{b} = (\mathbf{l}_1 + \mathbf{l}_2)/|\mathbf{l}_1 + \mathbf{l}_2|$ of the two bond vectors, $\mathbf{l}_1$ and $\mathbf{l}_2$. The red and white spheres are the oxygen and hydrogen atoms, respectively. The green sphere is the electronic site M of the oxygen atom.

A.2 Free energy of non-interacting Einstein molecule A_{A}

From the canonical partition function, Q_{A}, we obtain the Helmholtz free energy of the non-interacting Einstein molecule, A_{A},

$$\frac{A_{\mathrm{A}}}{Nk_BT} = -\frac{1}{N}\ln\left(Q_{\mathrm{A}}\right) \tag{A.1}$$

For N water molecules distributed in a periodic box of volume V, Q_{A} reads:

$$Q_{\mathrm{A}} = \frac{(q_t q_r q_v q_e)^N}{N!}\int\cdots\int \exp\left(-\frac{U_{\mathrm{A}}\left(\mathbf{r}_1,\phi_1,\cdots,\mathbf{r}_N,\phi_N\right)}{k_BT}\right)\times d\mathbf{r}_1 d\phi_1\cdots d\mathbf{r}_N d\phi_N \tag{A.2}$$

where $q_t = V\Lambda^{-3}$ is the individual translational partition function while q_r, q_v, q_e are the individual rotational, vibrational, and electronic partition functions, respectively. q_r, q_v, q_e are dimensionless and are identical in the two coexisting phases, so that we assign them an arbitrary value of one. The harmonic potential energy U_{A} includes the translation $U_{\mathrm{A},T}$ and rotation $U_{\mathrm{A},R}$ contributions:

$$\begin{aligned} U_{\mathrm{A}} &= U_{\mathrm{A}}\left(\mathbf{r}_1,\phi_1,\cdots,\mathbf{r}_N,\phi_N\right) \\ &= U_{\mathrm{A},T}\left(\mathbf{r}_1,\cdots,\mathbf{r}_N\right) + U_{\mathrm{A},R}\left(\phi_1,\cdots,\phi_N\right) = U_{\mathrm{A},T} + U_{\mathrm{A},R} \end{aligned} \tag{A.3}$$

where $U_{\mathrm{A},T}$ only depends on the positions $\mathbf{r}_i$ of the N molecules while $U_{\mathrm{A},R}$ depends on their two vector angles, $\phi_i = \left(\phi_{\mathbf{a},i},\phi_{\mathbf{b},i}\right)$. Q_{A} can be recast as:

$$\begin{aligned} Q_{\mathrm{A}} &= \frac{1}{N!\Lambda^{3N}}\int\cdots\int \exp\left(-\frac{U_{\mathrm{A}}}{k_BT}\right)\times d\mathbf{r}_1 d\phi_1\cdots d\mathbf{r}_N d\phi_N \\ &= \frac{1}{N!\Lambda^{3N}}\int\cdots\int \exp\left(-\frac{U_{\mathrm{A},T}+U_{\mathrm{A},R}}{k_BT}\right)\times d\mathbf{r}_1 d\phi_1\cdots d\mathbf{r}_N d\phi_N \\ &= \frac{1}{N!\Lambda^{3N}}\int\cdots\int \exp\left(-\frac{U_{\mathrm{A},T}}{k_BT}\right)\times d\mathbf{r}_1\cdots d\mathbf{r}_N \int\cdots\int \exp\left(-\frac{U_{\mathrm{A},R}}{k_BT}\right)\times d\phi_1\cdots d\phi_N \\ &= Q_{\mathrm{A},T}Q_{\mathrm{A},R} \end{aligned} \tag{A.4}$$

Q_{A} can be viewed as the product of the translation contribution $Q_{\mathrm{A},T}$ (the term $\frac{1}{N!\Lambda^{3N}}$ is included in $Q_{\mathrm{A},T}$) and the rotation contribution $Q_{\mathrm{A},R}$. Therefore, A_{A} consists of a translation $A_{\mathrm{A},T}$ and a rotation $A_{\mathrm{A},R}$ contributions, Noya et al. (2008); Vega et al. (2008)

$$\begin{aligned}\frac{A_{\mathrm{A}}}{Nk_BT} &= -\frac{1}{N}\ln\left(Q_{\mathrm{A}}\right) = -\frac{1}{N}\ln\left(Q_{\mathrm{A},T}Q_{\mathrm{A},R}\right) \\ &= -\frac{1}{N}\ln\left(Q_{\mathrm{A},T}\right) - \frac{1}{N}\ln\left(Q_{\mathrm{A},R}\right) \\ &= \frac{A_{\mathrm{A},T}}{Nk_BT} + \frac{A_{\mathrm{A},R}}{Nk_BT}\end{aligned} \tag{A.5}$$

All free energies are normalized by the total thermal energy Nk_BT.

Translation contribution to the free energy of the non-interacting Einstein molecule, $A_{\mathbf{A},T}$. $A_{\mathrm{A},T}$,which arises from $U_{\mathrm{A},T} = U_{\mathrm{A},T}\left(\mathbf{r}_1,\cdots,\mathbf{r}_N\right)$, only depends on the relative positions of the water molecules: the set of positions of all water molecules $\left(\mathbf{r}_1,\cdots,\mathbf{r}_N\right)$ can be rewritten as a set of the relative positions with respect to the first water molecule $\left(\mathbf{r}_1,\mathbf{r}_2-\mathbf{r}_1,\cdots,\mathbf{r}_N-\mathbf{r}_1,\right)$. $Q_{\mathrm{A},T}$ can therefore be rewritten as:

$$\begin{aligned}Q_{\mathrm{A},T} &= \frac{1}{N!\Lambda^{3N}}\int\cdots\int \exp\left(-\frac{U_{\mathrm{A},T}\left(\mathbf{r}_1,\cdots,\mathbf{r}_N\right)}{k_BT}\right)\times d\mathbf{r}_1\cdots d\mathbf{r}_N \\ &= \frac{1}{N!\Lambda^{3N}}\int\cdots\int \exp\left(-\frac{U\left(\mathbf{r}_1,\mathbf{r}_2-\mathbf{r}_1,\cdots,\mathbf{r}_N-\mathbf{r}_1\right)}{k_BT}\right)\times d\mathbf{r}_1 d(\mathbf{r}_2-\mathbf{r}_1)\cdots d(\mathbf{r}_N-\mathbf{r}_N) \\ &= \frac{1}{N!\Lambda^{3N}}\int d\mathbf{r}_1\int\cdots\int \exp\left(-\frac{U\left(\mathbf{r}_2-\mathbf{r}_1,\cdots,\mathbf{r}_N-\mathbf{r}_1\right)}{k_BT}\right)\times d(\mathbf{r}_2-\mathbf{r}_1)\cdots d(\mathbf{r}_N-\mathbf{r}_N) \\ &= \frac{V}{N!\Lambda^{3N}}\int\cdots\int \exp\left(-\frac{U\left(\mathbf{r}_2-\mathbf{r}_1,\cdots,\mathbf{r}_N-\mathbf{r}_1\right)}{k_BT}\right)\times d(\mathbf{r}_2-\mathbf{r}_1)\cdots d(\mathbf{r}_N-\mathbf{r}_N)\end{aligned} \tag{A.6}$$

From the integration corresponding to one permutation (between particles 1 and 2 for instance) $\kappa(U_{\mathrm{A},T})$, the above partition function is the product of $\kappa(U_{\mathrm{A},T})$ with the total number of all possible permutations $(N-1)!$:

$$Q_{\mathrm{A},T} = \frac{(N-1)!V}{N!\Lambda^{3N}}\kappa_T\left(U_{\mathrm{A},T}\right) = \frac{V}{N\Lambda^{3N}}\kappa_T\left(U_{\mathrm{A},T}\right) \tag{A.7}$$

where $\kappa(U_{\mathrm{A},T})$ is the integral for $(N-1)$ 3D oscillators,

$$\begin{aligned}
Q_{\mathrm{A},T} &= \frac{V}{N\Lambda^{3N}}\left(\int_0^{+\infty}\int_0^{\pi}\int_0^{2\pi}\exp\left(-\frac{\lambda_T}{k_BT}r^2\right)r^2 sin\theta dr d\theta d\phi\right)^{(N-1)} \\
&= \frac{V}{N\Lambda^{3N}}\left(4\pi\int_0^{+\infty}\exp\left(-\frac{\lambda_T}{k_BT}r^2\right)r^2 dr\right)^{(N-1)} \\
&= \frac{V}{N\Lambda^{3N}}\left(-\frac{2\pi k_BT}{\lambda_T}\int_0^{+\infty} rd\left[\exp\left(-\frac{\lambda_T}{k_BT}r^2\right)\right]\right)^{(N-1)} \\
&= \frac{V}{N\Lambda^{3N}}\left(\frac{2\pi k_BT}{\lambda_T}\int_0^{+\infty}\exp\left(-\frac{\lambda_T}{k_BT}r^2\right)dr\right)^{(N-1)} \\
&= \frac{V}{N\Lambda^{3N}}\left(\frac{2\pi(k_BT)^{3/2}}{\lambda_T^{3/2}}\frac{\pi^{1/2}}{2}erf(+\infty)\right)^{(N-1)} = \frac{V}{N\Lambda^{3N}}\left(\frac{\pi k_BT}{\lambda_T}\right)^{3(N-1)/2}
\end{aligned} \tag{A.8}$$

Using the last equation, we obtain:

$$\begin{aligned}
\frac{A_{\mathrm{A},T}}{Nk_BT} &= -\frac{1}{N}\ln\left(Q_{\mathrm{A},T}\right) \\
&= \frac{1}{N}\ln\left(\frac{N\Lambda^3}{V}\right) + \frac{3}{2}\left(1-\frac{1}{N}\right)\ln\left(\frac{\Lambda^2\lambda_T}{k_BT\pi}\right)
\end{aligned} \tag{A.9}$$

Rotation contribution to the free energy of the non-interacting Einstein molecule, $A_{\mathrm{A},R}$. $A_{\mathrm{A},R}$ is obtained from $Q_{\mathrm{A},R}$. Each molecule in the Einstein molecule is equivalent and independent, so that $Q_{\mathrm{A},R}$ is the product of the integral for each molecule,

$$\begin{aligned}
\frac{A_{\mathrm{A},R}}{Nk_BT} &= -\frac{1}{N}\ln(Q_{\mathrm{A},R}) \\
&= -\frac{1}{N}\ln\left(\frac{1}{8\pi^2}\int_0^{\pi}\int_0^{2\pi}\int_0^{2\pi}\exp\left\{-\frac{\lambda_R}{k_BT}\left[\sin^2\phi_a+\left(\frac{\phi_b}{\pi}\right)^2\right]\right\}\sin\alpha d\alpha d\varphi d\gamma\right)^N \\
&= -\ln\left(\frac{1}{8\pi^2}\int_0^{\pi}\int_0^{2\pi}\int_0^{2\pi}\exp\left\{-\frac{\lambda_R}{k_BT}\left[\sin^2\phi_a+\left(\frac{\phi_b}{\pi}\right)^2\right]\right\}\sin\alpha d\alpha d\varphi d\gamma\right)
\end{aligned} \tag{A.10}$$

where α, φ, and γ are the Euler angles. The integral above can be simplified as follows:

1. By taking the vector $\mathbf{a}^{(0)}$ as the z-axis so that the Euler angle α is identical to ϕ_a,

$$\frac{A_{\mathrm{A},R}}{Nk_BT} = -\ln\left(\frac{1}{8\pi^2}\int_0^{\pi}\int_0^{2\pi}\int_0^{2\pi}\exp\left\{-\frac{\lambda_R}{k_BT}\left[\sin^2\alpha + \left(\frac{\phi_b}{\pi}\right)^2\right]\right\}\sin\alpha d\alpha d\varphi d\gamma\right) \tag{A.11}$$

2. By considering that the main contribution to the intergral arises from $\alpha \sim 0$ in the case of very large coupling parameters λ_R, and that the Euler angle ϕ_b is identical to γ,

$$\begin{aligned}\frac{A_{\mathrm{A},R}}{Nk_BT} &= -\ln\left(\frac{1}{8\pi^2}\int_0^{\pi}\int_0^{2\pi}\int_0^{2\pi}\exp\left\{-\frac{\lambda_R}{k_BT}\left[\sin^2\alpha + \left(\frac{\gamma}{\pi}\right)^2\right]\right\}\sin\alpha d\alpha d\varphi d\gamma\right) \\ &= -\ln\left(\frac{1}{2\pi}\int_0^{\pi}\exp\left(-\frac{\lambda_R}{k_BT}\sin^2\alpha\right)\sin\alpha d\alpha\int_0^{\pi}\exp\left[-\frac{\lambda_R}{k_BT}\left(\frac{\gamma}{\pi}\right)^2\right]d\gamma\right)\end{aligned} \tag{A.12}$$

which can be simplified as,

$$\begin{aligned}\frac{A_{\mathrm{A},R}}{Nk_BT} &= -\ln\left(\int_0^1\exp\left[-\frac{\lambda_R}{k_BT}\left(1-x^2\right)\right]dx\int_0^1\exp\left(-\frac{\lambda_R}{k_BT}x^2\right)dx\right) \\ &= -\ln\left[\left(\frac{k_BT}{\lambda_R}\right)\mathrm{erfi}\left(\sqrt{\frac{\lambda_R}{k_BT}}\right)\mathrm{erf}\left(\sqrt{\frac{\lambda_R}{k_BT}}\right)\right]\end{aligned} \tag{A.13}$$

A.3 Free energy difference ΔA_1 and ΔA_2

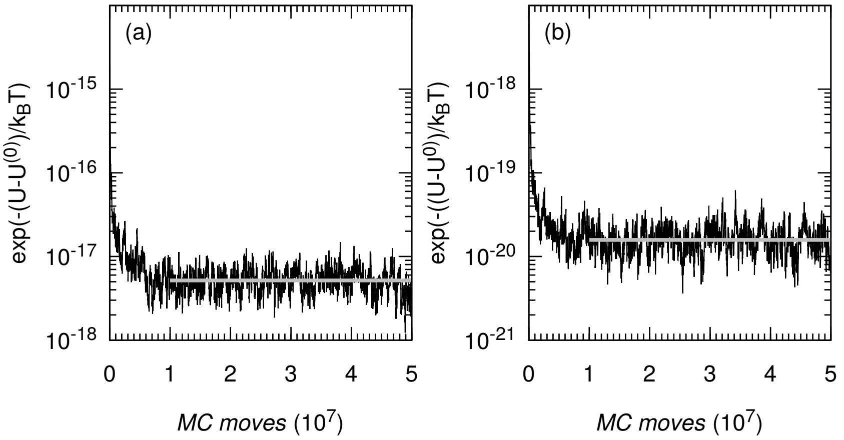

Figure A.2 Intermolecular potential energy U of the zero-occupancy methane hydrate along the canonical ensemble MC simulation at $T = 250$ K and $P = 100$ atm (black line) (only the harmonic potential U_{A^*} is considered in the acceptance probability): (a) TIP4P/2005 water model; (b) TIP4P/Ice water model. Note that the figure shows $\exp\left(-(U-U^{(0)})/k_BT\right)$ where $U^{(0)}$ is the potential energy of the reference lattice system . The gray horizontal line is the canonical ensemble averaged value, $\left\langle \exp\left(-(U-U^{(0)})/k_BT\right)\right\rangle_{NVT}$. All energies are normalized to the thermal energy k_BT.

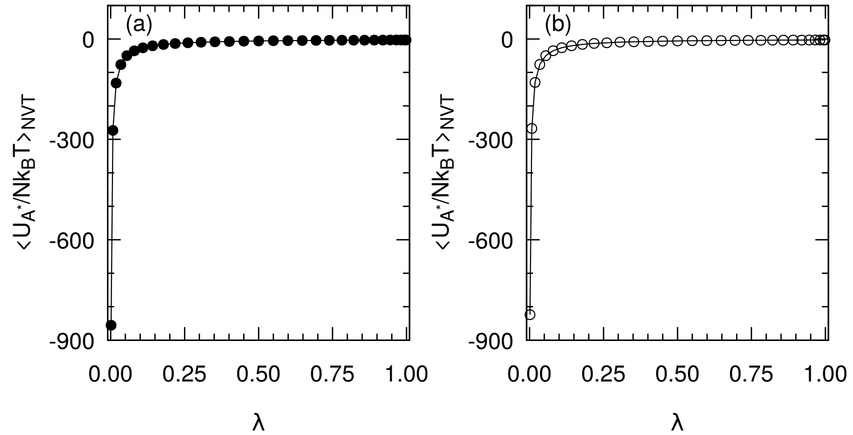

Figure A.3 Canonical ensemble average of the harmonic potential energy U_{A^*} as a function of the coupling parameter λ at $T = 250$ K and $P = 100$ atm: (a) TIP4P/2005 water model (filled circles) and (b) TIP4P/ICE water model (empty circles). These values are obtained from several canonical ensemble MC simulations for the hybrid potential energy, $U(\lambda) = (1-\lambda)U_{C^*} + \lambda U_{B^*}$. The first molecule in the corresponding molecular system have a fixed position in all these MC simulations. All energies are normalized to the thermal energy k_BT. The absolute error bar for each average energy is smaller than 0.6.

A.4 Chemical potentials: water and methane

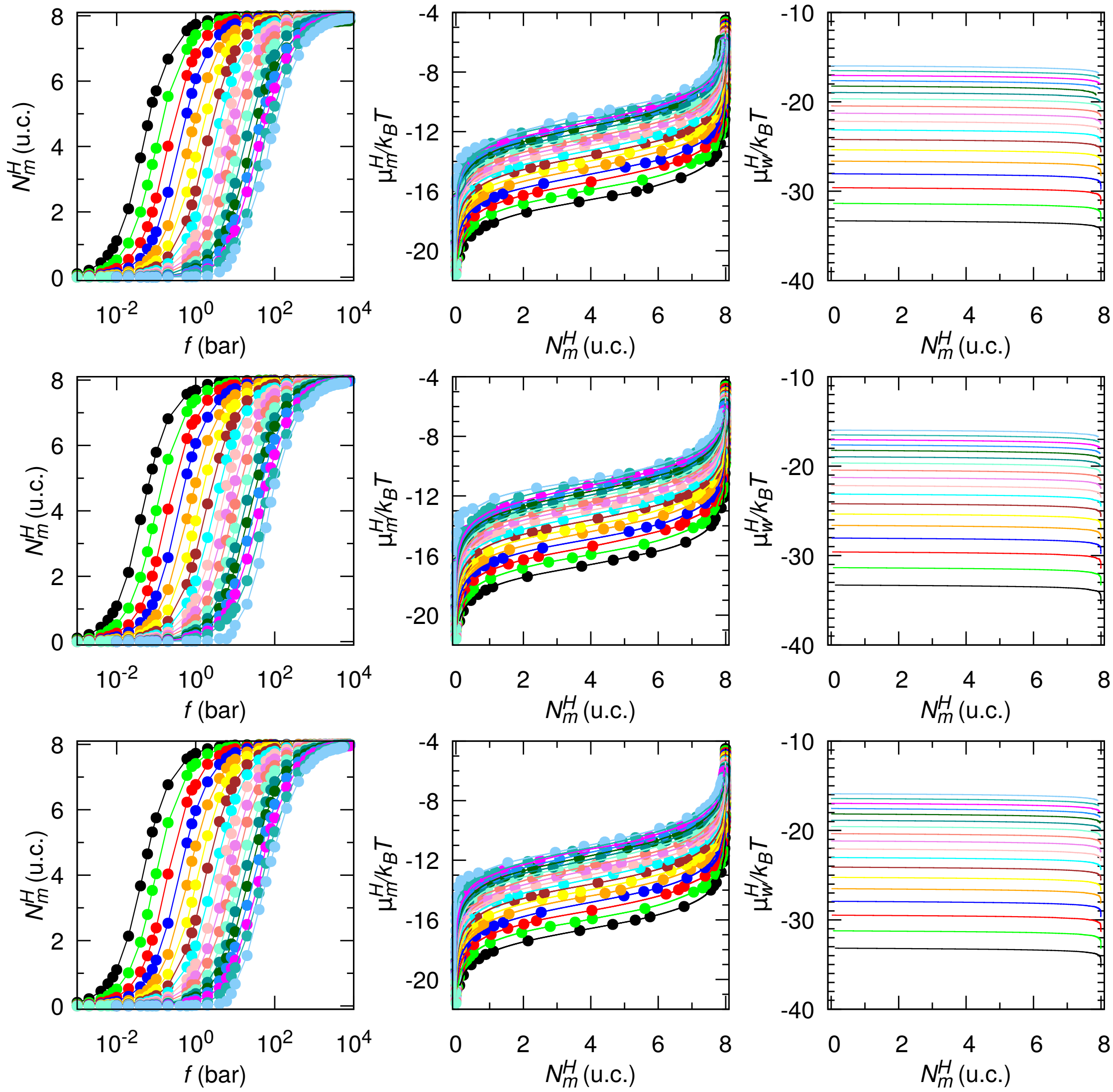

Figure A.4 Determination of the chemical potential of methane and water in methane hydrate using TIP4P/2005 water in combination with OPLS-UA methane model: (1) methane occupancy N_m^{H} (the number of molecules per unit cell) versus fugacity f (left panel), (2) chemical potential of methane $\mu_m^{\mathrm{H}}/k_BT = \ln\frac{f\Lambda^3}{k_BT}$ (center panel) and water $\mu_w^{\mathrm{H}}/k_BT = \mu_w^{(0)}/k_BT - \frac{1}{N_wk_BT}\int_{-\infty}^{\mu_m} N_m d\mu_m$ (right panel) versus N_m^{H}. In the left panel, the temperature increases from 180 to 350 K ($\Delta T = 10$ K) (from left to right); In the center and right panels, temperature increases from 180 to 350 K ($\Delta T = 10$ K) (from top to bottom). The pressures are $P = 1$ atm (top), 10 atm (middle), and 100 atm (bottom). All chemical potentials are normalized to the thermal energy, k_BT.

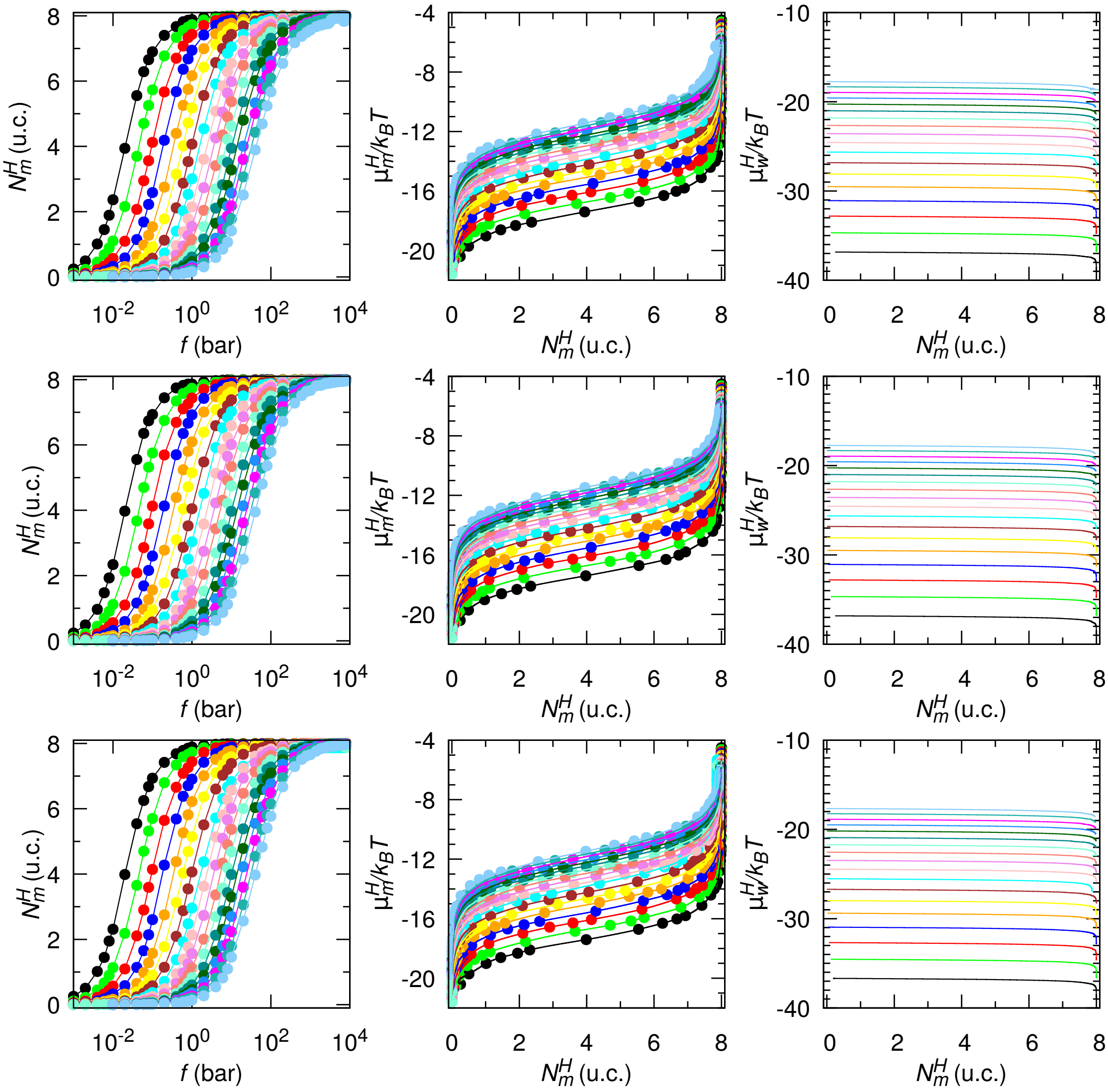

Figure A.5 Same as Figure A.4 but for the TIP4P/Ice water model.

A.5 Contributions to chemical potential of water in methane hydrate

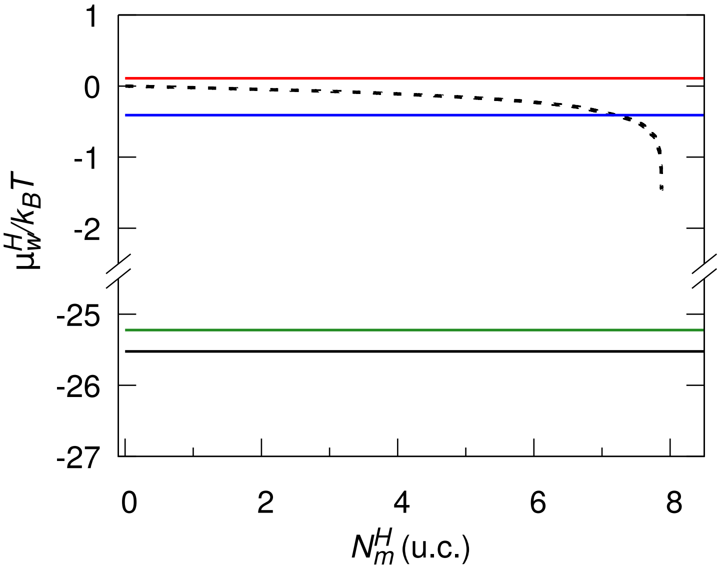

Figure A.6 Contributions to the chemical potential of water in methane hydrate $\mu_w^{\mathrm{H}}(x_m)/k_BT$ at $T = 250$ K and $P = 100$ atm. $\mu_w^{\mathrm{H}}(x_m)/k_BT = \mu_w^{\mathrm{H}}(x_m = 0)/k_BT + \Delta\mu_w^{\mathrm{H}}(x_m)/k_BT$ where $\mu_w^{\mathrm{H}}(x_m = 0)/k_BT$ (black solid line) is the chemical potential of water in zero-occupancy methane hydrate and $\Delta\mu_w^{\mathrm{H}}(x_m)/k_BT$ (black dashed line) is the contribution due to the methane occupancy. $\mu_w^{\mathrm{H}}(x_m = 0)/k_BT = A_w(x_m = 0)/N_wk_BT + A_{disorder}/N_wk_BT + PV/N_wk_BT$ where $A_w(x_m = 0)/k_BT$ is the contribution from the Helmholtz free energy of zero-occupancy methane hydrate using Einstein molecule approach (green solid line), $A_{disorder}$ is the proton disorder correction (blue solid line), and PV/N_wk_BT term (red solid line). The data shown here are for the TIP4P/Ice water model (similar qualitative results were obtained for the TIP4P/2005 water model). Note the use of a broken axis along the y-axis.

Appendix B

Finite Size Effects

B.1 Vacuum layer width effect

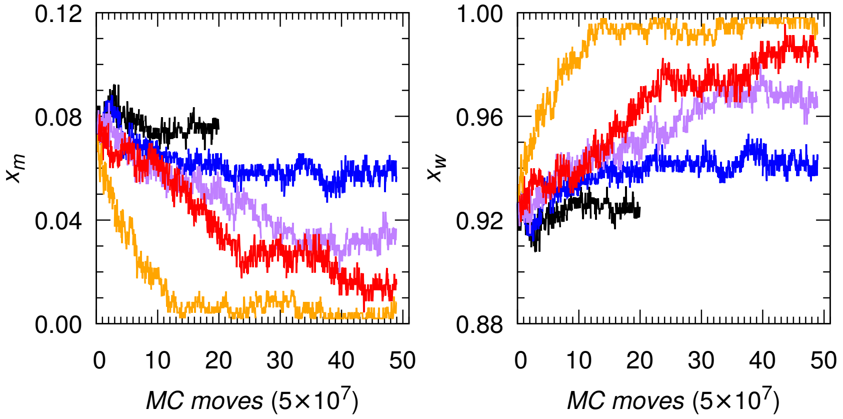

Figure B.1 (color online) Methane (x_m, *left*) and water (x_w, *right*) mole fractions during the different GCMC simulation runs: T = 230 K (black), 240 K (blue), 250 K (purple), 260 K (red), and 270 K (orange). The x-axis, which indicates progress along the GCMC simulation, is expressed as a number of attempted MC moves where one move is a molecule translation, rotation, insertion or deletion. The dimensions of the simulation box are: $L_x = L_y = 2.3754$ nm and $L_z = 8.3674$ nm (corresponding to $D_p = 2.8554$ nm with a vacuum layer $D_v = 2.0000$ nm in each side).

B.2 Molecular system size effect

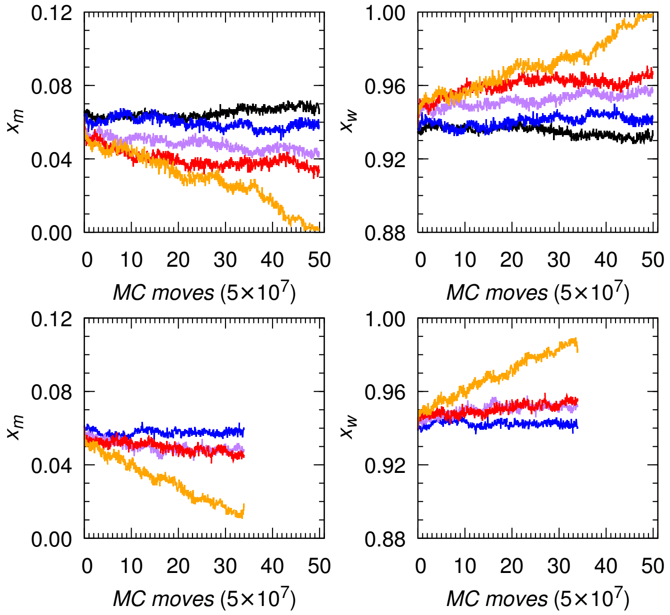

Figure B.2 (color online) Methane (x_m, *left panels*) and water (x_w, *right panels*), mole fractions during the different GCMC simulation runs: T = 230 K (black), 240 K (blue), 250 K (purple), 260 K (red), and 270 K (orange) for $D_p = 2.8554$ nm (*top panels*); and T = 260 K (blue), 270 K (purple), 280 K (red), and 290 K (orange) for $D_p = 5.2308$ nm (*bottom panels*). The x-axis, which indicates progress along the GCMC simulation, is expressed as a number of attempted MC moves where one move is a molecule translation, rotation, insertion or deletion. The dimensions of the simulation box are: $L_x = 2.3754$ nm, $L_y = 4.7508$ nm, and $L_z = 4.3670$ nm for $D_p = 2.8554$ nm (*top panels*) while $L_z = 6.7424$ nm for $D_p = 5.2308$ nm (*bottom panels*).

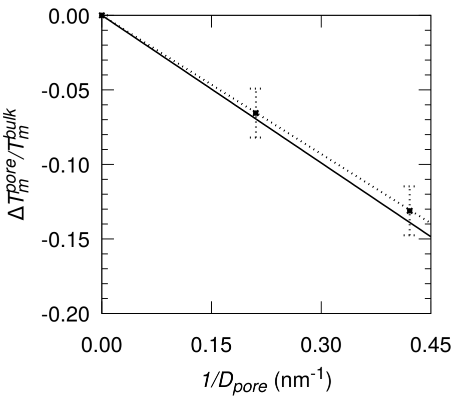

Figure B.3 Shift in the melting temperature of confined methane hydrate with respect to the bulk, $\Delta T_m^{pore}/T_m^{bulk}$, as a function of the reciprocal of the pore width, $1/D_p$: the dashed line is for the larger molecular system (i.e., $L_y = 4.3670$ nm); while the solid line is for the smaller one (i.e., $L_y = 2.3754$ nm). Note that T_m^{pore} for larger system reads from Figure B.2, while T_m^{bulk} and k_{GB} are estimated using these data.

B.3 Pore width effects at P = 10 atm

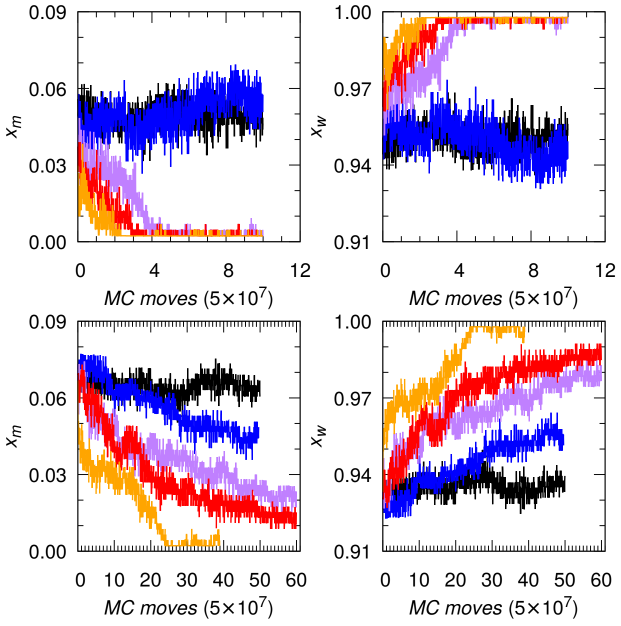

Figure B.4 (color online) Methane (x_m, *left panels*) and water (x_w, *right panels*) mole fractions during the different GCMC simulation runs: T = 250 K (black), 260 K (blue), 270 K (purple), 280 K (red), and 290 K (orange) for bulk phase (*top panels*); while T = 210 K (black), 220 K (blue), 230 K (purple), 240 K (red), and 250 K (orange) for confined system with $D_p = 2.8554$ nm (*bottom panels*). The x-axis, which indicates progress along the GCMC simulation, is expressed as a number of attempted MC moves where one move is a molecule translation, rotation, insertion or deletion. The dimensions of the simulation box in x– and y–directions are $L_x = L_y = 2.3754$ nm, and in z–direction are $L_z = 2.3754$ nm for bulk system while $L_z = 4.3670$ nm for confined system. $T_m^{bulk} = 265 \pm 5$ K and $T_m^{pore} = 225 \pm 5$ K at $P = 10$ atm for methane hydrate are summarized in Table 4.1.

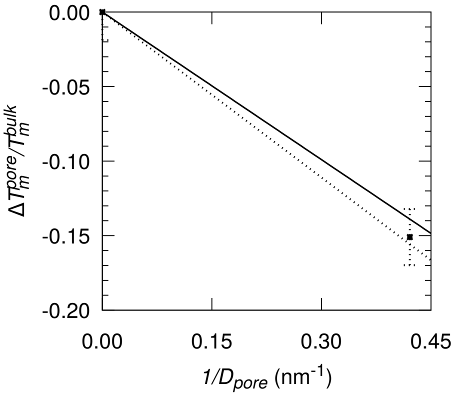

Figure B.5 Shift in the melting temperature of confined methane hydrate with respect to the bulk, $\Delta T_m^{pore}/T_m^{bulk}$, as a function of the reciprocal of the pore width, $1/D_p$: the dashed line is for $P = 10$ atm while the solid line is for $P = 100$ atm. The black circles read from Figure B.4 (DCM simulations); while the dashed and solid lines are computed using $k_{GB} = (\gamma_{LS} v^{\mathrm{L}} - \gamma_{HS} v^{\mathrm{H}})/\Delta h_{fus}$.

B.4 Surface wettability effect

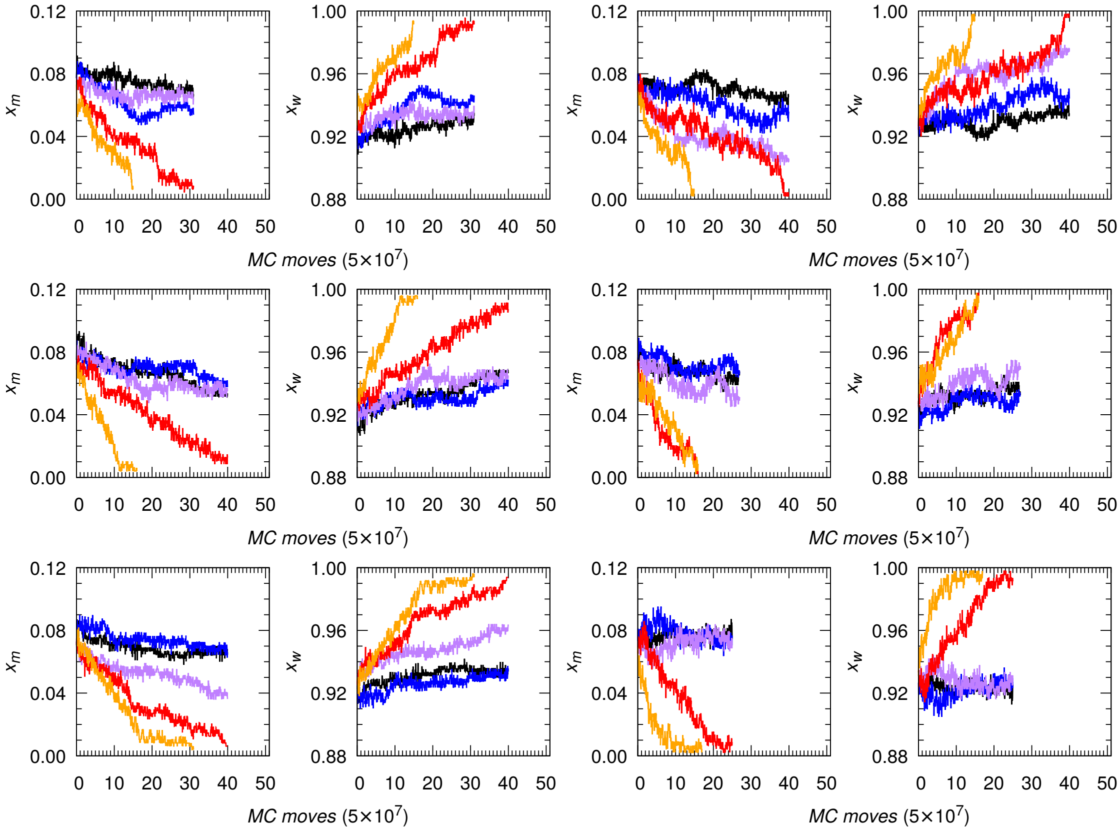

Figure B.6 Same as Figure 4.3 but for the decreased LJ energy parameter (two left panels: one for methane, x_m, and another one for water, x_w): $\varepsilon' = 1/2\varepsilon$ (*top panels*), $1/3\varepsilon$ (*center panels*), and $1/4\varepsilon$ (*bottom panels*); and for the increased LJ energy parameters (two right panels: one for methane, x_m, and another one for water, x_w): $\varepsilon' = 2\varepsilon$ (*top panels*), 3ε (*center panels*), 4ε (*bottom panels*). ε' is for the pair of atoms between solid walls and hydrate/liquid phase.

B.5 Surface tension γ_{HS}

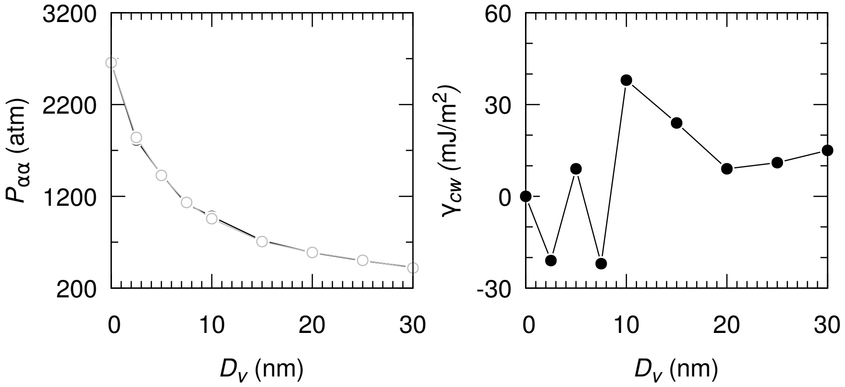

Figure B.7 The normal (black), $P_N = P_{zz}$, and tangential (gray), $P_T = \frac{1}{2}(P_{xx} + P_{yy})$, pressure tensors for methane hydrate (*left*), and the surface tension (*right*), γ_{HS}, as a function of the vacuum layer width D_v at $T = 290$ K. $D_v \geq 15$ nm is required to determine γ_{HS}.

References

Abascal, J. L. F., Sanz, E., Fernández, R. G., and Vega, C. (2005). A potential model for the study of ices and amorphous water: TIP4p/Ice. *J. Chem. Phys.*, 122:234511.

Abascal, J. L. F. and Vega, C. (2005). A general purpose model for the condensed phases of water: TIP4P/2005. *J. Chem. Phys.*, 123:234505.

Agrawal, K. V., Shimizu, S., Drahushuk, L. W., Kilcoyne, D., and Strano, M. S. (2016). Observation of extreme phase transition temperatures of water confined inside isolated carbon nanotubes. *Nat. Nano*, advance online publication.

Alabarse, F. G., Haines, J., Cambon, O., Levelut, C., Bourgogne, D., Haidoux, A., Granier, D., and Coasne, B. (2012). Freezing of water confined at the nanoscale. *Phys. Rev. Lett.*, 109:035701.

Aladko, E. Y., Dyadin, Y. A., Fenelonov, V. B., Larionov, E. G., Mel'gunov, M. S., Manakov, A. Y., Nesterov, A. N., and Zhurko, F. V. (2004). Dissociation conditions of methane hydrate in mesoporous silica gels in wide ranges of pressure and water content. *J. Phys. Chem. B*, 108:16540–16547.

Alavi, S. and Ohmura, R. (2016). Understanding decomposition and encapsulation energies of structure I and II clathrate hydrates. *J. Chem. Phys.*, 145:154708.

Alavi, S. and Ripmeester, J. A. (2010). Nonequilibrium adiabatic molecular dynamics simulations of methane clathrate hydrate decomposition. *J. Chem. Phys.*, 132:144703.

Aman, Z. M. and Koh, C. A. (2016). Interfacial phenomena in gas hydrate systems. *Chem. Soc. Rev.*, 45:1678–1690.

Anderson, G. K. (2004). Enthalpy of dissociation and hydration number of methane hydrate from the clapeyron equation. *J. Chem. Thermodyn.*, 36:1119–1127.

Anderson, R., Llamedo, M., Tohidi, B., and Burgass, R. W. (2003). Experimental measurement of methane and carbon dioxide clathrate hydrate equilibria in mesoporous silica. *J. Phys. Chem. B*, 107:3507–3514.

Angioletti-Uberti, S., Ceriotti, M., Lee, P. D., and Finnis, M. W. (2010). Solid-liquid interface free energy through metadynamics simulations. *Phys. Rev. B*, 81:125416.

Aragones, J. L., Conde, M. M., Noya, E. G., and Vega, C. (2009). The phase diagram of water at high pressures as obtained by computer simulations of the TIP4P/2005 model: the appearance of a plastic crystal phase. *Phys. Chem. Chem. Phys.*, 11:543–555.

Arnaudov, L. N., Cayre, O. J., Cohen Stuart, M. A., Stoyanov, S. D., and Paunov, V. N. (2010). Measuring the three-phase contact angle of nanoparticles at fluid interfaces. *Phys. Chem. Chem. Phys.*, 12:328–331.

Arora, A., Cameotra, S. S., Kumar, R., Balomajumder, C., Singh, A. K., Santhakumari, B., Kumar, P., and Laik, S. (2016). Biosurfactant as a promoter of methane hydrate formation: Thermodynamic and kinetic studies. *Sci. Rep.*, 6:20893.

Babakhani, S. M., Bouillot, B., Ho-Van, S., Douzet, J., and Herri, J.-M. (2018). A review on hydrate composition and capability of thermodynamic modeling to predict hydrate pressure and composition. *Fluid Phase Equilibria*, 472:22–38.

Babu, P., Yee, D., Linga, P., Palmer, A., Khoo, B. C., Tan, T. S., and Rangsunvigit, P. (2013). Morphology of methane hydrate formation in porous media. *Energy Fuels*, 27:3364–3372.

Báez, L. A. and Clancy, P. (1994). Computer simulation of the crystal growth and dissolution of natural gas hydratesa. *Ann. N. Y. Acad. Sci.*, 715(1):177–186.

Bagherzadeh, S. A., Alavi, S., Ripmeester, J., and Englezos, P. (2015). Formation of methane nano-bubbles during hydrate decomposition and their effect on hydrate growth. *J. Chem. Phys.*, 142:214701.

Bai, D., Chen, G., Zhang, X., and Wang, W. (2011). Microsecond molecular dynamics simulations of the kinetic pathways of gas hydrate formation from solid surfaces. *Langmuir*, 27:5961–5967.

Bai, D., Chen, G., Zhang, X., and Wang, W. (2012). Nucleation of the CO_2 hydrate from three-phase contact lines. *Langmuir*, 28:7730–7736.

Bai, D., Zhang, D., Zhang, X., and Chen, G. (2015). Origin of self-preservation effect for hydrate decomposition: Coupling of mass and heat transfer resistances. *Sci. Rep.*, 5:14599.

Barmavath, T., Mekala, P., and Sangwai, J. S. (2014). Prediction of phase stability conditions of gas hydrates of methane and carbon dioxide in porous media. *J. Natural Gas Sci. Eng.*, 18:254–262.

Barroso, M. A. and Ferreira, A. L. (2002). Solid–fluid coexistence of the lennard-jones system from absolute free energy calculations. *J. Chem. Phys.*, 116:7145–7150.

Bernal, J. D. and Fowler, R. H. (1933). A theory of water and ionic solution, with particular reference to hydrogen and hydroxyl ions. *J. Chem. Phys.*, 1:515–548.

Bi, Y., Cabriolu, R., and Li, T. (2016). Heterogeneous ice nucleation controlled by the coupling of surface crystallinity and surface hydrophilicity. *J. Phys. Chem. C*, 120:1507–1514.

Bi, Y. and Li, T. (2014). Probing methane hydrate nucleation through the forward flux sampling method. *J. Phys. Chem. B*, 118:13324–13332.

Birkedal, K. A., Freeman, C. M., Moridis, G. J., and Graue, A. (2014). Numerical predictions of experimentally observed methane hydrate dissociation and reformation in sandstone. *Energy Fuels*, 28:5573–5586.

Borchardt, L., Casco, M. E., and Silvestre-Albero, J. (2018). Methane hydrate in confined spaces: an alternative storage system. *Chem. Phys. Chem.*, 19:1298–1314.

Borchardt, L., Nickel, W., Casco, M., Senkovska, I., Bon, V., Wallacher, D., Grimm, N., Krause, S., and Silvestre-Albero, J. (2016). Illuminating solid gas storage in confined spaces–methane hydrate formation in porous model carbons. *Phys. Chem. Chem. Phys.*, 18:20607–20614.

Brovchenko, I., Geiger, A., and Oleinikova, A. (2004). Water in nanopores. i. coexistence curves from gibbs ensemble monte carlo simulations. *J. Chem. Phys.*, 120:1958–1972.

Brumby, P. E., Yuhara, D., Wu, D. T., Sum, A. K., and Yasuoka, K. (2016). Cage occupancy of methane hydrates from gibbs ensemble monte carlo simulations. *Fluid Phase Equilibria*, 413:242–248.

Buch, V., Sandler, P., and Sadlej, J. (1998). Simulations of H_2O solid, liquid, and clusters, with an emphasis on ferroelectric ordering transition in hexagonal ice. *J. Phys. Chem.*, 102:8641–8653.

Burnham, C. J. and English, N. J. (2016). Communication: Librational dynamics in water, sI and sII clathrate hydrates, and ice ih: Molecular-dynamics insights. *J. Chem. Phys.*, 144:051101.

Cabriolu, R. and Li, T. (2015). Ice nucleation on carbon surface supports the classical theory for heterogeneous nucleation. *Phys. Rev. E*, 91:052402.

Cao, X., Huang, Y., Li, W., Zheng, Z., Jiang, X., Su, Y., Zhao, J., and Liu, C. (2016). Phase diagrams for clathrate hydrates of methane, ethane, and propane from first-principles thermodynamics. *Phys. Chem. Chem. Phys.*, 18:3272–3279.

Casco, M. E., Cuadrado-Collados, C., Martínez-Escandell, M., Rodríguez-Reinoso, F., and Silvestre-Albero, J. (2017). Influence of the oxygen-containing surface functional groups in the methane hydrate nucleation and growth in nanoporous carbon. *Carbon*, 123:299–301.

Casco, M. E., Silvestre-Albero, J., Ramírez-Cuesta, A. J., Rey, F., Jordá, J. L., Bansode, A., Urakawa, A., Peral, I., Martínez-Escandell, M., Kaneko, K., and Rodríguez-Reinoso, F. (2015). Methane hydrate formation in confined nanospace can surpass nature. *Nat. Commun.*, 6:6432.

Cha, S. B., Ouar, H., Wildeman, T. R., and Sloan, E. D. (1988). A third-surface effect on hydrate formation. *J. Phys. Chem.*, 92:6492–6494.

Chakraborty, N. S. and Gelb, L. D. (2012a). A monte carlo simulation study of methane clathrate hydrates confined in slit-shaped pores. *J. Phys. Chem. B*, 116:2183–2197.

Chakraborty, S. N. and Gelb, L. D. (2012b). A monte carlo simulation study of methane clathrate hydrates confined in slit-shaped pores. *J. Phys. Chem. B*, 116:2183–2197.

Chau, P.-L. and Hardwick, A. J. (1998). A new order parameter for tetrahedral configurations. *Mol. Phys.*, 93:511–518.

Chialvo, A. A., Houssa, M., and Cummings, P. T. (2002). Molecular dynamics study of the structure and thermophysical properties of model sI clathrate hydrates. *J. Phys. Chem. B*, 106:442–451.

Coasne, B. (2005). Freezing of mixtures confined in a slit nanopore. *Adsorption*, 11:301–306.

Coasne, B., Czwartos, J., Gubbins, K. E., Hung, F. R., and Sliwinska-Bartkowiak, M. (2004). Freezing and melting of binary mixtures confined in a nanopore. *Mol. Phys.*, 102:2149–2163.

Cole, D. J., Payne, M. C., and Ciacchi, L. C. (2009). Water structuring and collagen adsorption at hydrophilic and hydrophobic silicon surfaces. *Phys. Chem. Chem. Phys.*, 11:11395–11399.

Conde, M. M., Gonzalez, M. A., Abascal, J. L. F., and Vega, C. (2013). Determining the phase diagram of water from direct coexistence simulations: The phase diagram of the TIP4P/2005 model revisited. *J. Chem. Phys.*, 139:154505.

Conde, M. M., Torré, J. P., and Miqueu, C. (2016). Revisiting the thermodynamic modelling of type I gas–hydroquinone clathrates. *Phys. Chem. Chem. Phys.*, 18:10018–10027.

Conde, M. M. and Vega, C. (2010). Determining the three-phase coexistence line in methane hydrates using computer simulations. *J. Chem. Phys.*, 133:064507.

Conde, M. M., Vega, C., McBride, C., Noya, E. G., Ramírez, R., and Sesé, L. M. (2010). Can gas hydrate structures be described using classical simulations? *J. Chem. Phys.*, 132:114503.

Cuadrado-Collados, C., Fauth, F., Such-Basanez, I., Martínez-Escandell, M., and Silvestre-Albero, J. (2018). Methane hydrate formation in the confined nanospace of activated carbons in seawater environment. *Microporous Mesoporous Materials*, 255:220–225.

Czwartos, J., Coasne, B., Gubbins, K. E., Hung, F. R., and Sliwinska-Bartkowiak, M. (2005). Freezing and melting of azeotropic mixtures confined in nanopores: Experiment and molecular simulation. *Mol. Phys.*, 103:3103–3113.

Damm, W., Frontera, A., Tirado-Rives, J., and Jorgensen, W. L. (1997). OPLS all-atom force field for carbohydrates. *J. Comput. Chem.*, 18:1955–1970.

Dartois, E., Duret, P., Marboeuf, U., and Schmitt, B. (2012). Hydrogen sulfide clathrate hydrate ftir spectroscopy: a help gas for clathrate formation in the solar system? *Icarus*, 220:427–434.

Davy, H. (1800). The bakerian lecture: On some of the combinations of oxymuriatic gas and oxygene, and on the chemical relations of these principles, to inflammable bodies. *Philos. Trans. R. Soc. London, Ser. B*, 1:385–388.

de Azevedo Medeiros, F., Shiguematsu, F. M., Campos, F. B., Segtovich, I. S. V., da Silva Ourique, J. E., Barreto, A. G., and Tavares, F. W. (2016). Alternative eos-based model for predicting water content, metastable phases and hydrate formation in natural gas systems. *J. Natural Gas Sci. Eng.*, 36:550–562.

de Pablo, J. J., Laso, M., and Suter, U. W. (1992). Simulation of polyethylene above and below the melting point. *J. Chem. Phys.*, 96:2395–2403.

Demurov, A., Radhakrishnan, R., and Trout, B. L. (2002). Computations of diffusivities in ice and CO_2 clathrate hydrates via molecular dynamics and monte carlo simulations. *J. Chem. Phys.*, 116:702–709.

Desmedt, A., Bedouret, L., Pefoute, E., Pouvreau, M., Say-Liang-Fat, S., and Alvarez, M. (2012). Energy landscape of clathrate hydrates. *Eur. Phys. J. Spec. Top.*, 213:103–127.

Di Crescenzo, A., Di Profio, P., Siani, G., Zappacosta, R., and Fontana, A. (2016). Optimizing the interactions of surfactants with graphitic surfaces and clathrate hydrates. *Langmuir*, 32:6559–6570.

Docherty, H., Galindo, A., Vega, C., and Sanz, E. (2006). A potential model for methane in water describing correctly the solubility of the gas and the properties of the methane hydrate. *J. Chem. Phys.*, 125:074510.

Dornan, P., Alavi, S., and Woo, T. K. (2007). Free energies of carbon dioxide sequestration and methane recovery in clathrate hydrates. *J. Chem. Phys.*, 127:124510.

Duan, Z., Li, D., Chen, Y., and Sun, R. (2011). The influence of temperature, pressure, salinity and capillary force on the formation of methane hydrate. *Geoscience Frontiers*, 2:125–135.

Dureckova, H., Woo, T. K., and Alavi, S. (2016). Molecular simulations and density functional theory calculations of bromine in clathrate hydrate phases. *J. Chem. Phys.*, 144:044501.

El-Sheikh, S. M., Barakat, K., and Salem, N. M. (2006). Phase transitions of methane using molecular dynamics simulations. *J. Chem. Phys.*, 124:124517.

English, N. J., Gorman, P. D., and MacElroy, J. M. D. (2012). Mechanisms for thermal conduction in hydrogen hydrate. *J. Chem. Phys.*, 136:044501.

English, N. J., Johnson, J. K., and Taylor, C. E. (2005). Molecular-dynamics simulations of methane hydrate dissociation. *J. Chem. Phys.*, 123:244503.

English, N. J. and MacElroy, J. M. D. (2004). Theoretical studies of the kinetics of methane hydrate crystallization in external electromagnetic fields. *J. Chem. Phys.*, 120:10247–10256.

English, N. J. and Tse, J. S. (2009). Mechanisms for thermal conduction in methane hydrate. *Phys. Rev. Lett.*, 103:015901.

English, N. J., Tse, J. S., and Carey, D. J. (2009). Mechanisms for thermal conduction in various polymorphs of methane hydrate. *Phys. Rev. B*, 80:134306.

Errington, J. R. and Debenedetti, P. G. (2001). Relationship between structural order and the anomalies of liquid water. *Nature*, 409:318–321.

Fábián, B., Picaud, S., Jedlovszky, P., Guilbert-Lepoutre, A., and Mousis, O. (2018). Ammonia clathrate hydrate as seen from grand canonical monte carlo simulations. *ACS Earth and Space Chem.*, 2(5):521–531.

Ferdows, M. and Ota, M. (2005). Molecular simulation study for CO_2 clathrate hydrate. *Chem. Eng. Technol.*, 28:168–173.

Fernández, R. G., Abascal, J. L. F., and Vega, C. (2006). The melting point of ice Ih for common water models calculated from direct coexistence of the solid-liquid interface. *J. Chem. Phys.*, 124:144506.

Florusse, L. J., Peters, C. J., Schoonman, J., Hester, K. C., Koh, C. A., Dec, S. F., Marsh, K. N., and Sloan, E. D. (2004). Stable low-pressure hydrogen clusters stored in a binary clathrate hydrate. *Science*, 306:469.

Fortes, A. D., Wood, I. G., Grigoriev, D., Alfredsson, M., Kipfstuhl, S., Knight, K. S., and Smith, R. I. (2004). No evidence for large-scale proton ordering in antarctic ice from powder neutron diffraction. *J. Chem. Phys.*, 120:11376.

Fray, N., Marboeuf, U., Brissaud, O., and Schmitt, B. (2010). Equilibrium data of methane, carbon dioxide, and xenon clathrate hydrates below the freezing point of water. applications to astrophysical environments. *J. Chem. Eng. Data*, 55(11):5101–5108.

Frenkel, D. and Ladd, A. J. C. (1984). New monte carlo method to compute the free energy of arbitrary solids. application to the fcc and hcp phases of hard spheres. *J. Chem. Phys.*, 81:3188–3193.

Frenkel, D. and Smit, B. (2002). *Understanding Molecular Simulation: From Algorithms to Applications*. Computational Science. Academic Press, 2nd edition.

Gai, L., Iacovella, C. R., Wan, L., McCabe, C., and Cummings, P. T. (2015). Examination of the phase transition behavior of nano-confined fluids by statistical temperature molecular dynamics. *J. Chem. Phys.*, 143:054504.

Ganji, H., Manteghian, M., zadeh, K. S., Omidkhah, M., and Mofrad, H. R. (2007). Effect of different surfactants on methane hydrate formation rate, stability and storage capacity. *Fuel*, 86:434–441.

Gasser, U., Weeks, E. R., Schofield, A., Pusey, P. N., and Weitz, D. A. (2001). Real-space imaging of nucleation and growth in colloidal crystallization. *Science*, 292:258–262.

Ghaedi, H., Ayoub, M., Bhat, A. H., Mahmood, S. M., Akbari, S., and Murshid, G. (2016). The effects of salt, particle and pore size on the process of carbon dioxide hydrate formation: A critical review. *AIP Conference Proceedings*, 1787:060001.

Govindaraj, V., Mech, D., Pandey, G., Nagarajan, R., and Sangwai, J. S. (2015). Kinetics of methane hydrate formation in the presence of activated carbon and nano-silica suspensions in pure water. *J. Nat. Gas Sci. Eng.*, 26:810–818.

Habershon, S. and Manolopoulos, D. E. (2011). Free energy calculations for a flexible water model. *Phys. Chem. Chem. Phys.*, 13:19714–19727.

Hachikubo, A., Takeya, S., Chuvilin, E., and Istomin, V. (2011). Preservation phenomena of methane hydrate in pore spaces. *Phys. Chem. Chem. Phys.*, 13:17449–17452.

Hakim, L., Koga, K., and Tanaka, H. (2010). Phase behavior of different forms of ice filled with hydrogen molecules. *Phys. Rev. Lett.*, 104:115701.

Handa, Y. P. and Stupin, D. Y. (1992). Thermodynamic properties and dissociation characteristics of methane and propane hydrates in 70-.ang.-radius silica gel pores. *J. Phys. Chem.*, 96:8599–8603.

Harvey, A. H. (1996). Semiempirical correlation for henry's constants over large temperature ranges. *AIChE J.*, 42:1491–1494.

Harvey, A. H. and Sengers, J. M. H. L. (1990). Correlation of aqueous henry's constants from 0°C to the critical point. *AIChE J.*, 36:539–546.

Henriet, J. P. and Mienert, J. (1998). *Gas Hydrates: Relevance to World Margin Stability and Climatic Change*. Geological Society of London.

Hersant, F., Gautier, D., and Lunine, J. I. (2004). Enrichment in volatiles in the giant planets of the solar system. *Planet. Space Sci.*, 52:623–641.

Hjertenaes, E., Trinh, T. T., and Koch, H. (2016). Chemically accurate energy barriers of small gas molecules moving through hexagonal water rings. *Phys. Chem. Chem. Phys.*, 18:17831–17835.

Hoover, W. G. (1985). Canonical dynamics: Equilibrium phase–space distributions. *Phys. Rev. A*, 31:1695–1697.

Huang, T., Li, C., Jia, W., and Peng, Y. (2016a). Application of equations of state to predict methane solubility under hydrate-liquid water two-phase equilibrium. *Fluid Phase Equilibria*, 427:35–45.

Huang, Y., Zhu, C., Wang, L., Cao, X., Su, Y., Jiang, X., Meng, S., Zhao, J., and Zeng, X. C. (2016b). A new phase diagram of water under negative pressure: The rise of the lowest-density clathrate s-III. *Sci. Adv.*, 2.

Huo, Z., Hester, K., Sloan, E. D., and Miller, K. T. (2003). Methane hydrate nonstoichiometry and phase diagram. *AIChE J.*, 49:1300–1306.

Ilani-Kashkouli, P., Hashemi, H., Gharagheizi, F., Babaee, S., Mohammadi, A. H., and Ramjugernath, D. (2013). Gas hydrate phase equilibrium in porous media: An assessment test for experimental data. *Fluid Phase Equilibria*, 360:161–168.

Jacobson, L. C., Hujo, W., and Molinero, V. (2009). Thermodynamic stability and growth of guest-free clathrate hydrates: A low-density crystal phase of water. *J. Phys. Chem. B*, 113:10298–10307.

Jacobson, L. C., Hujo, W., and Molinero, V. (2010a). Amorphous precursors in the nucleation of clathrate hydrates. *J. Am. Chem. Soc.*, 132:11806–11811.

Jacobson, L. C., Hujo, W., and Molinero, V. (2010b). Nucleation pathways of clathrate hydrates: Effect of guest size and solubility. *J. Phys. Chem. B*, 114:13796–13807.

Jacobson, L. C. and Molinero, V. (2010). A methane–water model for coarse-grained simulations of solutions and clathrate hydrates. *J. Phys. Chem. B*, 114:7302–7311.

Jacobson, L. C. and Molinero, V. (2011). Can amorphous nuclei grow crystalline clathrates? the size and crystallinity of critical clathrate nuclei. *J. Am. Chem. Soc.*, 133:6458–6463.

Jendi, Z. M., Servio, P., and Rey, A. D. (2016). Ab initio modelling of methane hydrate thermophysical properties. *Phys. Chem. Chem. Phys.*, 18:10320–10328.

Jensen, L., Thomsen, K., von Solms, N., Wierzchowski, S., Walsh, M. R., Koh, C. A., Sloan, E. D., Wu, D. T., and Sum, A. K. (2010). Calculation of liquid water–hydrate–methane vapor phase equilibria from molecular simulations. *J. Phys. Chem. B*, 114:5775–5782.

Jhung, K. S., Kum, O., and Lee, H. W. (1991). Monte carlo calculations of free energy in the solid phase. *J. Chem. Phys.*, 94:1470–1473.

Jorgensen, W. L., Chandrasekhar, J., Madura, J. D., Impey, R. W., and Klein, M. L. (1983). Comparison of simple potential functions for simulating liquid water. *J. Chem. Phys.*, 79:926–935.

Jorgensen, W. L., Madura, J. D., and Swenson, C. J. (1984). Optimized intermolecular potential functions for liquid hydrocarbons. *J. Am. Chem. Soc.*, 106:6638–6646.

Jorgensen, W. L., Maxwell, D. S., and Tirado-Rives, J. (1996). Development and testing of the OPLS all-atom force field on conformational energetics and properties of organic liquids. *J. Am. Chem. Soc.*, 118:11225–11236.

Kaminski, G., Duffy, E. M., Matsui, T., and Jorgensen, W. L. (1994). Free energies of hydration and pure liquid properties of hydrocarbons from the OPLS all-atom model. *J. Phys. Chem.*, 98:13077–13082.

Kang, H., Koh, D.-Y., and Lee, H. (2014). Nondestructive natural gas hydrate recovery driven by air and carbon dioxide. *Sci. Rep.*, 4:6616.

Kang, S.-P. and Lee, J.-W. (2010). Kinetic behaviors of CO_2 hydrates in porous media and effect of kinetic promoter on the formation kinetics. *Chemical Engineering Science*, 65:1840 – 1845.

Kang, S.-P., Lee, J.-W., and Ryu, H.-J. (2008). Phase behavior of methane and carbon dioxide hydrates in meso- and macro-sized porous media. *Fluid Phase Equilibria*, 274:68–72.

Kang, S.-P., Ryu, H.-J., and Seo, Y. (2009a). Phase behavior of CO_2 and CH_4 hydrate in porous media. *Eng. Technol.*, 33:3711–3715.

Kang, S.-P., Seo, Y., and Jang, W. (2009b). Kinetics of methane and carbon dioxide hydrate formation in silica gel pores. *Energy Fuels*, 23:3711–3715.

Kato, M., Matsumoto, S., Takashima, A., Fujii, Y., Takasu, Y., and Nishio, I. (2016). Energy-dissipation of OH-stretching in tetrahydrofuran clathrate hydrate by raman spectroscopy and DFT calculation. *Vib. Spectrosc.*, 85:11–15.

Katsumasa, K., Koga, K., and Tanaka, H. (2007). On the thermodynamic stability of hydrogen clathrate hydrates. *J. Chem. Phys.*, 127:044509.

Kieffer, S. W., Lu, X. L., Bethke, C. M., Spencer, J. R., Marshak, S., and Navrotsky, A. (2006). A clathrate reservoir hypothesis for enceladus' south polar plume. *Science*, 314:1764–1766.

Kirchner, M. T., Boese, R., Billups, W. E., and Norman, L. R. (2004). Gas hydrate single-crystal structure analyses. *J. Am. Chem. Soc.*, 126:9407–9412.

Kirkwood, J. G. and Buff, F. P. (1949). The statistical mechanical theory of surface tension. *J. Chem. Phys.*, 17:338–343.

Knott, B. C., Molinero, V., Doherty, M. F., and Peters, B. (2012). Homogeneous nucleation of methane hydrates: Unrealistic under realistic conditions. *J. Am. Chem. Soc.*, 134:19544–19547.

Krouskop, P. E., Madura, J. D., Paschek, D., and Krukau, A. (2006). Solubility of simple, nonpolar compounds in TIP4P–Ew. *J. Chem. Phys.*, 124:016102.

Kumar, A., Bhattacharjee, G., Kulkarni, B. D., and Kumar, R. (2015). Role of surfactants in promoting gas hydrate formation. *Ind. Eng. Chem. Res.*, 54:12217–12232.

Kvenvolden, K. A. (1988). Methane hydrate – a major reservoir of carbon in the shallow geosphere? *Chem. Geol.*, 71:41.

Kyung, D., Lim, H.-K., Kim, H., and Lee, W. (2015). CO_2 hydrate nucleation kinetics enhanced by an organo-mineral complex formed at the montmorillonite–water interface. *Environ. Sci. Technol.*, 49:1197–1205.

Lasich, M., Mohammadi, A. H., Bolton, K., Vrabec, J., and Ramjugernath, D. (2014). Phase equilibria of methane clathrate hydrates from grand canonical monte carlo simulations. *Fluid Phase Equilibria*, 369:47–54.

Lechner, W. and Dellago, C. (2008). Accurate determination of crystal structures based on averaged local bond order parameters. *J. Chem. Phys.*, 129:114707.

Lee, H., Lee, J.-w., Kim, D. Y., Park, J., Seo, Y.-T., Zeng, H., Moudrakovski, I. L., Ratcliffe, C. I., and Ripmeester, J. A. (2005). Tuning clathrate hydrates for hydrogen storage. *Nature*, 434:743–746.

Lee, H.-H., Ahn, S.-H., Nam, B.-U., Kim, B.-S., Lee, G.-W., Moon, D., Shin, H. J., Han, K. W., and Yoon, J.-H. (2012). Thermodynamic stability, spectroscopic identification, and gas storage capacity of CO_2–CH_4–n_2 mixture gas hydrates: Implications for landfill gas hydrates. *Environ. Sci. Technol.*, 46:4184–4190.

Lee, S. and Seo, Y. (2010). Experimental measurement and thermodynamic modeling of the mixed CH_4 + C_3H_8 clathrate hydrate equilibria in silica gel pores: Effects of pore size and salinity. *Langmuir*, 26:9742–9748.

Lehmkühler, F., Paulus, M., Sternemann, C., Lietz, D., Venturini, F., Gutt, C., and Tolan, M. (2009). The carbon dioxide–water interface at conditions of gas hydrate formation. *J. Am. Chem. Soc.*, 131:585–589.

Li, J., Liang, D., Guo, K., Wang, R., and Fan, S. (2006). Formation and dissociation of hfc134a gas hydrate in nano-copper suspension. *Energy Convers. Manag.*, 47:201–210.

Liang, S., Yi, L., and Liang, D. (2014). Molecular insights into the homogeneous melting of methane hydrates. *J. Phys. Chem. C*, 118:28542–28547.

Linga, P., Daraboina, N., Ripmeester, J. A., and Englezos, P. (2012). Enhanced rate of gas hydrate formation in a fixed bed column filled with sand compared to a stirred vessel. *Chem. Eng. Sci.*, 68:617–623.

Luis, D. P., Herrera-Hernández, E. C., and Saint-Martin, H. (2015). A theoretical study of the dissociation of the sI methane hydrate induced by an external electric field. *J. Chem. Phys.*, 143:204503.

Lyubartsev, A. P., Fo/rrisdahl, O. K., and Laaksonen, A. (1998). Solvation free energies of methane and alkali halide ion pairs: An expanded ensemble molecular dynamics simulation study. *J. Chem. Phys.*, 108:227–233.

MacDonald, G. J. (1990). The future of methane as an energy resource. *Annu. Rev. Energy*, 15:53.

Madden, M. E., Ulrich, S., Szymcek, P., McCallum, S., and Phelps, T. (2009). Experimental formation of massive hydrate deposits from accumulation of ch4 gas bubbles within synthetic and natural sediments. *Mar. Pet. Geol.*, 26:369 – 378.

Mak, T. C. W. and McMullan, R. K. (1965). Polyhedral clathrate hydrates. X. structure of the double hydrate of tetrahydrofuran and hydrogen sulfide. *J. Chem. Phys.*, 42:2732–2737.

Marboeuf, U., Mousis, O., Petit, J.-M., and Schmitt, B. (2010). Clathrate hydrates formation in short-period comets. *ApJ*, 708:812–816.

Małolepsza, E., Kim, J., and Keyes, T. (2015). Entropic description of gas hydrate ice-liquid equilibrium via enhanced sampling of coexisting phases. *Phys. Rev. Lett.*, 114:170601.

McLaurin, G., Shin, K., Alavi, S., and Ripmeester, J. A. (2014). Antifreezes act as catalysts for methane hydrate formation from ice. *Angew. Chem. Int. Ed.*, 53:10429–10433.

McMullan, R. K. and Jeffrey, G. A. (1965). Polyhedral clathrate hydrates. IX. structure of ethylene oxide hydrate. *J. Chem. Phys.*, 42:2725.

Mel'nikov, V. P., Podenko, L. S., Nesterov, A. N., Drachuk, A. O., Molokitina, N. S., and Reshetnikov, A. M. (2016). Self-preservation of methane hydrates produced in “dry water”. *Doklady Chem.*, 466:53–56.

Michalis, V. K., Costandy, J., Tsimpanogiannis, I. N., Stubos, A. K., and Economou, I. G. (2015). Prediction of the phase equilibria of methane hydrates using the direct phase coexistence methodology. *J. Chem. Phys.*, 142:044501.

Michalis, V. K., Moultos, O. A., Tsimpanogiannis, I. N., and Economou, I. G. (2016a). Molecular dynamics simulations of the diffusion coefficients of light n-alkanes in water over a wide range of temperature and pressure. *Fluid Phase Equilibria*, 407:236–242.

Michalis, V. K., Tsimpanogiannis, I. N., Stubos, A. K., and Economou, I. G. (2016b). Direct phase coexistence molecular dynamics study of the phase equilibria of the ternary methane–carbon dioxide–water hydrate system. *Phys. Chem. Chem. Phys.*, 18:23538–23548.

Misyura, S. Y. (2016). The influence of porosity and structural parameters on different kinds of gas hydrate dissociation. *Sci. Rep.*, 6:30324.

Miyawaki, J., Kanda, T., Suzuki, T., Okui, T., Maeda, Y., and Kaneko, K. (1998). Macroscopic evidence of enhanced formation of methane nanohydrates in hydrophobic nanospaces. *J. Phys. Chem. B*, 102:2187–2192.

Molinero, V. and Moore, E. B. (2009). Water modeled as an intermediate element between carbon and silicon. *J. Phys. Chem. B*, 113:4008–4016.

Moore, E. B., de la Llave, E., Welke, K., Scherlis, D. A., and Molinero, V. (2010). Freezing, melting and structure of ice in a hydrophilic nanopore. *Phys. Chem. Chem. Phys.*, 12:4124–4134.

Mousis, O., Lunine, J. I., Picaud, S., and Cordier, D. (2010). Volatile inventories in clathrate hydrates formed in the primordial nebula. *Faraday Discuss.*, 147:509–525.

Myshakin, E. M., Jiang, H., Warzinski, R. P., and Jordan, K. D. (2009). Molecular dynamics simulations of methane hydrate decomposition. *J. Phys. Chem. A*, 113:1913–1921.

Míguez, J. M., Conde, M. M., Torré, J.-P., Blas, F. J., Piñeiro, M. M., and Vega, C. (2015). Molecular dynamics simulation of CO_2 hydrates: Prediction of three phase coexistence line. *J. Chem. Phys.*, 142:124505.

Naeiji, P., Varaminian, F., and Rahmati, M. (2016). Thermodynamic and structural properties of methane/water systems at the threshold of hydrate formation predicted by molecular dynamic simulations. *J. Natural Gas Sci. Eng.*, 31:555–561.

Nagle, J. F. (1966). Lattice statistics of hydrogen bonded crystals. i. the residual entropy of ice. *J. Math. Phys.*, 7:1484.

Narten, A. H. and Levy, H. A. (1971). Liquid water: Molecular correlation functions from x-ray diffraction. *J. Chem. Phys.*, 55:2263–2269.

Nguyen, A. H. and Molinero, V. (2015). Identification of clathrate hydrates, hexagonal ice, cubic ice, and liquid water in simulations: the CHILL+ algorithm. *J. Phys. Chem. B*, 119:9369–9376.

Nijmeijer, M. J. P., Bruin, C., Bakker, A. F., and van Leeuwen, J. M. J. (1990). Wetting and drying of an inert wall by a fluid in a molecular-dynamics simulation. *Phys. Rev. A*, 42:6052–6059.

Ning, F., Yu, Y., Kjelstrup, S., Vlugt, T. J. H., and Glavatskiy, K. (2012). Mechanical properties of clathrate hydrates: status and perspectives. *Energy Environ. Sci.*, 5:6779.

Ning, F. L., Glavatskiy, K., Ji, Z., Kjelstrup, S., and H. Vlugt, T. J. (2015). Compressibility, thermal expansion coefficient and heat capacity of CH_4 and CO_2 hydrate mixtures using molecular dynamics simulations. *Phys. Chem. Chem. Phys.*, 17:2869–2883.

Nosé, S. (1984). A unified formulation of the constant temperature molecular dynamics methods. *J. Chem. Phys.*, 81:511–519.

Noya, E. G., Conde, M. M., and Vega, C. (2008). Computing the free energy of molecular solids by the Einstein molecule approach: Ices XIII and XIV, hard-dumbbells and a patchy model of proteins. *J. Chem. Phys.*, 129:104704.

Ogata, S. (1992). Monte carlo simulation study of crystallization in rapidly supercooled one-component plasmas. *Phys. Rev. A*, 45:1122–1134.

Ohgaki, K., Nakatsuji, K., Takeya, K., Tani, A., and Sugahara, T. (2008). Hydrogen transfer from guest molecule to radical in adjacent hydrate-cages. *Phys. Chem. Chem. Phys.*, 10:80–82.

Okano, Y. and Yasuoka, K. (2006). Free-energy calculation of structure-h hydrates. *J. Chem. Phys.*, 124:024510.

Paschek, D. (2004). Temperature dependence of the hydrophobic hydration and interaction of simple solutes: An examination of five popular water models. *J. Chem. Phys.*, 120:6674–6690.

Patchkovskii, S. and Tse, J. S. (2003). Thermodynamic stability of hydrogen clathrates. *Proc. Natl. Acad. Sci. U.S.A.*, 100:14645–14650.

Patt, A., Simon, J.-M., Picaud, S., and Salazar, J. M. (2018). A grand canonical monte carlo study of the N_2, CO, and mixed N_2–CO clathrate hydrates. *J. Phys. Chem. C*, 122(32):18432–18444.

Pefoute, E., Prager, M., Russina, M., and Desmedt, A. (2016). Quasi-elastic neutron scattering investigation of the guest molecule dynamics in the bromomethane clathrate hydrate. *Fluid Phase Equilibria*, 413:116 – 122. Special Issue: Gas Hydrates and Semiclathrate Hydrates.

Petuya, C., Damay, F., Chazallon, B., Bruneel, J.-L., and Desmedt, A. (2018a). Guest partitioning and metastability of the nitrogen gas hydrate. *J. Phys. Chem. C*, 122:566–573.

Petuya, C., Damay, F., Desplanche, S., Talaga, D., and Desmedt, A. (2018b). Selective trapping of CO_2 gas and cage occupancy in CO_2–N_2 and CO_2–CO mixed gas hydrates. *Chem. Commun.*, 54:4290–4293.

Phan, A., Cole, D. R., and Striolo, A. (2014). Aqueous methane in slit-shaped silica nanopores: high solubility and traces of hydrates. *J. Phys. Chem. C*, 118:4860–4868.

Pirzadeh, P. and Kusalik, P. G. (2013). Molecular insights into clathrate hydrate nucleation at an ice–solution interface. *J. Am. Chem. Soc.*, 135:7278–7287.

Plimpton, S. (1995). Fast parallel algorithms for short-range molecular dynamics. *J. Comput. Phys.*, 117:1–19.

Polson, J. M., Trizac, E., Pronk, S., and Frenkel, D. (2000). Finite-size corrections to the free energies of crystalline solids. *J. Chem. Phys.*, 112:5339–5342.

Prasad, P. S., Chari, V. D., Sharma, D. V., and Murthy, S. R. (2012). Effect of silica particles on the stability of methane hydrates. *Fluid Phase Equilibria*, 318:110–114.

Radhakrishnan, R. and Trout, B. L. (2002). A new approach for studying nucleation phenomena using molecular simulations: Application to CO_2 hydrate clathrates. *J. Chem. Phys.*, 117:1786–1796.

Radhakrishnan, R. and Trout, B. L. (2003a). Nucleation of crystalline phases of water in homogeneous and inhomogeneous environments. *Phys. Rev. Lett.*, 90:158301.

Radhakrishnan, R. and Trout, B. L. (2003b). Nucleation of hexagonal ice (*I* <i> $_h$ </i>) in liquid water. *J. Am. Chem. Soc.*, 125:7743–7747.

Reinhardt, A., Doye, J. P. K., Noya, E. G., and Vega, C. (2012). Local order parameters for use in driving homogeneous ice nucleation with all-atom models of water. *J. Chem. Phys.*, 137:194504.

Ripmeester, J. A., Tse, J. S., Ratcliffe, C. I., and Powell, B. M. (1987). A new clathrate hydrate structure. *Nature (London)*, 325:135.

Rodrigues, P. C. R. and Fernandes, F. M. S. S. (2007). Phase diagrams of alkali halides using two interaction models: A molecular dynamics and free energy study. *J. Chem. Phys.*, 126:024503.

Román-Pérez, G., Moaied, M., Soler, J. M., and Yndurain, F. (2010). Stability, adsorption, and diffusion of CH 4 , CO 2 , and h 2 in clathrate hydrates. *Phys. Rev. Lett.*, 105.

Rosenbaum, E. J., English, N. J., Johnson, J. K., Shaw, D. W., and Warzinski, R. P. (2007). Thermal conductivity of methane hydrate from experiment and molecular simulation. *J. Phys. Chem. B*, 111(46):13194–13205.

Sa, J.-H., Kwak, G.-H., Han, K., Ahn, D., and Lee, K.-H. (2015). Gas hydrate inhibition by perturbation of liquid water structure. *Sci. Rep.*, 5:11526.

Sa, J.-H., Kwak, G.-H., Lee, B. R., Park, D.-H., Han, K., and Lee, K.-H. (2013). Hydrophobic amino acids as a new class of kinetic inhibitors for gas hydrate formation. *Sci. Rep.*, 3:2428.

Said, S., Govindaraj, V., Herri, J.-M., Ouabbas, Y., Khodja, M., Belloum, M., Sangwai, J. S., and Nagarajan, R. (2016). A study on the influence of nanofluids on gas hydrate formation kinetics and their potential: application to the co_2 capture process. *J. Nat. Gas Sci. Eng.*, 32:95 – 108.

Sarupria, S. and Debenedetti, P. G. (2012). Homogeneous nucleation of methane hydrate in microsecond molecular dynamics simulations. *J. Phys. Chem. Lett.*, 3:2942–2947.

Saykally, R. J. (2013). Air/water interface: Two sides of the acid–base story. *Nat. Chem.*, 5:82–84.

Schulz, H. D. and Zabel, M. (2006). *Marine Geochemistry*. Springer-Verlag Berlin Heidelberg, 2nd edition.

Schüth, F. (2005). Technology: Hydrogen and hydrates. *Nature (London)*, 434:712.

Seo, Y. and Kang, S.-P. (2010). Enhancing CO_2 separation for pre-combustion capture with hydrate formation in silica gel pore structure. *Chem. Eng. J.*, 161:308–312.

Seo, Y., Lee, H., and Uchida, T. (2002). Methane and carbon dioxide hydrate phase behavior in small porous silica gels: Three-phase equilibrium determination and thermodynamic modeling. *Langmuir*, 18:9164–9170.

Seo, Y., Lee, S., Cha, I., Lee, J. D., and Lee, H. (2009). Phase equilibria and thermodynamic modeling of ethane and propane hydrates in porous silica gels. *J. Phys. Chem. B*, 113:5487–5492.

Shen, W.-N. and Monson, P. A. (1995). Solid-fluid equilibrium in a nonlinear hard sphere triatomic model of propane. *J. Chem. Phys.*, 103:9756.

Shetty, R. and Escobedo, F. A. (2002). On the application of virtual gibbs ensembles to the direct simulation of fluid–fluid and solid–fluid phase coexistence. *J. Chem. Phys.*, 116:7957–7966.

Shimizu, H., Kumazaki, T., Kume, T., and Sasaki, S. (2002). Elasticity of single-crystal methane hydrate at high pressure. *Phys. Rev. B*, 65:212102–212106.

Siangsai, A., Rangsunvigit, P., Kitiyanan, B., Kulprathipanja, S., and Linga, P. (2015). Investigation on the roles of activated carbon particle sizes on methane hydrate formation and dissociation. *Chem. Eng. Sci.*, 126:383–389.

Sloan, E. D. (2003). Fundamental principles and applications of natural gas hydrates. *Nature*, 426:353–363.

Sloan, E. D. and Koh, C. A. (2007). *Clathrate Hydrates of Natural Gases*. Chemical Industries. CRC Press, 3rd edition.

Smelik, E. A. and King, H. E. (1997). Crystal-growth studies of natural gas clathrate hydrates using a pressurized optical cell. *Am. Mineralogist*, 82:88.

Smirnov, G. S. and Stegailov, V. V. (2012). Melting and superheating of sI methane hydrate: Molecular dynamics study. *J. Chem. Phys.*, 136:044523.

Smirnov, K. S. (2017). A modeling study of the methane hydrate decomposition in contact with the external surface of zeolite. *Phys. Chem. Chem. Phys.*, pages –.

Smirnov, V. G., Manakov, A. Y., Ukraintseva, E. A., Villevald, G. V., Karpova, T. D., Dyrdin, V. V., Lyrshchikov, S. Y., Ismagilov, Z. R., Terekhova, I. S., and Ogienko, A. G. (2016). Formation and decomposition of methane hydrate in coal. *Fuel*, 166:188–195.

Soper, A. K. and Benmore, C. J. (2008). Quantum differences between heavy and light water. *Phys. Rev. Lett.*, 101:065502.

Steinhardt, P. J., Nelson, D. R., and Ronchetti, M. (1983). Bond-orientational order in liquids and glasses. *Phys. Rev. B*, 28:784–805.

Strobel, T. A., Sloan, E. D., and Koh, C. A. (2009). Raman spectroscopic studies of hydrogen clathrate hydrates. *J. Chem. Phys.*, 130:014506.

Sun, L., Tanskanen, J. T., Hirvi, J. T., Kasa, S., Schatz, T., and Pakkanen, T. A. (2015). Molecular dynamics study of montmorillonite crystalline swelling: Roles of interlayer cation species and water content. *Chem. Phys.*, 455:23–31.

Susilo, R., Alavi, S., Ripmeester, J. A., and Englezos, P. (2008). Molecular dynamics study of structure h clathrate hydrates of methane and large guest molecules. *J. Chem. Phys.*, 128:194505.

Takeya, S., Uchida, T., Kamata, Y., Nagao, J., Kida, M., Minami, H., Sakagami, H., Hachikubo, A., Takahashi, N., Shoji, H., Khlystov, O., Grachev, M., and Soloviev, V. (2005). Lattice expansion of clathrate hydrates of methane mixtures and natural gas. *Angew. Chem. Int. Ed.*, 44:6928–6931.

Tanaka, H. (2012). Bond orientational order in liquids: Towards a unified description of water-like anomalies, liquid-liquid transition, glass transition, and crystallization. *Eur. Phys. J. E*, 35:113.

Thomas, C., Mousis, O., Picaud, S., and Ballenegger, V. (2009). Variability of the methane trapping in martian subsurface clathrate hydrates. *Planet. Space Sci.*, 57(1):42 – 47.

Trinh, T. T., Waage, M. H., van Erp, T. S., and Kjelstrup, S. (2015). Low barriers for hydrogen diffusion in sII clathrate. *Phys. Chem. Chem. Phys.*, 17:13808–13812.

Tsiberkin, K., Lyubimov, D. V., Lyubimova, T. P., and Zikanov, O. (2014). Evolution of a spherical hydrate-free inclusion in a porous matrix filled with methane hydrate. *Phys. Rev. E*, 89:023008.

Tsimpanogiannis, I. N. and Lichtner, P. C. (2013). Gas saturation resulting from methane hydrate dissociation in a porous medium: Comparison between analytical and pore-network results. *J. Phys. Chem. C*, 117:11104–11116.

Tung, Y.-T., Chen, L.-J., Chen, Y.-P., and Lin, S.-T. (2010). The growth of structure i methane hydrate from molecular dynamics simulations. *J. Phys. Chem. B*, 114:10804–10813.

Uchida, T., Ebinuma, T., and Ishizaki, T. (1999). Dissociation conditions measurements of methane hydrate in confined small pores of porous glass. *J. Phys. Chem. B*, 103:3659–3662.

Uchida, T., Ebinuma, T., Takeya, S., Nagao, J., and Narita, H. (2002). Effects of pore sizes on dissociation temperatures and pressures of methane, carbon dioxide, and propane hydrate in porous media. *J. Phys. Chem. B*, 106:820–826.

Udachin, K. A., Enright, G. D., Ratcliffe, C. I., and Ripmeester, J. A. (1997). Structure, stoichiometry, and morphology of bromine hydrate. *J. Am. Chem. Soc.*, 119:11481–11486.

Ueno, H., Akiba, H., Akatsu, S., and Ohmura, R. (2015). Crystal growth of clathrate hydrates formed with methane + carbon dioxide mixed gas at the gas/liquid interface and in liquid water. *New J. Chem.*, 39:8254–8262.

Vega, C., Abascal, J. L. F., and Nezbeda, I. (2006). Vapor-liquid equilibria from the triple point up to the critical point for the new generation of TIP4P-like models: TIP4P/Ew, TIP4P/2005, and TIP4P/Ice. *J. Chem. Phys.*, 125:034503.

Vega, C. and Monson, P. A. (1998). Solid–fluid equilibrium for a molecular model with short ranged directional forces. *J. Chem. Phys.*, 109:9938–9949.

Vega, C. and Noya, E. G. (2007). Revisiting the frenkel-ladd method to compute the free energy of solids: The einstein molecule approach. *J. Chem. Phys.*, 127:154113.

Vega, C., Paras, E. P. A., and Monson, P. A. (1992). Solid–fluid equilibria for hard dumbbells via monte carlo simulation. *J. Chem. Phys.*, 96:9060–9072.

Vega, C., Sanz, E., Abascal, J. L. F., and Noya, E. G. (2008). Determination of phase diagrams via computer simulation: methodology and applications to water, electrolytes and proteins. *J. Phys.: Condens. Matter*, 20:153101.

Verlet, L. (1967). Computer experiments on classical fluids: I. thermodynamical properties of lennard–jones molecules. *Phys. Rev.*, 159:98–103.

Vidal-Vidal, a., Perez-Rodriguez, M., and Pineiro, M. M. (2016). Direct transition mechanism for molecular diffusion in gas hydrates. *RSC Adv.*, 6:1966–1972.

Waage, M. H., Vlugt, T. J. H., and Kjelstrup, S. (2017). Phase diagram of methane and carbon dioxide hydrates computed by monte carlo simulations. *J. Phys. Chem. B*, 121:7336–7350.

Waite, W. F., Stern, L. A., Kirby, S. H., Winters, W. J., and Mason, D. H. (2007). Simultaneous determination of thermal conductivity, thermal diffusivity and specific heat in sI methane hydrate. *Geophys. J. Int.*, pages 767–774.

Wang, F., Luo, S.-J., Fu, S.-F., Jia, Z.-Z., Dai, M., Wang, C.-S., and Guo, R.-B. (2015). Methane hydrate formation with surfactants fixed on the surface of polystyrene nanospheres. *J. Mater. Chem. A*, 3:8316–8323.

Wierzchowski, S. J. and Monson, P. A. (2006). Calculating the phase behavior of gas-hydrate-forming systems from molecular models. *Ind. Eng. Chem. Res.*, 45:424–431.

Wierzchowski, S. J. and Monson, P. A. (2007). Calculation of free energies and chemical potentials for gas hydrates using monte carlo simulations. *J. Phys. Chem. B*, 111:7274–7282.

Wu, J.-Y., Chen, L.-J., Chen, Y.-P., and Lin, S.-T. (2015). Molecular dynamics study on the equilibrium and kinetic properties of tetrahydrofuran clathrate hydrates. *J. Phys. Chem. C*, 119:1400–1409.

Xu, P., Lang, X., Fan, S., Wang, Y., and Chen, J. (2016). Molecular dynamics simulation of methane hydrate growth in the presence of the natural product pectin. *J. Phys. Chem. C*, 120:5392–5397.

Yagasaki, T., Matsumoto, M., and Tanaka, H. (2015). Effects of thermodynamic inhibitors on the dissociation of methane hydrate: a molecular dynamics study. *Phys. Chem. Chem. Phys.*, 17:32347–32357.

Yan, L., Chen, G., Pang, W., and Liu, J. (2005). Experimental and modeling study on hydrate formation in wet activated carbon. *J. Phys. Chem. B*, 109:6025–6030.

Yan, Q. and de Pablo, J. J. (1999). Hyper-parallel tempering monte carlo: Application to the lennard-jones fluid and the restricted primitive model. *J. Chem. Phys.*, 111:9509–9516.

Yan, Q. and de Pablo, J. J. (2000). Hyperparallel tempering monte carlo simulation of polymeric systems. *J. Chem. Phys.*, 113:1276–1282.

Yang, M., Fu, Z., Zhao, Y., Jiang, L., Zhao, J., and Song, Y. (2016a). Effect of depressurization pressure on methane recovery from hydrate–gas–water bearing sediments. *Fuel*, 166:419–426.

Yang, Y., Shin, D., Choi, S., Lee, J.-W., Cha, M., Kim, D., and Yoon, J.-H. (2016b). Cage occupancy and stability of n $_2$ o-encaged structure i and II clathrate hydrates. *Energy Fuels*, 30:9628–9634.

Yezdimer, E. M., Cummings, P. T., and Chialvo, A. A. (2002). Determination of the gibbs free energy of gas replacement in SI clathrate hydrates by mol. simul. *J. Phys. Chem. A*, 106:7982–7987.

Yoon, J.-H., Chun, M.-K., and Lee, H. (2002). Generalized model for predicting phase behavior of clathrate hydrate. *AIChE J.*, 48:1317–1330.

Zhang, Z. (2015). Heat transfer during the dissociation of hydrate in porous media. *Proc. Eng.*, 126:502–506.

Zhang, Z., Walsh, M. R., and Guo, G.-J. (2015). Microcanonical molecular simulations of methane hydrate nucleation and growth: evidence that direct nucleation to sI hydrate is among the multiple nucleation pathways. *Phys. Chem. Chem. Phys.*, 17:8870–8876.

Zhao, W., Francisco, J. S., and Zeng, X. C. (2016). CO separation from h2 via hydrate formation in single-walled carbon nanotubes. *J. Phys. Chem. Lett.*, 7:4911–4915.

Zhao, W., Wang, L., Bai, J., Francisco, J. S., and Zeng, X. C. (2014). Spontaneous formation of one-dimensional hydrogen gas hydrate in carbon nanotubes. *J. Am. Chem. Soc.*, 136:10661–10668.

Zhou, X., Long, Z., Liang, S., He, Y., Yi, L., Li, D., and Liang, D. (2016). In situ raman analysis on the dissociation behavior of mixed CH_4–CO_2 hydrates. *Energy Fuels*, 30:1279–1286.

Zhu, J., Du, S., Yu, X., Zhang, J., Xu, H., Vogel, S. C., Germann, T. C., Francisco, J. S., Izumi, F., Momma, K., Kawamura, Y., Jin, C., and Zhao, Y. (2014). Encapsulation kinetics and dynamics of carbon monoxide in clathrate hydrate. *Nat. Comm.*, 5:4128.